IDENTIFICATION OF GEOTHERMAL ANOMALIES WITH THERMAL INFRARED REMOTE SENSING AND FIELD APPLICATIONS

A THESIS SUBMITTED TO
THE GRADUATE SCHOOL OF NATURAL AND APPLIED SCIENCES
OF
MIDDLE EAST TECHNICAL UNIVERSITY

BY

SELİM CAMBAZOĞLU

IN PARTIAL FULFILLMENT OF THE REQUIREMENTS
FOR
THE DEGREE OF DOCTOR OF PHILOSOPHY
IN
GEOLOGICAL ENGINEERING

JULY 2024

Approval of the thesis:

IDENTIFICATION OF GEOTHERMAL ANOMALIES WITH THERMAL INFRARED REMOTE SENSING AND FIELD APPLICATIONS

submitted by **SELİM CAMBAZOĞLU** in partial fulfillment of the requirements for the degree of **Doctor of Philosophy in Geological Engineering, Middle East Technical University** by,

Prof. Dr. Naci Emre Altun
Dean, Graduate School of **Natural and Applied Sciences** ________________

Prof. Dr. Erdin Bozkurt
Head of the Department, **Geological Engineering** ________________

Prof. Dr. Haluk Akgün
Supervisor, **Geological Engineering, METU** ________________

Examining Committee Members:

Prof. Dr. Asuman Günal Türkmenoğlu
Geological Engineering, METU ________________

Prof. Dr. Haluk Akgün
Geological Engineering, METU ________________

Prof. Dr. Uğur Murat Leloğlu
Astronautical Engineering, TAAU ________________

Prof. Dr. Candan Gökçeoğlu
Geological Eng., Hacettepe University ________________

Assoc. Prof. Dr. Mustafa Kerem Koçkar
Civil Eng., Hacettepe University ________________

Date: 23.07.2024

I hereby declare that all information in this document has been obtained and presented in accordance with academic rules and ethical conduct. I also declare that, as required by these rules and conduct, I have fully cited and referenced all material and results that are not original to this work.

Name Last name : Selim Cambazoğlu

Signature :

ABSTRACT

IDENTIFICATION OF GEOTHERMAL ANOMALIES WITH THERMAL INFRARED REMOTE SENSING AND FIELD APPLICATIONS

Cambazoğlu, Selim
Doctor of Philosophy, Geological Engineering
Supervisor : Prof. Dr. Haluk Akgün

July 2024, 237 pages

Western Anatolia, Türkiye is among the most important geothermal regions in the world. In search of new and blind geothermal fields where abundant additional potential is present, this study focuses on combining satellite based alteration mineral, lineament and geothermal anomaly mapping with field and laboratory applications.

Alteration mineral maps were generated by utilizing different methodologies and thermal anomaly map was generated through correction of non-geothermal effects by utilizing ASTER satellite images. DEM and ASTER images were used to generate lineament map of the study area.

In order to compare the results of generated maps, each application was matched with field applications where XRD analyses were performed for identification of alteration minerals, long term temperature measurements were collected through data loggers developed as part of this study and drone based orthophotographs were collected along with scanline surveys to identify area based fracture system. Finally, GIS based Multi-criteria decision analysis (MCDA) was performed to assess geothermal favorability and compare the results with field measurements.

The results have shown that alteration mineral mapping is compatible with the results of the XRD analyses. Satellite based thermal anomaly mapping have presented inconclusive results due to climatic conditions and shallow groundwater presence masking anomalies to be detected at the surface. Field temperature measurements have provided results compatible with decreasing reservoir depth, underlining the importance of field applications in exploration of blind geothermal fields. GIS based MCDA have shown that known deep geothermal wells and locations with highest thermal gradient are located in most favorable class.

Keywords: Thermal Remote Sensing, GIS, Geothermal, Alteration Mineral Mapping, Büyük Menderes Graben

ÖZ

TERMAL KIZILÖTESİ UZAKTAN ALGILAMA VE ARAZİ UYGULAMALARI İLE JEOTERMAL ANOMALİLERİN TAYİNİ

Cambazoğlu, Selim
Doktora, Jeoloji Mühendisliği
Tez Yöneticisi: Prof. Dr. Haluk Akgün

Temmuz 2024, 237 sayfa

Batı Anadolu, Türkiye, Dünya'daki en önemli jeotermal alanlardan biridir. Yeni ve kayda değer potansiyelin var olduğu kör jeotermal alanların belirlenmesi amacıyla bu çalışma kapsamında uydu görüntülerinden alterasyon mineralleri, çizgiselliğin ve jeotermal anomali haritalaması çalışmalarının arazi ölçümleri ile laboratuvar analizleriyle bir araya getirilmesi hedeflenmiştir.

Bu kapsamda, ASTER uydu görüntüleri kullanılarak farklı yöntemler ile alterasyon mineral haritaları ve jeotermal olmayan etkilerin düzeltilmesi ile termal anomali yüzey sıcaklığı haritası elde edilmiştir. Ayrıca sayısal yükseklik modeli ve ASTER görüntüleri kullanılarak çizgisellik haritası oluşturulmuştur.

Oluşturulan haritaların sonuçlarının karşılaştırılması amacıyla her yönteme karşılık gelen arazi çalışmaları gerçekleştirilmiştir. Alterasyon minerallerinin belirlenmesi için XRD analizleri yapılmış, bu çalışma kapsamında geliştirilen kayıtçılar kullanılarak uzun dönem sıcaklık ölçümleri alınmış ve insansız hava aracı ile alınan görüntüler ve hat etüdleri ile alansal çatlak sistemi değerlendirilmiştir. Son olarak

CBS tabanlı çok-kriterli karar analizi yöntemi ile sahanın jeotermal uygunluğu değerlendirilmiş ve sonuçlar arazi ölçümleri ile karşılaştırılmıştır.

Elde edilen sonuçlar alterasyon mineral haritalamasının XRD analiz sonuçları ile uyumlu olduğunu göstermiştir. Uydu görüntüsü bazlı termal anomali haritalaması çalışması bölgenin iklim ve sığ yeraltı suyu koşulları nedeni ile kesin bir sonuç ortaya koymamasına karşın araziden alınan sıcaklık ölçümleri güneyden kuzeye sığlaşan rezervuar derinliği ile uyumlu sonuçlar ortaya koymuştur ve bu bağlamda, kör jeotermal sahaların arama çalışmalarında arazi ölçümlerinin önemini net bir şekilde ortaya koymuştur. CBS bazlı çok-kriterli karar analizi sonuçları, derin jeotermal kuyularının ve araziden elde edilen en yüksek termal gradyan değerine sahip ölçüm noktalarının lokasyonlarının en uygun jeotermal alan sınıfında yer aldığını göstermiştir.

Anahtar Kelimeler: Termal Uzaktan Algılama, CBS, Jeotermal, Alterasyon Mineral Haritalaması, Büyük Menderes Grabeni

Dedication

To my mother

Who believed in me, even when I did not; always.

ACKNOWLEDGMENTS

The author wishes to express his deepest gratitude to his supervisor Prof. Dr. Haluk Akgün for his guidance, advice, criticism, encouragements and insight throughout the research.

The author would also like to thank Assoc. Prof. Mustafa Kerem Koçkar his endless support through this study.

Valuable comments and contributions, and continued support and patience of Thesis Examination Committee members Prof. Dr. Asuman Günal Türkmenoğlu and Prof. Dr. Uğur Murat Leloğlu are gratefully acknowledged.

I would like to thank Prof. Dr. Candan Gökçeoğlu for his valuable comments that enabled this study to be better.

I would like to express my sincere thanks to Ms. Gözde Pınar Yal for her support, brainstorming and guidance throughout this study.

I would also like to thank Dr. Arzu Arslan Kelam for her support both during fieldwork and also during laboratory assessments as well as her insights.

I would like to thank SDS Energy and especially Mr. İrfan Acar and Dr. Osman Şen for supporting and encouraging the scientific research in the license area and Mr. Kutlu Celtemen who supported field applications along with Mr. Salih Kaymak for his support during field works.

Finally, I would like to thank my family, Mustafa Kemal Cambazoğlu, Özlem Cambazoğlu, Gencer Cambazoğlu, Dilek Önay and Adviye İpek Cambazoğlu for their never ending support and patience.

This work has been partially funded by the Middle East Technical University Scientific Research Projects Coordination Unit under grant number GAP-10185.

TABLE OF CONTENTS

ABSTRACT v

ÖZ… vii

ACKNOWLEDGMENTS x

TABLE OF CONTENTS xi

LIST OF TABLES xiv

LIST OF FIGURES xvi

CHAPTERS

1 INTRODUCTION 1

2 STUDY AREA 5

2.1 Geomorphology 6

2.2 Climate 11

2.3 Geology of the Study Area 13

2.3.1 General Geology of Büyük Menderes Graben 13

2.3.2 Geothermal Geology of the Kuyucak Area 16

3 ALTERATION MINERAL MAPPING 19

3.1 Literature Review 21

3.1.1 Literature Review on Hydrothermal Alteration 21

3.1.2 Literature Review for Satellite Based Alteration Mineral Mapping 25

3.1.3 Literature Review on Use of XRD Analyses in Geothermal Exploration 26

3.2 Satellite Image Analysis 28

3.2.1 ASTER Satellite 28

3.2.2 Image Analysis Methods 30

3.2.3 Image Processing and Analysis 34
3.3 Fieldwork and Sample Collection 42
3.4 XRD Analysis 44
3.4.1 Sample Preparation 44
3.4.2 Interpretation of XRD Analysis Results 49
3.5 Comparison of XRD and Satellite Image Results 57
3.6 Results and Discussion of Results for Alteration Mineral Mapping 63
4 LINEAMENT MAPPING 65
4.1 Literature Review 66
4.2 Lineament Extraction from Satellite Imagery 68
4.3 Lineament Extraction from Drone Imagery 75
4.4 Results and Discussion of Results of Lineament Mapping 83
5 SHALLOW TEMPERATURE MAPPING 85
5.1 Literature Review 85
5.1.1 Literature Review on Shallow Temperature Surveys for Geothermal Exploration 87
5.1.2 Literature Review on Use of Satellite Imagery for Geothermal Anomaly Detection 90
5.2 Equipment for Shallow Temperature Surveys 92
5.2.1 Sensor Calibration and Co-calibration 94
5.3 Fieldwork 111
5.3.1 First Fieldwork 111
5.3.2 Second Fieldwork 117
5.3.3 Third Fieldwork 129

5.4 Results of the Data Collected from the Field 134

5.5 Satellite Image Analysis 146

5.5.1 Pre-processing of ASTER Images 149

5.5.2 Topographical Slope and Albedo Correction 151

5.5.3 Heat Energy Correction 155

5.5.4 Thermal Inertia Correction 156

5.5.5 Elevation Correction 161

5.6 Results of the Satellite Based Temperature Mapping 163

5.7 Results and Conclusion on Shallow Temperature Mapping 171

6 GIS BASED MULTI CRITERIA DECISION ANALYSIS 175

6.1 Literature Review 176

6.2 Methodology 178

6.3 Data Layers 182

6.4 Results and Conclusion on GIS Based MCDA 192

7 RESULTS AND DISCUSSION 193

8 CONCLUSION AND RECOMMENDATION FOR FUTURE STUDIES ..197

REFERENCES 201

APPENDICES

A. Example Arduino Code for Data Loggers 229

CURRICULUM VITAE 233

LIST OF TABLES

TABLES

Table 3.1. Conditions for formation of hydrothermal alteration products 24
Table 3.2. Sensor characteristics of ASTER. 30
Table 3.3. XRD Sample locations and IDs from north to south.............................48
Table 3.4. Mineral abbreviations used in XRD analysis results figures (Warr, 2020; Warr, 2021)...49
Table 3.5. XRD Sampling locations and identified minerals from thin film samples from North to South...53
Table 3.6. Minerals identified from powder XRD results from north to south.......55
Table 3.7. XRD Sampling Locations from South to North....................................58
Table 3.8 Min. Max. and Average values for Indices for the processed images....59
Table 3.9. Pixel values of XRD sample locations...62
Table 4.1. Drone image acquisition information..77
Table 4.2. Discontinuity dip amount and dip directions acquired from scanline survey measurements (Akgün et al., 2024). 78
Table 4.3. Scanline field survey measurements (Akgün et al., 2024). 79
Table 5.1. Arduino connections..93
Table 5.2. Logger-2 calibration results...100
Table 5.3. Logger-5 calibration results...101
Table 5.4. Logger-6 calibration results...102
Table 5.5. Logger-7 calibration results...103
Table 5.6. Logger-8 calibration results...104
Table 5.7. Logger-10 calibration results...105
Table 5.8. Logger-11 calibration results...106
Table 5.9. Logger-12 calibration results...107
Table 5.10. Calibration results..109
Table 5.11. Surface parameters of logger locations. 113
Table 5.12. Logger to UART cable connections..118

Table 5.13. Summary table for each data logger from the second fieldwork for battery replacement. 124
Table 5.14. Logger ID and location list with summary notes. 130
Table 5.15. Summary statistics of the data collected from the field. 135
Table 5.16. Summary statistics of the temperature data fit to sinusoidal wave function. 137
Table 5.17. Annual average temperature gradient values of each logger. 142
Table 5.18. Dates of minimum temperatures for each sensor according to sinusoidal fit results. 144
Table 5.19. April 21st, 2022 gradient values of each logger. 145
Table 5.20. ASTER image information for images utilized in the analyses. 146
Table 5.21. Gain coefficients of ASTER bands (Abrams, 2000). 150
Table 5.22. Weighing coefficients for albedo image for VNIR bands of ASTER day-time image. 152
Table 5.23. Temperature comparison of ASTER image data and meteorological station data (units are in °C). 157
Table 5.24. Day-night image combination coefficients. 159
Table 5.25. Descriptive statistics of the NDVI layer. 164
Table 5.26. Coefficients of determination for the main and masked images. 171
Table 6.1. Layers and data sources utilized in TOPSIS analysis. 179
Table 6.2. Pairwise comparison matrix and weights of layers. 181

LIST OF FIGURES

FIGURES

Figure 1.1. Flowchart of the overall study 4
Figure 2.1. Location map of the study area. 7
Figure 2.2. Digital Elevation Model of the study area and its vicinity. 8
Figure 2.3. Slope map of the study area and its vicinity. 9
Figure 2.4. Aspect map of the study area and its vicinity. 10
Figure 2.5. Köppen-Geiger climate map of the study area and its vicinity (adapted from Beck et al., 2018). 11
Figure 2.6. Location of ground water wells and irrigation cooperatives within the study area (DSİ, 2012; Aydin and Akçay, 2023). 12
Figure 2.7. Geological map of the region (modified from MTA, 2002). 15
Figure 2.8. Geologıcal map of the study area (Yal et al., 2017). 18
Figure 3.1. Flow chart for the alteration mineral mapping studies. 20
Figure 3.2. Generalized summary of the temperature ranges over which alumino-silicate alteration minerals have been observed (adapted from Henley and Ellis, 1983). 23
Figure 3.3. Location of the study area on the ASTER satellite image. 29
Figure 3.4. Comparison between ASTER and LandSat-7 (ETM+) and Landsat-8 (OLI, TIRS) sensors (Duda et al., 2015). 29
Figure 3.5. Examples from reflectance spectra with ASTER band locations (ASTER band spectral ranges adapted from Abrams, 2000 and mineral spectral signatures adapted from Clark et al., 1993). 31
Figure 3.6. Example laboratory reflectance spectra resampled to ASTER band passes 33
Figure 3.7. Relative band depth method (after Crowley et al., 1989). 34
Figure 3.8. (4+6)/5 band ratio magnifying advanced argillic alteration. Areas dominated by alteration minerals are in red color. 36

Figure 3.9. 742 band combination; blue and purple colors indicate altered zones with high clay content and overlain green color is the vegetation mask. 37
Figure 3.10. Advanced argillic alteration, 5/6-7/6-7/5 band combination (Phengite-Muscovite-Kaolinite) (Hewson et al., 2001, 2004) overlain by bright green colored vegetation mask. 38
Figure 3.11. 4/5 (alunite-red) - 4/6 (kaolinite-green) - 4/7 (hydroxil minerals-blue) band combination overlain by vegetation mask (bright green)............................. 39
Figure 3.12. Advanced argillic alteration image.. 40
Figure 3.13. Phylllic alteration image.. 41
Figure 3.14. Alunite index image... 41
Figure 3.15. Kaolinite index image.. 42
Figure 3.16. Alteration sample locations. 43
Figure 3.17. Sample weighing after sieving. 45
Figure 3.18. NaOAc treatment.. 45
Figure 3.19. Centrifuge setup.. 46
Figure 3.20. Ethylene glycol treatment... 46
Figure 3.21. Samples before 300°C treatment. 47
Figure 3.22. Samples before 550°C treatment. 47
Figure 3.23. Samples after 550°C treatment. 48
Figure 3.24. XRD results of AY-2 Sample (13) 50
Figure 3.25. XRD results of DMR-Son Sample (131).. 50
Figure 3.26. XRD results of DMR-3 Sample (15)... 51
Figure 3.27. XRD results of DMR-1 Sample (14)... 51
Figure 3.28. XRD results of Kayran Sample (17)... 52
Figure 3.29. XRD results of Dereağzı Sample (18)... 52
Figure 3.30. XRD Results of the powder samples... 56
Figure 3.31. Advanced argillic alteration image.. 59
Figure 3.32. Phylllic alteration image.. 60
Figure 3.33. Alunite index image... 60
Figure 3.34. Kaolinite index image.. 61

Figure 4.1. Flow chart for the lineament mapping studies. 65
Figure 4.2. Principal Component image of the study area. 70
Figure 4.3. Digital Elevation Model (DEM) of the study area. 71
Figure 4.4. Hillshade image generated from DEM based on ASTER daytime image acquisition. 72
Figure 4.5. Extracted lineaments overlain on DEM image of the study area. 73
Figure 4.6. Extracted lineaments overlain on PCA resultant RGB image. 74
Figure 4.7. Rose diagram of the extracted lineaments. 75
Figure 4.8. Scanline and drone data acquisition location. 76
Figure 4.9. a) N-S image acquisition, b) E-W image locations, c) N-S image locations. 77
Figure 4.10. Stereonet representation of the discontinuities interpreted from measurements acquired as part of scanline survey in the field (Akgün et al., 2024). 78
Figure 4.11. Lineaments extracted from drone imagery. 82
Figure 5.1. Flow chart of the shallow temperature mapping and comparison steps. 86
Figure 5.2. Location of ground water wells and irrigation cooperatives within the study area (DSİ, 2012; Aydin and Akçay, 2023). 89
Figure 5.3. Arduino connection diagram. 94
Figure 5.4. Logger 2 calibration data. 95
Figure 5.5. Logger 5 calibration data. 95
Figure 5.6. Logger 6 calibration data. 96
Figure 5.7. Logger 7 calibration data. 96
Figure 5.8. Logger 8 calibration data. 97
Figure 5.9. Logger 10 calibration data. 97
Figure 5.10. Logger 11 calibration data. 98
Figure 5.11. Logger 12 calibration data. 98
Figure 5.12. Logger-5 vs. logger-12 calibration data. 110
Figure 5.13. Lineament map of the study area. 112

Figure 5.14. 3DMT, reservoir depth (Yal et al., 2017). 113
Figure 5.15. Drilling locations. 114
Figure 5.16. KS1 location drilling operation. 115
Figure 5.17. KS1 location logger preparation. 115
Figure 5.18. KS1 location deployed logger. 115
Figure 5.19. Backfilling PVC casing. 116
Figure 5.20. Location 8, KS-2, data retrieval. 119
Figure 5.21. Location 8, KS-2, data retrieval. 120
Figure 5.22. Location 8, KS-2, location market. 120
Figure 5.23.Location 6, tabela, data collection preparation. 121
Figure 5.24. Location 6, tabela, data collection preparation. 122
Figure 5.25. Location 3, Benzinlik, water damage. 122
Figure 5.26. Location 3, Benzinlik, water damage. 123
Figure 5.27. Location 4, Kule, re-deployment. 123
Figure 5.28. Location 1, KS-2, Logger 2, all data up-to 25 February data collection. 125
Figure 5.29. Location 2, KS-1, Logger-5, water damage, data until 4th of December, 2021 126
Figure 5.30. Location 3, Benzinlik, Logger-6, water damage, data until 30th of November, 2021. 126
Figure 5.31. Location 4, Logger-7, Kule, all data compete until data collection on 26th of February. 127
Figure 5.32. Location 5, Tabela, Logger-8, data collected, until 29.01.2022 127
Figure 5.33. Location 6, Yatık, Logger-10, all data complete until data collection on 26 February 128
Figure 5.34. Location 8, Dolmuslar, Logger-11, data available until January 2nd, 2022, battery at 3.36V. 128
Figure 5.35. Location 1, KS-2, Logger 2, data up to March 2. 131
Figure 5.36. Location 2, KS-1, Logger-5, water damage, data until 4th of December, 2021 131

Figure 5.37. Location 3, Benzinlik, Logger-6, water damage, data until 30th of November, 2021. 132
Figure 5.38. Location 4, Logger-7, Kule, data until data 27/08/2023. 132
Figure 5.39. Location 5, Tabela, Logger-8, data collected, until 25.07.2022 133
Figure 5.40. Location 6, Yatık, Logger-10, all data complete until data collection on 24/06/2023 133
Figure 5.41. Location 8, Dolmuslar, Logger-11, data available until 02/01/2022, 27.04.2022 final date. 134
Figure 5.42. Location 1, KS-2, Logger 2, sinusoidal data fit. 138
Figure 5.43. Location 2, KS-1, Logger-5, sinusoidal data fit. 138
Figure 5.44. Location 3, Benzinlik, Logger-6, sinusoidal data fit. 139
Figure 5.45. Location 4, Logger-7, Kule, sinusoidal data fit. 139
Figure 5.46. Location 5, Tabela, Logger-8, sinusoidal data fit. 140
Figure 5.47. Location 6, Yatık, Logger-10, sinusoidal data fit. 140
Figure 5.48. Location 8, Dolmuslar, Logger-11, sinusoidal data fit. 141
Figure 5.49. Linear regression fit between UTM Y Coordinate and Thermal Gradient at sensors on April 21st, 2022 for sensors between 3 m and 5 m. 145
Figure 5.50. ASTER daytime image dated 16.04.2015. 147
Figure 5.51. ASTER night-time image dated 23.04.2015. 148
Figure 5.52. Shaded relief (hillshade) map of the study area at the date and time of ASTER day-time image acquisition on 16.04.2015. 153
Figure 5.53. Surface albedo map generated from day-time ASTER image. 154
Figure 5.54. Variance values of day-time and night-time images. 156
Figure 5.55. Distribution of meteorology stations and ASTER day-, night-time image coverage. 159
Figure 5.56. Corrected relative temperature map of the study area. 160
Figure 5.57. Scatter-plot of night-time ASTER surface temperature vs. elevation (DEM). 161
Figure 5.58. Elevation corrected surface temperature image. 162
Figure 5.59. Histogram of the NDVI layer. 164

Figure 5.60. NDVI image of the study area. 166
Figure 5.61. Scatterplot of final surface temperature image versus lineament density map. 167
Figure 5.62. Scatterplot of final surface temperature image versus south-to-north index map. 167
Figure 5.63. Scatterplot of final surface temperature image versus lineament density map with 0.671838 NDVI threshold value. 168
Figure 5.64. Scatterplot of final surface temperature image versus lineament density map with 0.53932 NDVI threshold value. 168
Figure 5.65. Scatterplot of final surface temperature image versus lineament density map with 0. 0.406802 NDVI threshold value. 169
Figure 5.66. Scatterplot of final surface temperature image versus south-to-north index with 0.671838 NDVI threshold value. 169
Figure 5.67. Scatterplot of final surface temperature image versus south-to-north index with 0.53932 NDVI threshold value. 170
Figure 5.68. Scatterplot of final surface temperature image versus south-to-north index with 0.406802 NDVI threshold value. 170
Figure 6.1. Flow chart for the GIS based MCDA studies. 175
Figure 6.2. Elevation corrected surface temperature image. 183
Figure 6.3. Lineament Density layer. 184
Figure 6.4. Distance to Cover Units layer. 185
Figure 6.5. Advanced Argillic Alteration layer. 186
Figure 6.6. Phyllic Alteration Layer. 187
Figure 6.7. Kaolinite Index Layer. 188
Figure 6.8. Alunite Index Layer. 189
Figure 6.9. TOPSIS result map. 190
Figure 6.10. Favorability classes. 191

CHAPTER 1

INTRODUCTION

The purpose of this study is to identify geothermal anomalies through assessment of satellite images and field applications through utilization of open-source datasets (e.g., satellite data, digital elevation models, meteorological data) and off the shelf equipment for long term monitoring of temperature. The cost in geothermal exploration process increases from reconnaissance to detailed assessment and the highest cost incurs as part of the drilling campaign (Cambazoğlu et al., 2019). In order to identify the most suitable locations for further exploration, the purpose of this study is to allow a cost effective, affordable and accessible methodology for assessment of geothermal anomalies in a blind geothermal area where no surface manifestations are present. More importantly, the purpose of this study is to provide a straight forward methodology in a blind geothermal area having climate conditions different from previously conducted similar studies in desert environment with limited vegetation cover (e.g., Coolbaugh et al., 2007a; Kratt et al., 2009; Sladek et al, 2009). Therefore, through combining and correlating desktop studies with field applications for each methodology (i.e., alteration mineral mapping, lineament mapping and temperature mapping), this study attempted to allow a comprehensive resource for any future application for geothermal exploration and anomaly detection.

The satellite data assessment included alteration mineral mapping, lineament mapping and temperature anomaly mapping whereas field applications included alteration mineral sampling for XRD analysis, drone image acquisition and scanline surveys for lineament mapping, and design and deployment of long term temperature loggers. Therefore, each desktop assessment was combined with specific field applications to compare the datasets. For this purpose, Kuyucak geothermal area, located within Aydın province in the Büyük Menderes Graben was selected since Büyük Menderes Graben is the most important geothermal area in Turkey with more than 1000 MW (mega-watt) installed power capacity as of 2023.

During this study, several steps have been followed involving satellite image analysis, field applications including shallow borehole drilling and temperature measurements as well as sample collection for laboratory tests and drone image acquisition for lineament extraction, XRD (X-Ray Diffraction) laboratory tests, and finally GIS applications to assess and correlate the acquired data.

As part of desktop studies, ASTER (Advanced Spaceborne Thermal Emission Radiometer) satellite images were used to derive surface temperature map as well as to perform alteration mineral mapping. Furthermore, previous site specific borehole and geophysical datasets were utilized to correlate the temperature survey results. Along with these, meteorological station and topographical map datasets were acquired from relevant government organizations and utilized as part of this study.

Field applications included development of temperature data loggers, drilling 5 m shallow temperature boreholes and data collection, sample collection for XRD analysis for alteration mineral identification as well as drone based image acquisition and scanline surveys.

Laboratory works included XRD analysis of samples acquired from the field.

GIS applications were performed in order to compile all the acquired data and finally to assess the results.

A flowchart of the overall study is presented in Figure 1.1 to summarize each study and survey as well as their connection.

To the knowledge of the author, this study is first of its kind in terms of long term shallow temperature measurements in Türkiye and in a Mediterranean climate region. Furthermore, to the knowledge of the author, this is the first study combining desktop studies, field measurements and laboratory tests in terms of alteration mineral mapping, temperature mapping and lineament mapping to provide a comprehensive geothermal feasibility assessment through utilization of a GIS based MCDA methodology at a blind geothermal area in Türkiye.

This dissertation is organized in eight different chapters where, in this Chapter 1 – Introduction, overall purpose and organization of this study is presented. The study area is discussed in terms of location, geology and geothermal geology in Chapter 2 – Study Area; alteration mineral mapping methods in terms of both satellite image and laboratory works are discussed in Chapter 3 – Alteration Mineral Mapping. Following this, lineament extraction from both field drone surveys and satellite imagery and their comparison is presented in Chapter 4 – Lineament Extraction. The data logger development, shallow borehole drilling and satellite image analysis for temperature mapping is discussed in Chapter 5 – Shallow Temperature Mapping; and data compilation and assessment within Geographic Information Systems (GIS) environment by utilizing datasets acquired in previous sections is explained in Chapter 6 – GIS Based Multi Criteria Decision Analysis. Following all the assessments, results of applied methods are discussed collectively in Chapter 7 – Results and Discussion. Finally, Chapter 8 – Conclusion and Recommendation for Future Studies are presented where the limitation of this study, possible improvements and recommendation for future studies are discussed.

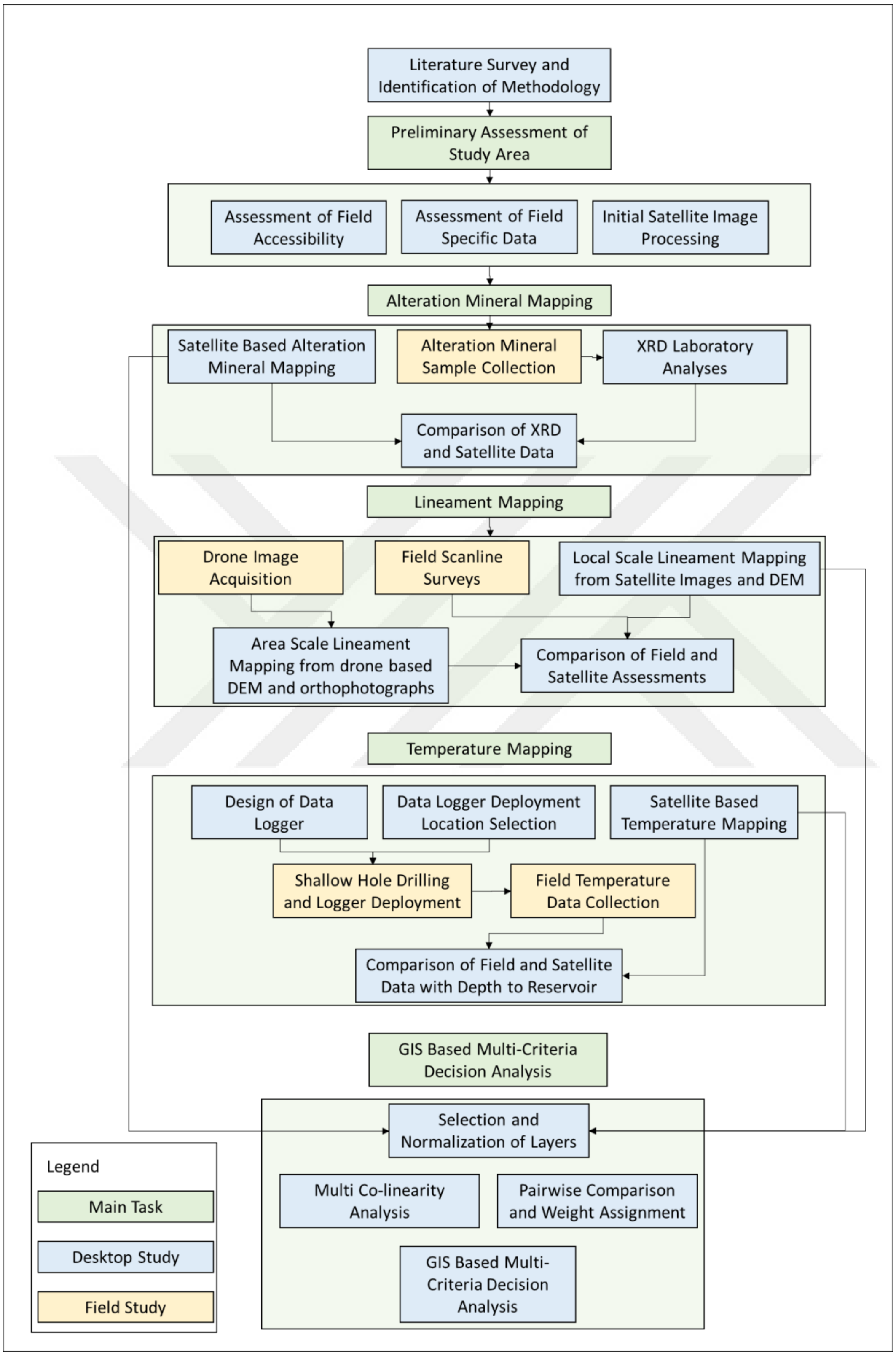

Figure 1.1. Flowchart of the overall study

CHAPTER 2

STUDY AREA

The study area is located at the northern flank of Büyük Menderes Graben at Kuyucak district of Aydın province, in the Aegean region of western Türkiye. The study area is immediately north of Kuyucak district center and 6 km northeast of Nazilli district center, and includes Sinekler, Yalınkuyu, Kestel, Demirciler, Kozdere, Çamköy, Haydarlı and Ovacık settlement areas from south to north, and Kayran settlement at the northeast as well as Pamukören at the southeast (Figure 2.1). Kuyucak district of Aydin Province is located on İzmir-Denizli railway and E-24 motorway, and approximately 10 km north of Aydin city center. Kuyucak district is bounded by Buldan and Sarayköy district of Denizli province from east, Nazilli district from west, Sarıgöl district of Manisa province from north and Karacasu district from south. The study area is located at the northern flank of Büyük Menderes Graben bounded by normal faults. The area is located on a relatively basement block north of a tectonic depression. Büyük Menderes Graben has E-W trend, is a regional graben and extends from east of Denizli Province to Aegean Sea in the west reaching approximately 200 km E-W length. The width of the graben in N-S direction varies from place to place and is 30 km in Söke, 20 km in Germencik, 10 km in Aydin city center, 20 km in Salavatlı and 5 km in Buharkent districts.

The study area is bounded by X: 622540 and Y: 4212162 coordinates from northwest, and X: 636212 and Y: 4196079 coordinates from southeast according to UTM (universal transverse Mercator) coordinate system zone 35 North and ED50 (European 1950) datum.

2.1 Geomorphology

The Büyük Menderes Graben has asymmetric graben characteristics and the slip amounts of step-faults at the northern flank of the graben is higher when compared with the southern boundary faults. Büyük Menderes Graben is divided into two by Kızılcagedik Horst located north of Germencik district. The secondary graben north of the main graben is named Arzular Graben. Prominent horst-graben structures in the region from south to north are Koçarlı Horst, Büyük Menderes Graben, Kızılcagedik Horst, Arzular Graben and Bozköy Horst. Furthermore, Gümüşdağ (Samsundağ) Horst is located due west. The study area is located approximately WNW of Çamur-Bozköy field.

The digital elevation, slope and aspect maps of the study area are generated by digitization of contour lines of 1:25.000 scale topographic maps in GIS environment. Elevation within the study area ranges from approximately 62 m to 1574 m while the average elevation is approximately 550 m (Figure 2.2). The slope map generated as the first derivative of DEM shows that the values within the study area range between 0° and 53° while the average value is approximately 16° (Figure 2.3). The slope orientation varies throughout the study area and the general trend in the west is due east, south-southeast while generally due west-northwest-north in the eastern section of the study area (Figure 2.4). In summary, the study area is located within an area controlled by normal faults and is relatively at a high elevation above sea level with moderately inclined topography.

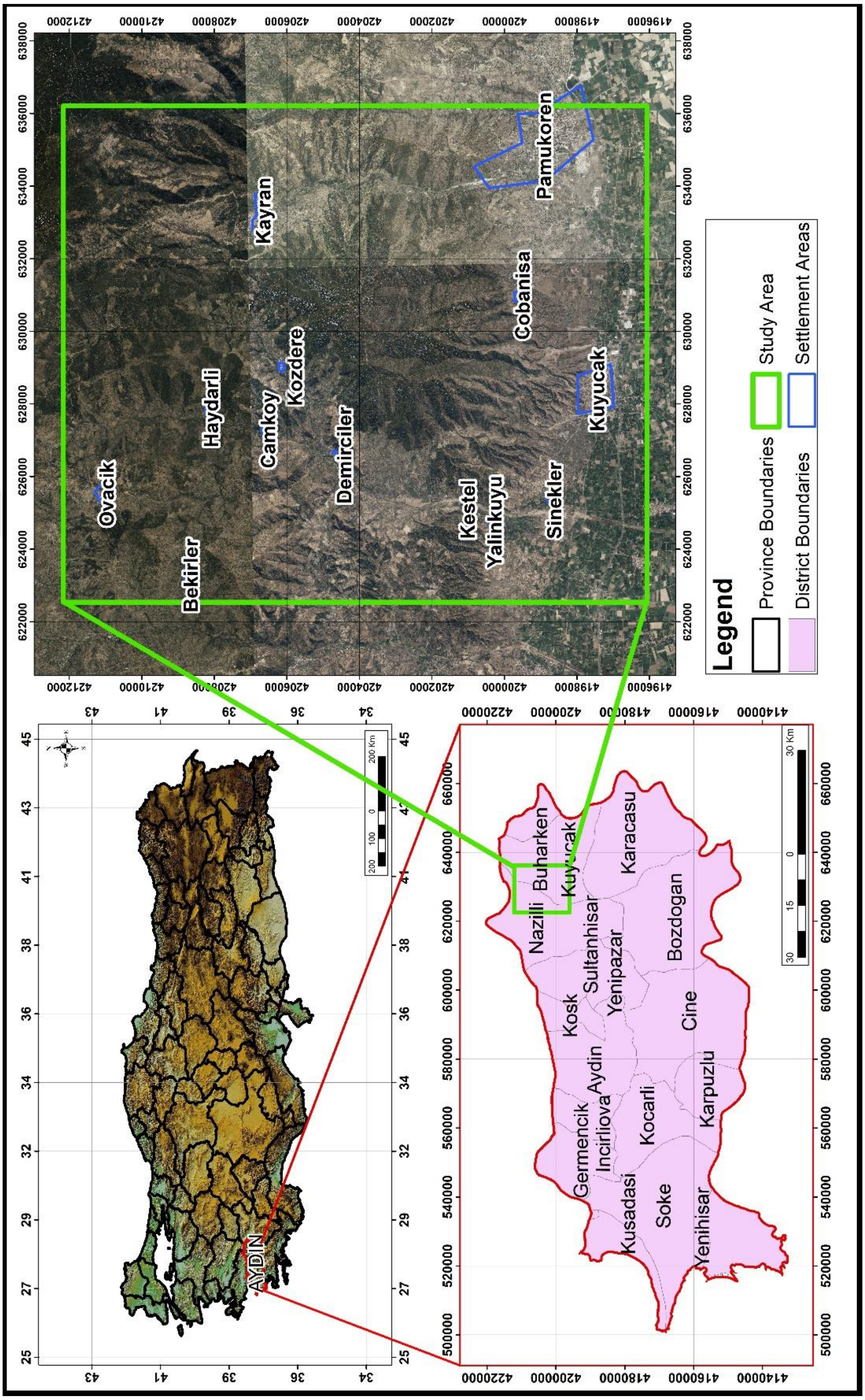

Figure 2.1. Location map of the study area.

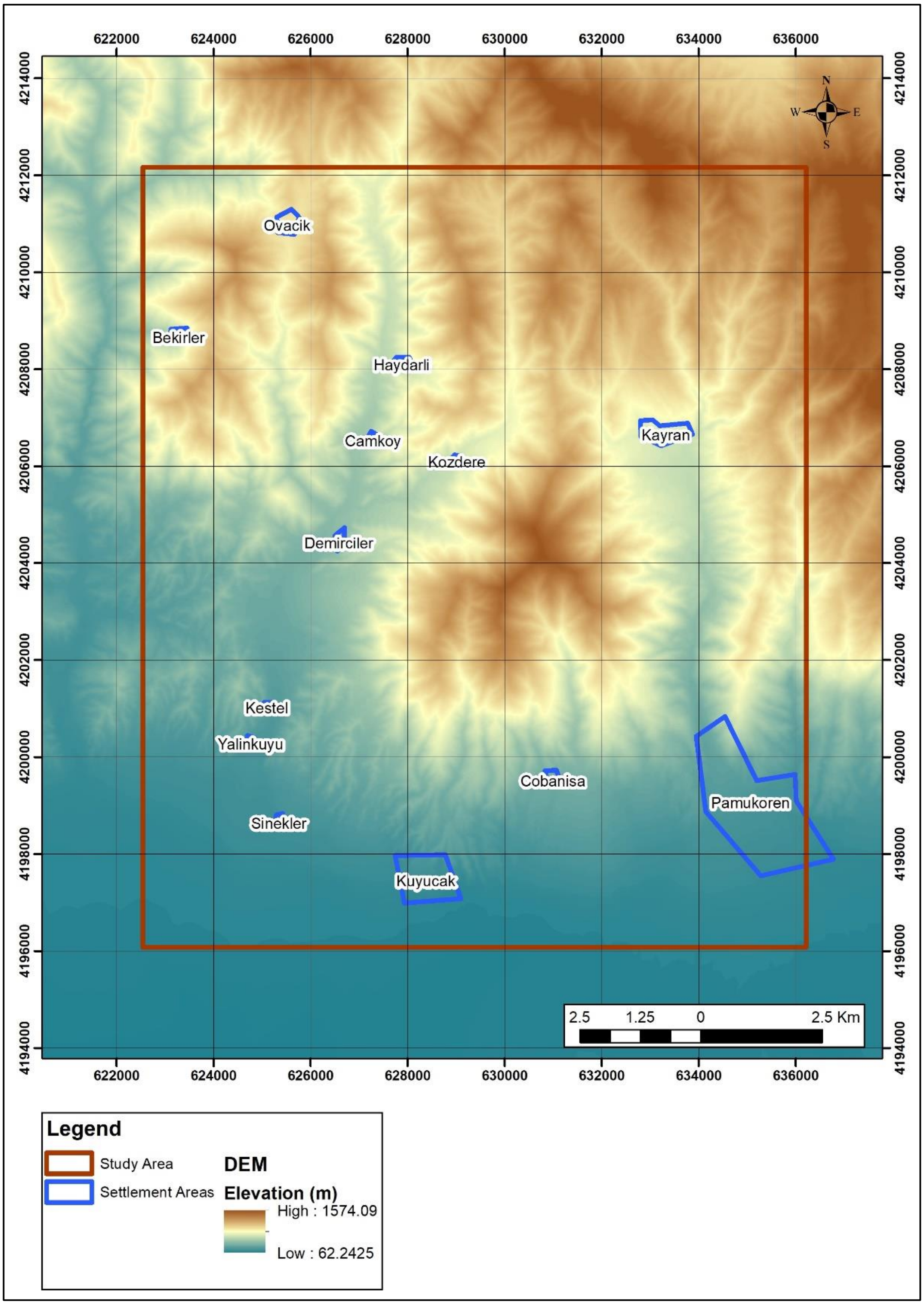

Figure 2.2. Digital Elevation Model of the study area and its vicinity.

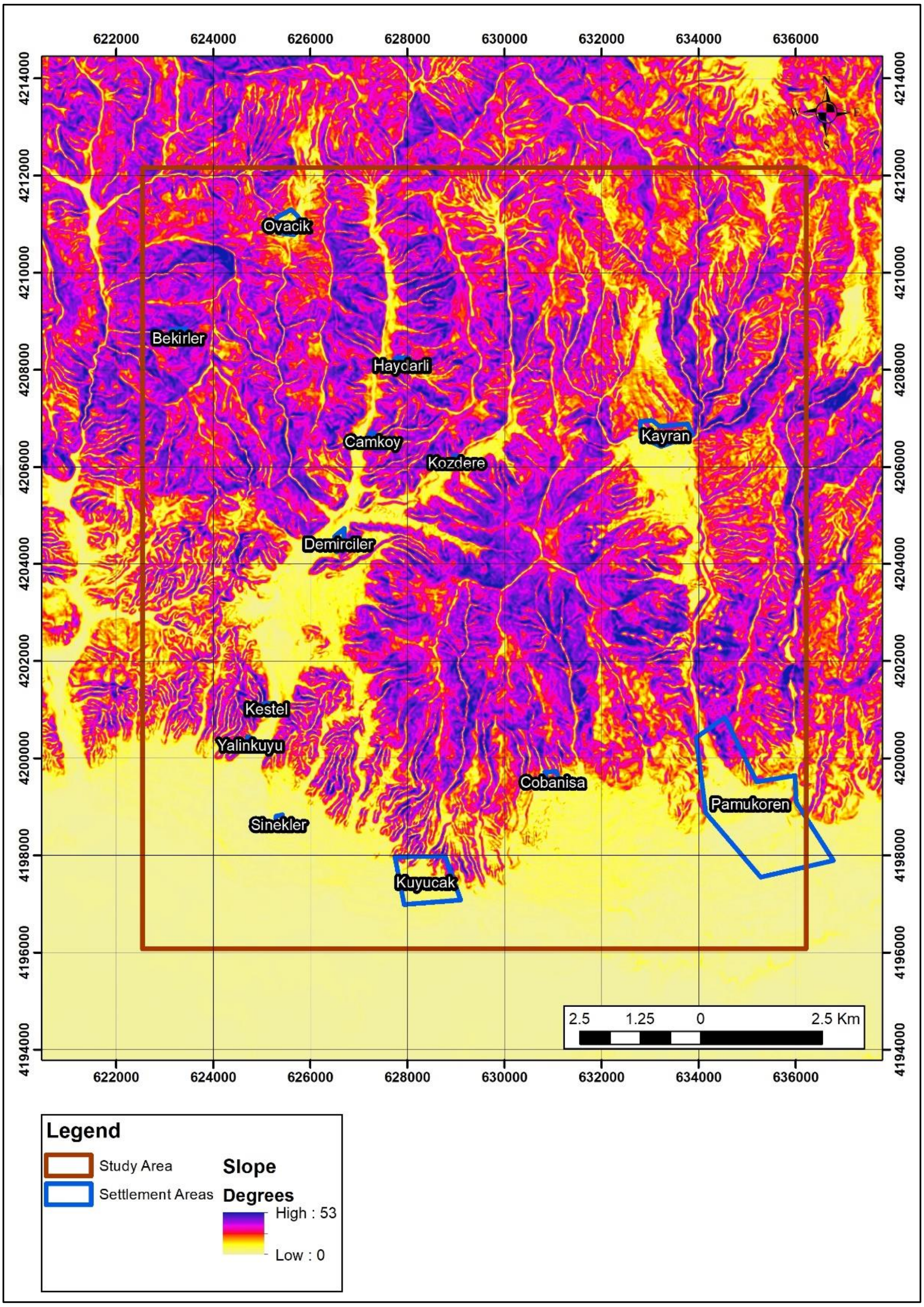

Figure 2.3. Slope map of the study area and its vicinity.

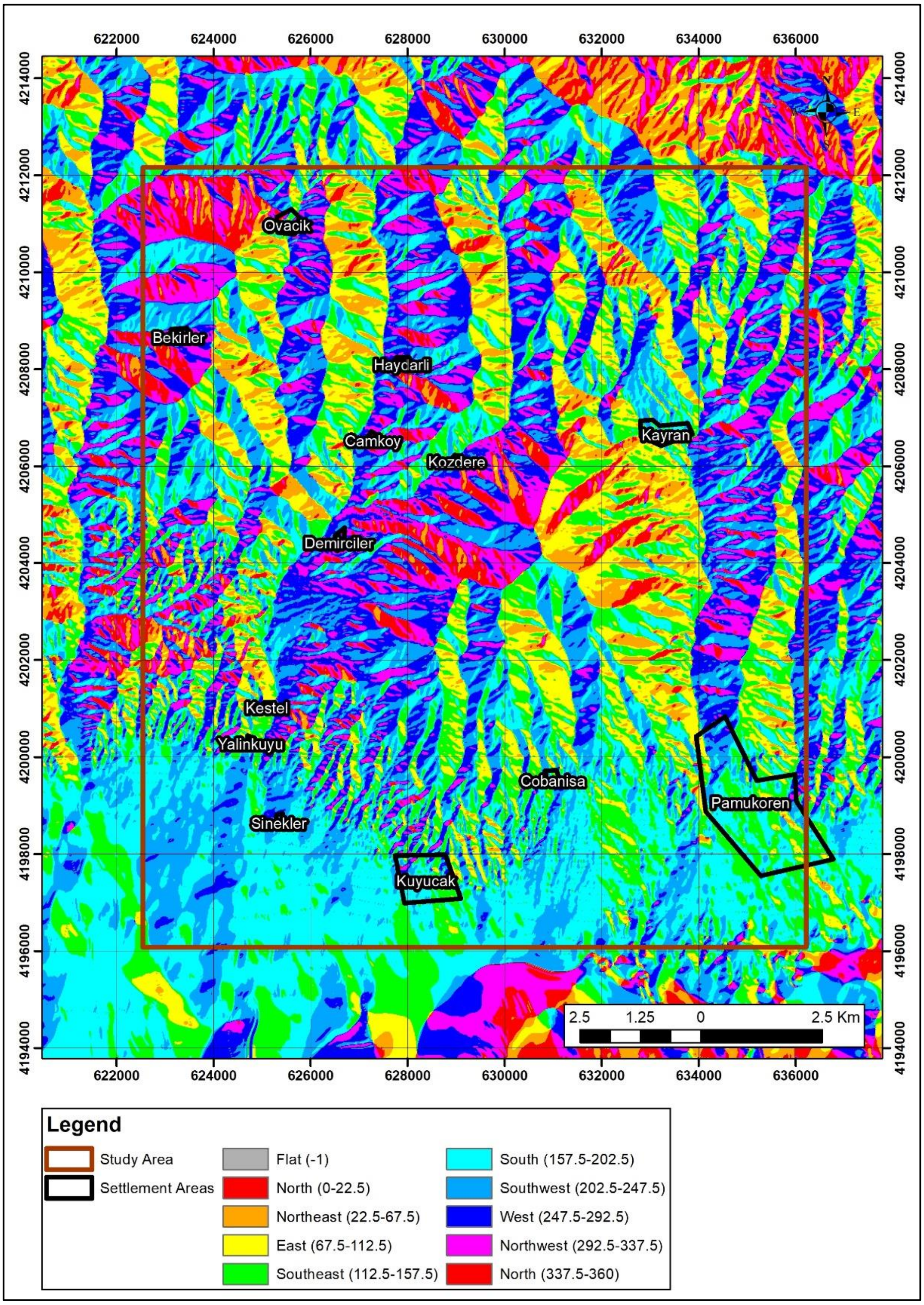

Figure 2.4. Aspect map of the study area and its vicinity.

2.2 Climate

Western Anatolian region where the study area comprising Büyük Menderes Graben is located is situated at IIIa: Mediterranean microclimate according to Erinç (1996) where the microclimate is defined as having high annual precipitation with severe summer aridity with very high summer temperature and small amount of snow in the winters. Furthermore, for the Büyük Menderes Graben region, the Köppen-Geiger climate classification (Köppen, 1936; Geiger, 1961) is hot summer Mediterranean climate (Csa) (Beck et al., 2018) (Figure 2.5). Average precipitation in Aydın province is 55 mm and total annual precipitation is 660 mm (Turkish State Meteorology Service, 2024).

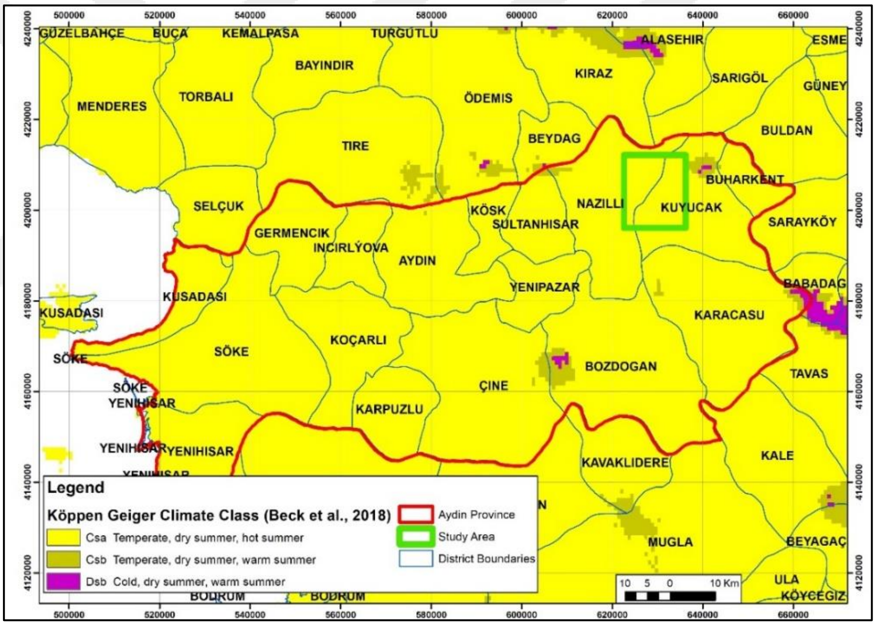

Figure 2.5. Köppen-Geiger climate map of the study area and its vicinity (adapted from Beck et al., 2018).

Furthermore, presence of more than five irrigation cooperatives within and in the vicinity of the study area indicates presence of groundwater (Aydın and Akçay, 2023) and data compiled from State Hydraulic Works (DSİ, 2012) show that static groundwater level as shallow as 5 m are present within and specially the southern section of the study area (Figure 2.6).

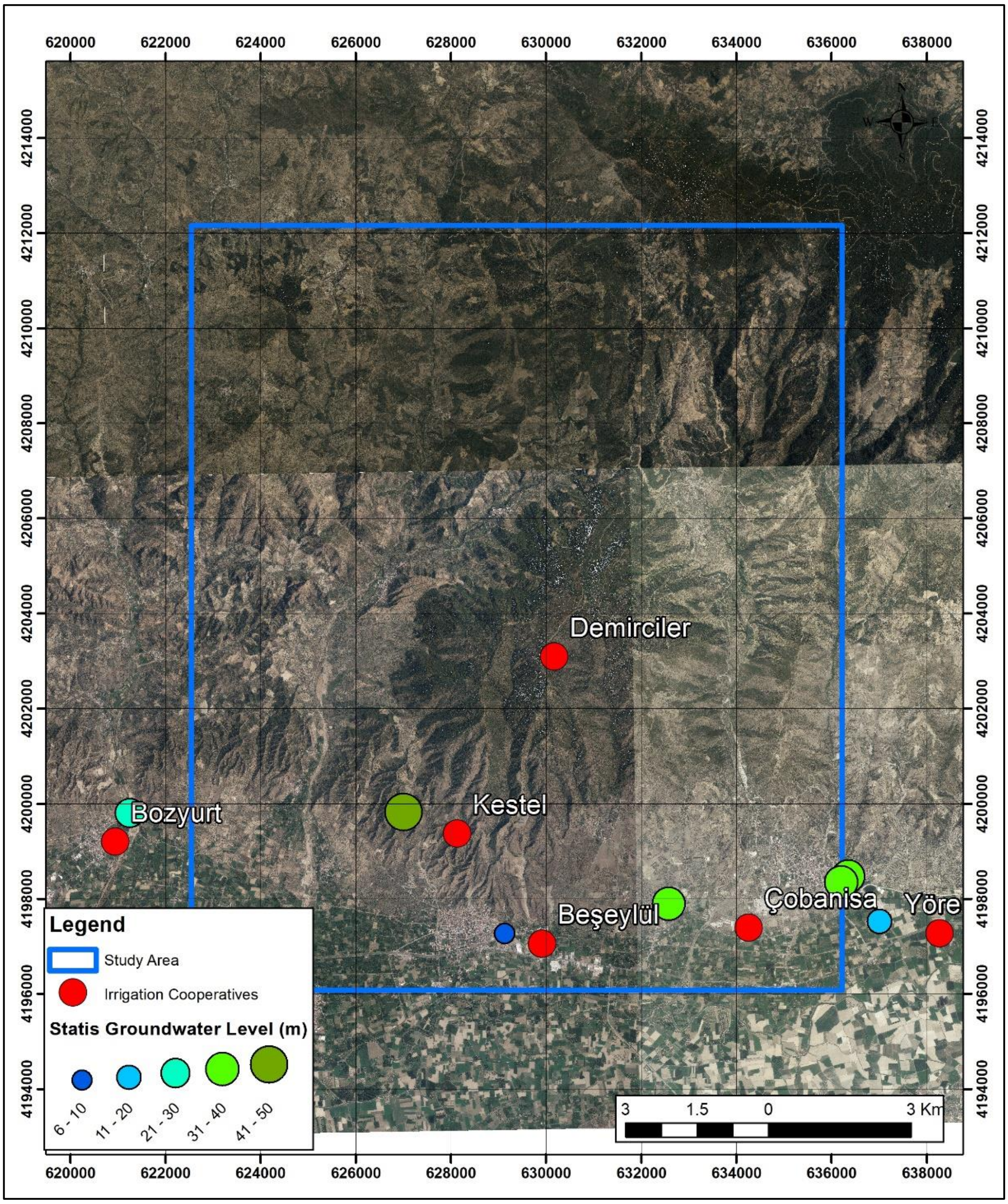

Figure 2.6. Location of ground water wells and irrigation cooperatives within the study area (DSİ, 2012; Aydin and Akçay, 2023).

2.3 Geology of the Study Area

2.3.1 General Geology of Büyük Menderes Graben

In order to provide a basis for the fieldwork activities performed at the following stages of this study, a series of basemaps for the general Büyük Menderes Graben region was included in the GIS environment.

Initially, 1/500,000 scale geological map of General Directorate of Mineral Exploration (MTA, 2002) was used as base map and digitized in Geographical Information Systems (GIS) environment (Figure 2.7).

Western Anatolia exhibits high seismic activity and extension. The region is currently experiencing a north-south continental extensional regime (Bozkurt and Sözbilir, 2006) with an annual extension rate of 3-4 cm (Ferill et al., 1996; Kahle et al., 2000). This extension is balanced by slip on active normal faults with significant seismicity (Eyidoğan and Jackson, 1985).

The tectonic framework of the area is complex, and the origins and mechanisms of continental extension remain a topic of ongoing debate. Various models have been proposed, including the Tectonic Escape Model (Şengör et al., 1985; Görür et al., 1995), the Back-Arc Extension Model (McKenzie, 1978), the Orogenic Collapse Model (Seyitoğlu et al., 1991), and the Episodic Model (Koçyiğit et al., 1999).

At the base of the region's stratigraphic succession lie the Paleozoic Menderes Massif metamorphic units. As the oldest formations in the area, these units serve as the basement rock. The Menderes Massif is a large, regional NE-SW trending metamorphic core complex (Verge, 1995; Bozkurt and Park, 1997; Bozkurt, 2001; Koçyiğit, 2015). It consists of metamorphic rocks with varied lithological characteristics both horizontally and vertically, including marble, various schists, quartzite, and gneiss. The marble layers in the Menderes Metamorphics act as the reservoir rock, covered by Neogene deposits from the Miocene and Pliocene epochs. Quaternary deposits, which are widespread throughout the Menderes Graben, form the uppermost layer over the Neogene deposits. The fine-grained sedimentary sequence of the graben fills has low permeability, making it suitable as a cap rock for the geothermal system, in conjunction with the schistic levels of the Menderes Massif and Neocene deposits at certain locations (Figure 2.1).

According to Ring et al., 1999, 2001 and Gessner et al., 2001, Bayındır Nappe has a geothermal reservoir character within the Büyük Menderes Graben (BMG) having phillite, quartzite, marble, schist and Miocene granitic rock units. Similarly, study conducted by Okay (2001) also mentions Göktepe formation in comparison with the previous study and indicates that phillite, marble and metaquartzite units are present in this formation.

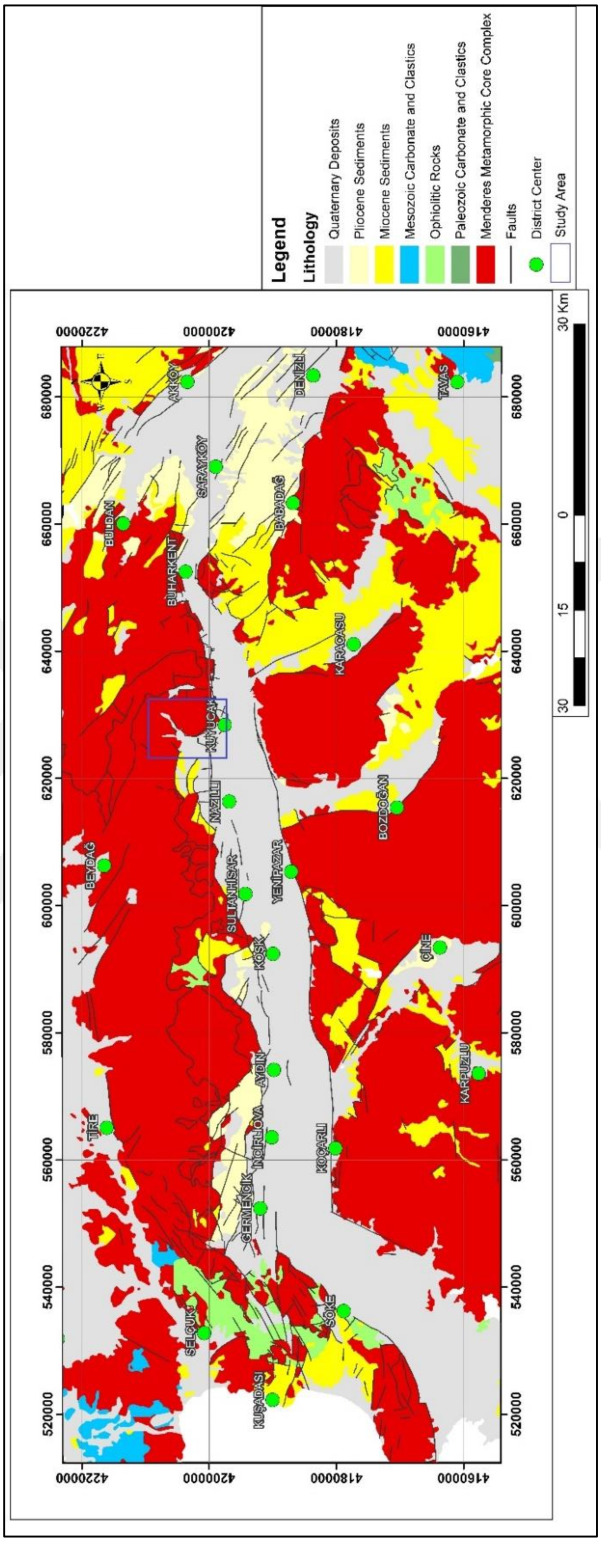

Figure 2.7. Geological map of the region (modified from MTA, 2002).

2.3.2 Geothermal Geology of the Kuyucak Area

Kuyucak area is located at a mini graben system at the northern flank of the Büyük Menderes Graben (BMG). The Kuyucak site has a N-W mini graben structure perpendicular to the E-W trending BMG. Paleozoic-Mesozoic Menderes Massif Metamorphics constitute the basement rock within the study area and Neogene sedimentary units unconformably overly the Menderes massif which in turn are overlain by Quaternary deposits.

The Paleozoic-Mesozoic Menderes Metamorphics form the basement of the study area. They are unconformably overlain by the Neogene deposits and in turn overlain by the Quaternary graben fills. The Menderes Massif is composed of "core" and "cover" rock assemblages. Core assemblage is composed of augen gneiss, metagranite, schist and metagabbro whereas the cover assemblage is composed of metapelites, amphibolite with dolomitic marble intercalations and marble dominated re-crystallized sedimentary sequence. In the Menderes Massif the highly fractured augen gneisses, quartzites and marbles present high porosity due to the multiphase brittle deformation and underground dissolution openings form the geothermal reservoir while the schists, such as the mica and chlorite schists, represent the cap rocks of the geothermal system at places (Koçyiğit, 2015). The graben fill units (Neogene) are the Middle Miocene conglomerate and sandstone units at its bottom followed by coal bearing sandstone, claystone, siltstone and marl. Upper Miocene units, comprised of red gravelstone, sandstone, claystone deposits conformably overlie the Middle Miocene units. These units are further overlain by the Quaternary alluvial and Pleistocene continental deposits. The fine grained sedimentary sequence of the graben fills have low permeability allowing them to serve as the cap rock of the geothermal system. The simplified geological map of the study area can be in Figure 2.8.

According to geophysical magnetotellouric surveys conducted in the study area (SDS Energy, 2012; Schlumberger, 2012) depth to reservoir rock is shallower towards the north of the study area. Two deep wells have been drilled in the area where both have encountered geothermal reservoir coinciding with the reservoir depth interpreted from the 3D magnetotellouric data (Yal et al., 2017).

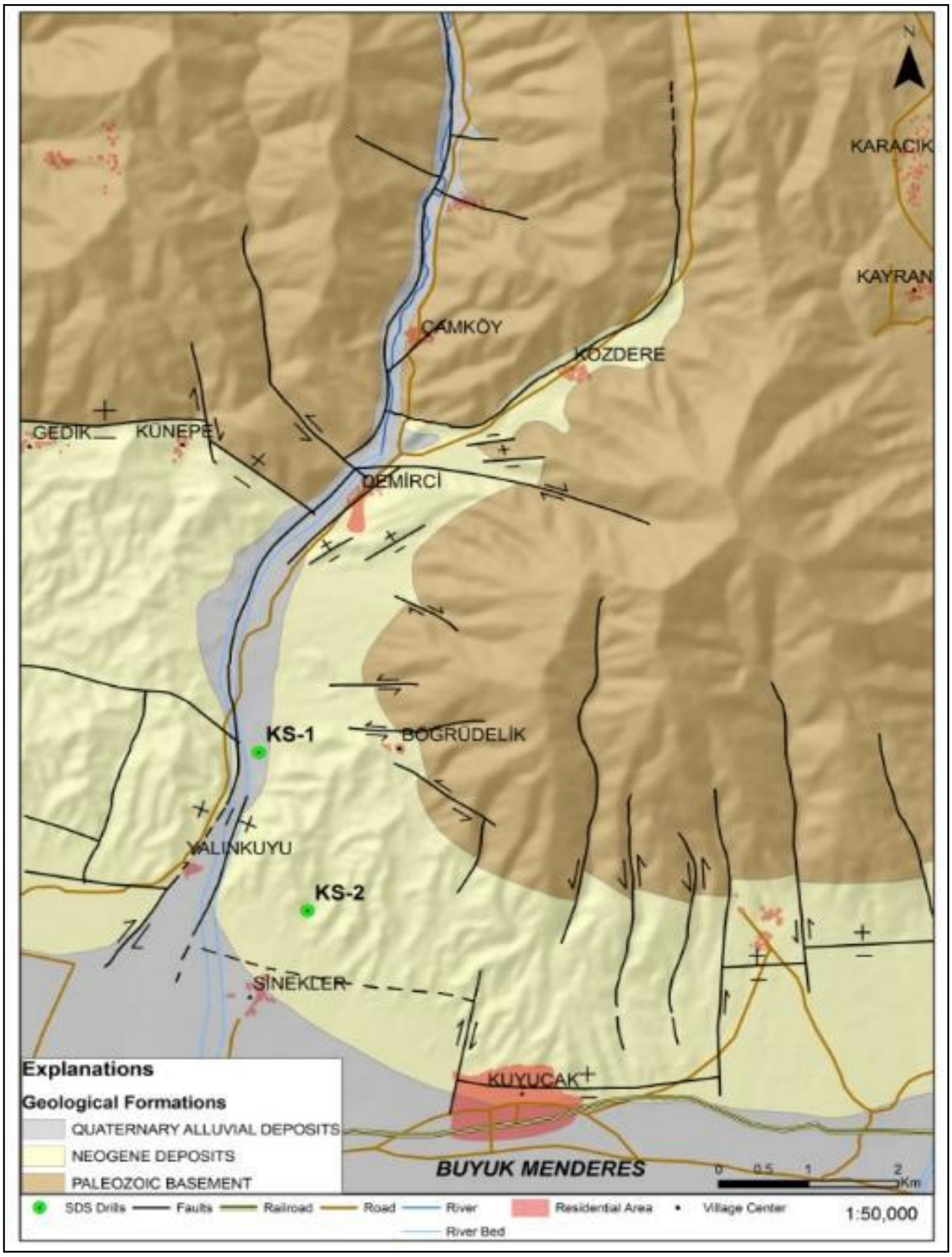

Figure 2.8. Geologıcal map of the study area (Yal et al., 2017).

CHAPTER 3

ALTERATION MINERAL MAPPING

In this chapter, the process followed in terms of alteration mineral mapping, including satellite image analysis, field sample collection and XRD laboratory tests are discussed. Initially, a detailed literature survey in terms of importance of alteration minerals in geothermal exploration studies, methodology to identify alteration minerals through use of satellite images and utilization of XRD assessment in alteration mineral identification was conducted. Following this, satellite image assessment, namely assessment of ASTER imagery conducted through utilization of different techniques is discussed. In addition to the satellite image analysis, samples were collected from the field for XRD analyses and the methodology followed to prepare the samples for XRD analysis and interpretation of results is discussed in Section 3.4. Finally, results of the satellite image analysis and XRD interpretation have been compared and discussed. The results of the satellite image analysis constituted input layer to GIS based MCDA discussed in Chapter 6. A flowchart summarizing the alteration mineral mapping processes followed in this study is given in Figure 3.1.

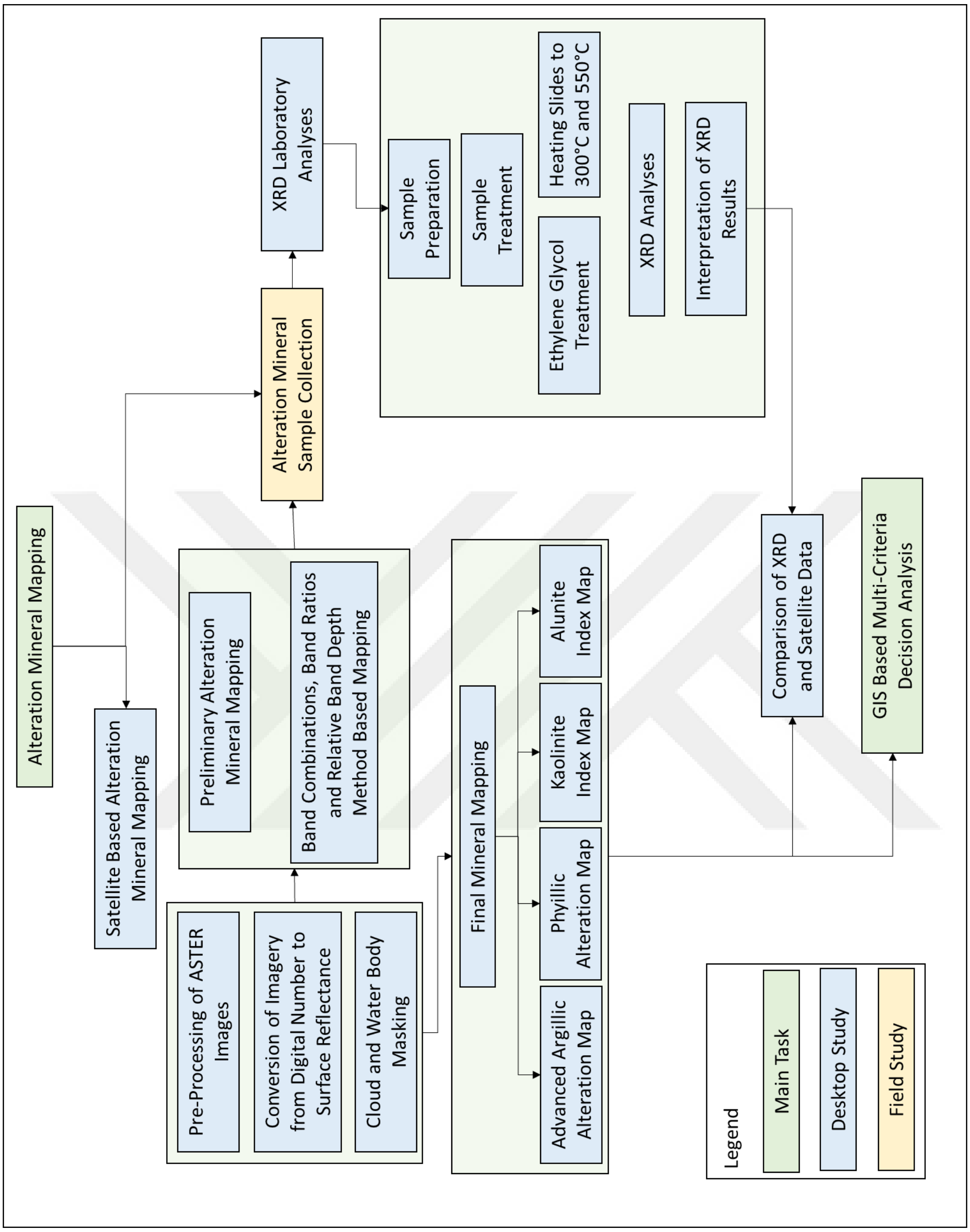

Figure 3.1. Flow chart for the alteration mineral mapping studies.

3.1 Literature Review

In the following sections, literature review on hydrothermal alteration in general satellite based alteration mineral mapping and use of XRD analysis in hydrothermal alteration mineral identification and geothermal exploration are presented.

3.1.1 Literature Review on Hydrothermal Alteration

Rock alteration simply means changing the mineralogy of the rock. The primary minerals are replaced by the secondary minerals because there has been a change in the prevailing conditions that the rock has been subjected to. These changes could be changes in temperature, pressure, or chemical conditions or any combination of these. Hydrothermal alteration is a change in the mineralogy as a result of interaction of the rock with hot water fluids, called "hydrothermal fluids".

Hydrothermal fluids cause hydrothermal alteration of rocks by passing hot water fluids through the rocks and changing their composition by adding or removing or redistributing components. Temperatures can range from weakly elevated to boiling.

Hydrothermal alteration is a general term embracing the mineralogical, textural, and chemical response of rocks to a changing thermal and chemical environment in the presence of hot water, steam, or gas (Henley and Ellis, 1983) (Figure 3.2). By mapping alteration mineral assemblages at the surface, it is possible to locate the zones with highest temperatures, pressures, or permeabilities—all of which are important in geothermal exploration. The factors that usually control alteration in geothermal systems are temperature, pressure, rock type, permeability, fluid composition and the duration of fluid-rock interactions (Browne, 1978; Elders et al., 1981) Table 3.1).

Argillic and advanced argillic alteration are shallow types of alteration encountered in a variety of different types of hydrothermal systems. Argillic alteration forms at lower temperatures and primarily consists of kaolinite + montmorillonite clay minerals.

Advanced argillic alteration forms at higher temperatures and lower pH conditions (e.g., the acid-steam condensate zone of a hydrothermal system). It consists primarily of kaolinite + dickite clay minerals at lower temperatures and pyrophyllite + andalusite minerals at temperatures > 300°C. Advanced argillic alteration may also be associated with alunite.

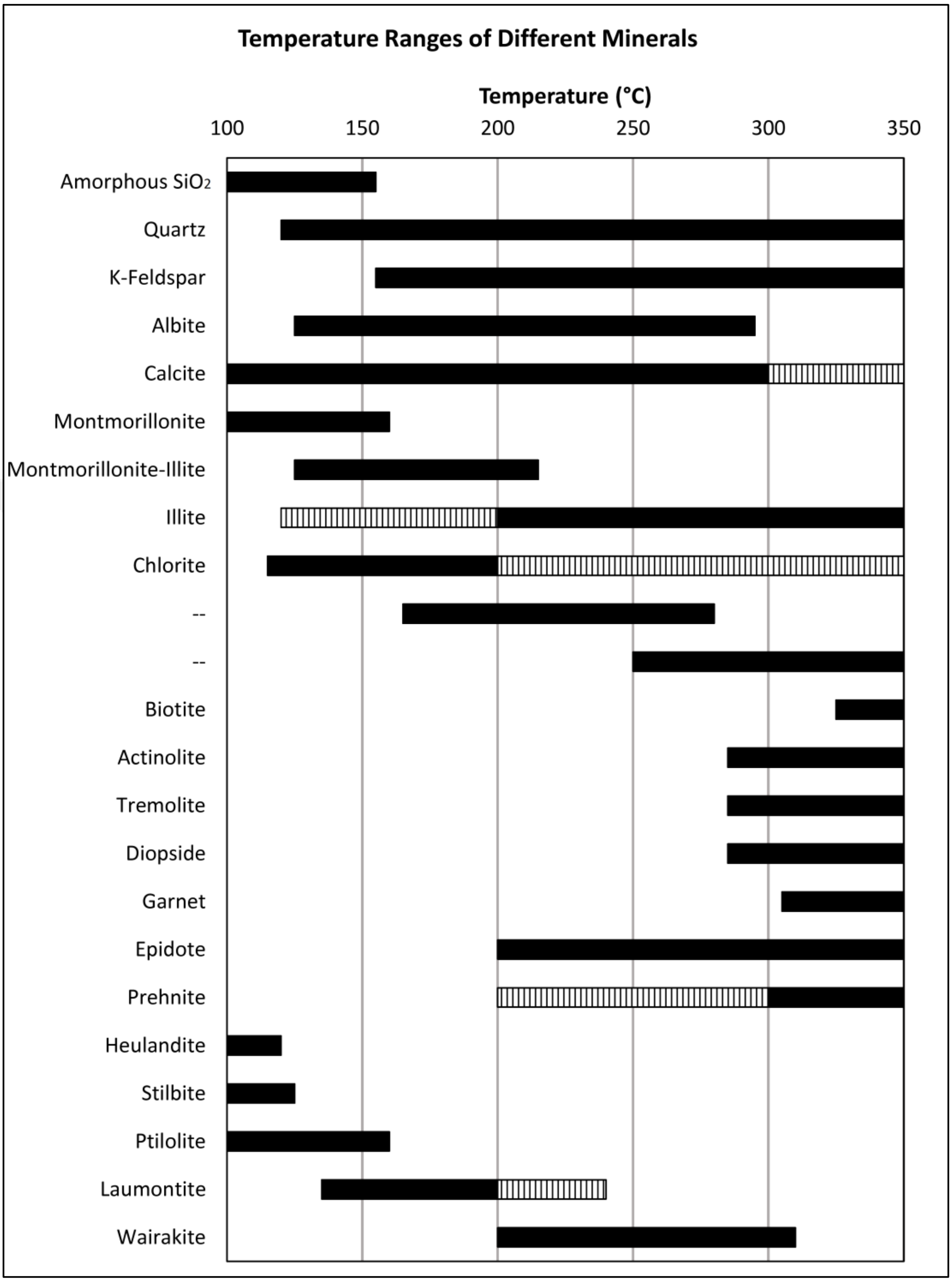

Figure 3.2. Generalized summary of the temperature ranges over which alumino-silicate alteration minerals have been observed (adapted from Henley and Ellis, 1983).

Table 3.1. Conditions for formation of hydrothermal alteration products

Minerals	***Fluid Type***	***Temperature (°C)***	**P_{fluid} (bars)[b]**
Cristobalite	Strong acid	<100	<15
Quartz	Acid	100–230	30-50
Alunite + cristobalite	Strong acid	<100	<15
Alunite + quartz	Strong acid	100–230	15-50
Kaolinite + cristobalite	Acid	<100	<15
Kaolinite + quartz	Acid	100–200	<30
Dickite + pyrophyllite + quartz	Acid	150–250	<60
Pyrophyllite + quartz	Acid	>230	>50
Montmorillonite + cristobalite	Weak acid	<100	<15
Montmorillonite, sericite-montmorillonite + quartz	Weak acid	100–200	<30
Chlorite + sericite-montmorillonite + quartz	Weak acid	150–250	<60
Sericite + quartz	Neutral	>230	<50
Heulandite + cristobalite	Neutral	<100	<15
Laumontite + wairakite + quartz	Neutral	100–200	<30
Albite + quartz	Weak alkaline	150–250	<60
Adularia + quartz	Weak alkaline	>230	>50
Data are from the Otake geothermal area; from Browne (1977) after Hayashi (1973).			

3.1.2 Literature Review for Satellite Based Alteration Mineral Mapping

Use of hyperspectral and multispectral satellite data for identification of alteration minerals is common in geothermal exploration (Van der Meer et al., 2014; Abubakar et al., 2017).

As summarized by Abubakar et al. (2017); the Advanced Spaceborne Thermal Emission and Reflection Radiometer (ASTER) on the Terra satellite, launched on December 18, 1999, has enhanced mineral mapping capabilities for geologic remote sensing. Availability of six shortwave infrared (SWIR) bands having spectral wavelengths located specific to identify alteration minerals have allowed utilization of ASTER satellite commonly in mineral mapping (Abrams et al., 2015). ASTER features three bands in the visible and near-infrared (VNIR), six in the shortwave infrared (SWIR), and five in the thermal infrared (TIR), with spatial resolutions of 15 m, 30 m, and 90 m, respectively, and enables an initial regional survey of surface mineral alteration features, helping to pinpoint promising areas for geothermal exploration (Van der Meer et al., 2014).

ASTER satellite data have provided enhanced mineral mapping capabilities for the geologic remote sensing in hydrothermal systems (Carranza et al., 2008a; Crosta et al., 2003; Hubbard et al., 2003; Mars and Rowan, 2006, 2010; Rowan et al., 2003).

Kratt et al. (2006) employed ASTER data and field spectrometers to identify borate minerals in Nevada, which can indicate geothermal activity. Kratt et al. (2010) combined ASTER data with airborne hyperspectral data to identify geothermal indicator minerals and explore their structural controls and to map alunite, kaolinite, montmorillonite/illite, chlorite, and carbonate at the Pyramid Lake geothermal site.

Calvin et al. (2015) integrated spaceborne and airborne instruments with field spectral validation to map geothermal minerals in Nevada, such as sinter, tufa, travertine, and various alteration minerals. They highlighted the effectiveness of combining remote sensing with field temperature surveys for identifying small thermal anomalies. Their work summarized key minerals associated with geothermal systems, including clays, sulfates, carbonates, silica, and borates, which can serve as indicators of geothermal activity and help locate hidden geothermal systems.

Further details on ASTER satellite data and alteration mineral mapping is provided in Section 3.2.

3.1.3 Literature Review on Use of XRD Analyses in Geothermal Exploration

There are various studies in the literature which make use of satellite-based image analysis by using data from Lansat-7, Landsat-8 and ASTER satellites as well as other satellite sources to identify and map hydrothermal alteration minerals and zones for geothermal exploration and these studies use XRD analysis results to correlate and confirm image processing results. Along with these, there are studies focusing on identification of alteration minerals as a temperature indicator through XRD analysis on samples collected from field outcrops or boreholes. Some of these studies are provided below as a summary.

Pour et al. (2013) utilized satellite image analysis of Landsat ETM+, Hyperion and PALSAR to detect hydrothermally altered rocks and structural elements associated with gold mineralization in the Bau area and compared the results of image analysis with field spectrometer and XRD analyses results identifying advanced argillic alteration zones and detecting kaolinite, dickite, illite, limonite, sericite, calcite and quartz.

Abubakar et al. (2019) used Landsat 7, Landsat-8 and ASTER satellite images for alteration mineral mapping for geothermal exploration and utilized ASD measurements and XRD analysis to confirm presence of kaolinite, dickite, illite, calcite, hematite and quartz on the samples collected from the field.

Yalcin et al. (2020) used ASTER satellite images to map hydrothermal alterations related with geothermal activity in Akcay Basin, Afyonkarahisar, Türkiye and used qualitative XRD analysis results to correlate image processing results with the identified alteration minerals.

El-Desoky et al. (2021) utilized ASTER satellite images to identify hydrothermal alteration zones and the structural elements represented by lithologic contacts and faults/fracture zones in northwestern Allaqi District, South Eastern Desert, Egypt and utilized XRD analyses to confirm the image analyses.

Aden (2020) utilized Landsat 8 OLI/TIRS images to map hydrothermal alteration zones and XRD analyses to compare satellite image analysis results in Ghoubbet Area, Djibouti.

Sekandari et al. (2020) utilized ASTER and WorldView-3 (WV-3) satellite remote sensing data for mapping lithological units and hydrothermal alteration zones associated with Pb-Zn mineralization in the Kerman–Kashmar Tectonic Zone (KKTZ), Iran, and used XRD analysis as well as ASD spectrometry and Coupled Plasma Mass Spectrometry (ICP-MS) analysis to confirm the satellite based mapping results by identifying minerals such as dolomite, calcite, muscovite, gypsum, illite, jarosite, malachite quartz and albite.

Canbaz et al. (2018) utilized ASTER satellite image processing in order to identify hydrothermal alteration areas in Kösedag-Zara (Sivas), Turkey and compared the image analysis results with XRD and Analytical Spectral Devices (ASD) spectrometer analyses to identify illite and kaolinite clay alteration minerals.

Atif et al. (2021) used ASTER satellite data to identify argillic, phyllic and propylitic alteration zones in Imiter Morocco and the XRD analyses results were used to estimate the relative quantitative determination of the predominant mineral species in the alteration zones.

In addition to the above examples on utilization of satellite images and XRD analysis comparatively, various studies have been performed utilizing XRD analysis to identify hydrothermal alteration minerals in different applications including geothermal exploration. Deon et al. (2022) used analytical techniques including

XRD analysis to identify calcite, cristobalite, barite, rutile, alunite, tridymite, jarosite and ilmenite which are commonly formed during natural and technological geothermal processes. Pandarinath et al. (2006) used XRD analysis to identify hydrothermal quartz, calcite, and pyrite, as well as other alteration mineral phases (e.g., chabazite and chlorite) that are difficult to identify by traditional petrography in Los Azufres Geothermal System, Mexico. Other researchers including Schiffman and Frileiefsson (1991) and Vazquez et al. (2014) used XRD analyses to identify mineral transitions in geothermal areas and wells to identify temperature ranges. Furthermore, Karamanderesi (2013) and Yildiz et al. (2020) used XRD analyses on samples from wells in different geothermal wells in Turkey to identify alteration mineral transition zones as an indicator of temperature.

As can be clearly seen from the above examples, use of satellite image processing and more importantly, correlation of image processing data with XRD analysis is a common practice in geothermal and hydrothermal alteration studies.

3.2 Satellite Image Analysis

3.2.1 ASTER Satellite

Alteration mineral analyses were performed for Kuyucak area via utilizing ASTER satellite images. ASTER (Level 3A) satellite image acquired on 06.07.2007 was used in this study. License areas and the entire satellite image is presented below in Figure 3.3 where RGB band combination used for band numbers 3, 2 and 1, and vegetated areas are indicated in shades of red.

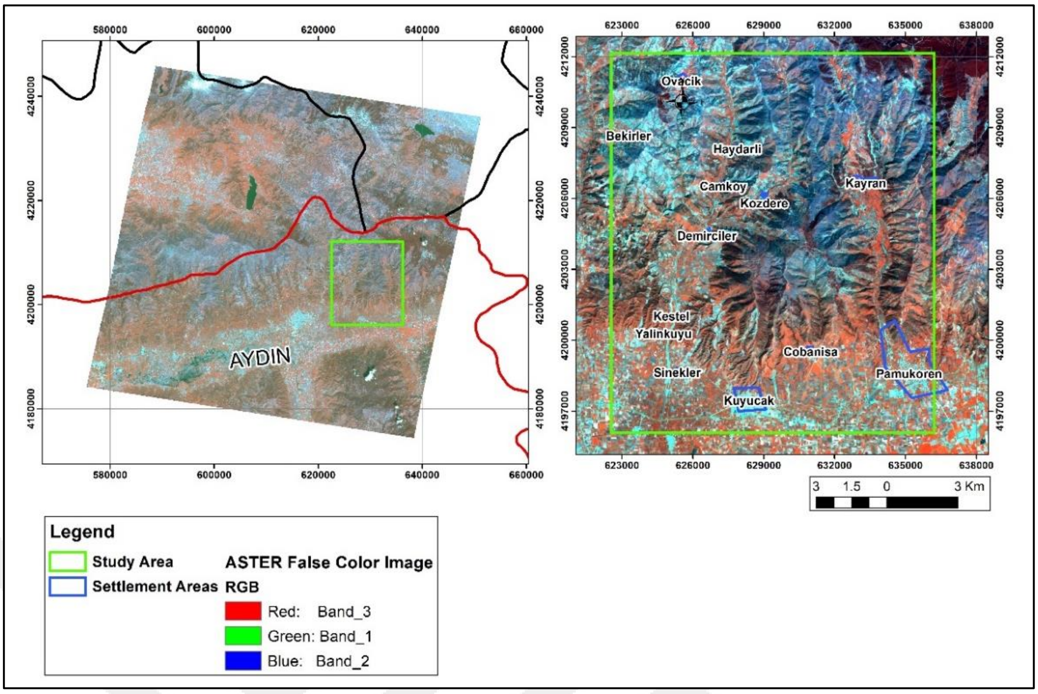

Figure 3.3. Location of the study area on the ASTER satellite image.

ASTER satellite sensor has fourteen different bands which can collect data on three different wavelength ranges. Three of these bands are located within visible near infrared (VNIR), six of them are at Short Wave Infrared (SWIR) and five of these bands are located at Thermal Infrared (TIR) wavelength range. Spatial resolutions of these band ranges are 15, 30 and 90 m, respectively (Figure 3.4 and Table 3.2).

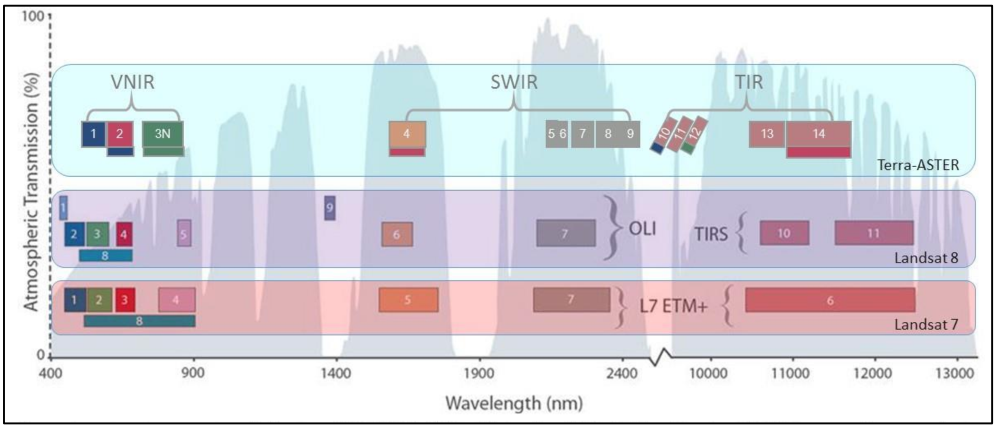

Figure 3.4. Comparison between ASTER and LandSat-7 (ETM+) and Landsat-8 (OLI, TIRS) sensors (Duda et al., 2015).

Table 3.2. Sensor characteristics of ASTER.

Sub-System	Band No.	Spectral Range (μm)	Spatial Resolution (m)	Radiometric Resolution
VNIR	1	0.52-0.60	15	8 bit
	2	0.63-0.69		
	3N (Nadir)	0.78-0.86		
	3B (Back)	0.78-0.86		
SWIR	4	1.60-1.70	30	8 bit
	5	2.145-2.185		
	6	2.185-2.225		
	7	2.235-2.285		
	8	2.295-2.365		
	9	2.360-2.430		
TIR	10	8.125-8.475	90	12 bit
	11	8.475-8.825		
	12	8.925-9.275		
	13	10.25-10.95		
	14	10.95-11.65		

Prior to image analysis, necessary corrections were made on the image. These included, masking water bodies, masking clouds and their shadows, masking vegetation cover (Gozzard, 2006), if present, and atmospheric correction was performed to convert radiance at sensor image to surface reflectance by utilizing the FLAASH module of ENVI Software (Matthew et al., 2000).

3.2.2 Image Analysis Methods

Within the context of geothermal potential assessment, the studies in order to detect and identify the alteration minerals are performed since these alteration minerals provide information on formation temperatures. ASTER (Advanced Spaceborne Thermal Emission and Reflection Radiometer) satellite image includes three bands at visible near infra-red bandwidth, 6 bands at short wave infra-red wavelength and five bands at thermal infra-red wavelength range which can be used for alteration mapping. Mineral mapping by utilizing ASTER imagery is based on reflectance spectra of alteration minerals (Figure 3.5).

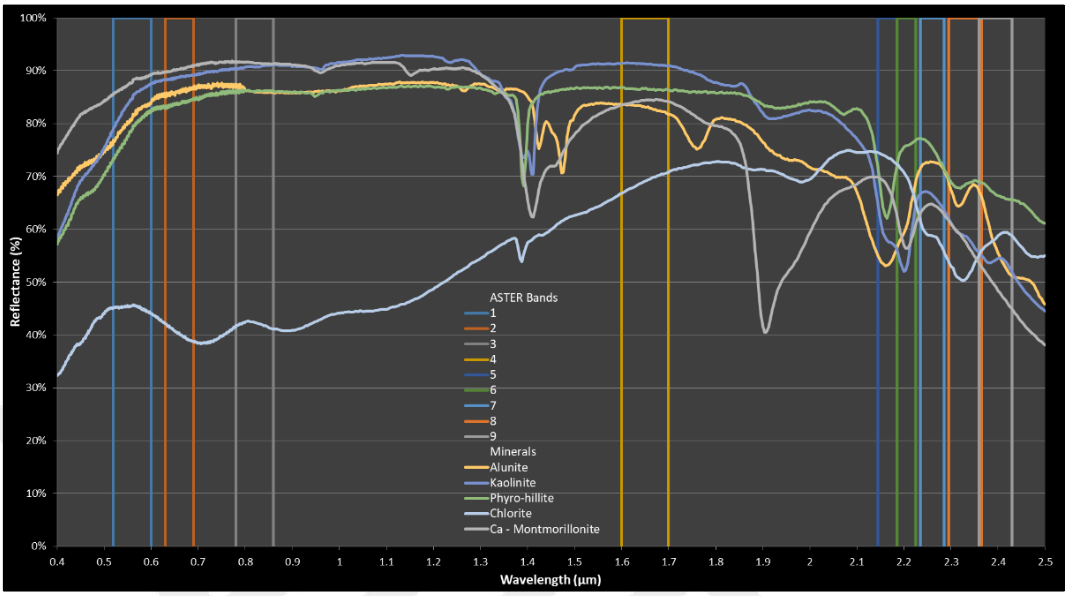

Figure 3.5. Examples from reflectance spectra with ASTER band locations (ASTER band spectral ranges adapted from Abrams, 2000 and mineral spectral signatures adapted from Clark et al., 1993).

The spectral bands of the ASTER SWIR subsystem were designed to measure reflected solar radiation in one band centered at 1.65 µm, and five bands in the 2.10–2.45 µm region in order to distinguish Al-OH, Fe, Mg-OH, H-O-H, and CO_3 absorption features. Several investigators have documented identification of specific minerals, such as calcite, dolomite, and muscovite, as well as mineral groups, through analysis of ASTER data (Rowan and Mars, 2003; Rowan et al., 2003). The 2.17 µm and 2.20 µm absorption features to map kaolinite and alunite, which are typical in argillic-altered rocks, and muscovite, which is a common mineral in phyllic-altered rocks (Mars and Rowan, 2006).

Phyllic alteration spectral characteristics include illite/muscovite reflectance spectra that exhibit an intense Al-OH absorption feature, which is typically centered at 2.20 µm (ASTER band 6), and a less intense feature near 2.38 µm (ASTER band 8). Argillized rocks, including rocks classified as advanced argillic, also display an Al-

OH absorption feature near 2.20 µm, but both kaolinite and alunite exhibit significantly different spectral shapes compared to muscovite/illite (Figure 3.6) (Hunt, 1977; Hunt and Ashley, 1979; Rowan et al., 2003). Kaolinite displays a secondary feature or shoulder at 2.17 µm, whereas alunite exhibits a minimum at 2.17 µm (ASTER band 5), instead of 2.20 µm, and a minor feature at 2.20 µm (Figure 3.5); both minerals also exhibit secondary absorption features near 2.38 µm. These spectral differences are detectable in ASTER data because the SWIR spectral band passes of the instrument were tailored for this purpose (Rowan et al., 2003). Propylitic mineral-assemblage reflectance spectra are characterized by Fe, Mg-OH absorption features and CO_3 features caused by molecular vibrations in epidote and chlorite and in carbonate minerals, respectively (Spatz and Wilson, 1995). These absorption features are situated in the 2.35 µm region (ASTER band 8). In addition, Fe2+ absorption features are displayed by epidote and chlorite in the VNIR wavelength region. These spectral reflectance features contrast strongly with those of the phyllic and argillic assemblages (Mars and Rowan, 2006).

Another method is to use a relative band depth approach (Crowley et al., 1989, Mars and Rowan, 2006), which is based on use of two reflectance and one absorbance feature of a mineral spectra (Figure 3.7). Examples of RBD method include (4+6)/5 for detection of alunite–kaolinite–pyrophyllite and (5+7)/6 for detection of sericite–muscovite–illite–smectite (Rowan and Mars, 2003; Hewson et al., 2001, 2004).

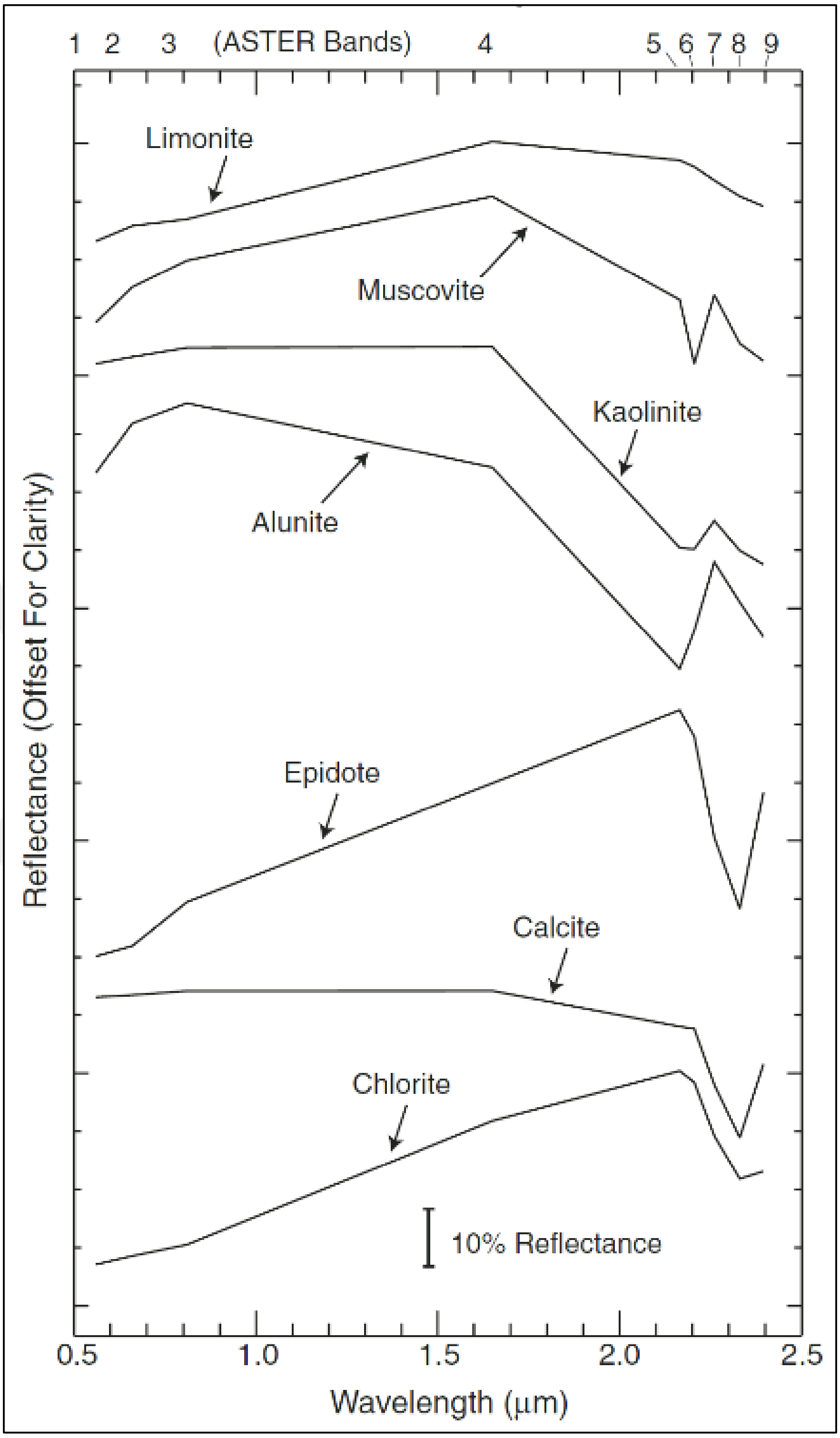

Figure 3.6. Example laboratory reflectance spectra resampled to ASTER band passes

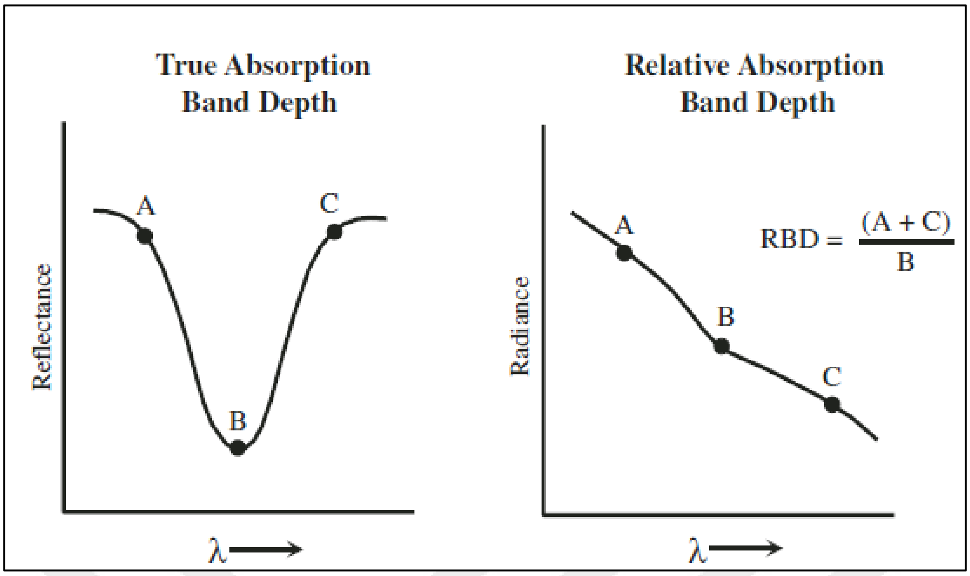

Figure 3.7. Relative band depth method (after Crowley et al., 1989).

In addition to the above discussed methodologies, several mineral indices were proposed for different alteration minerals over the years by utilizing different sensors of ASTER satellite (Ninomiya and Fu, 2001; 2002; Ninomiya 2002; Ninomiya et al., 2005; Ninomiya and Fu, 2003; Ninomiya, 2003, 2004; Ninomiya and Fu, 2016, and Ninomiya and Fu, 2019). These indices have been successfully utilized by various researchers in different areas (e.g. DiTommaso and Rubinstein, 2007; Rockwell and Hofstra, 2008; Pour and Hashim, 2012; Pournamdari and Hashim, 2014; Guha and Kumar 2016).

3.2.3 Image Processing and Analysis

Image processing of the ASTER image was performed in two steps, where an initial analysis was performed by utilizing band combinations of 5/6 for red, 7/6 for green and 7/5 for blue bands of an RGB image for advanced argillic alteration mapping (Hewson et al., 2001, 2004); band ratios of (4+6)/5 as proposed by Rowan and Mars (2003) for advanced argillic alteration, band combination of 7-4-2 to enhance structural features (Rowan and Mars, 2003) and finally band ratio combination proposed by DiTommaso and Rubenstein (2007) where 4/5 (alunite-red), 4/6 (kaolinite-green) and 4/7 (hydroxil minerals-blue) is used for mapping of alteration minerals. These four initial images were assessed to identify potential alteration mineral locations prior to field sample collection.

Band ratios and band combinations methods were used in mapping of alteration minerals. Results of band combination method is visualized by using RGB (Red, Green, Blue) color composites.

Apart from this band combination, band ratios of (4+6)/5 was used (Figure 5). This band ratios is known to enhance advanced argillic alteration minerals of pyrophillite, alunite and kaolinite. The color coding for this band ratios map is presented as red color for areas with high alteration mineral content (Rowan and Mars, 2003; Gozzard, 2006) (Figure 3.8).

In terms of band combinations, 742 color composite was used (Rowan and Mars, 2003). In this image, blue and purple colors indicate altered zones with high clay content and overlain green color is the vegetation mask (Figure 3.9).

Furthermore, band ratio combination proposed by Hewson et al. (2001 and 2004) is used for advanced argillic alteration mapping where RGB composite is formed by 5/6 (phengite-red), 7/6 (muscovite-green) and 7/5 (kaolinite-blue) band ratios (Figure 3.10). As previously mentioned, in this image, green dominated areas indicate muscovite, blue color indicates kaolinite and cyan color (combination of green and blue) indicates where these two minerals may co-exist.

Furthermore, another band ratio combination proposed and successfully utilized by DiTommasso and Rubenstein (2007) is 4/5 (alunite-red), 4/6 (kaolinite-green) and 4/7 (hydroxil minerals-blue) which is used for mapping of alteration minerals. An example of interpretation of this image is that green dominated areas indicate kaolinite abundant areas and yellow color can be interpreted where alunite and kaolinite co-exist. Similarly, white color can be interpreted where all three mineral group exist (Figure 3.11).

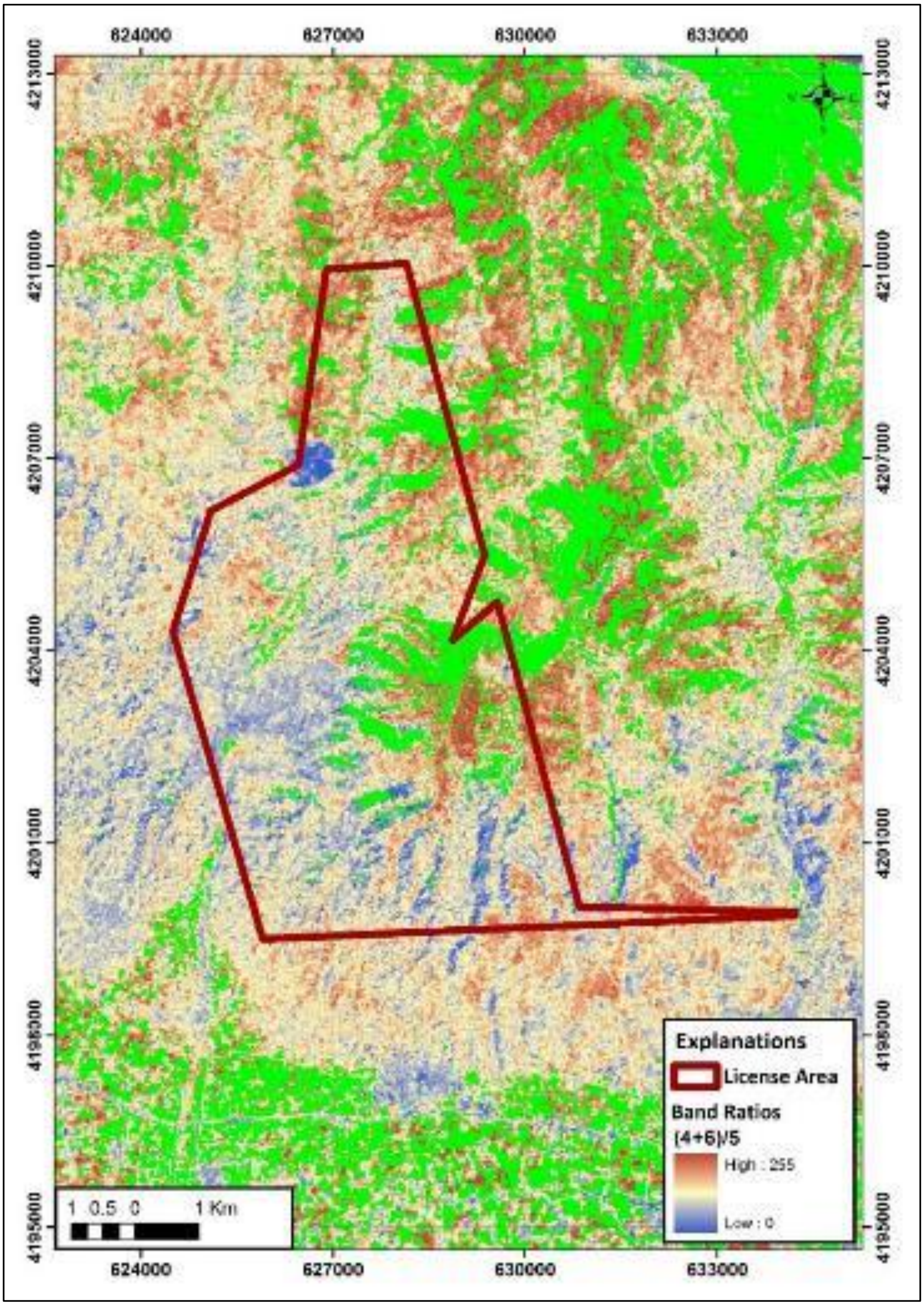

Figure 3.8. (4+6)/5 band ratio magnifying advanced argillic alteration. Areas dominated by alteration minerals are in red color.

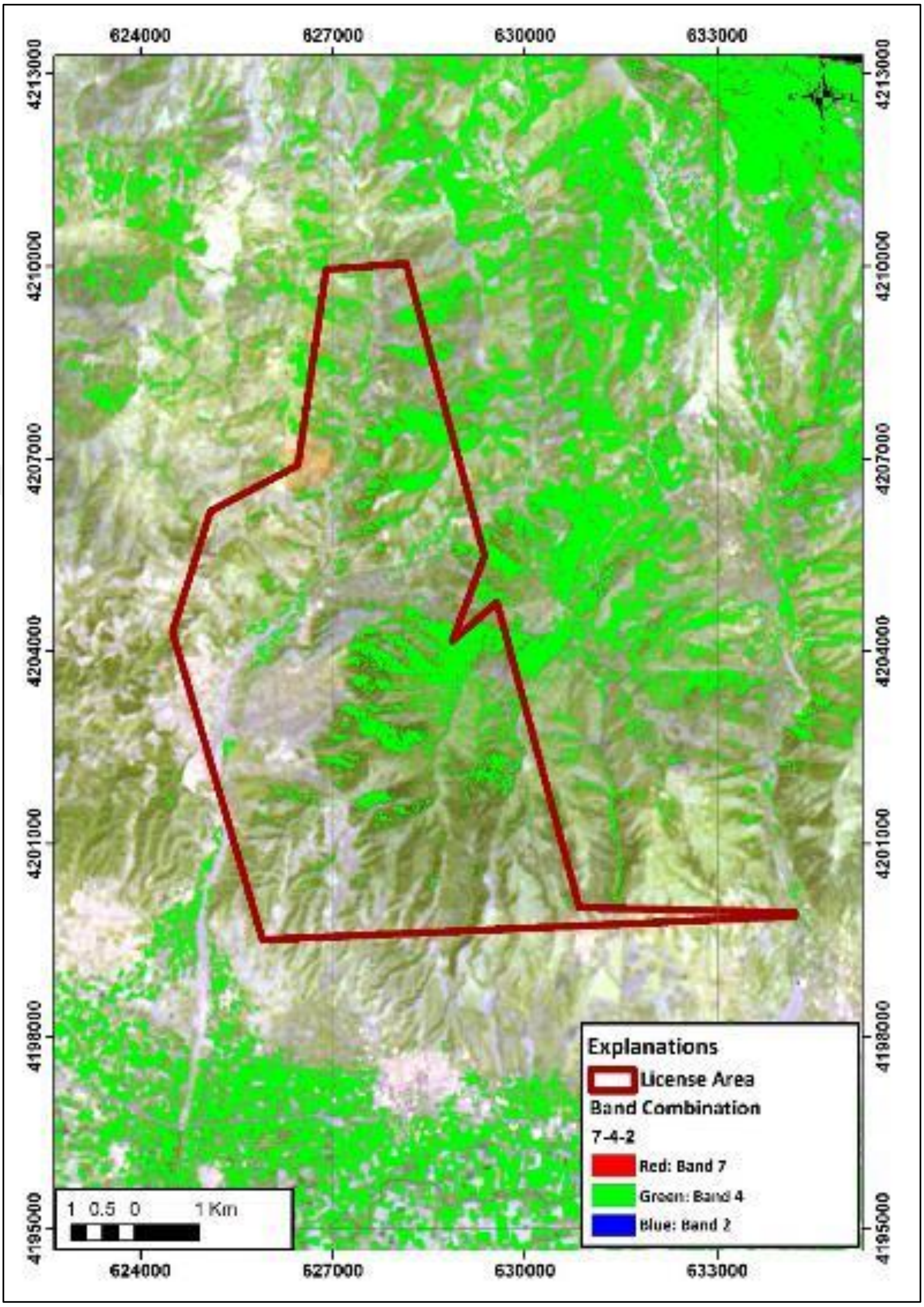

Figure 3.9. 742 band combination; blue and purple colors indicate altered zones with high clay content and overlain green color is the vegetation mask.

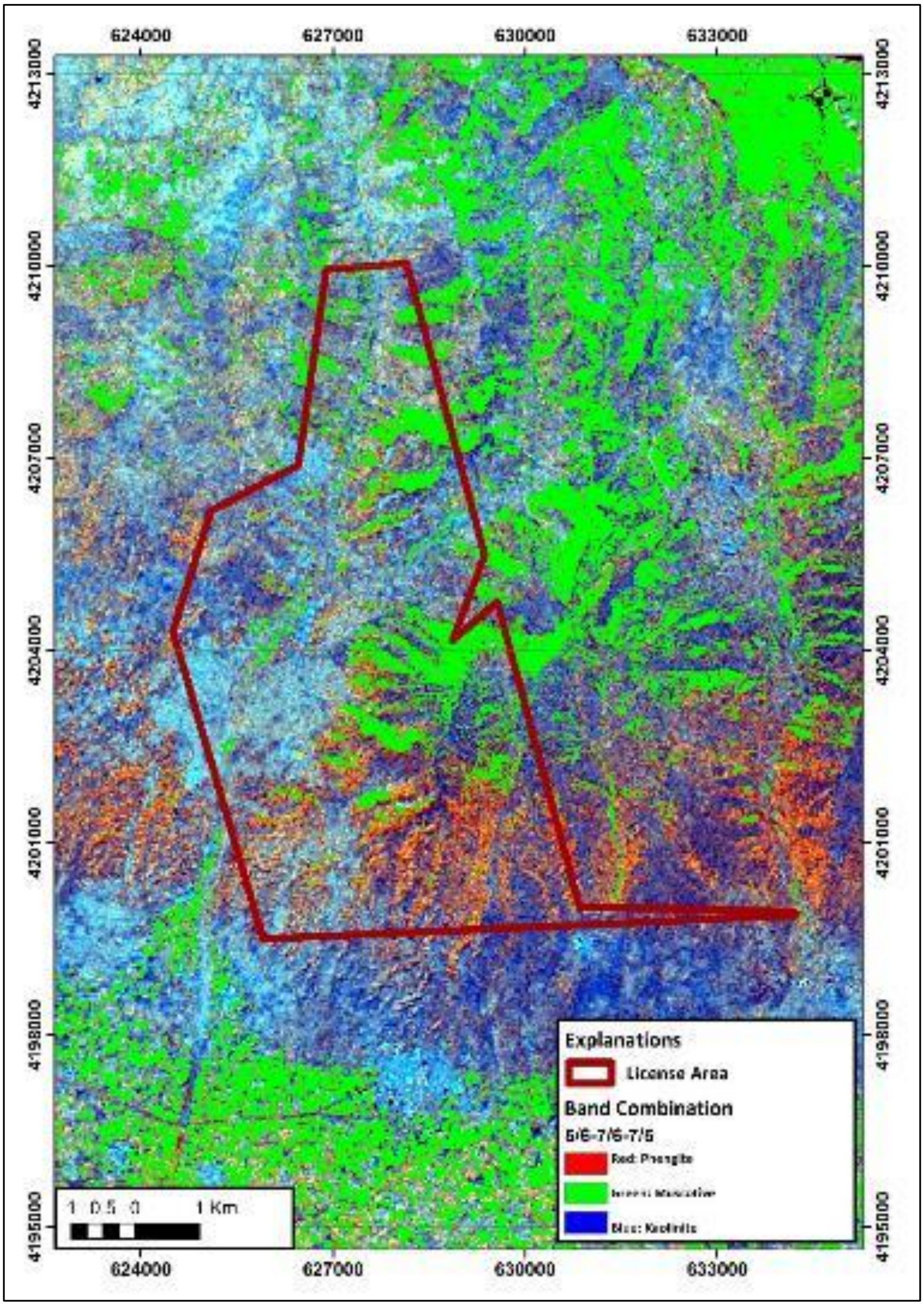

Figure 3.10. Advanced argillic alteration, 5/6-7/6-7/5 band combination (Phengite-Muscovite-Kaolinite) (Hewson et al., 2001, 2004) overlain by bright green colored vegetation mask.

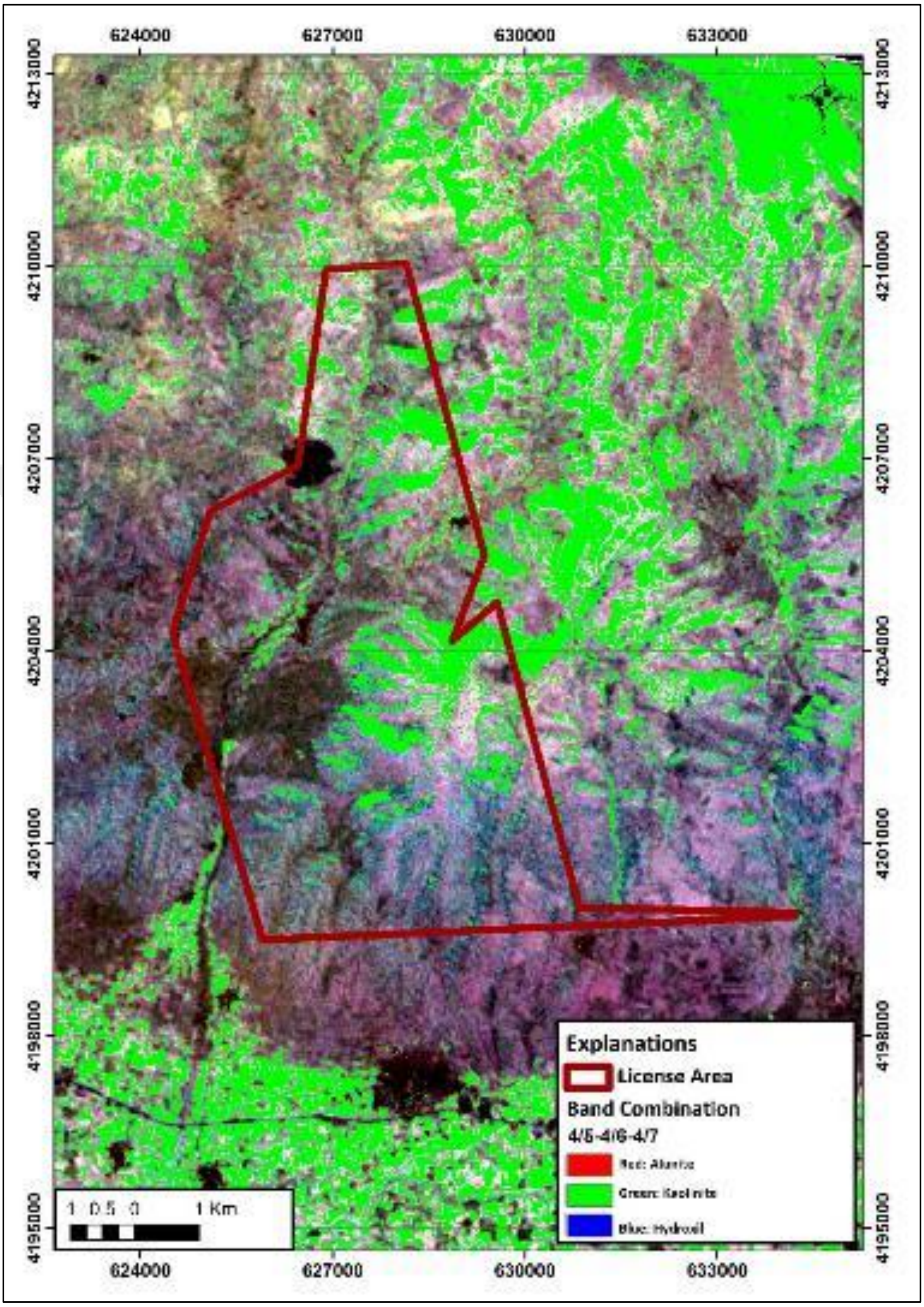

Figure 3.11. 4/5 (alunite-red) - 4/6 (kaolinite-green) - 4/7 (hydroxil minerals-blue) band combination overlain by vegetation mask (bright green).

As can be observed from the above given images, denser alteration mineral distribution is present where Menderes Metamorphics outcrop. Furthermore, denser alteration distribution was also observed at the south of the license area where power generation from geothermal energy is underway. Apart from alluvium and vegetation covered areas, this alteration distribution can be observed due north in the license area. This also indicates that geothermal potential is high at the north of the license area. Therefore, based on the assessment of these initial images, initial sampling locations from south to north were identified for the field applications.

Secondly, four different methods were selected to be utilized for final alteration mineral mapping. For the generation of final layers, the methods listed below were utilized:

- Advanced Argillic Alteration Relative Band Depth: (4+6)/5 (Rowan and Mars, 2003)
- Phyllic Alteration Relative Band Depth: (5+7)/6, (Rowan and Mars, 2003)
- Alunite Index: (7*7)/(5*8) (Ninomiya, 2004)
- Kaolinite Index (4*8)/(5*6) (Ninomiya, 2004)

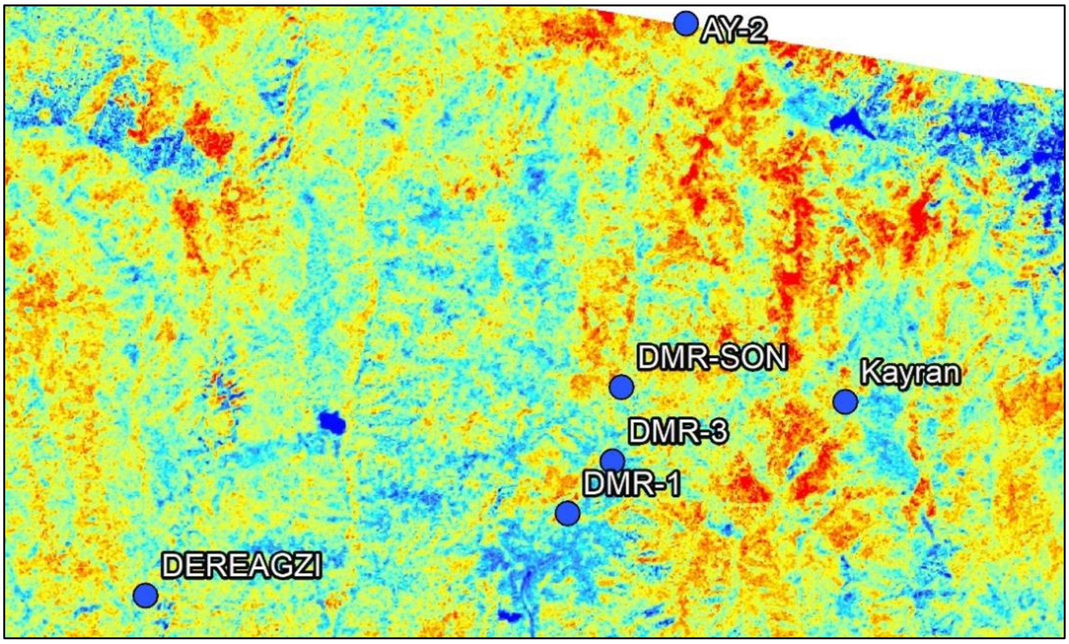

Figure 3.12. Advanced argillic alteration image.

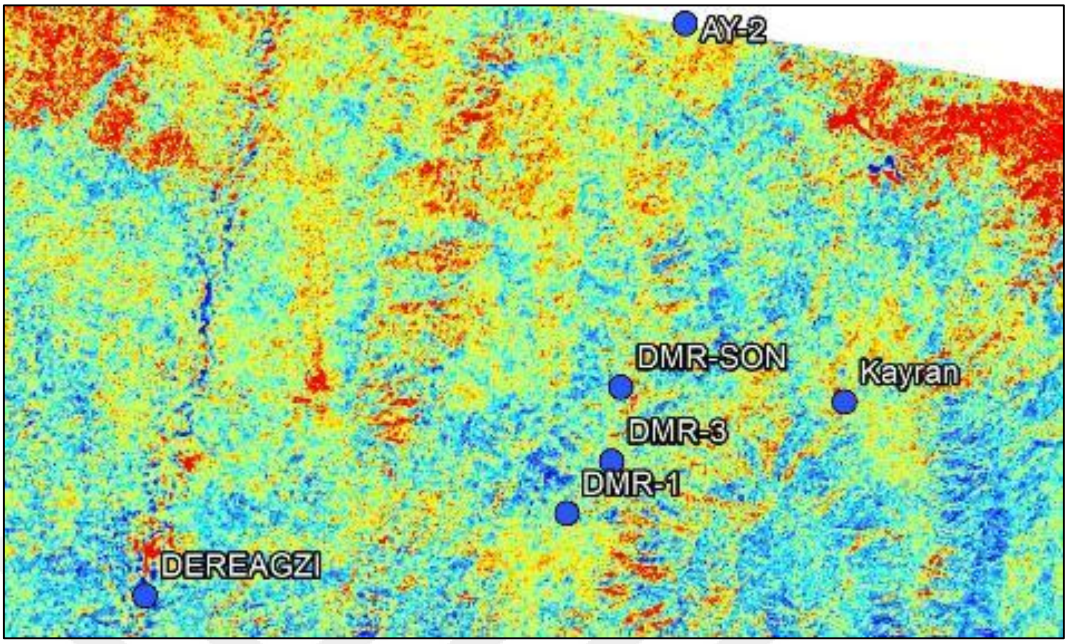

Figure 3.13. Phylllic alteration image.

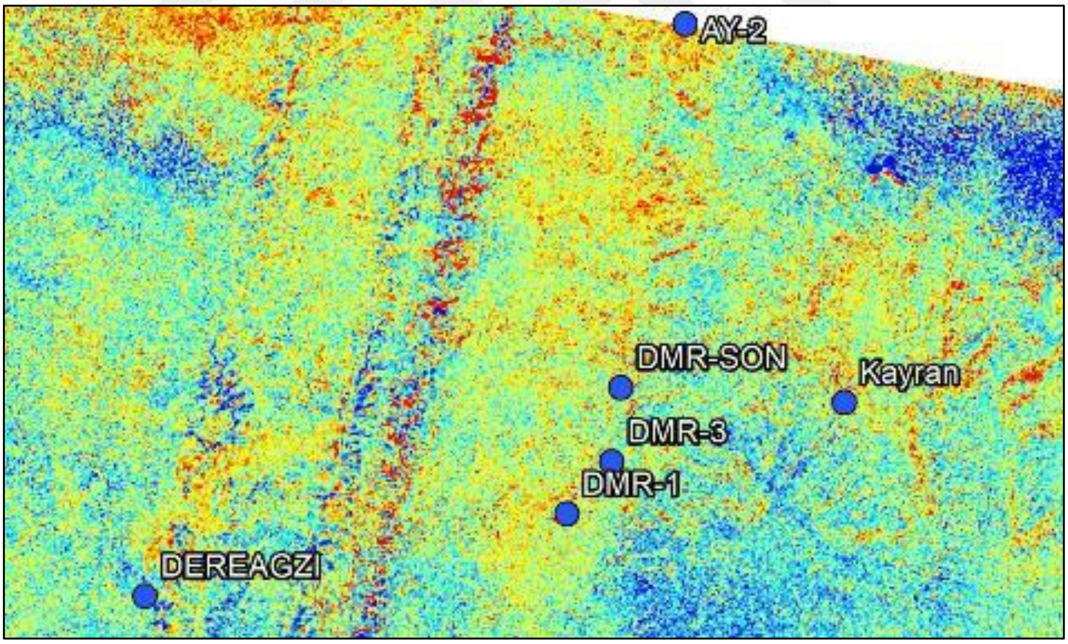

Figure 3.14. Alunite index image.

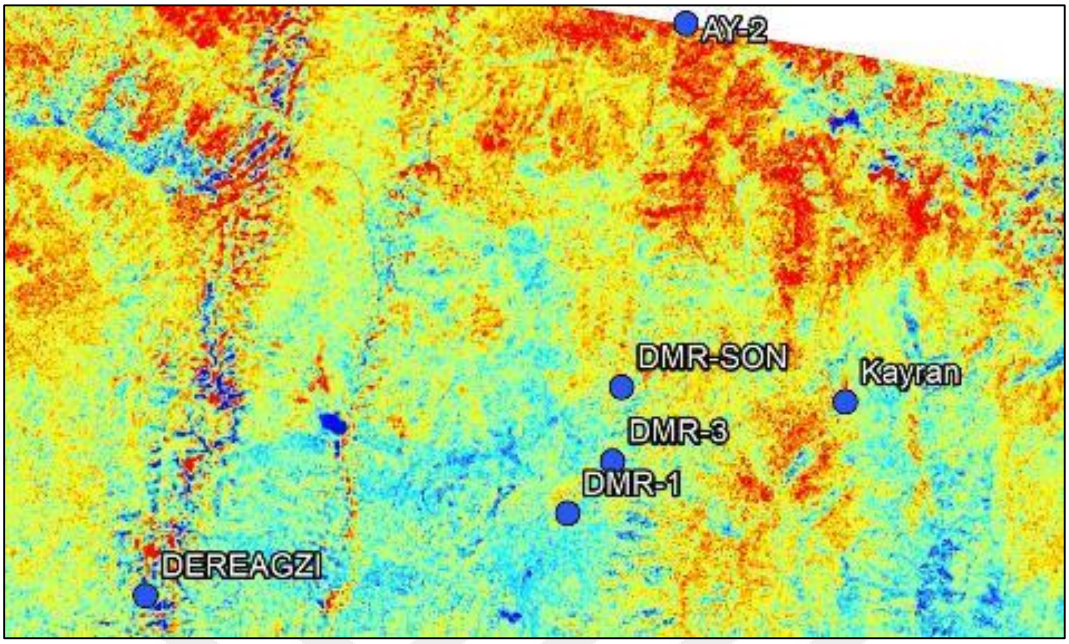

Figure 3.15. Kaolinite index image.

3.3 Fieldwork and Sample Collection

In order to compare with the satellite images, samples were collected from the field for XRD (X-ray Diffraction) analysis during fieldwork conducted on September 2021. Sampling locations are shown in Figure 3.16. The initial locations were identified through preliminary image analysis results. During field activity, the locations were finalized based on field observations of possible alteration locations and possible faults. Finally, samples were collected from eight locations and XRD analyses were performed on six of those samples.

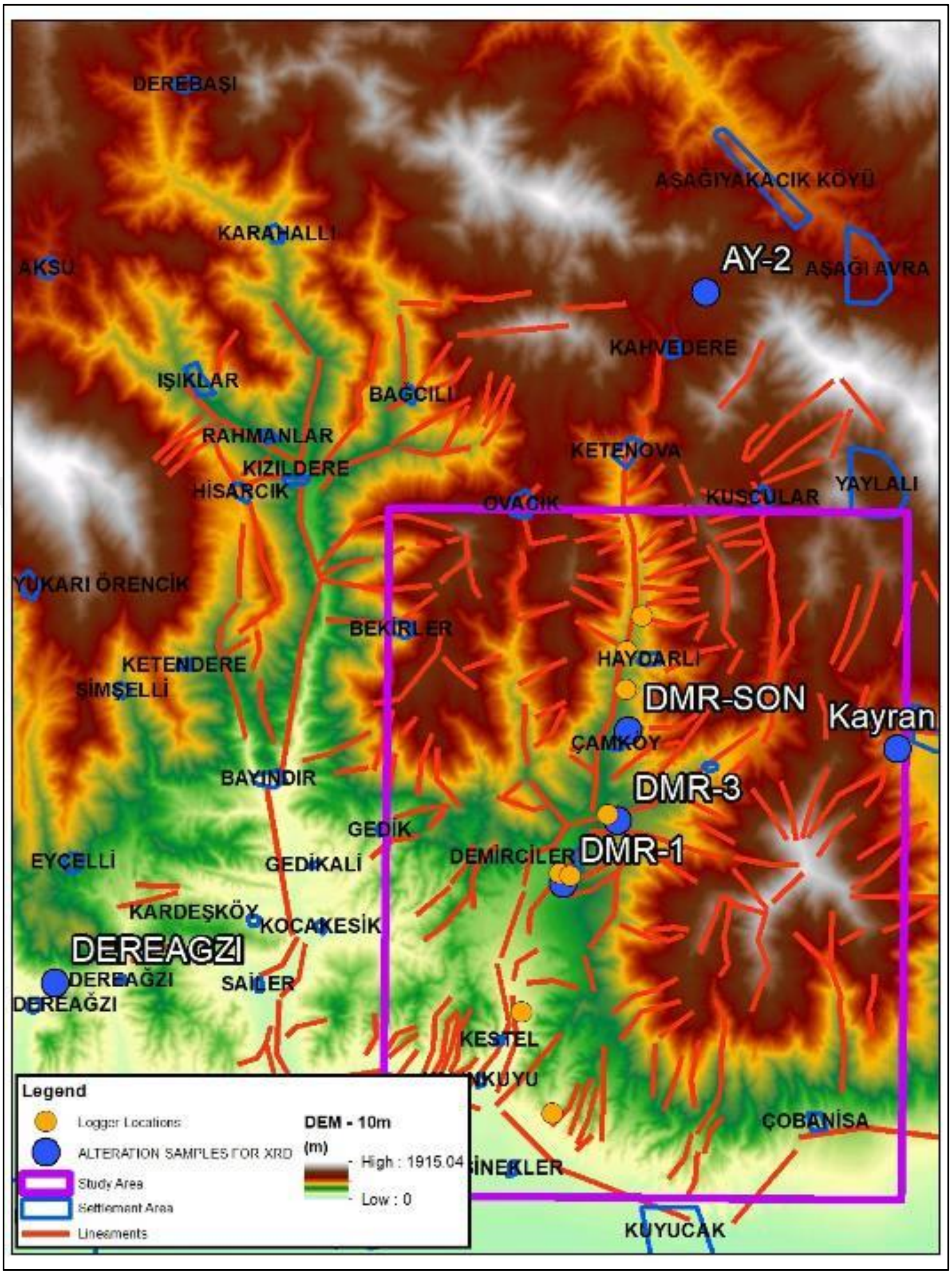

Figure 3.16. Alteration sample locations.

3.4 XRD Analysis

From ten samples collected from nine locations in the field, six samples were selected for XRD analyses. Following sections provide details on sample preparation and assessment of results.

3.4.1 Sample Preparation

As part of XRD analyses, 6 samples collected from the field were selected for analyses. The sample preparation steps were as follows:

Samples collected from the field were tested for carbonate content with HCl. Those reacted with HCl were further treated.

Material collected from the field were sieved to retain <170 µm particle size to obtain at least 12 gr. powder. Samples that reacted were removed from the carbonates by the addition of 50 mL of 1N sodium acetate-acetic acid (NaOAc) buffer (pH 4.5).

Powder samples were added to 1 lt of water and the top 10 cm part of the sample prepared possessed only 2µm sized clay particles after eight hours according to Stoke's Law.

This acquired portion was centrifuged with 6000 rpm for approximately ten minutes

Four slides were prepared from centrifuged samples to represent samples with the conditions given below in addition to powdered samples:

- Air dried
- Ethylene glicolated
- 300°C heated
- 550°C heated

Therefore, five different XRD analyses were performed for each sample in order to differentiate between different clay minerals.

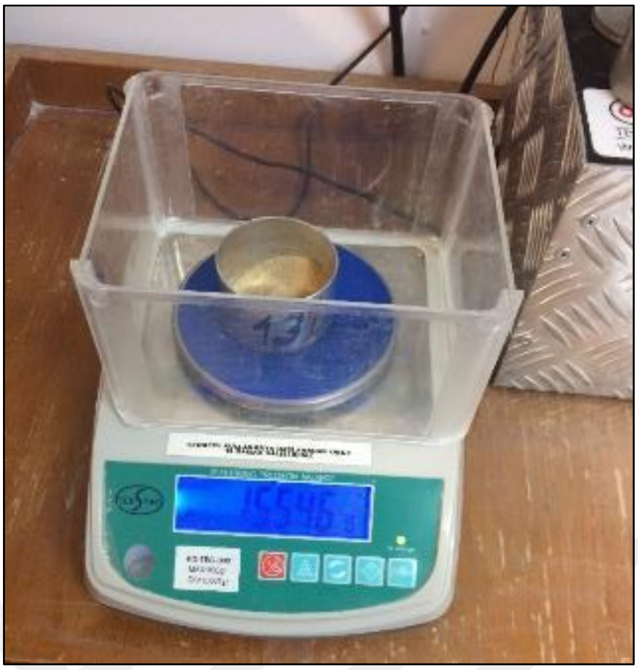

Figure 3.17. Sample weighing after sieving.

Figure 3.18. NaOAc treatment.

Figure 3.19. Centrifuge setup.

Figure 3.20. Ethylene glycol treatment.

Figure 3.21. Samples before 300°C treatment.

Figure 3.22. Samples before 550°C treatment.

Figure 3.23. Samples after 550°C treatment.

Following the sample preparation process, the thin film slides along with 2 gr powder samples were delivered for XRD analyses. The sample numbers and corresponding field sample IDs are given below (Table 3.3). Location map showing XRD sample locations with along with temperature data logger locations are presented in Figure 3.16.

Table 3.3. XRD Sample locations and IDs from north to south.

Field ID	Field Location	XRD Sample ID
AY-2	North of Study Area	13
DMR-Son-Çamköy	Along main Demirciler Road	131
L20-DMR-3	Along main Demirciler Road – Near Tabela logger location	15
L18-DMR-1	Along main Demirciler Road- Near Benzinlik logger location	14
L22-Kayran	East of Study Area	17
L13-Dereağzı	West of Study Area	18

3.4.2 Interpretation of XRD Analysis Results

XRD analysis was performed on a total of six samples for four different thin film conditions, namely: a) air dried, b) ethylene glycolated, c) 300°C heated and d) 550°C heated and also for powder samples. Results of thin film XRD analysis in 2θ (degrees) versus intensity count and identified minerals are presented in Figure 3.24 and results of powder sample XRD analysis are presented in Figure 3.30. Abbreviations in the figures are presented based on Warr (2020) and Warr (2021) and given in Table 3.4 below.

Table 3.4. Mineral abbreviations used in XRD analysis results figures (Warr, 2020; Warr, 2021).

Mineral	Abbreviation
Albite	Ab
Alunite	Alu
Illite	Ilt
Kaolinite	Kln
Mica	Mca
Montmorillonite	Mnt
Pyrophyllite	Prl
Quartz	Qz
Smectite	Sme

Summary of interpretation of XRD analysis results, identified minerals and their temperature ranges are presented in Table 3.5 below.

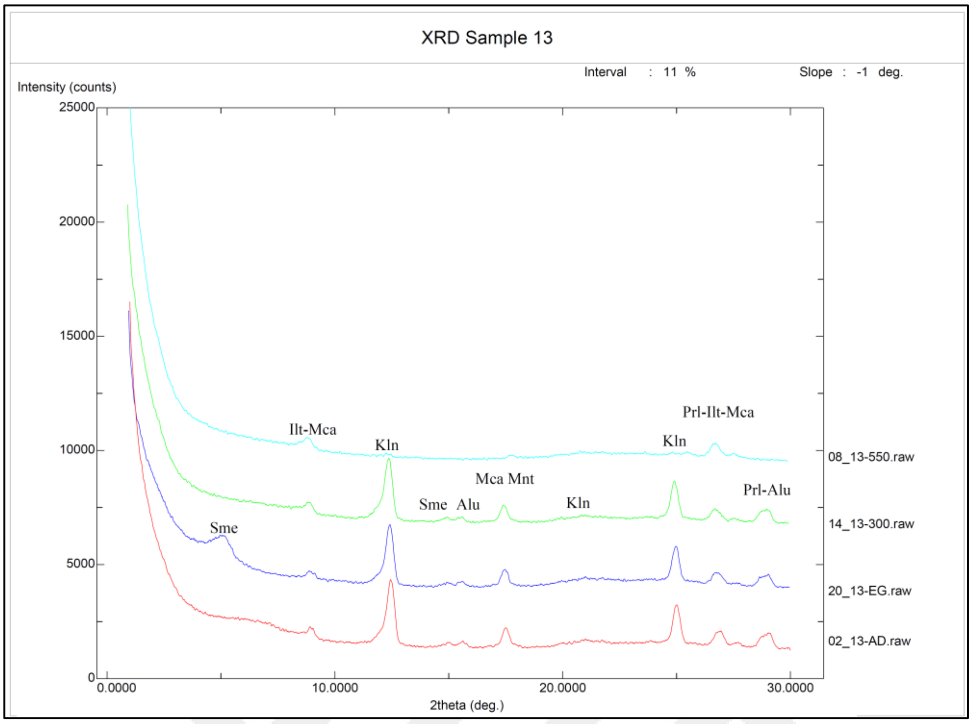

Figure 3.24. XRD results of AY-2 Sample (13)

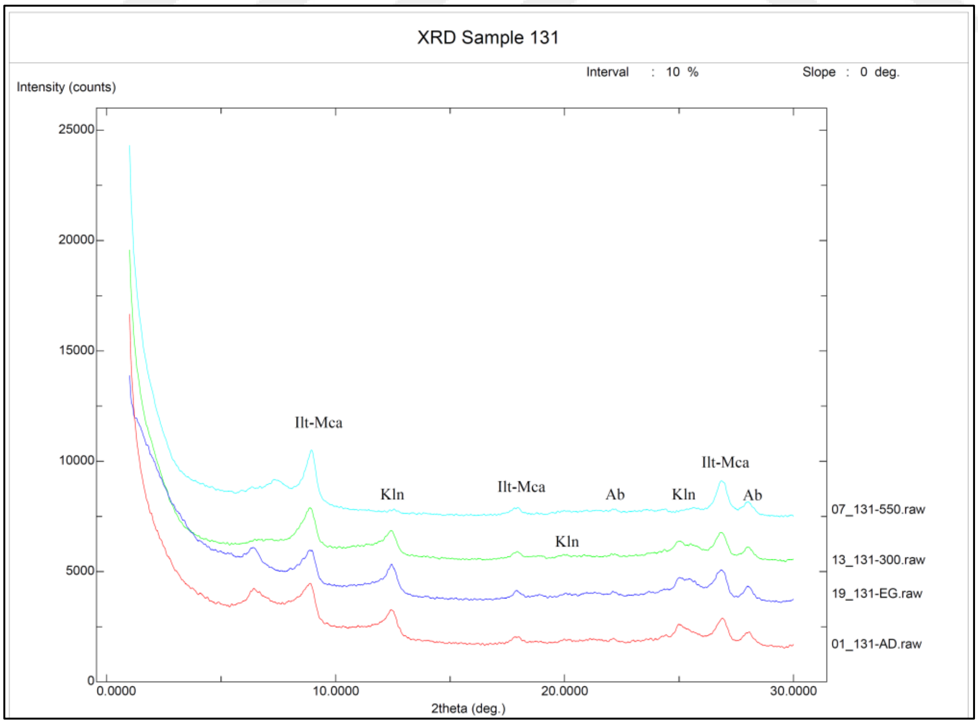

Figure 3.25. XRD results of DMR-Son Sample (131).

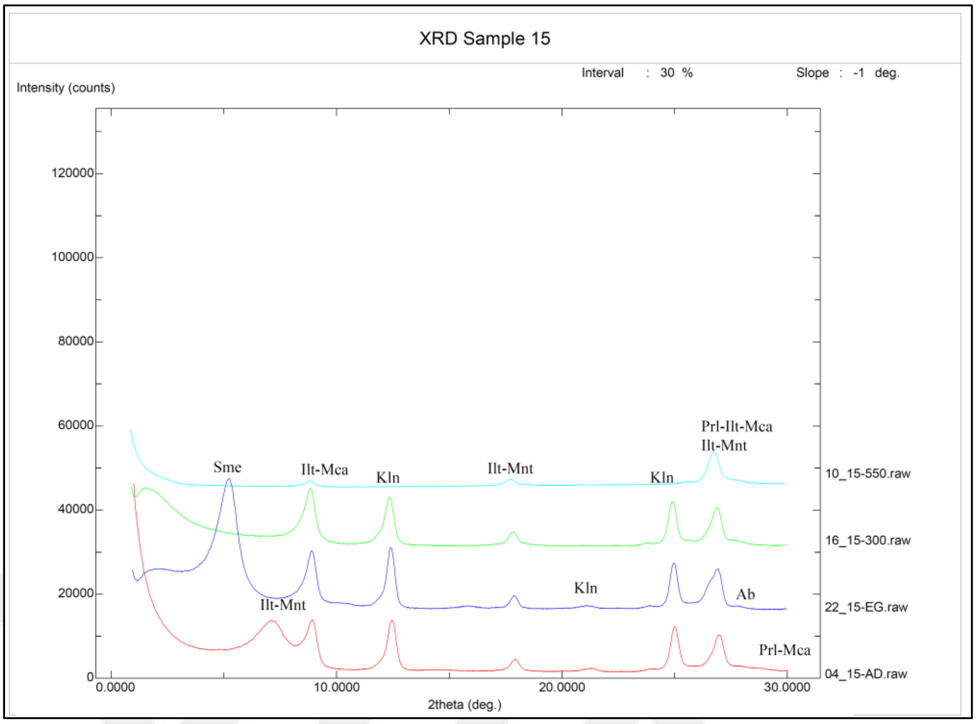

Figure 3.26. XRD results of DMR-3 Sample (15).

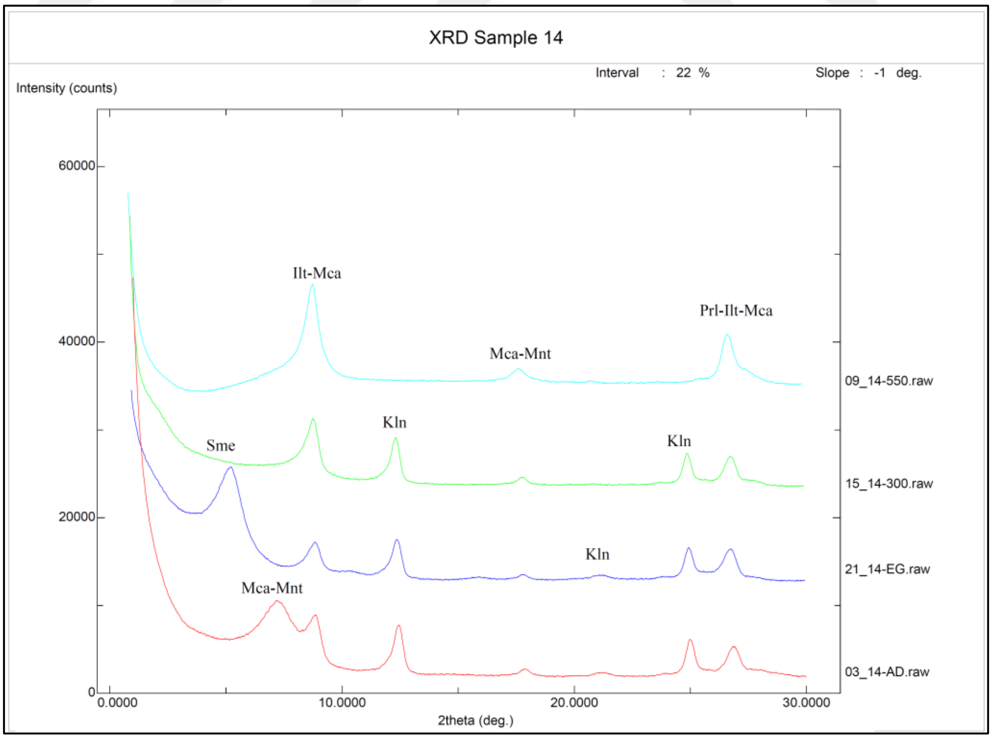

Figure 3.27. XRD results of DMR-1 Sample (14).

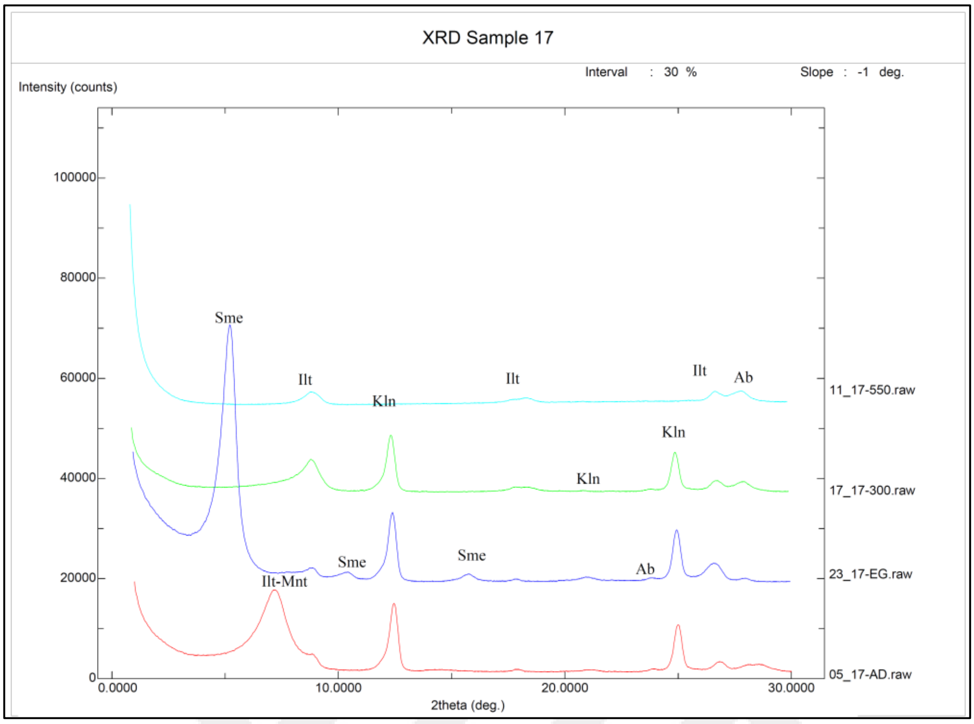

Figure 3.28. XRD results of Kayran Sample (17).

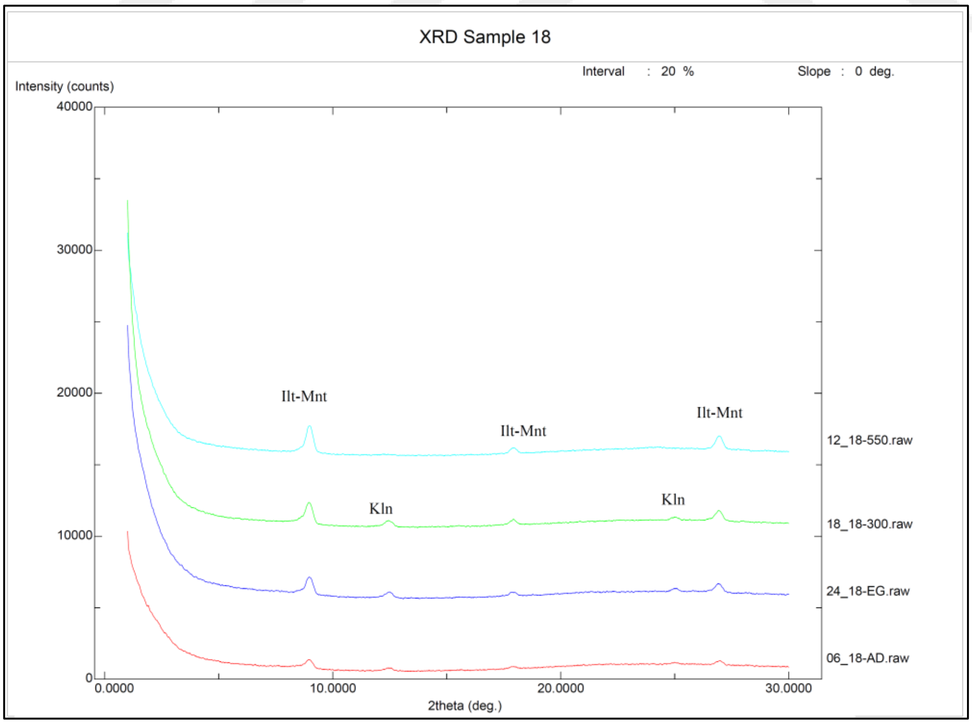

Figure 3.29. XRD results of Dereağzı Sample (18).

Table 3.5. XRD Sampling locations and identified minerals from thin film samples from North to South

Field ID	XRD Sample ID	Identified Clay Minerals	Indicative Temperature Range
AY-2	13	• Illite and Mica • Kaolinite • Smectite • Pyrophyllite • Quartz	• 140-200 • ~100 • 100-150 • ~200 • 100-200 (+Kln) • >230 (+Pyro.)
DMR-Son-Çamköy	131	• Illite and Mica • Kaolinite • Albite • Quartz	• 140-200 • ~100 • 150-300 • 100-200 (+Kln)
L20-DMR-3	15	• Illite and Montmorillonite • Illite and Mica • Smectite • Kaolinite • Albite • Pyrophyllite?	• 150-220 • 140-200 • 100-150 • ~100 • 150-300 • ~200
L18-DMR-1	14	• Illite and Mica • Kaolinite • Smectite • Pyrophyllite • Alunite	• 140-200 • ~100 • 100-150 • ~200 (if with Q) • ~200 (if with Q)
L22-Kayran	17	• Illite and Montmorillonite • Illite • Kaolinite • Smectite • Albite	• 150-220 • 120-350 • ~100 • 100-150 • 150-300
L13-Dereağzı	18	• Illite and Montmorillonite • Kaolinite	• 150-220 • ~100

Furthermore, results of the XRD analyses on powder samples are given in Figure 3.30 and a summary of identified peaks and matching minerals are presented in Table 3.6.

As can be seen from the interpretation of thin film samples, minerals identified from south to north indicate higher temperatures in general. Also, as a result of the interpretation of XRD results of powder samples, minerals summarized in Table 3.7 have been identified.

Table 3.6. Minerals identified from powder XRD results from north to south.

Sample ID	**Identified Minerals**	**Identified Peaks (2-theta°)**
13	Feldspar	20.84, 27.57, 32.96
	Gypsum	11.6, 15.1, 20.0
	Illite	14.825, 15.41, 17.718, 19.778, 20.31 20.814, 20.94, 21.20, 21.99, 22.41, 22.936, 23.437
	Kaolinite	8.825, 11.579, 12.312
	Mica	7.77, 8.825, 17.323, 17.718
	Montmorillonite	24.809, 25.22, 25.575, 26.5765, 26.749, 27.002, 27.418, 27.837, 28.24, 28.543, 28.879, 29.748
	Quartz	22.41, 26.58, 36.48, 50.12
131	Chlorite	30.437
	Illite	17.788, 19.29, 19.84, 20.13, 20.828, 21.991, 23.011, 23.515, 23.83, 24.115, 25.142, 25.314, 25.552, 25.78, 26.386, 26.590, 26.806, 27.8725, 28.238
	Kaolinite	12.483, 25.142, 25.314
	Quartz	20.828, 26.386, 27.684, 36.486, 39.453
	Smectite	6.211, 19.84
15	Feldspar	8.796, 11.644, 12.3934, 24.809, 25.22, 27.837, 30.331, 31.134, 34.910, 37.382, 38.344
	Gypsum	11.579, 12.312, 14.825
	Illite	8.9292, 20.866, 24.921, 27.725
	Kaolinite	7.77, 12.37, 24.71
	Mica	9.50, 19.80
	Pyrophyllite	11.10, 20.10
	Quartz	20.31, 26.5765, 27.418, 28.24, 29.748, 34.352, 35.076
14	Chlorite	30.438, 52.87
	Garnet	22.992, 23.536
	Illite	17.806
	Kaolinite	11.63, 26.6084
	Montmorillonite	13.830
	Quartz	8.862, 25.479, 34.27, 49.192, 50.0884, 55.76, 59.928,
17	Chlorite	7.7, 14.1, 16.6
	Illite	9.91, 10.15, 10.65
	Kaolinite	12.4, 20.8, 21.2
	Quartz	20.8, 26.6, 36.5
	Sericite	9.23, 19.69, 24.12
	Smectite	5.8, 19.9, 24.3
18	Chlorite	16.277, 17.292, 17.756, 18.807
	Illite	19.826, 20.774, 22.418, 22.890, 23.344, 24.292
	Kaolinite	12.296, 12.902
	Montmorillonite	7.32, 19.826, 24.292
	Quartz	26.114, 26.595, 27.639, 30.257
	Sericite	12.296, 19.826

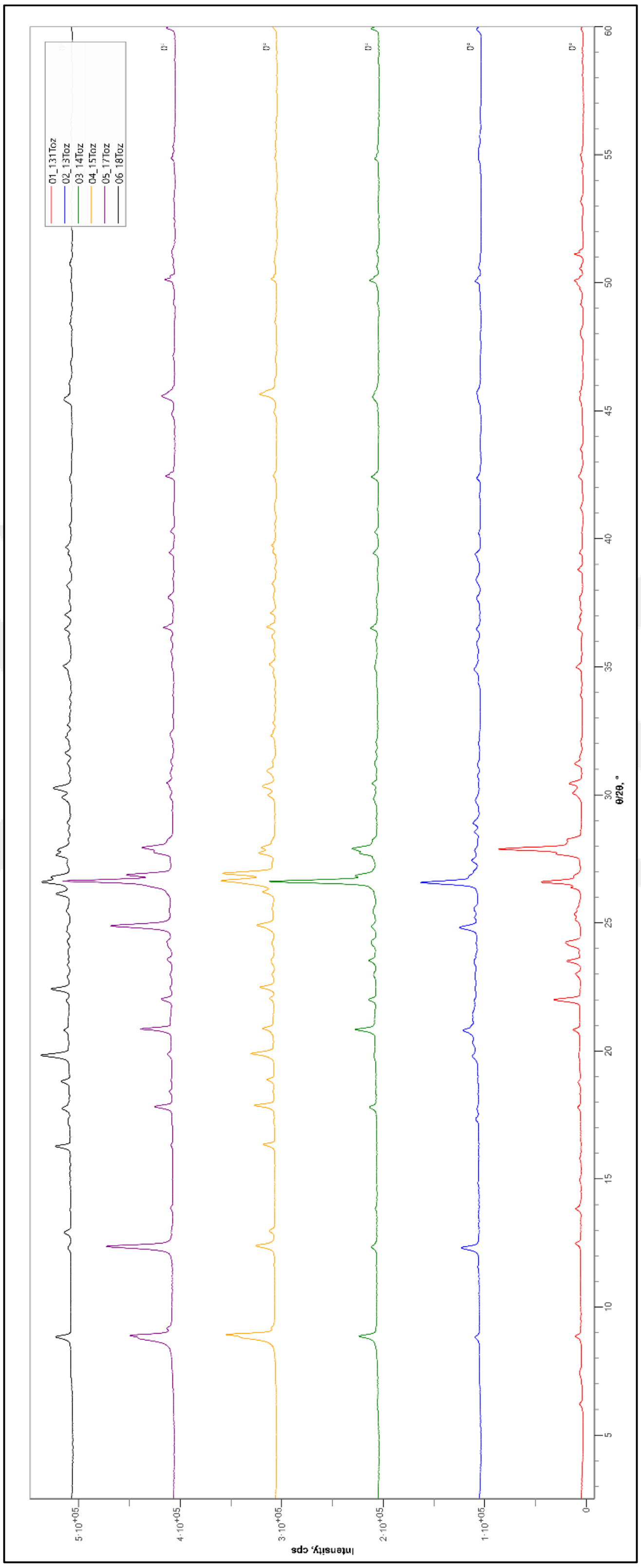

Figure 3.30. XRD Results of the powder samples.

3.5 Comparison of XRD and Satellite Image Results

The second study was the assessment of XRD analyses conducted on samples collected during the previous fieldworks. Previously, out of ten samples collected from the field, six of them were selected for the XRD analyses. The results of XRD analyses were compared with the processed ASTER images. According to the assessment of the XRD results and comparison with the alteration maps processed from ASTER satellite images, it can be observed that the highest pixel values for the argillic alteration map were for the XRD Samples 14 and 13 where in the XRD results of Sample 14 all three alteration minerals, namely alunite, kaolinite and pyrophyllite were observed, and for Sample 13 both kaolinite and pyrophyllite were observed. For the phyllic alteration map results, the highest pixel value was observed in Sample no. 15 and both illite and smectite were observed in this sample. For the alunite index map, the highest pixel value was observed for the sample location where alunite was interpreted from XRD thin film results. For kaolinite index, since all samples had kaolinite, no distinct interpretation has been made.

Table 3.7. XRD Sampling Locations from South to North

Field ID	XRD Sample ID	Identified Clay Minerals	Indicative Temperature Range
L18-DMR-1	14	• Illite and Mica • Kaolinite • Smectite • Pyrophyllite • Alunite?	• 140-200 • ~100 • 100-150 • ~200 (if with Q) • ~200 (if with Q)
L20-DMR-3	15	• Illite and Montmorillonite • Illite and Mica • Smectite • Kaolinite • Albite • Pyrophyllite?	• 150-220 • 140-200 • 100-150 • ~100 • 150-300 • ~200
DMR-Son-Çamköy	131	• Illite and Mica • Kaolinite • Albite	• 140-200 • ~100 • 150-300
AY-2	13	• Illite and Mica • Kaolinite • Smectite • Pyrophyllite • Quartz	• 140-200 • ~100 • 100-150 • ~200 • 100-200 (+Kao) • >230 (+Pyro.)
L22-Kayran	17	• Illite • Kaolinite • Smectite • Albite	• 120-350 • ~100 • 100-150 • 150-300
L13-Dereağzı	18	• Illite and Montmorillonite • Kaolinite	• 150-220 • ~100

For the samples collected from the field, comparison with ASTER image for 4 different analyses were made. The minimum and maximum values for these maps are provided in the table below. The final alteration maps produced were:

- Advanced Argillic Alteration Relative Band Depth: (4+6)/5 (Rowan and Mars, 2003)
- Phyllic Alteration Relative Band Depth: (5+7)/6, (Rowan and Mars, 2003)
- Alunite Index: (7*7)/(5*8) (Ninomiya, 2004)
- Kaolinite Index (4*8)/(5*6) (Ninomiya, 2004)

Table 3.8 Min. Max. and Average values for Indices for the processed images.

Index	Max. Image Value	Min Image Value	Mean Value
Advanced Arg. Alteration	3.056	2.085	2.578
Phyllic Alteration	2.398	1.710	1.984
Alunite Index	1.651	0.838	1.090
Kaolinite Index	1.956	0.866	1.377

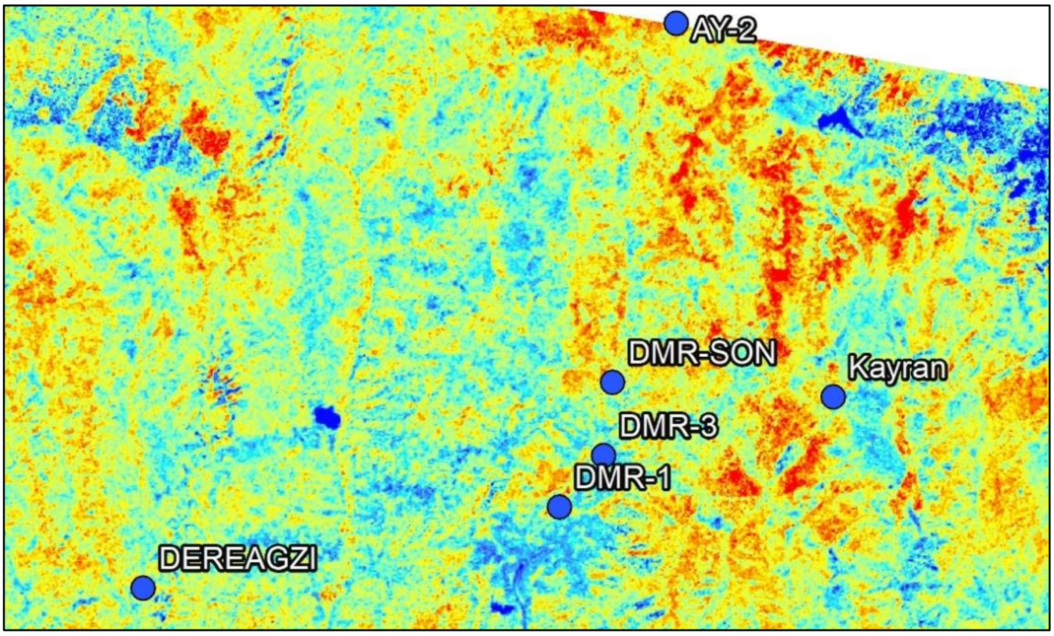

Figure 3.31. Advanced argillic alteration image.

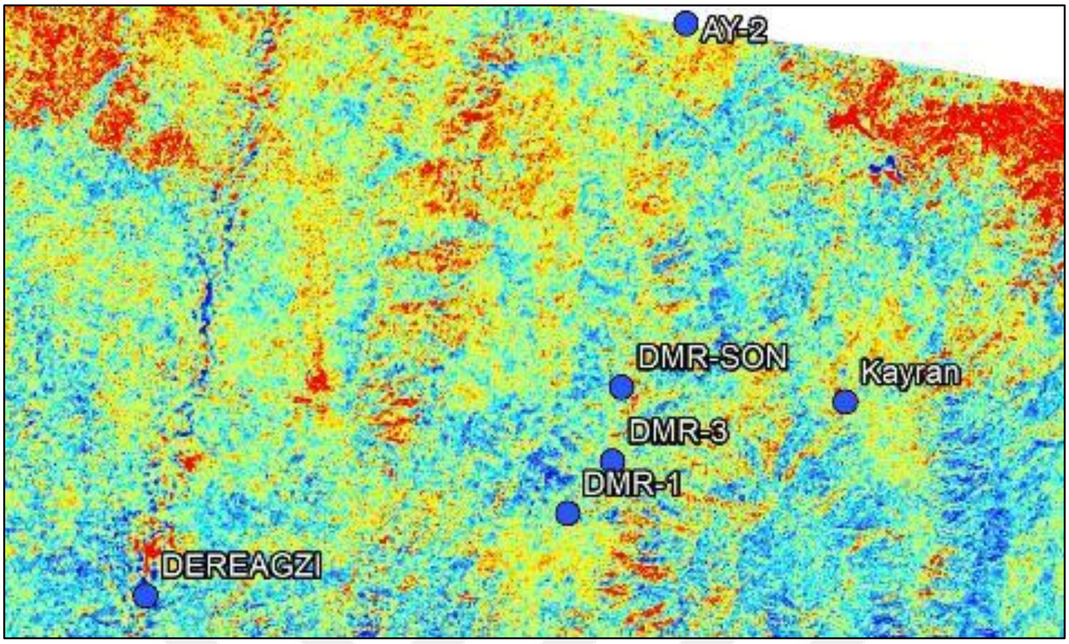

Figure 3.32. Phylllic alteration image.

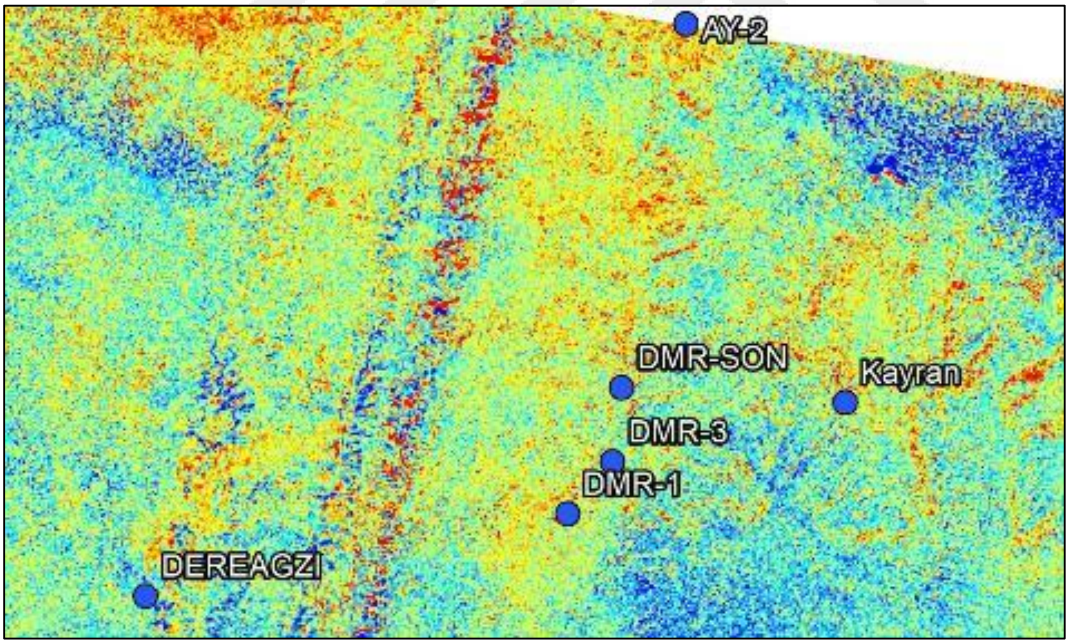

Figure 3.33. Alunite index image.

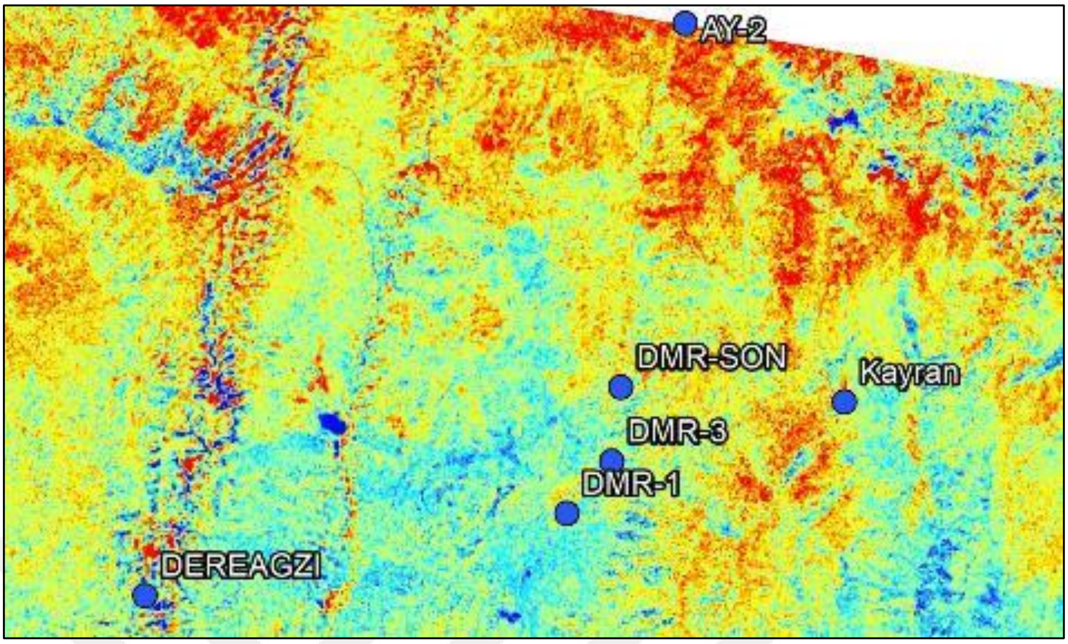

Figure 3.34. Kaolinite index image.

Table 3.9. Pixel values of XRD sample locations

Field ID	Field Location	XRD Sample ID	Identified Clay Minerals	Advanced Arg. Alteration (Alunite–kaolinite–pyrophyllite)	Phyllic Alteration (Sericite–muscovite–illite–smectite)	Alunite Index	Kaolinite Index
L18-DMR-1	Along main Demirciler Road- Near Benzinlik	14	• Illite and Mica • Kaolinite • Smectite • Pyrophyllite • Alunite	**2.64565**	2.03364	**1.13811**	1.42913
L20-DMR-3	Along main Demirciler Road – Near Tabela Location	15	• Illite and Montmorillonite • Illite and Mica • Smectite • Kaolinite • Albite • Pyrophyllite?	2.43744	**2.10068**	1.05306	**1.25298**
DMR-Son-Çamköy	Along main Demirciler Road	131	• Illite and Mica • Kaolinite • Albite	2.49765	2	1.043	**1.26695**
AY-2	North of Study Area	13	• Illite and Mica • Kaolinite • Smectite • Pyrophyllite • Quartz	**2.68116**	2.04545	1.07001	1.54172
L22-Kayran	East of Study Area	17	• Illite • Kaolinite • Smectite • Albite	2.63982	2	1.05346	1.39121
L13-Dereağzı	West of Study Area	18	• Illite and Montmorillonite • Kaolinite	2.5471	2.08781	1.08353	1.56932

3.6 Results and Discussion of Results for Alteration Mineral Mapping

As part of alteration mineral mapping, a two phased approach was followed. First, initial alteration maps were generated by utilizing different band combination and band ratios methodologies prior to fieldworks to guide initial assessment. Then, based on these initial maps and field observations, samples were collected from potential alteration zones and lineament locations. As part of second phase, four different methods were selected for final alteration mineral mapping, namely: a) advanced argillic alteration relative band depth (Rowan and Mars, 2003), b) phyllic alteration relative band depth (Rowan and Mars, 2003), c) Alunite index (Ninomiya, 2004) and d) Kaolinite index (Ninomiya, 2004).

XRD analyses were performed on six samples collected from the field and alteration minerals were identified according to the peaks observed based on known peak values provided in Chen (1977). The qualitative interpretation of the results has shown that alteration minerals significant for hydrothermal alterations related with geothermal presence are present in all of the samples, showing that, even though the study area is a blind geothermal system with no surface geothermal manifestation, presence of alteration minerals can be a guiding indicator for geothermal exploration.

Finally, alteration maps generated from ASTER satellite images were compared with the qualitative assessment of the XRD analyses results showing the highest pixel values in the argillic alteration map correlated with XRD Samples 13 and 14. Sample 14 exhibited all three alteration minerals: alunite, kaolinite, and pyrophyllite, while Sample 13 showed kaolinite and pyrophyllite. In the phyllic alteration map, the highest pixel value was observed for Sample 15, which contained both illite and smectite. The alunite index map showed the highest pixel value for the sample where alunite was detected. For the kaolinite index map, no distinct interpretation was possible as kaolinite was present in all samples.

As a conclusion, the results of the alteration mineral mapping have provided compatible results with the qualitative assessment of XRD analyses and has indicated to be a valuable method for geothermal exploration in blind geothermal systems.

CHAPTER 4

LINEAMENT MAPPING

In this chapter, lineament mapping (i.e., lineament extraction) from both satellite imagery and also from drone imagery as well as comparison of results with field scanline surveys are discussed. The study is conducted in three scales, namely local scale through assessment of satellite images and Digital Elevation Model, area scale through assessment of drone imagery acquired as part of this study and in location scale where scanline surveys were conducted at outcrop locations at the northwest of the study area where drone images were captured as well. A summary flow chart showing the steps conducted as part of lineament mapping is given in Figure 4.1.

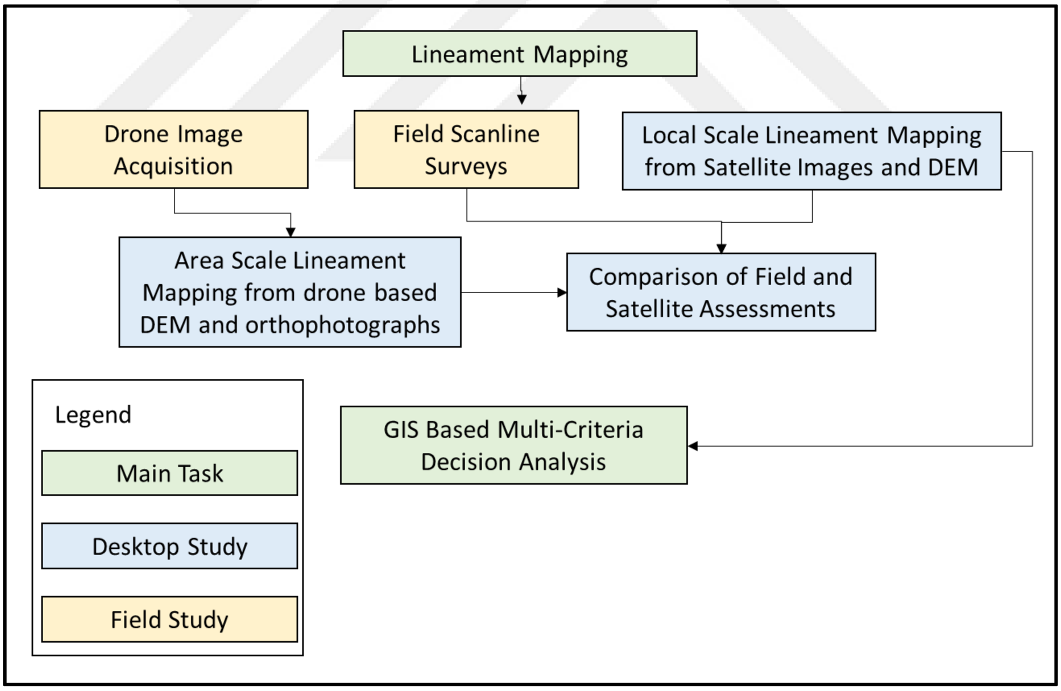

Figure 4.1. Flow chart for the lineament mapping studies.

4.1 Literature Review

Previous studies conducted by Faulds et al. (2010), Faulds et al. (2011), Faulds et al. (2012), and Faulds and Hinz (2015) clearly shows the importance of structural characterization of a geothermal field to identify the potential upwelling zones. This is especially significant where "blind geothermal" systems which is the case for the Kuyucak study area is under consideration since no surface manifestation such as hot springs could be identified. The identification and characterization of faults, especially Quaternary faults which would create a conduit between surface and deep seated geothermal systems is important. Van der Meer et al. (2014) mentioned that fault and lineament mapping are pre-requisites in geothermal exploration since there usually is a structural control on the location of geothermal surface manifestations.

Faulds et al. (2010) indicated that many geothermal fields in Great Basin, USA and Western Anatolia, Türkiye present discrete steps in fault zones or lie in zones of intersecting, overlapping, and/or terminating faults. As summarized by Faulds et al. (2010), geothermal fields in extensional regions such as Western Anatolia, Turkey and Great Basin, USA often occur in specific geological settings:

- Adjacent to discrete steps in normal fault zones (e.g., Desert Peak, Brady's in Nevada, USA; Simav in Türkiye),
- At intersections of normal faults with transversely oriented oblique-slip faults (e.g., Astor Pass in Nevada, USA, Salihli in Turkey),
- Within overlapping oppositely dipping normal fault zones (e.g., Salt Wells in Nevada, USA),
- Terminating along major normal faults (e.g., Gerlach in Nevada, USA; Germencik and Kızıldere in Türkiye),
- Within transtensional pull-apart zones (e.g., Lee-Allen in Nevada, Canby in California, USA; Pamukkale in Turkey).

Western Anatolia, similar to Great Basin in the USA is a normal fault controlled extension dominated geothermal system described as non-magmatic (or amagmatic) with convection dominant heat transfer type (Moeck, 2014).

Kocyiğit (2015) summarized the importance of faults in geothermal system at Büyük Menderes Graben and in Kuyucak region indicating that the current structure of the Büyük Menderes Graben is shaped by the Kuyucak and Menderes high-angle normal fault zones, which consist of many fault segments that cut and displace the older detachment fault where hot springs are located along the older detachment faults indicating that geothermal fluids are still using the older low-angle detachment fault. Kocyigit (2015) further iterated that, geothermal fluids circulate through both the older detachment and the younger high-angle normal faults where they intersect, as faults are the primary pathways for the movement of both cold meteoric waters and geothermal fluids, and thus the geothermal system in southwestern Turkey is fault controlled.

Roche et al. (2019) also identified three geothermal regions within the Büyük Menderes Graben, namely, Germencik and Salavatlı fields due west and Kızıldere field due east of the study area as fault and fracture controlled systems related with intersections between E-W trending detachment fault, N-S trending strike slip faults and E-W trending normal faults.

As summarized by Brogi et al. (2021) in the research focusing on Denizli geothermal field in Western Anatolia; permeability significantly improves when two or more fault segments interact, such as at linkage zones and fault intersections (Curewitz and Karson, 1997; Brogi, 2004; Faulds et al., 2009, 2010, 2013; Camanni et al., 2019; Liotta and Brogi, 2020). The interaction between fault segments creates multiple overlapping minor structures, increasing fracture density in localized rock volumes and thereby enhancing permeability from depth to the surface (Curewitz and Karson, 1997; Hancock et al., 1999; Brogi et al., 2016a; Olvera-García et al., 2020). In this context, step-over zones or relay ramps in normal fault systems are considered particularly favorable for geothermal fluid flow (Fossen and Rotevatn, 2016; Faulds et al., 2011; Faulds and Hinz, 2015). Consequently, fault zones are of strategic importance for geothermal exploration.

As summarized by Cambazoğlu (2012), lineament extraction methods can be broadly categorized into manual and automated approaches. Automated methods involve using various software to extract lineaments by integrating multiple parameters. Examples of such automated lineament extraction tools include the Segment Tracing Algorithm (STA) (Koike et al., 1995, 1998), Lineament Extraction and Stripe Statistical Analysis (LESSA) (Zlatoposky, 1992, 1997), Haar Transform (Wang et al., 1990), LINDENS software (Casas et al., 2000), and the LINE algorithm of PCI Geomatica software (2010). While these automated programs streamline the extraction process and significantly reduce processing time, they rely on user-defined parameters (e.g., filtering diameter, line length threshold, line fitting threshold) and often overlook general geological and structural data available for the study area. As a result, these methods may extract every linear feature that meets the input criteria, which was a key reason for not using automated lineament extraction in this study.

Recent examples of utilization of satellite images in lineament mapping for geothermal exploration include Tanjung et al. (2020) who utilized ASTER Global DEM data to extract lineaments in order to identify geothermally favorable areas in Banten Province, Indonesia. Also, Maswi and Mshiu (2024), utilized SRTM (Shuttle Radar Topography Mission) DEM and ASTER image analysis for identification of geological features and lineaments to identify geothermally favorable areas in Lake Natron, Tanzania and observed that alterations occur along the major lineaments of which both sides of the Lake Natron are noted to be covered by these alteration minerals.

4.2 Lineament Extraction from Satellite Imagery

For the satellite-based lineament extraction, ASTER satellite images and a Digital Elevation Model (DEM) of the area were utilized. Principal component analysis

(PCA) was applied to the VNIR and SWIR bands of the ASTER satellite to produce a three-band RGB image. This technique is employed to reduce dimensionality within the bands of a single image (Richards, 1993). Essentially, PCA minimizes noise, identifies correlated bands, and combines them into a smaller number of uncorrelated bands (Gupta, 2003). In this study, the first three principal components (PCs) were visualized as an RGB color composite, effectively reducing data redundancy and noise while maximizing the representation of the data in a single RGB composite image, allowing acquisition of the ideal image for lineament extraction (Nama, 2004).

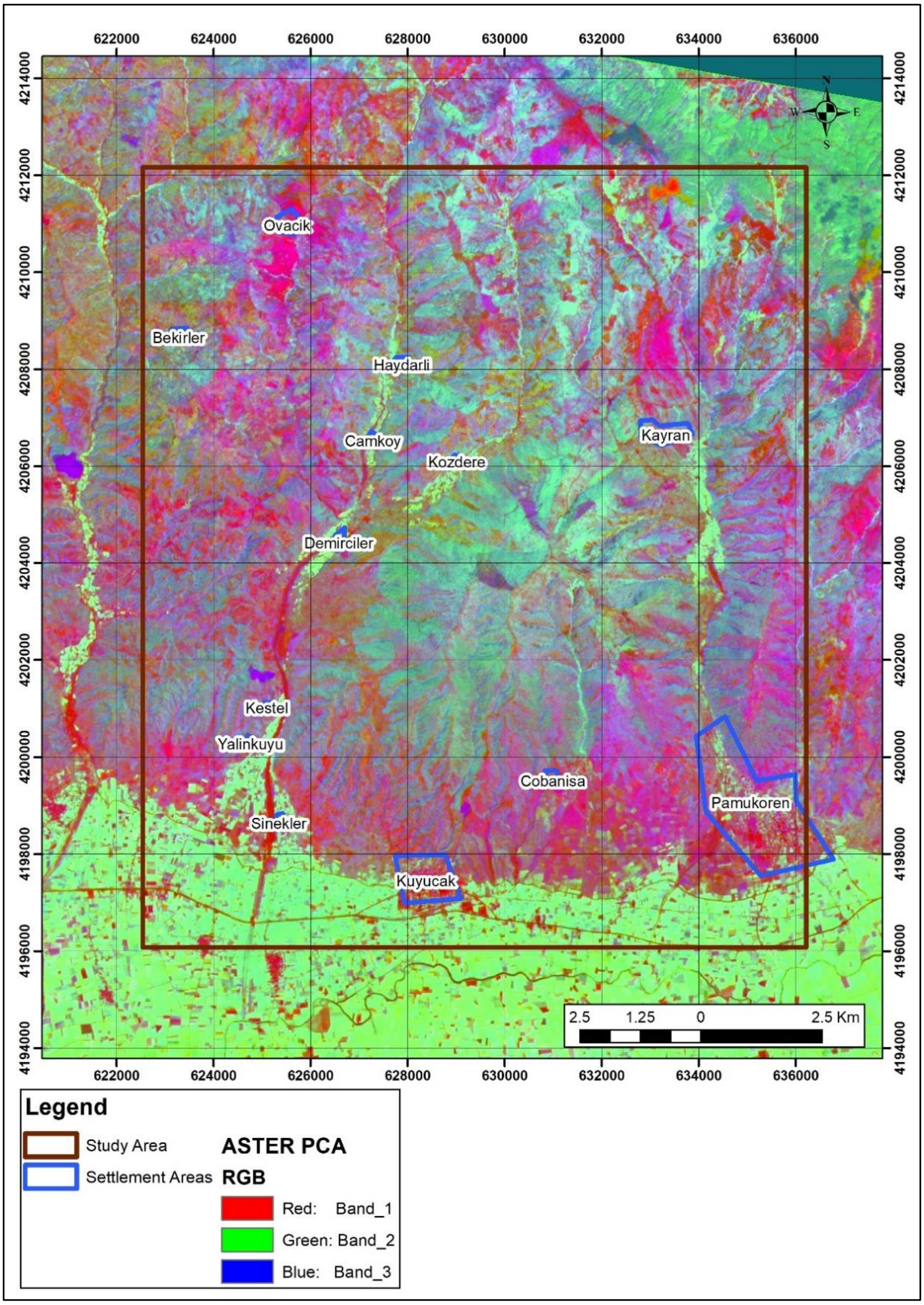

Figure 4.2. Principal Component image of the study area.

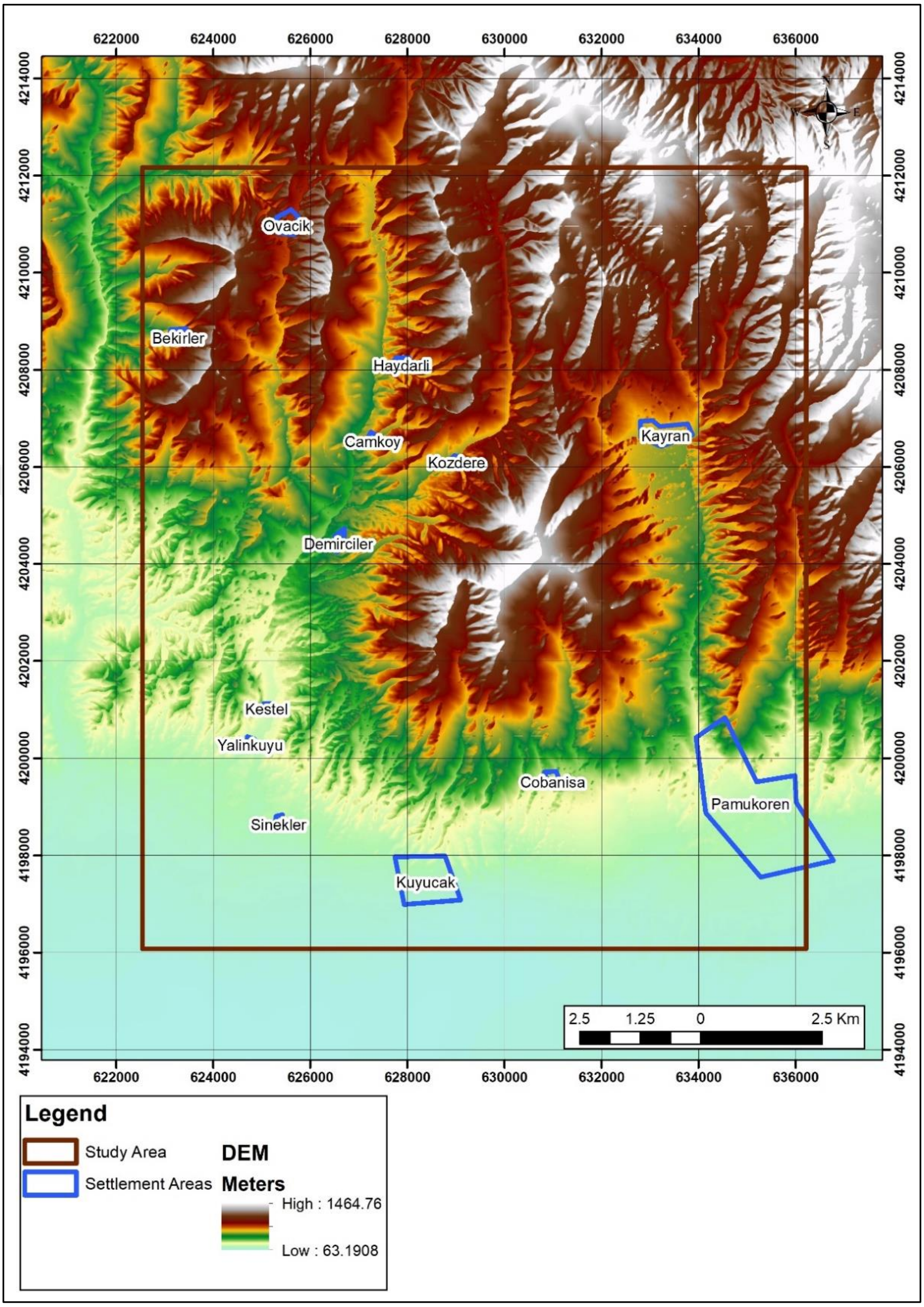

Figure 4.3. Digital Elevation Model (DEM) of the study area.

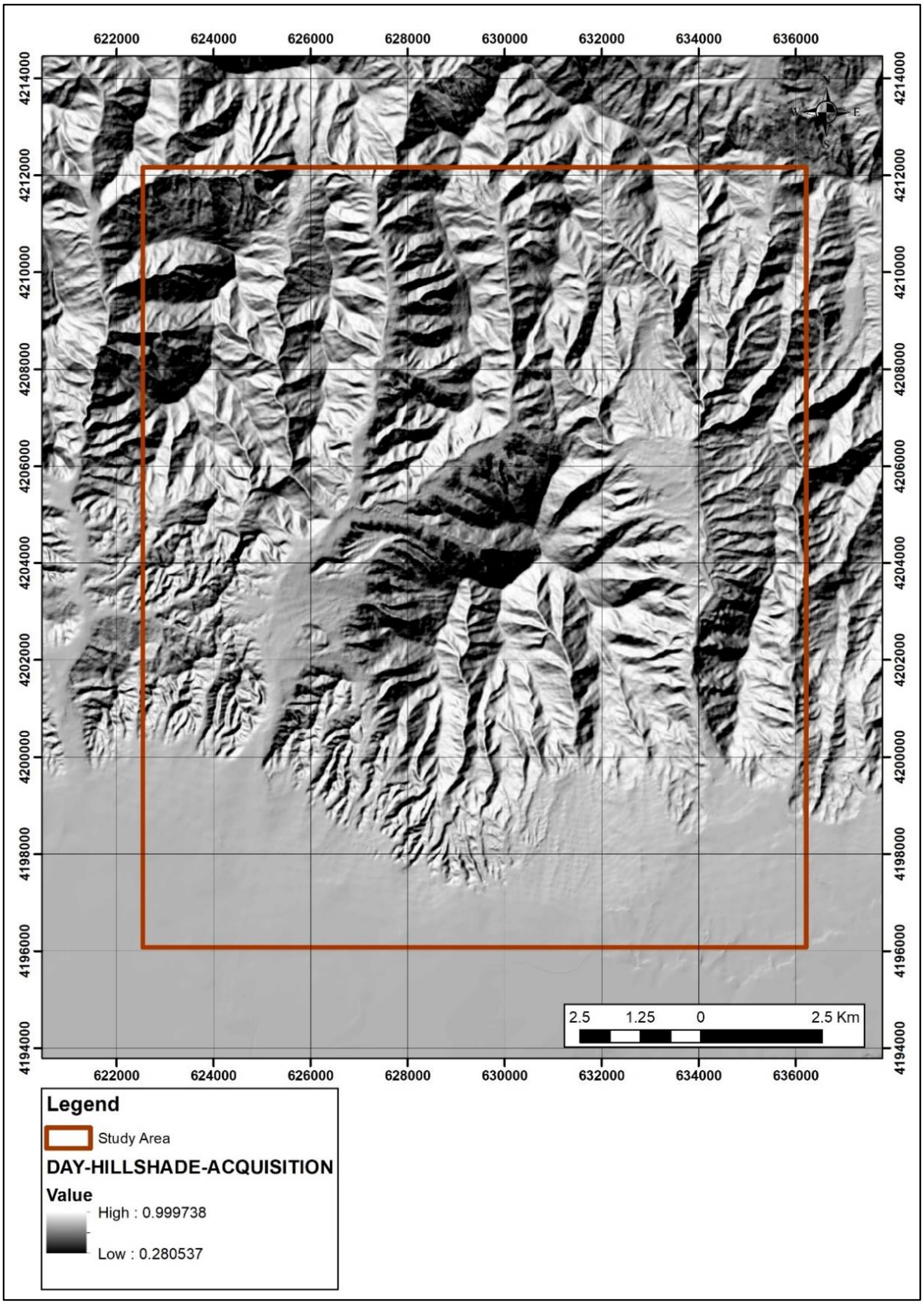

Figure 4.4. Hillshade image generated from DEM based on ASTER daytime image acquisition.

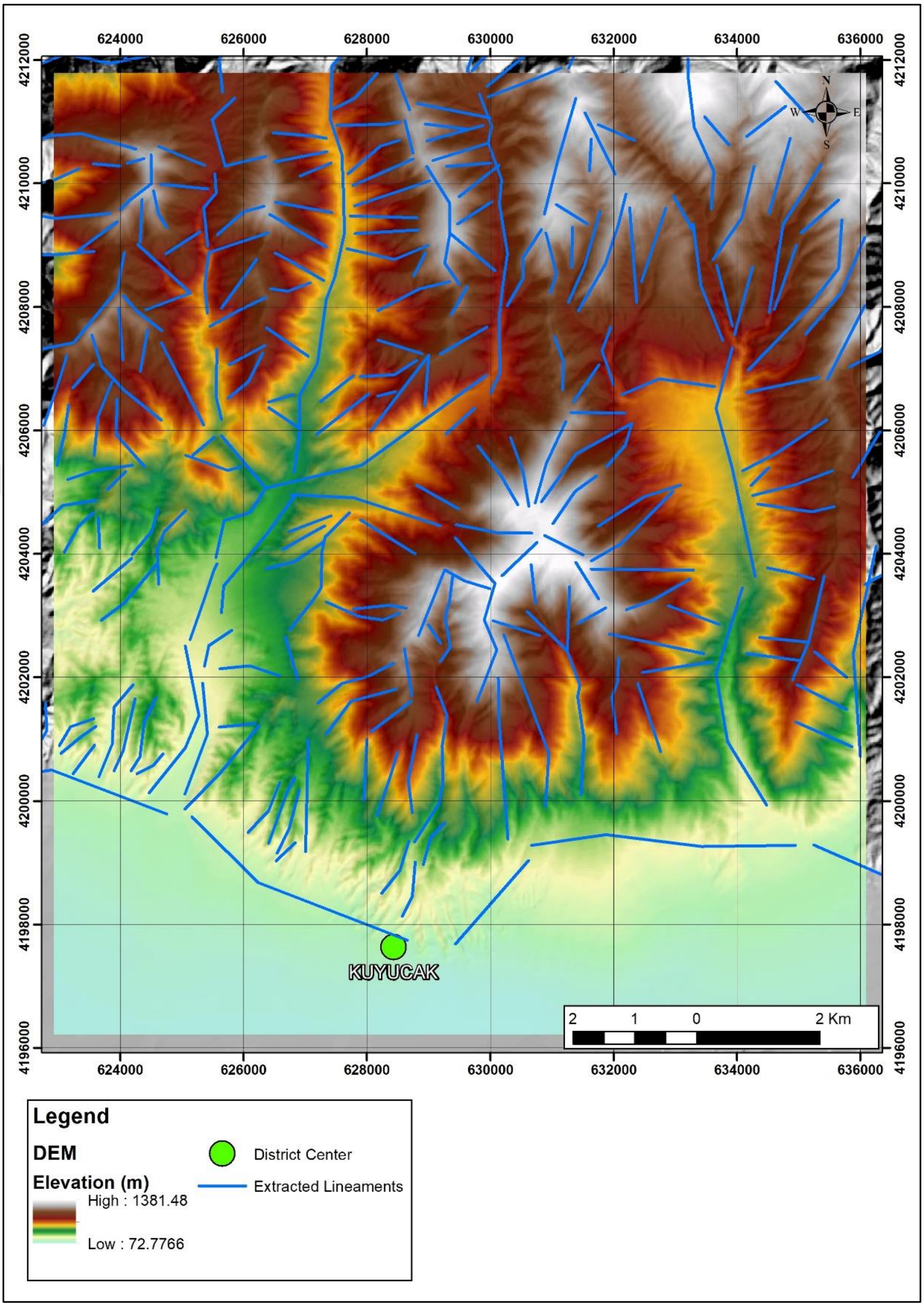

Figure 4.5. Extracted lineaments overlain on DEM image of the study area.

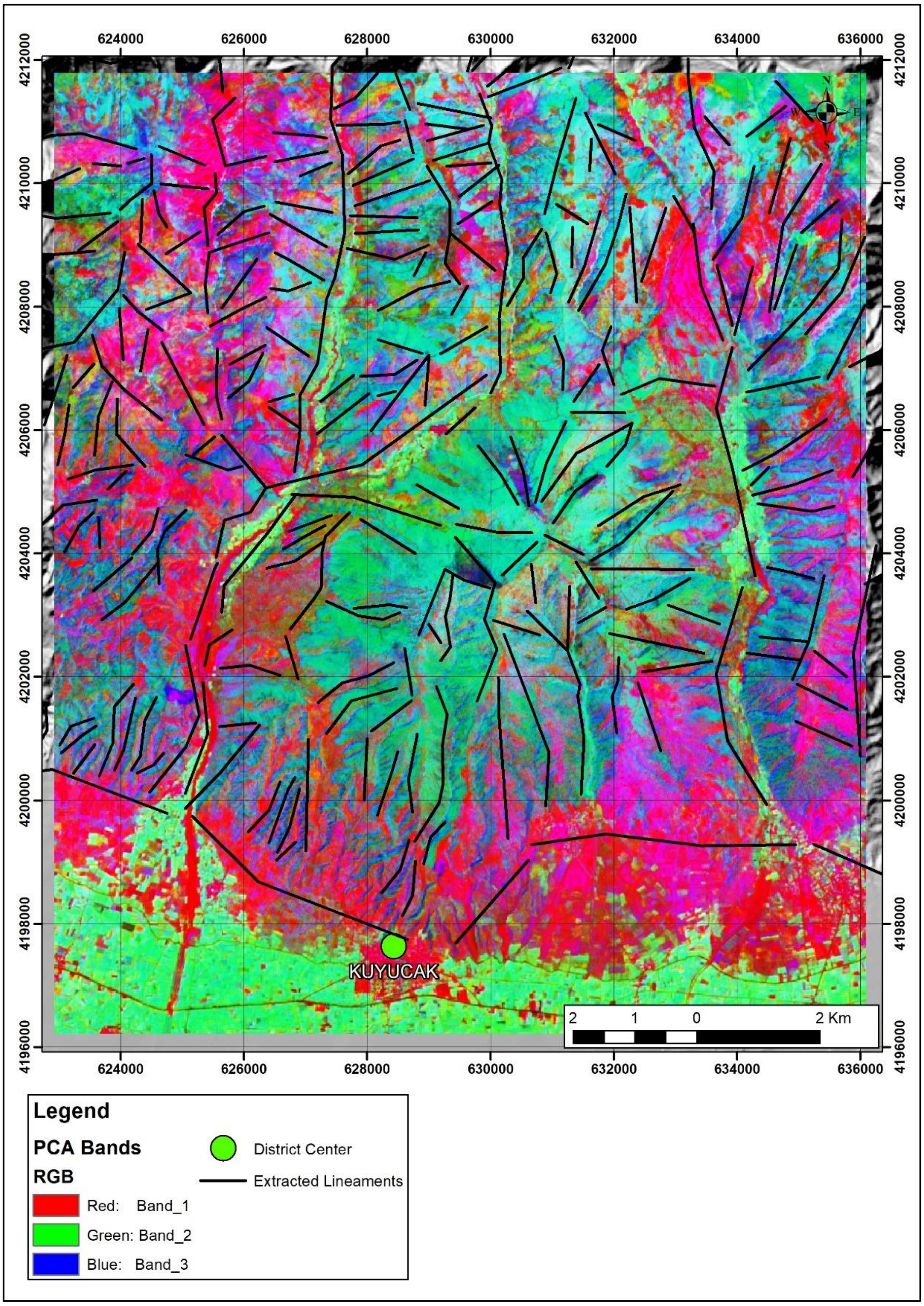

Figure 4.6. Extracted lineaments overlain on PCA resultant RGB image.

A total of 254 lineaments were extracted from the images with a minimum length of 284 m, maximum length of 6231 m and average length of 1194 m.

As can be seen from the rose diagram shown in Figure 4.7, the dominant directions for the lineaments are N0°E, N30°E and N60°E, respectively.

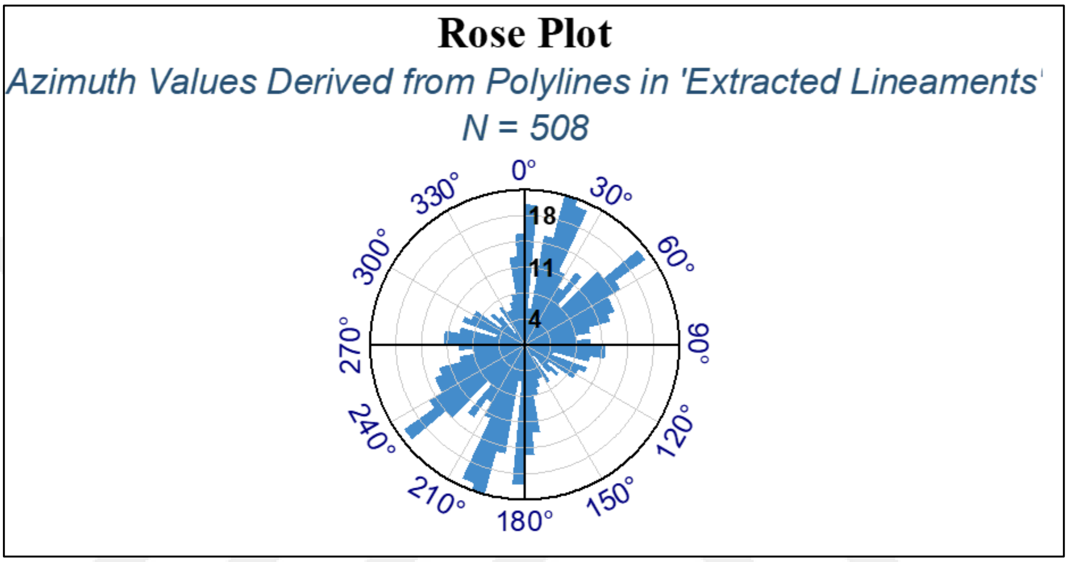

Figure 4.7. Rose diagram of the extracted lineaments.

4.3 Lineament Extraction from Drone Imagery

In order to assess lineaments in a local scale, drone based imagery was acquired from the field and processed (Figure 4.8). For this purpose, three different image acquisition was performed at two different times with DJI Mavic Mini brand drone. All image acquisition information is provided in Table 4.1 and image acquisition frequency is provided in Figure 4.9. All images were acquired with terrain follow with a nadir angle where a total area of 28,750 m^2 with 230 m length and 125 m width was covered.

From the acquired images, a dense point cloud, DEM and orthophoto mosaics were generated.

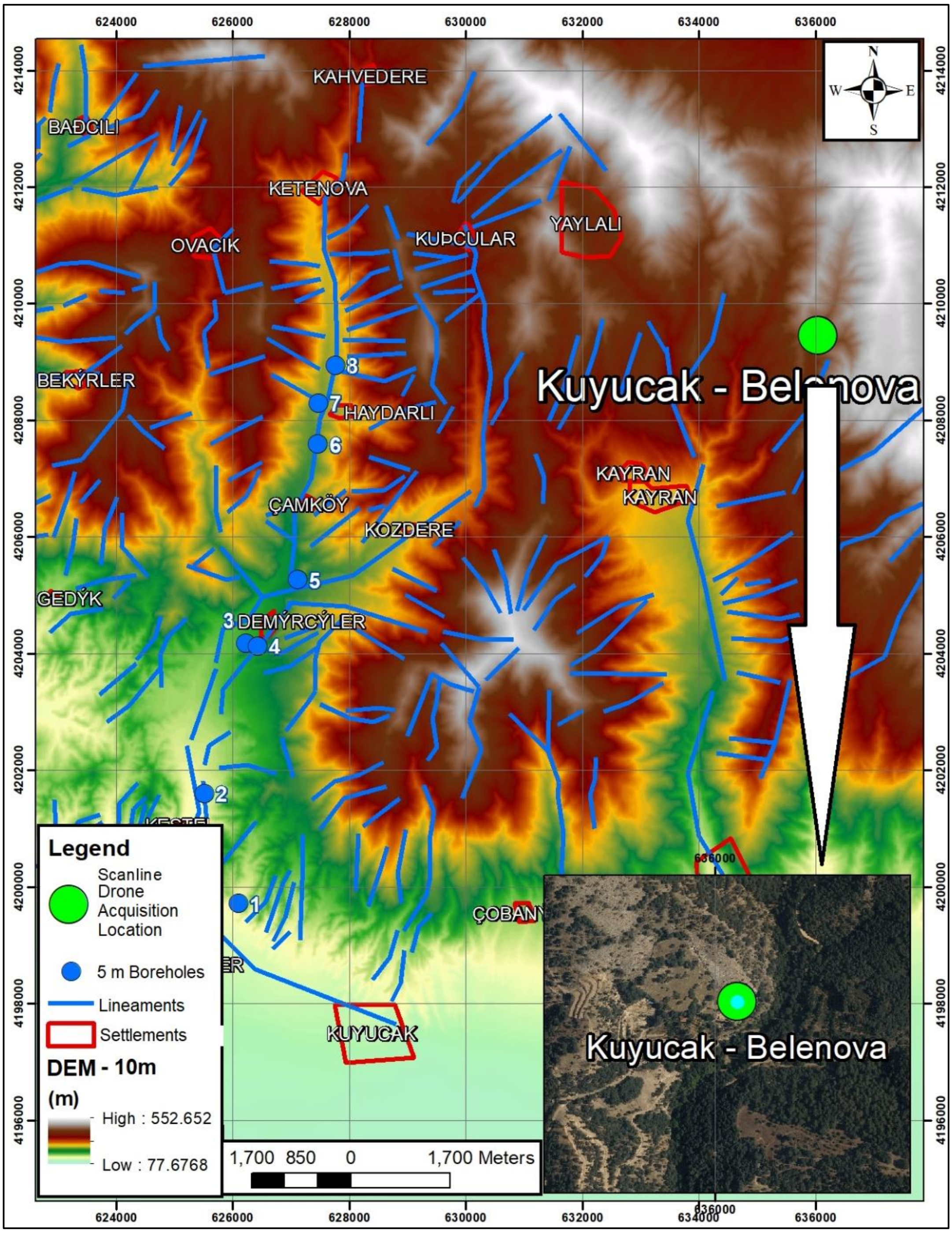

Figure 4.8. Scanline and drone data acquisition location.

Table 4.1. Drone image acquisition information.

Id	Dir.	Dur. (min.)	Image No.	Overlap	Alt. (m)	Res.	Sun Angle	Sun Azimuth	Sun Elev.
01	NS	18	146	66	38	1.29	23.02	290.54	11.54
02	EW	13	118	66	35	1.21	23.02	296.26	4.97
03	NS	50	851	85	30	1.02	22.97	198.88	72.06

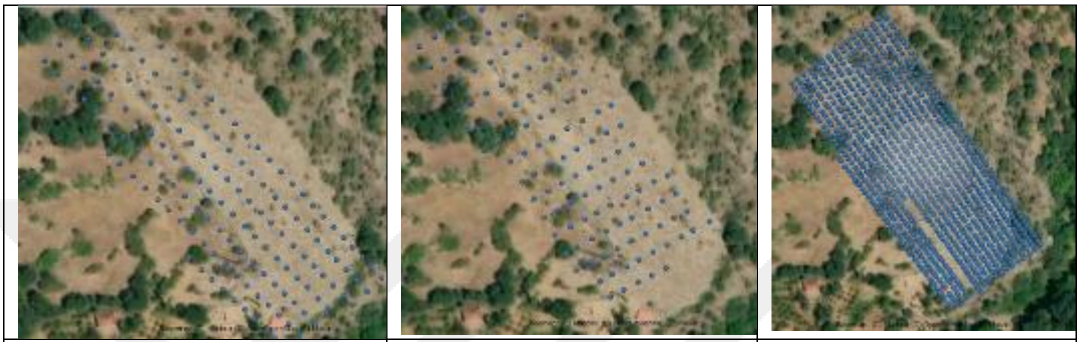

a)	b)	c)

Figure 4.9. a) N-S image acquisition, b) E-W image locations, c) N-S image locations.

From acquired images, LINE automated lineament extraction tool of PCI-Geomatica was used where it was observed that azimuth values between 0-30 and 280-330 degrees are main lineament directions (Figure 4.11). Finally, scanline survey was conducted at the outcrop where drone imagery was acquired (Akgün et al., 2024) and it was observed that the dominant lineament direction observed from the drone imagery is in line with the scanline survey conducted. Results of the scanline survey was consistent with the lineaments extracted from drone imagery as can be seen in Figure 4.10 and Table 4.2. Bedding plane and joint set 2 was also observed from the extracted lineaments.

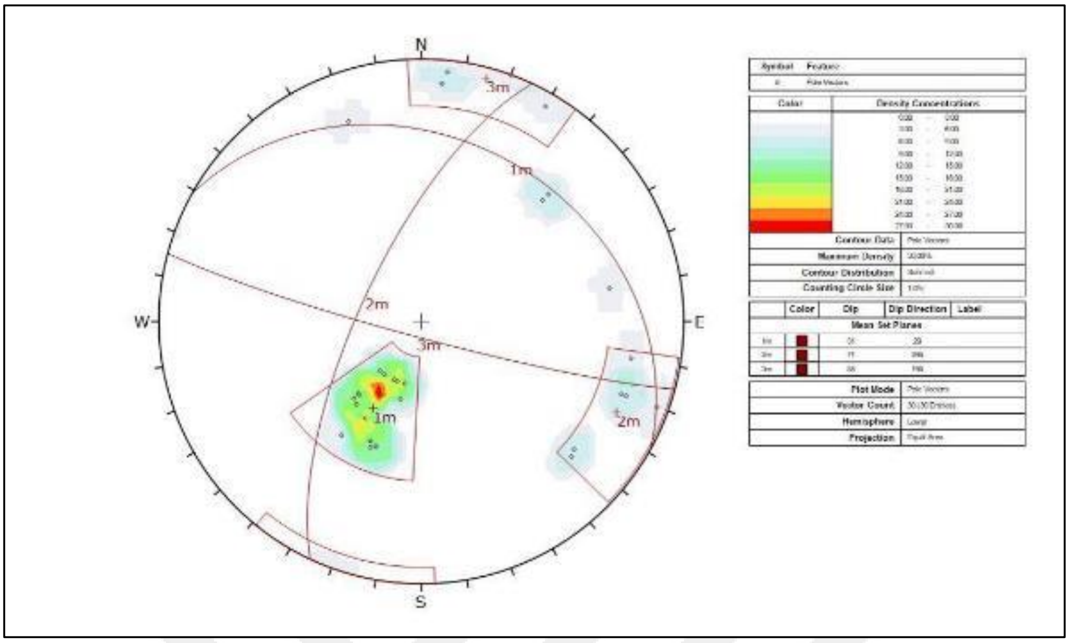

Figure 4.10. Stereonet representation of the discontinuities interpreted from measurements acquired as part of scanline survey in the field (Akgün et al., 2024).

Table 4.2. Discontinuity dip amount and dip directions acquired from scanline survey measurements (Akgün et al., 2024).

Location	Set	Results	
		Dip	Dip Direction
Kuyucak Belenova	Bedding Plane	31	29
	Joint Set 1	71	295
	Joint Set 2	85	195

Table 4.3. Scanline field survey measurements (Akgün et al., 2024).

Dip Amount	Dip Dir.	Color	Spacing (mm)	Persistence (m)	Infilling	Aperture (mm)	Roughness	Weathering
44	35	Grey-dark grey	150	80	Calc.	50	Wavy, rough	Slightly weathered
20	35	Grey-dark grey	250	60	Calc.	60	Wavy, rough	Slightly weathered
20	25	Grey-dark grey	200	100	Calc.	50	Wavy, rough	Slightly weathered
20	40	Grey-dark grey	500	90	Calc.	155	Wavy, smooth	Slightly weathered
30	41	Grey-dark grey	510	50	Calc.	350	Wavy, rough	Slightly weathered
30	40	Grey-dark grey	320	75	Calc.	60	Wavy, smooth	Slightly weathered
32	41	Grey-dark grey	360	80	Calc.	50	Wavy, rough	Slightly weathered
33	38	Grey-dark grey	100	90	Calc.	120	Wavy, rough	Moderately weathered
35	30	Grey-dark grey	130	100	Calc.	40	Wavy, rough	Slightly weathered
20	15	Grey-dark grey	400	50	Calc.	30	Wavy, rough	Slightly weathered
25	15	Grey-dark grey	440	90	Calc.	250	Wavy, rough	Slightly weathered

Table 4.3. Continued.

Dip Amount	Dip Direction	Color	Spacing (mm)	Persistence (m)	Infilling	Aperture (mm)	Roughness	Weathering
42	20	Grey-dark grey	250	80	Calc.	70	Wavy, rough	Slightly weathered
43	22	Grey-dark grey	140	100	Calc.	50	Wavy, rough	Slightly weathered
41	23	Grey-dark grey	260	110	Calc.	60	Wavy, smooth	Slightly weathered
20	22	Grey-dark grey	280	110	Calc.	40	Wavy, rough	Slightly weathered
84	210	Grey-dark grey	110	90	Calc.	10	Wavy, smooth	Slightly weathered
90	200	Grey-dark grey	150	100	Calc.	12	Wavy, rough	Slightly weathered
80	185	Grey-dark grey	130	120	Calc.	15	Wavy, rough	Slightly weathered
70	160	Grey-dark grey	250	80	Calc.	20	Wavy, smooth	Slightly weathered
55	225	Grey-dark grey	165	90	Calc.	25	Wavy, rough	Slightly weathered
58	225	Grey-dark grey	200	150	Calc.	15	Wavy, smooth	Slightly weathered
85	186	Grey-dark grey	140	140	Calc.	30	Wavy, smooth	Moderately weathered

Table 4.3. Continued.

Dip Amount	Dip Direction	Color	Spacing (mm)	Persistence (m)	Infilling	Aperture (mm)	Roughness	Weathering
70	290	Grey-dark grey	80	50	Calc.	20	Wavy, smooth	Slightly weathered
72	290	Grey-dark grey	50	60	Calc.	50	Wavy, smooth	Slightly weathered
70	280	Grey-dark grey	100	50	Calc.	30	Wavy, rough	Slightly weathered
65	310	Grey-dark grey	130	40	Calc.	25	Wavy, smooth	Slightly weathered
66	312	Grey-dark grey	150	60	Calc.	40	Wavy, smooth	Slightly weathered
85	290	Grey-dark grey	90	30	Calc.	20	Wavy, smooth	Slightly weathered
62	260	Grey-dark grey	110	40	Calc.	30	Wavy, rough	Slightly weathered

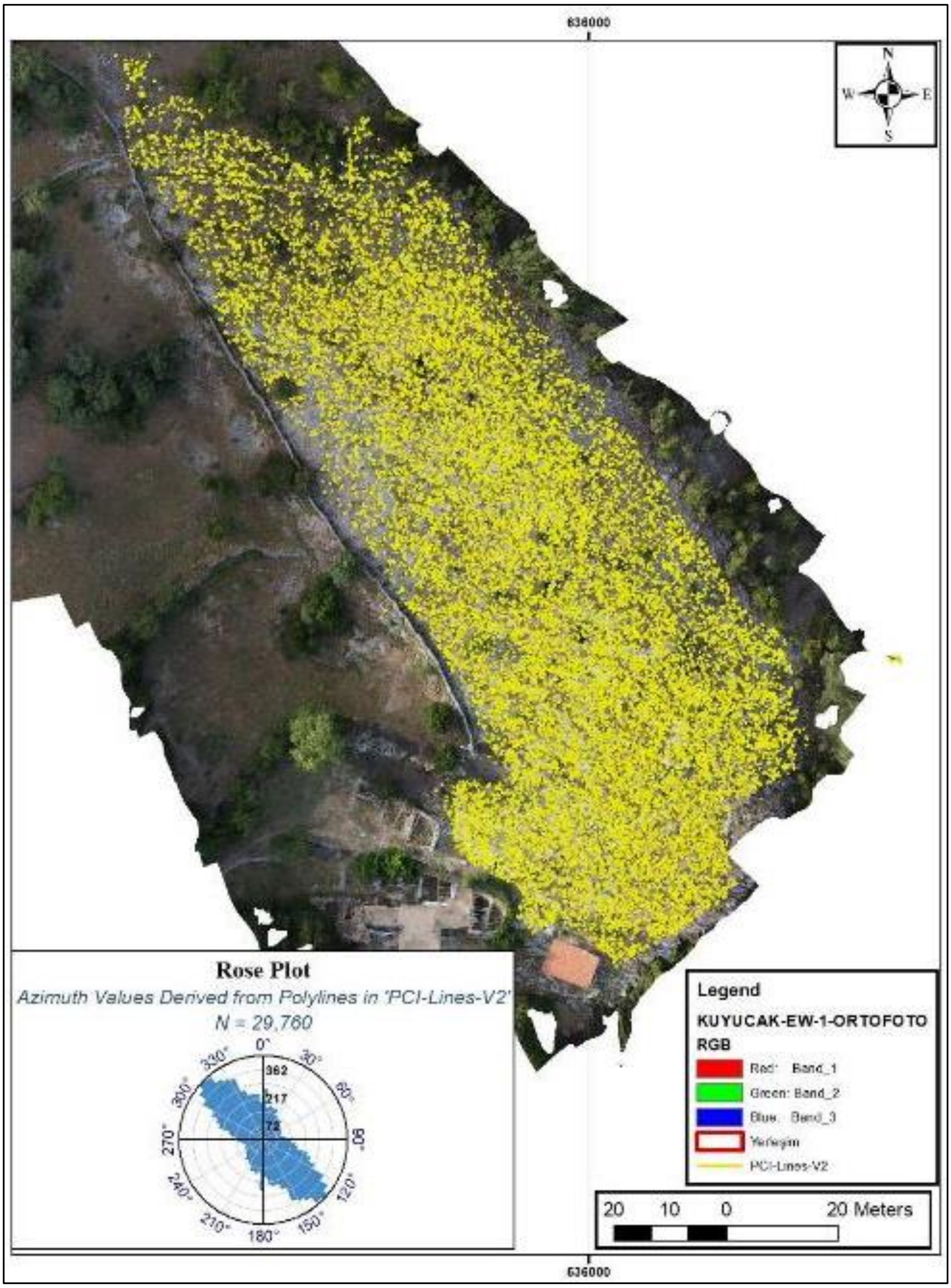

Figure 4.11. Lineaments extracted from drone imagery.

4.4 Results and Discussion of Results of Lineament Mapping

Lineaments extracted from the satellite images have dominant azimuth directions of N0°E, N30°E and N60°E, respectively, whereas lineaments extracted from the drone imagery of the marble unit located northwest of the study area have a dominant azimuth direction between N300°E and N330°E and secondary dominant direction between N0°E and N30°E. The satellite data assessment is in local scale covering an area of approximately 204 km^2 and drone image covers only 0.03km^2. Furthermore, drone imagery encompasses only a single unit, metamorphic marble unit which represents the reservoir of the study area. Consequently, lineaments extracted from satellite and drone imagery is partially complementary to each other. The lineaments extracted from drone imagery is representative of reservoir rock of the study area, whereas satellite based lineaments are representative of the local tectonic characteristics.

Furthermore, in order to check the accuracy of drone imagery, field scanline surveys were conducted and it was observed from the comparison of measurements that the dominant direction of the drone imagery is compatible with the azimuth direction of bedding plane with N299°E and secondary dominant direction is compatible with the N25°E azimuth of the identified joint set-1. These observations have indicated that in an area scale assessment, use of drone imagery is suitable for the characterization of fractures, which in this study was conducted on the marble outcrop of the Menderes Metamorphics.

However, since the main focus of this study is the local scale lineaments, only the results of the satellite based lineament extraction was considered and area scale drone imagery was not included in further analysis.

CHAPTER 5

SHALLOW TEMPERATURE MAPPING

For the purpose of shallow temperature mapping, satellite and field data was used. For this purpose, first a field deployment methodology for the measurement of subsurface temperatures at different depths and for a long term period was developed. Initially, an Arduino based data logger was developed including temperature sensors for four different depths, namely 1 m, 2 m, 3 m and 5 m. After identification of suitable locations for deployment through assessment of satellite and topographical maps as well as accessibility, these loggers were deployed at eight different locations.

Secondly, an ASTER satellite based surface temperature map was generated through following the methodology developed by Coolbaugh et al. (2007a) and Gutierrez et al. (2012).

Finally, both field observations and satellite based surface temperature maps were correlated with the expected temperature increase from south to north due to decrease in reservoir depth in this trend, and results were discussed.

Each methodology applied is described in detail in the following sections and a flow chart of the methodology followed is given in Figure 5.1.

5.1 Literature Review

The shallow temperature mapping in this study is composed of two parts; first deployment of long term temperature sensors and data interpretation, and second, assessment of satellite based thermal infrared data to identify geothermal anomalies.

Literature review of both applications are presented in the following sections.

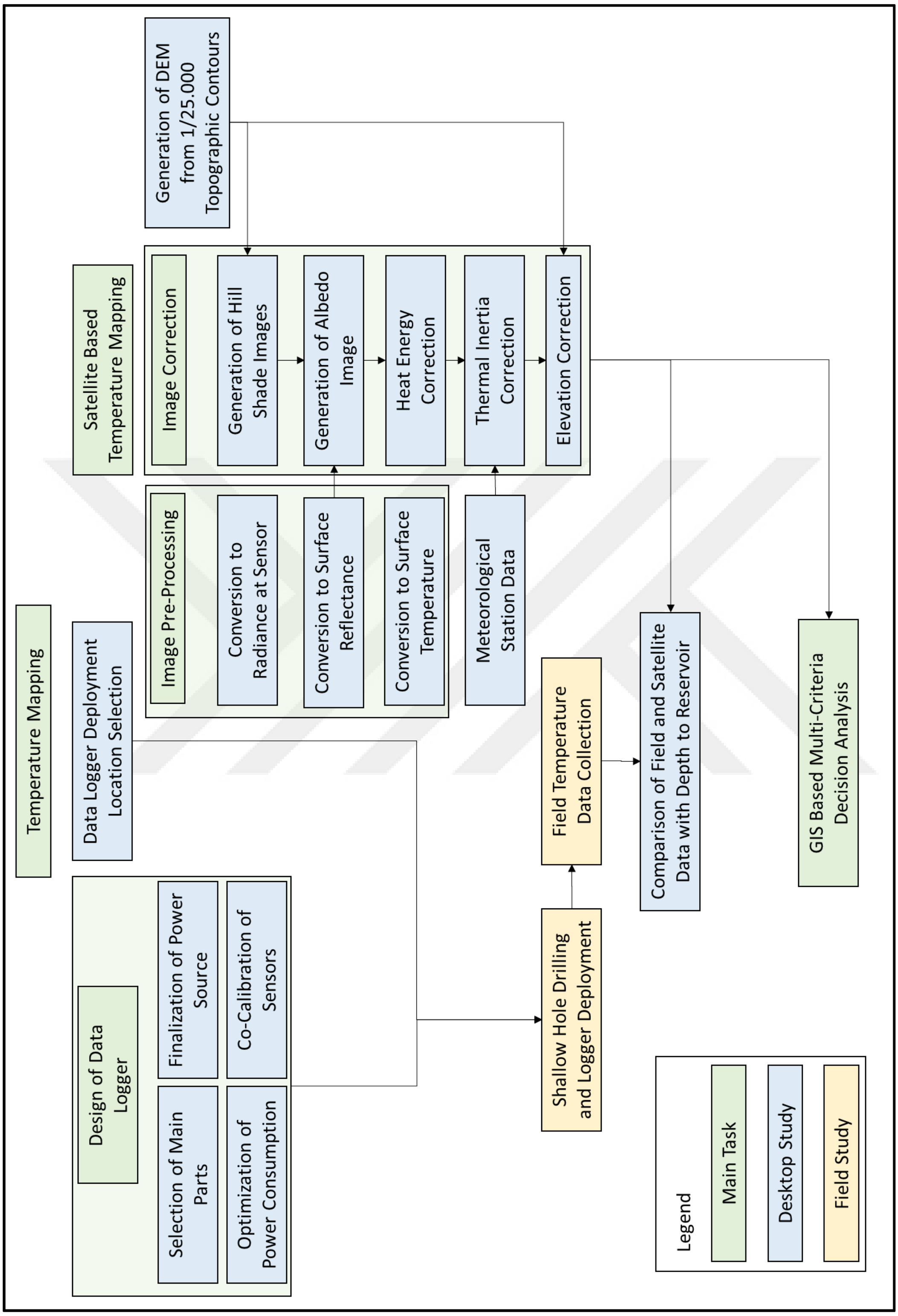

Figure 5.1. Flow chart of the shallow temperature mapping and comparison steps.

5.1.1 Literature Review on Shallow Temperature Surveys for Geothermal Exploration

The shallow temperature surveys were first utilized dominantly in early 1970's where the initial results were presented in the study conducted by Olmsted (1977) focusing on 1 m shallow temperature surveys. Following this initial study, especially in Nevada USA, various studies were conducted including Trexler et al., 1981, 1982; Lange et al., 1982; LeSchack and Lewis, 1983, Olmsted and Ingebritsen, 1986 which mainly focused on identifying extent of known geothermal systems (Kraal et al., 2024). Following these initial studies, the method was further developed and updated in order to identify greenfield and blind geothermal systems where no surface manifestation is present. The later studies, especially executed by Great Basin Center for Geothermal Energy (GBCGE) at the beginning of 2000's have allowed identification of several blind geothermal systems through utilization of 2 m shallow temperature surveys (Coolbaugh et al., 2007b; Sladek et al., 2007; Sladek et al., 2009; Kratt et al., 2008, 2009, 2010, Shevenell et al., 2014; Craig et al., 2021). Kraal et al. (2024) presents the methodology and data processing for 2 m shallow geothermal exploration. Along with the above summarized applications in the USA, Zhang et al. (2016) have conducted a similar study in Xiamen City, China having marine monsoon climate with abundant precipitation and sunshine falling within humid subtropical (Cfa) climate class of the Köppen-Geiger classification.

However, as can be seen from the above examples, most of the shallow temperature surveys, were conducted in a desert environment. According to the Köppen-Geiger classification, the Great basin where previous studies were conducted is located in Cold Desert Climate (BWk) and cold semi-arid climate (BSk) (Beck et al., 2018). In this study, conducted in western Türkiye, Büyük Menderes Graben region, the Koppen-Geiger climate classification (Köppen, 1936; Geiger, 1961) is hot summer Mediterranean climate (Csa) (Beck et al., 2018). The precipitation in cold desert climate and cold semi-arid climate where the Great Basin is located is annually 262 mm and with the lower precipitation at the southern part of the state with 180 mm

(Nevada State Climate Office, 2024). Average precipitation in Aydın province is 55 mm and total annual precipitation is 660 mm (Turkish State Meteorology Service, 2024). Therefore, in terms of climate conditions, this study is considered to be first of its kind for shallow geothermal temperature surveys. Furthermore, presence of more than five irrigation cooperative within and in the vicinity of the study area indicates presence of groundwater (Aydın and Akçay, 2023) (Figure 5.2) and data acquired from State Hydraulic Works show presence of shallow ground water in the vicinity of the study area.

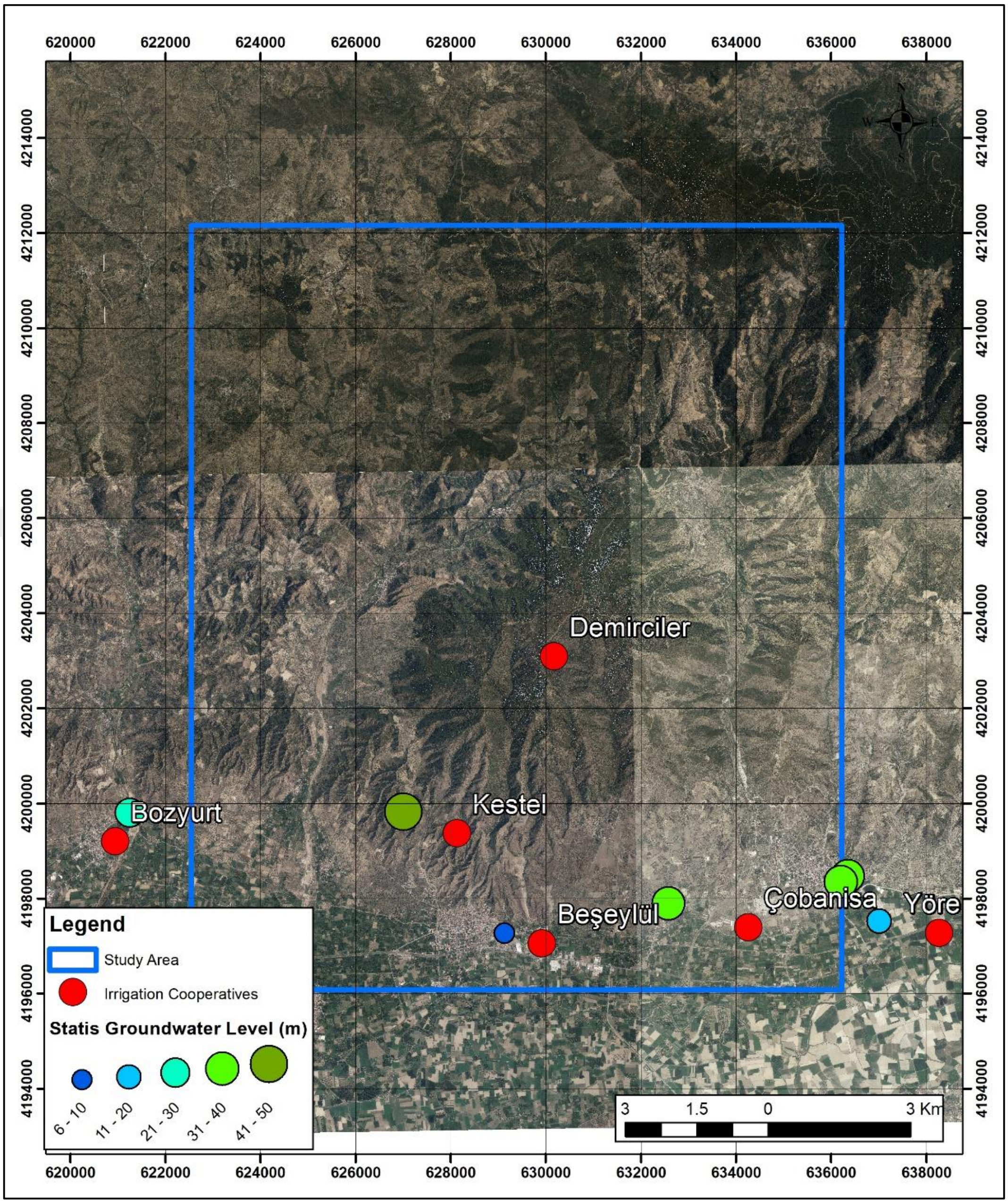

Figure 5.2. Location of ground water wells and irrigation cooperatives within the study area (DSİ, 2012; Aydin and Akçay, 2023).

5.1.2 Literature Review on Use of Satellite Imagery for Geothermal Anomaly Detection

Advancements in remote sensing from exploration to operational level in the recent decades through expansion of the number and technical capability of earth observation satellites as well as advancement in computational processing power have significantly allowed frequent utilization of thermal remote sensing and digital image processing for geothermal exploration (Haselwimmer and Praksh, 2013; Abubakar et al., 2017).

Thermal infrared remote sensing, allowing detection of emissions provides a unique dataset for geothermal exploration. Availability of global data from earth observations satellites such as thermal infrared multispectral scanner (TIMS), ASTER, MODIS/ASTER or MASTER and Landsat TM, Landsat-7 ETM+ and most recently from Landsat 8 OLI (Operationald Land Imager) and TIRS (Thermal Infrared Sensor) as well as ASTER (Advanced Spaceborne Thermal Emission and Reflection Radiometer) have allowed researchers to conduct numerous studies for thermal remote sensing of geothermal areas (Abubakar et al., 2017).

As summarized by Abubakar et al. (2017); recent years have seen a notable rise in geothermal exploration and detection studies, supported by advances in remote sensing technologies such as ASTER and Landsat thermal data (Bromley et al., 2011; Calvin et al., 2015; Chan et al. 2018; Coolbaugh et al. 2007a; Eneva et al., 2006; Eneva et al., 2006; Fitts, 2013; Hanson et al., 2014; Haselwimmer et al., 2013; Heasler et al., 2009; Hellman and Ramsey 2004; Hewson et al. 2020; Hodder 1970; Kratt et al., 2010; Mia et al., 2014; Nishar et al., 2016; Qin et al., 2011; Reath and Ramsey, 2013; Romaguera et al. 2018; Tian et al., 2015; Vaughan et al., 2012). These studies have utilized various satellite platforms to investigate thermal patterns and anomalies associated with geothermal activity across diverse geographic regions.

Coolbaugh et al. (2000) utilized thermal infrared multispectral scanner (TIMS) and advanced visible and infrared imaging spectrometer (AVIRIS) data to analyze thermal patterns at Steamboat Springs, Nevada, highlighting challenges posed by high albedo and thermal inertia in detecting pre-dawn anomalies. Eneva et al. (2006) examined ASTER imagery in Central East California, proposing a simplified model to enhance thermal anomaly detection while mitigating false positives due to topographic and albedo influences.

As summarized by Van Der Meer et al. (2014), several studies illustrate the application of thermal infrared (TIR) data for mapping surface temperatures and correlating the data with geothermal heat. Among these, study conducted by Coolbaugh et al. (2007a) proposed a comprehensive processing method using ASTER images, investigating materials with varying physical properties and their relationship to surface temperature throughout a daily cycle. These researchers acknowledged the inverse correlation between surface radiant temperature and emissivity, and developed empirical corrections for surface albedo and topographic slope. This approach enhanced the interpretability of surface temperature data in relation to geothermal sources.

Another significant study simulated ASTER TIR data to evaluate the detectability of thermal anomalies, considering that geothermal heat sources are often subpixel in size (Vaughan et al., 2010). Authors emphasized the importance of accurately accounting for elevation effects to minimize false anomalies in temperature interpretations (Eneva and Coolbaugh, 2009).

Additional examples of TIR remote sensing applications include studies on geothermal complexes in the Andes of Central Chile using ASTER data where impact of elevation difference (i.e., environmental lapse rate) was considered (Gutierrez et al., 2012), analysis of the Tengchong area in China utilizing Landsat-7 Enhanced Thematic Mapper+ (Qin et al., 2011), and research on fault-controlled hot springs in the Gulf of Suez waters (Kaiser and Ahmed, 2013).

Mia et al. (2014) explored thermal activity at Aso volcanic area, Japan, using Landsat ETM+ data for hydrothermal mapping and thermal anomaly identification. Lashin and Al Arifi (2014) assessed geothermal potential in Saudi Arabia, revealing promising petro-thermal properties and high reservoir temperatures. Tian et al. (2015) integrated Landsat 8 OLI & TIRS data with ground-based borehole temperatures in Hokkaido, Japan, highlighting the robustness of combining satellite and field data for geothermal resource assessment despite challenges in data availability and replication.

More recently, several studies have been conducted utilizing Landsat 8 TIRS sensor (Chao et al., 2023) and utilizing both Landsat 8 and ASTER multi-temporal datasets (Chao et al., 2024) to detect geothermal anomalies. Similarly, Li et al. (2023) have utilized multi-temporal Landsat 8 TIRS imagery to detect geothermal anomalies in southern Tibet. Hewson et al. (2020) also utilized ASTER day and night imagery to identify geothermal anomalies.

These studies collectively illustrate the evolving application of remote sensing in enhancing the detection and characterization of geothermal resources worldwide.

5.2 Equipment for Shallow Temperature Surveys

For main equipment component, Arduino pro mini 5v 16hz version was selected due to its low power consumption characteristics. Arduino pro mini incorporates Atmega328 microcontroller (Atmel, 2015).

The design and components of the temperature data logger is as follows

- A microcontroller (Arduino Pro Mini 5V)
- A microSD card module
- An RTC module
- 4 temperature sensors (1, 2, 3 and 5 meters).

The 1 m sensor was included to observe the effect of surface weather events. The 2 m sensor was included at the final stage of the design in order to observe attenuation of the weather and diurnal impact at depth, since the diurnal effects are not expected to be observed below 2 m. The 3 m and 5 m sensors were included in order to detect presence of any thermal anomalies. The main idea for adding a 2 m sensor was to check the difference between temperature measurements at 1 m and 2 m sensors. If it was observed that the 1 m and 2 m sensors showed different behavior, indicating that the 2 m sensor was not impacted from diurnal effects, the thermal difference would be checked between 2 and 5 m sensors. However, if a similar behavior is observed at 1 m and 2 m sensors, the thermal difference of 3 m and 5 m sensors would be checked. Cable connections are presented in Table 5.1 and Figure 5.3.

As for the power source, the final design included (after several trial and errors), the MP1584EN step-down converter based on its quiescence current consumption (Monolithicpower, 2014). The power consumption was decreased from around 10 mA to initially down to 2.6 mA during sleep period by removing power LED on microcontroller (3 mA), charging regulator at RTC (1.2 mA) and power LED on RTC (3 mA). Following these power saving steps, after trying a step-down regulator (7.4 – 7.8 mA) and a linear regulator (3 mA) MP1584EN was included in the final design since this step-down converter had the lowest quiescent current (around 0.1 mA), resulting in 1.5 to 1.8 mA current consumption at the 12V battery side. Therefore, for a 9AH 12V battery, with 80% efficiency, total runtime of the logger was expected to be around 160 days.

Table 5.1. Arduino connections.

Temp. Sensor	**Arduino**	**RTC**	**Arduino**	**SD Card Reader**	**Arduino**
Data	D2	SCL	A5	CS	D10
VCC	5V	SDA	A4	SCK	D13
GND	GND	VCC	5V	MOSI	D11
		GND	GND	MISO	D12
				VCC	5V
				GND	GND

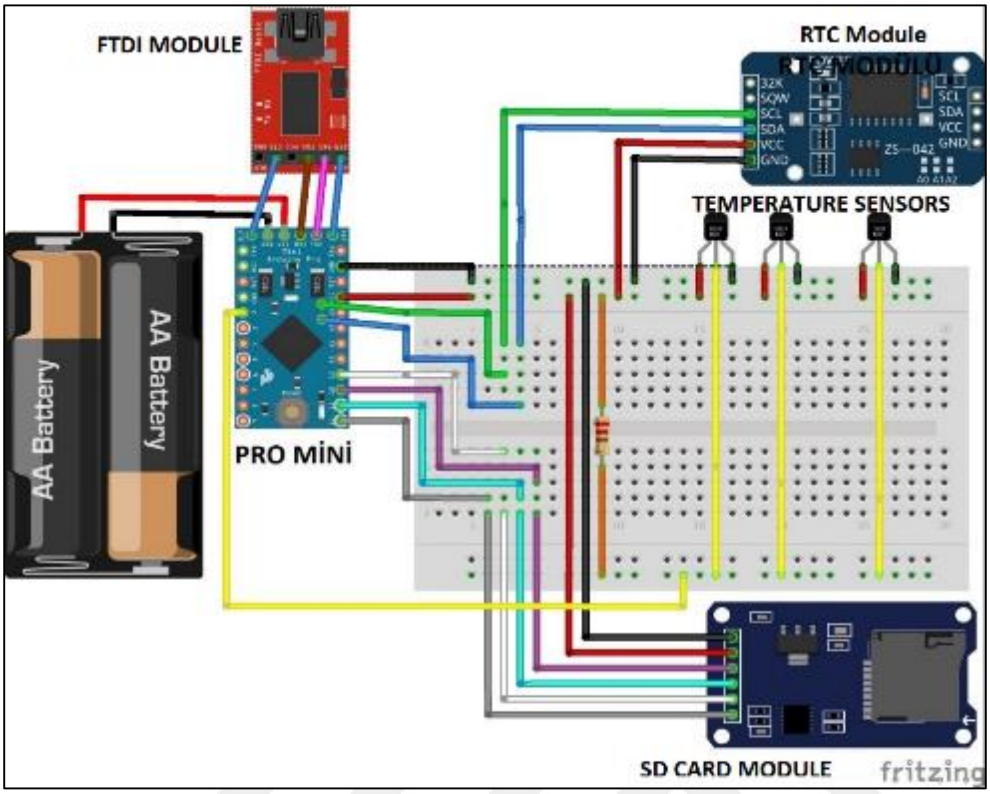

Figure 5.3. Arduino connection diagram.

5.2.1 Sensor Calibration and Co-calibration

The 12 bit temperature measurement resolution of the DS188B20 temperature sensors is 0.0625°C and accuracy of the sensors is 0.5°C (Maxim Integrated, 2019).

For the calibration process, sensors of each data logger were individually subjected to a heating/cooling cycle in order to observe response of the sensors and co-calibrate sensors of each logger. For this purpose, the temperature sensors were submerged into a container filled with water. While logger was taking measurements, hot water was added to the container to increase the temperature to around 50°C. Then the temperature was gradually decreased by adding first cold water, then ice to the container down to around 5°C. The entire process took about 2 hours where temperature of the sensors was recorded by the logger.

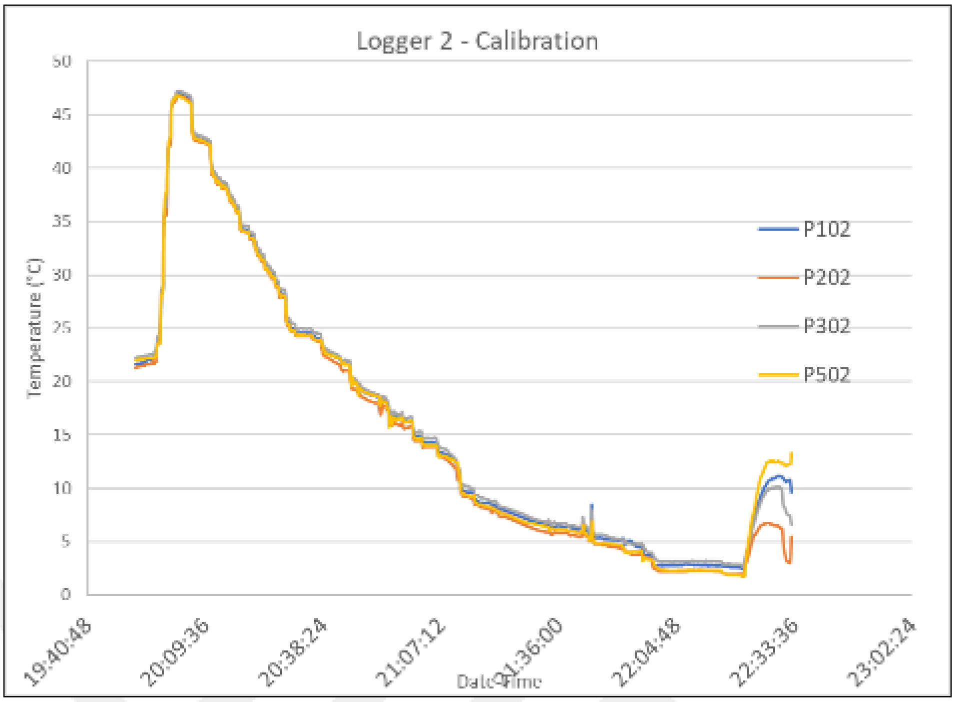

Figure 5.4. Logger 2 calibration data.

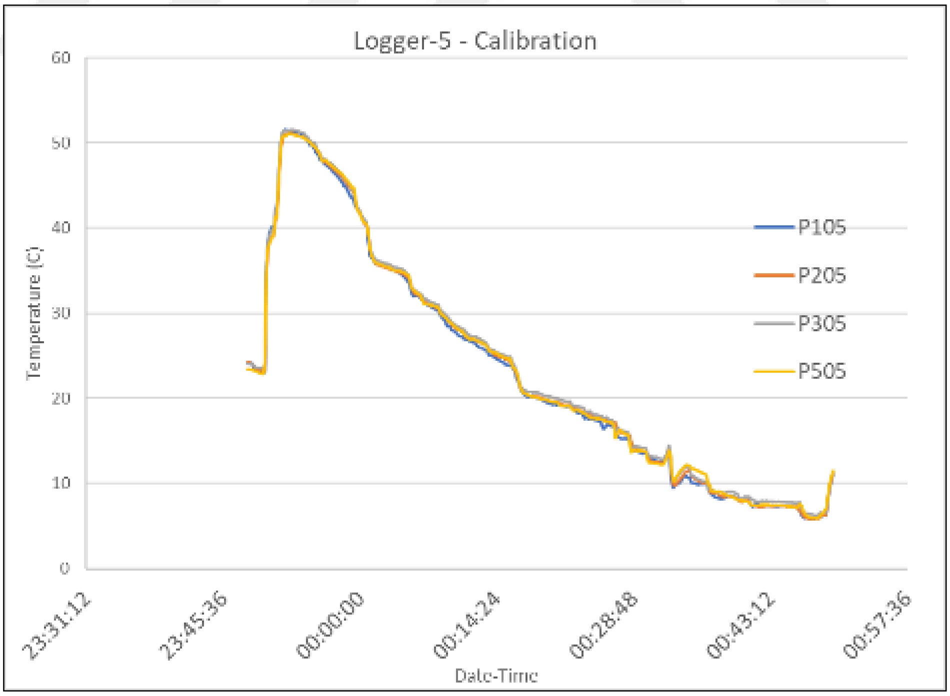

Figure 5.5. Logger 5 calibration data.

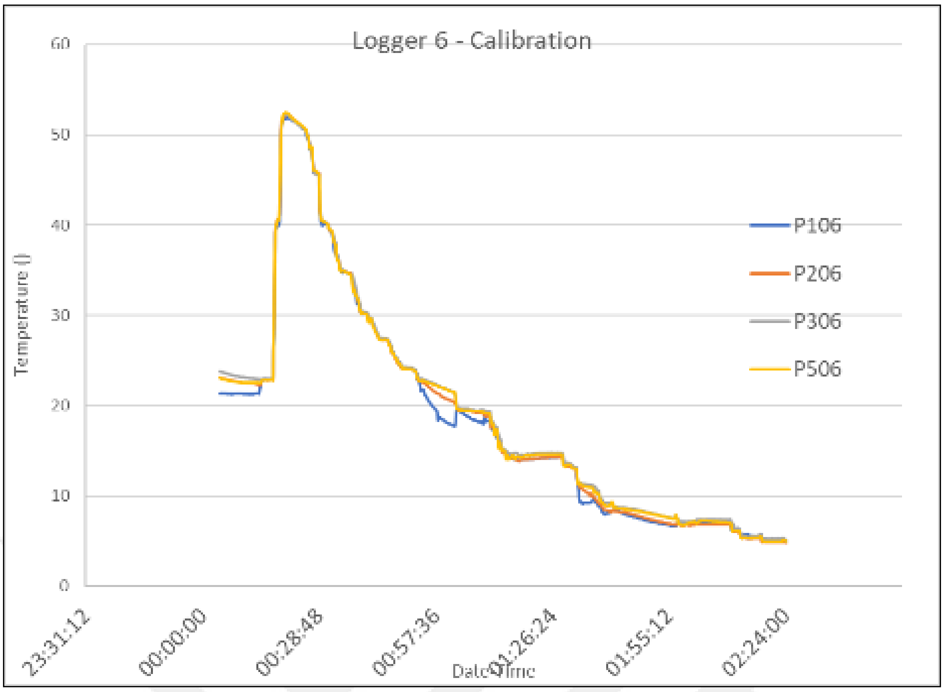

Figure 5.6. Logger 6 calibration data.

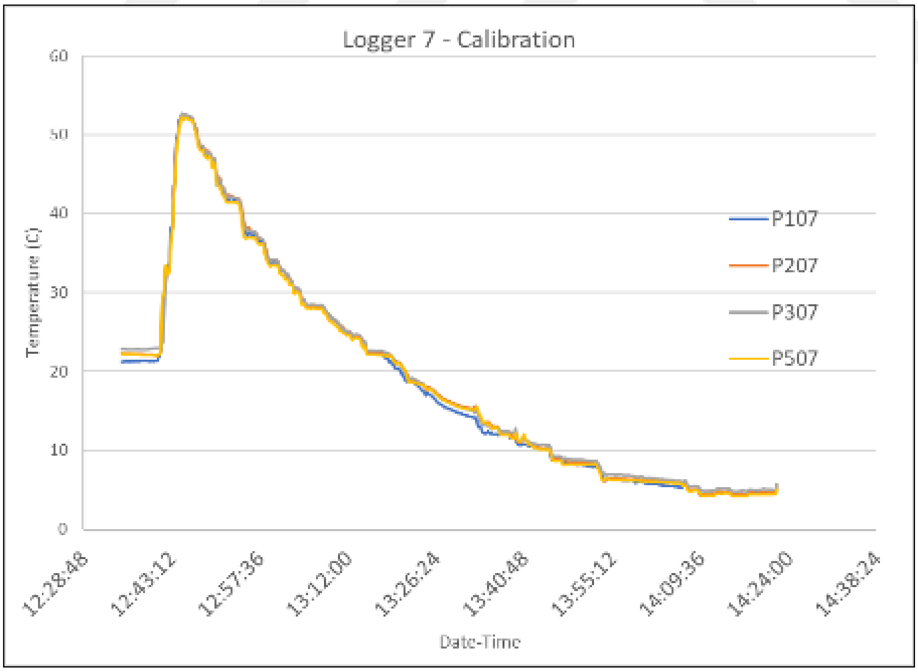

Figure 5.7. Logger 7 calibration data.

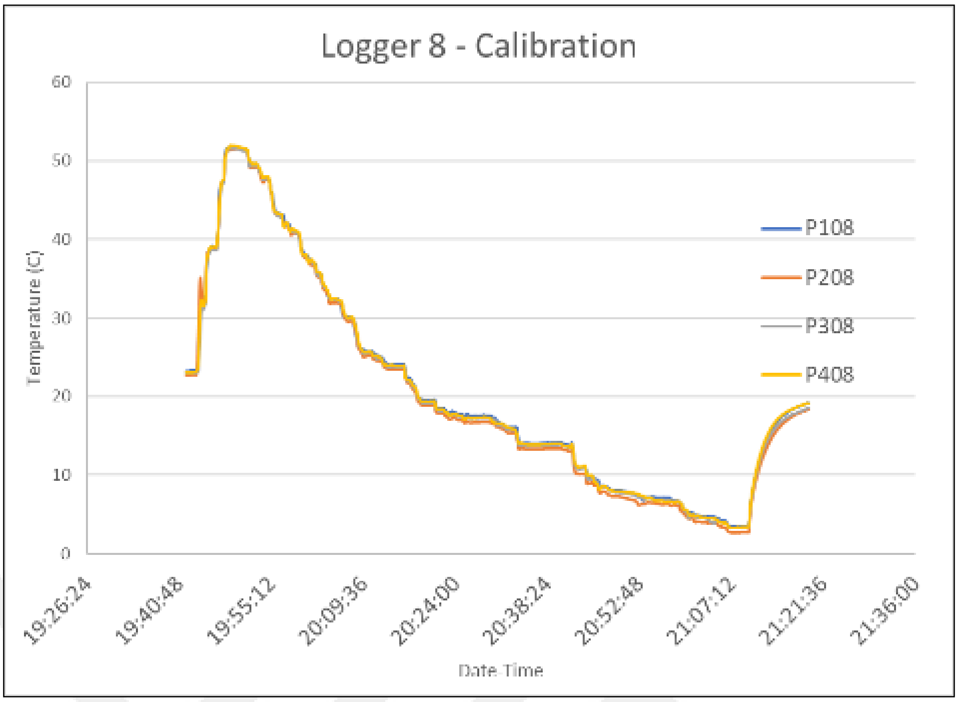

Figure 5.8. Logger 8 calibration data.

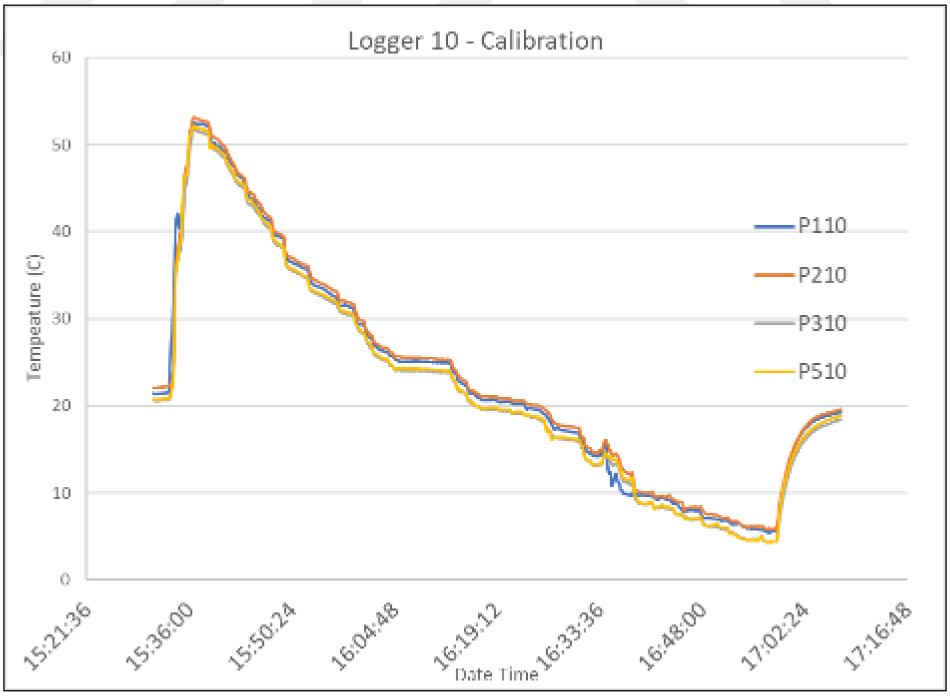

Figure 5.9. Logger 10 calibration data.

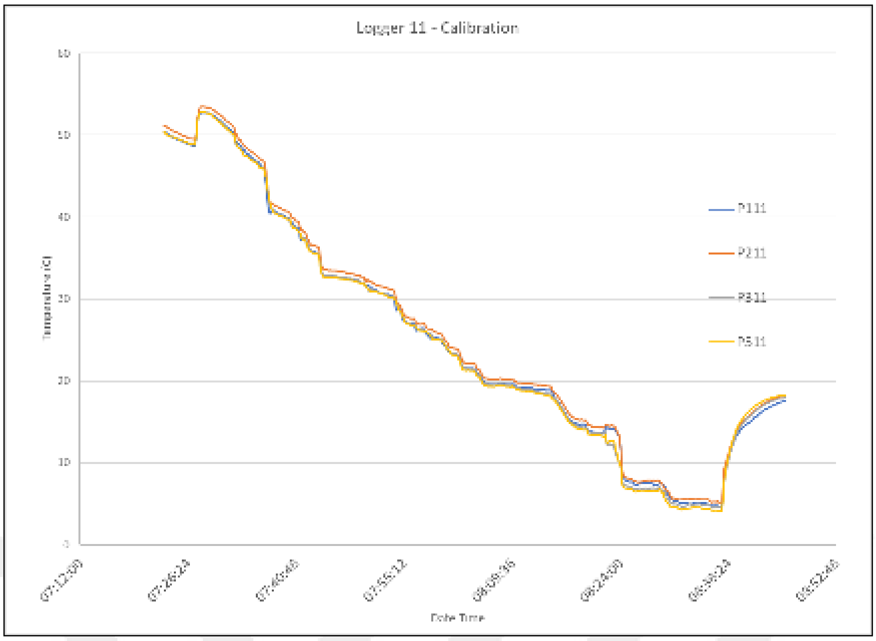

Figure 5.10. Logger 11 calibration data.

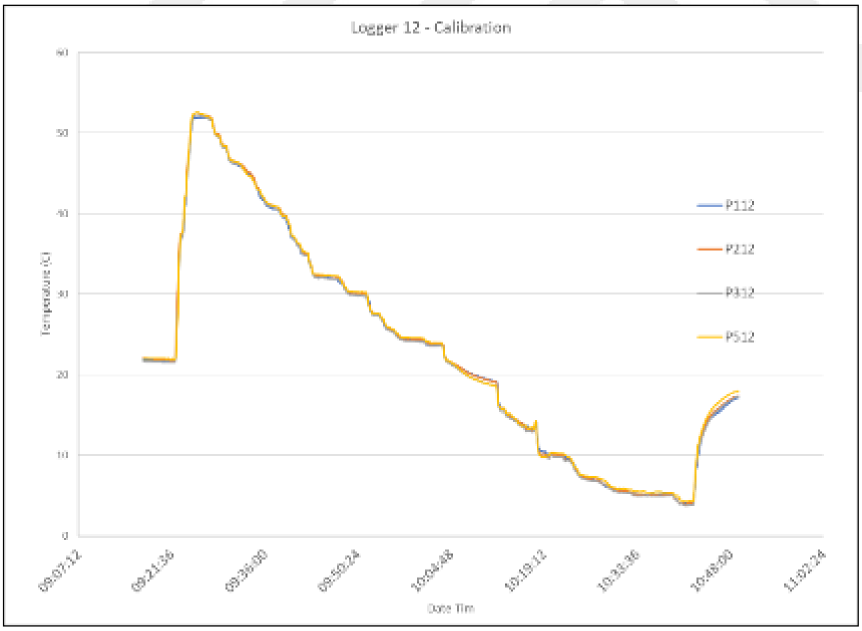

Figure 5.11. Logger 12 calibration data.

Following the calibration process for each logger, sensors were co-calibrated. This co-calibration was performed by taking the 1 m sensor of each logger as reference and fitting the remaining 2 m, 3 m and 5 m sensors to this primary sensor based on different fitting relations by using the Solver function of Excel through, i.e., a. linear shift, b. linear, c. cubic and d. quadratic. Below are the results of each fit for each logger. Based on the sum of squares of residuals (SSR), the equation presenting the best fit was used for further data processing. This was repeated for each logger. For the probe identification, the PXYY notation was used where X indicated temperature probe length (i.e. deployment depth) and YY indicated data logger number. Therefore, for example P512 indicated 5 m temperature sensor of the logger number 12.

Table 5.2. Logger-2 calibration results.

Probe	Series	a	b	c	d	Equation	SSR	St.Dev. of Res
P202	SHIFT				0.495	+d	32.959	0.197
	LINEER			0.991	0.642	xc+d	19.986	0.154
	QUADRATIC		-1.15E-04	0.996	0.613	bX2+cX+d	19.697	0.152
	CUBIC	1.00E-05	-8.16E-04	1.008	0.570	ax3+bX2+cX+d	19.394	0.151
P302	SHIFT				-0.303	+d	17.703	0.145
	LINEER			0.998	-0.266	xc+d	16.966	0.142
	QUADRATIC		1.58E-04	0.991	-0.221	bX2+cX+d	16.436	0.139
	CUBIC	-4.00E-06	5.15E-04	0.983	-0.180	ax3+bX2+cX+d	16.624	0.140
P502	SHIFT				0.271	+d	51.535	0.247
	LINEER			0.992	0.402	xc+d	41.485	0.221
	QUADRATIC		5.46E-04	0.968	0.541	bX2+cX+d	34.963	0.203
	CUBIC	-2.40E-05	1.37E-03	0.996	-0.274	ax3+bX2+cX+d	228.004	0.372

Table 5.3. Logger-5 calibration results.

Probe	Series	a	b	c	d	Equation	SSR	St.Dev. of Res
P205	SHIFT				-0.263	+d	40.931	0.328
	LINEER			1.002	-0.307	xc+d	40.669	0.327
	QUADRATIC		7.96E-04	0.959	0.115	bX2+cX+d	33.215	0.295
	CUBIC	-6.10E-05	6.12E-03	0.826	0.986	ax3+bX2+cX+d	37.668	0.314
P305	SHIFT				-0.608	+d	32.878	0.294
	LINEER			1.004	-0.702	xc+d	31.682	0.288
	QUADRATIC		6.36E-04	0.969	-0.352	bX2+cX+d	26.982	0.266
	CUBIC	-2.00E-06	8.76E-04	0.962	-0.297	ax3+bX2+cX+d	27.032	0.266
P505	SHIFT				-0.325	+d	82.757	0.466
	LINEER			1.003	-0.383	xc+d	82.283	0.465
	QUADRATIC		4.65E-04	0.977	-0.133	bX2+cX+d	79.785	0.458
	CUBIC	1.20E-05	-5.48E-04	1.000	-0.274	ax3+bX2+cX+d	79.299	0.456

Table 5.4. Logger-6 calibration results.

Probe	Series	a	b	c	d	Equation	SSR	St.Dev. of Res
P206	SHIFT				-0.260	+d	337.982	0.635
	LINEER			0.991	-0.103	xc+d	327.183	0.624
	QUADRATIC		1.13E-03	0.933	0.387	bX2+cX+d	291.927	0.590
	CUBIC	-6.30E-05	6.12E-03	0.826	0.986	ax3+bX2+cX+d	273.633	0.570
P306	SHIFT				-0.645	+d	535.775	0.799
	LINEER			1.004	-0.720	xc+d	533.521	0.797
	QUADRATIC		1.55E-03	0.923	-0.019	bX2+cX+d	469.309	0.748
	CUBIC	-1.09E-04	1.04E-02	0.730	1.032	ax3+bX2+cX+d	431.736	0.717
P506	SHIFT				-0.515	+d	582.203	0.833
	LINEER			0.999	-0.501	xc+d	582.115	0.833
	QUADRATIC		1.17E-03	0.938	0.025	bX2+cX+d	544.365	0.805
	CUBIC	-1.21E-04	1.10E-02	0.725	1.172	ax3+bX2+cX+d	496.554	0.769

Table 5.5. Logger-7 calibration results.

Probe	Series	a	b	c	d	Equation	SSR	St.Dev. of Res
P207	SHIFT				-0.284	+d	96.571	0.387
	LINEER			0.999	-0.275	xc+d	96.537	0.387
	QUADRATIC		6.20E-04	0.969	-0.035	bX2+cX+d	88.215	0.370
	CUBIC	-1.01E-04	8.91E-03	0.782	0.979	ax3+bX2+cX+d	89.052	0.370
P307	SHIFT				-0.445	+d	65.958	0.320
	LINEER			1.010	-0.635	xc+d	53.666	0.288
	QUADRATIC		1.35E-04	1.003	-0.580	bX2+cX+d	53.288	0.287
	CUBIC	-1.48E-04	1.22E-02	0.728	1.031	ax3+bX2+cX+d	94.802	0.371
P507	SHIFT				-0.011	+d	163.440	0.503
	LINEER			1.014	-0.265	xc+d	140.466	0.466
	QUADRATIC		6.14E-04	0.984	-0.034	bX2+cX+d	132.499	0.453
	CUBIC	-1.56E-04	1.29E-02	0.725	1.172	ax3+bX2+cX+d	97.188	0.387

Table 5.6. Logger-8 calibration results.

Probe	Series	a	b	c	d	Equation	SSR	St.Dev. of Res
P208	SHIFT				0.679	+d	37.704	0.268
	LINEER			0.987	0.946	xc+d	18.126	0.186
	QUADRATIC		-5.70E-05	0.990	0.922	bX2+cX+d	18.063	0.186
	CUBIC	1.00E-06	-1.00E-06	0.982	1.019	ax3+bX2+cX+d	18.691	0.188
P308	SHIFT				0.285	+d	30.999	0.243
	LINEER			0.999	0.314	xc+d	30.778	0.242
	QUADRATIC		-4.40E-05	1.001	0.294	bX2+cX+d	30.742	0.242
	CUBIC	-4.90E-05	4.31E-03	0.889	1.060	ax3+bX2+cX+d	51.314	0.310
P508	SHIFT				0.140	+d	37.589	0.268
	LINEER			0.994	0.254	xc+d	34.271	0.256
	QUADRATIC		-7.20E-05	0.998	0.221	bX2+cX+d	34.171	0.255
	CUBIC	-6.60E-05	5.77E-03	0.851	1.195	ax3+bX2+cX+d	61.990	0.340

Table 5.7. Logger-10 calibration results.

Probe	Series	a	b	c	d	Equation	SSR	St.Dev. of Res
P210	SHIFT				-0.582	+d	131.483	0.496
	LINEER			1.003	-0.646	xc+d	130.773	0.495
	QUADRATIC		1.18E-04	0.996	-0.580	bX2+cX+d	130.513	0.494
	CUBIC	-1.21E-04	1.04E-02	0.749	0.989	ax3+bX2+cX+d	134.985	0.502
P310	SHIFT				0.864	+d	169.975	0.564
	LINEER			1.005	0.758	xc+d	167.810	0.561
	QUADRATIC		-4.10E-05	1.007	0.738	bX2+cX+d	167.780	0.561
	CUBIC	-8.80E-05	6.46E-03	0.889	1.060	ax3+bX2+cX+d	179.242	0.576
P510	SHIFT				0.696	+d	222.791	0.646
	LINEER			0.996	0.782	xc+d	221.366	0.644
	QUADRATIC		-9.70E-05	1.001	0.734	bX2+cX+d	221.186	0.644
	CUBIC	-1.06E-04	7.89E-03	0.851	1.195	ax3+bX2+cX+d	234.802	0.659

Table 5.8. Logger-11 calibration results.

Probe	Series	a	b	c	d	Equation	SSR	St.Dev. of Res
P211	SHIFT				-0.630	+d	24.796	0.226
	LINEER			0.992	-0.417	xc+d	17.755	0.191
	QUADRATIC		3.66E-04	0.971	-0.194	bX2+cX+d	15.141	0.176
	CUBIC	-6.20E-05	6.16E-03	0.813	0.984	ax3+bX2+cX+d	35.593	0.268
P311	SHIFT				0.120	+d	128.728	0.514
	LINEER			0.990	0.374	xc+d	118.037	0.492
	QUADRATIC		7.01E-04	0.951	0.768	bX2+cX+d	108.310	0.472
	CUBIC	-1.70E-05	2.69E-03	0.874	1.759	ax3+bX2+cX+d	147.651	0.521
P511	SHIFT				0.223	+d	187.021	0.620
	LINEER			0.986	0.571	xc+d	166.673	0.585
	QUADRATIC		8.96E-04	0.936	1.067	bX2+cX+d	150.166	0.555
	CUBIC	-2.70E-05	1.42E-03	1.000	-0.274	ax3+bX2+cX+d	260.271	0.709

Table 5.9. Logger-12 calibration results.

Probe	Series	a	b	c	d	Equation	SSR	St.Dev. of Res
P212	SHIFT				-0.114	+d	22.603	0.209
	LINEER			0.993	0.056	xc+d	16.687	0.180
	QUADRATIC		5.90E-05	0.989	0.083	bX2+cX+d	16.619	0.179
	CUBIC	-8.20E-05	7.01E-03	0.826	0.986	ax3+bX2+cX+d	39.197	0.275
P312	SHIFT				0.153	+d	26.502	0.226
	LINEER			0.994	0.287	xc+d	22.758	0.210
	QUADRATIC		-9.50E-05	0.999	0.244	bX2+cX+d	22.584	0.209
	CUBIC	1.30E-05	-1.17E-03	1.024	0.112	ax3+bX2+cX+d	21.972	0.206
P512	SHIFT				-0.190	+d	72.126	0.374
	LINEER			0.998	-0.154	xc+d	71.861	0.373
	QUADRATIC		-1.70E-04	1.007	-0.235	bX2+cX+d	71.308	0.371
	CUBIC	1.20E-05	-5.48E-04	1.000	-0.274	ax3+bX2+cX+d	89.412	0.393

Summary of the best fit results are given in Table 5.10 where it can be seen that out of 24 sensors, 7 sensors have best fits with cubic equation and the remaining 17 have best fits with quadratic equation.

Finally, effect of temperature on the logger itself was checked. For this purpose, one of the loggers was put into a container and this container was submerged into water. Then sensors of this submerged logger were inserted into a container at room temperature whereas sensors of another container were inserted into the same water with the first logger. The temperature of the water was increased to 50°C and decreased down to 5°C meanwhile both loggers recorded temperature.

As can be seen from Figure 5.12, no discernible change in temperature readings were observed when the temperature of the water the container logger was inserted was placed in was increased and then decreased.

Table 5.10. Calibration results.

Prob.	a	b	c	d	Equation	SSR	St.Dev. of Res
P202	1.00E-05	-0.001	1.008	0.570	CUBIC	19.394	0.151
P302	1.58E-04	0.991	-0.221		QUADRATIC	16.436	0.139
P502	5.46E-04	0.968	0.541		QUADRATIC	34.963	0.203
P205	7.96E-04	0.959	0.115		QUADRATIC	33.215	0.295
P305	6.36E-04	0.969	-0.352		QUADRATIC	26.982	0.266
P505	1.20E-05	-0.001	1.000	-0.274	CUBIC	79.299	0.456
P206	-6.30E-05	0.006	0.826	0.986	CUBIC	273.633	0.570
P306	-1.09E-04	0.010	0.730	1.032	CUBIC	431.736	0.717
P506	-1.21E-04	0.011	0.725	1.172	CUBIC	496.554	0.769
P207	6.20E-04	0.969	-0.035		QUADRATIC	88.215	0.370
P307	1.35E-04	1.003	-0.580		QUADRATIC	53.288	0.287
P507	-1.56E-04	0.013	0.725	1.172	CUBIC	97.188	0.387
P208	-5.70E-05	0.990	0.922		QUADRATIC	18.063	0.186
P308	-4.40E-05	1.001	0.294		QUADRATIC	30.742	0.242
P508	-7.20E-05	0.998	0.221		QUADRATIC	34.171	0.255
P210	1.18E-04	0.996	-0.580		QUADRATIC	130.513	0.494
P310	-4.10E-05	1.007	0.738		QUADRATIC	167.780	0.561
P510	-9.70E-05	1.001	0.734		QUADRATIC	221.187	0.644
P211	3.66E-04	0.971	-0.194		QUADRATIC	15.141	0.176
P311	7.01E-04	0.951	0.768		QUADRATIC	108.310	0.472
P511	8.96E-04	0.936	1.067		QUADRATIC	150.166	0.555
P212	5.90E-05	0.989	0.083		QUADRATIC	16.619	0.179
P312	1.30E-05	-0.001	1.024	0.112	CUBIC	21.972	0.206
P512	-1.70E-04	1.007	-0.235		QUADRATIC	71.308	0.371

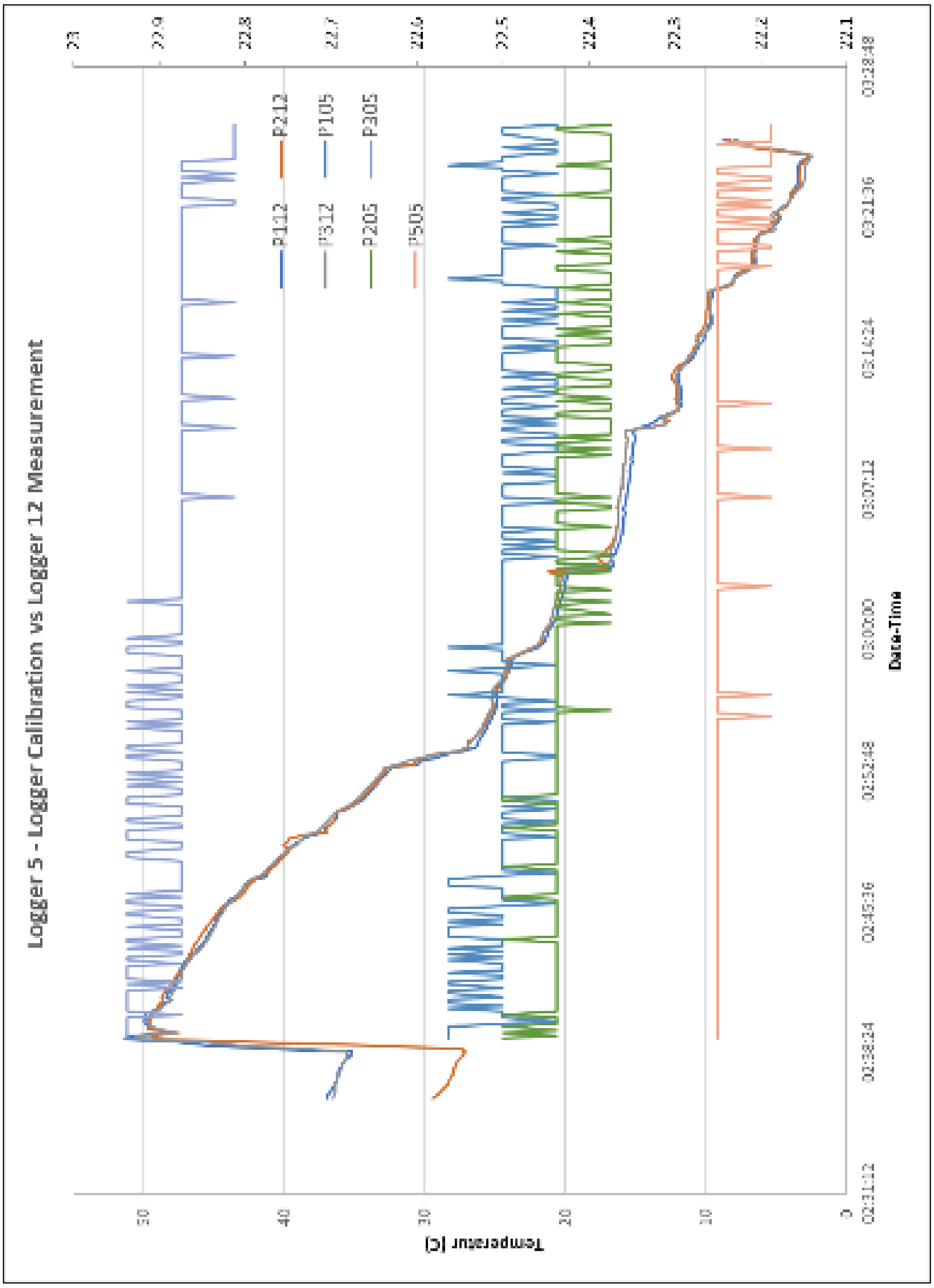

Figure 5.12. Logger-5 vs. logger-12 calibration data.

5.3 Fieldwork

Following the design and calibration of the temperature loggers, a total of eight loggers were deployed in the field on September 2021 at shallow holes drilled down to approximately 5.5 – 6 m depth. Following the first deployment, the second fieldwork was conducted on February 2022 to replace the batteries and the third and final fieldwork was conducted on February 2023 to collect the entire logger setups.

5.3.1 First Fieldwork

Before conducting this fieldwork, approximate logger locations were selected based on different topographic and surface material characteristics and final locations were identified based on this information (Figure 5.15, Table 5.11). Furthermore, lineaments (Figure 5.13) and reservoir characteristics (Figure 5.14) (Yal et al., 2017) were considered during location selection.

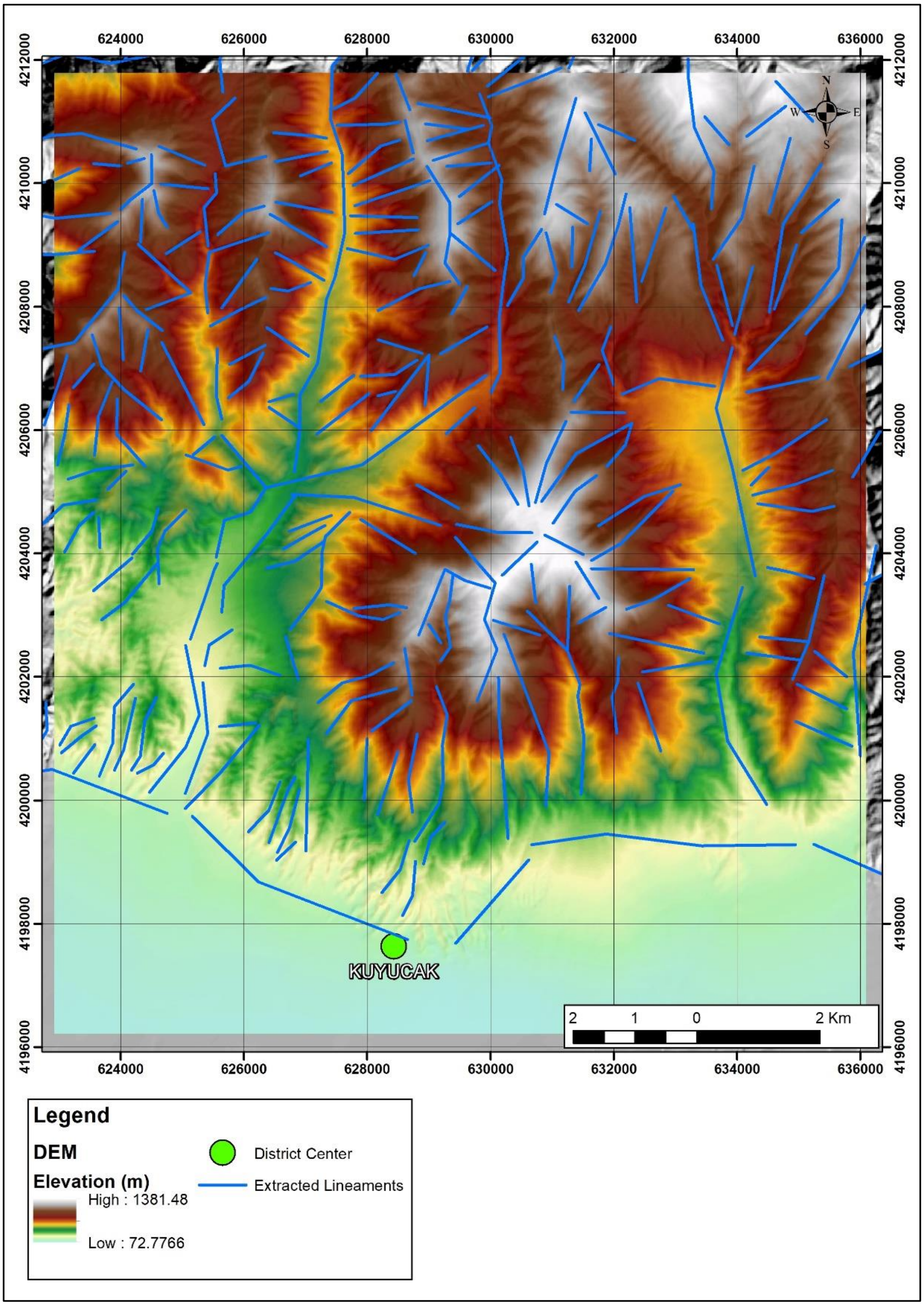

Figure 5.13. Lineament map of the study area.

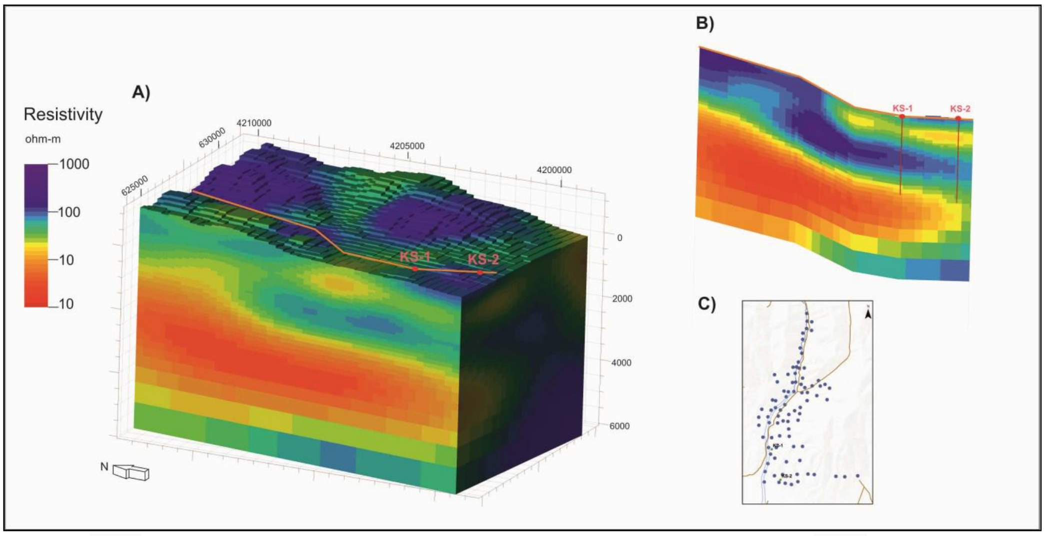

Figure 5.14. 3DMT, reservoir depth (Yal et al., 2017).

Table 5.11. Surface parameters of logger locations.

Logger	Location	ASTER Albedo	Elev.	Slope	Aspect	Relief	Depth to Reservoir
2	KS-2	0.31	217	3.51	189.28	0.87	3125.9
5	KS-1	0.30	234	7.01	247.55	0.81	2731.1
6	BENZINLIK-SLOPE-NORTH	0.47	356	31.15	320.09	0.43	2878.8
7	KULE-SLOPE-SOUTH	0.25	422	8.99	166.35	0.83	3056.7
8	TABELA	0.24	412	27.03	187.67	0.84	2999.4
10	YATIK	0.27	482	11.37	258.47	0.76	2392.2
12	KOPRU-ALTI	0.20	498	7.79	198.35	0.93	2226.1
11	DOLMUSLAR	0.23	553	9.63	313.57	0.77	2224.7

Therefore, eight loggers out of ten developed loggers with 1, 2, 3 and 5 m temperature sensors were deployed at the eight shallow drill borehole locations with 10 cm PVC casing and the PVCs were filled with soil material in order to limit air contact (Figure 5.16, Figure 5.17, Figure 5.18 and Figure 5.19).

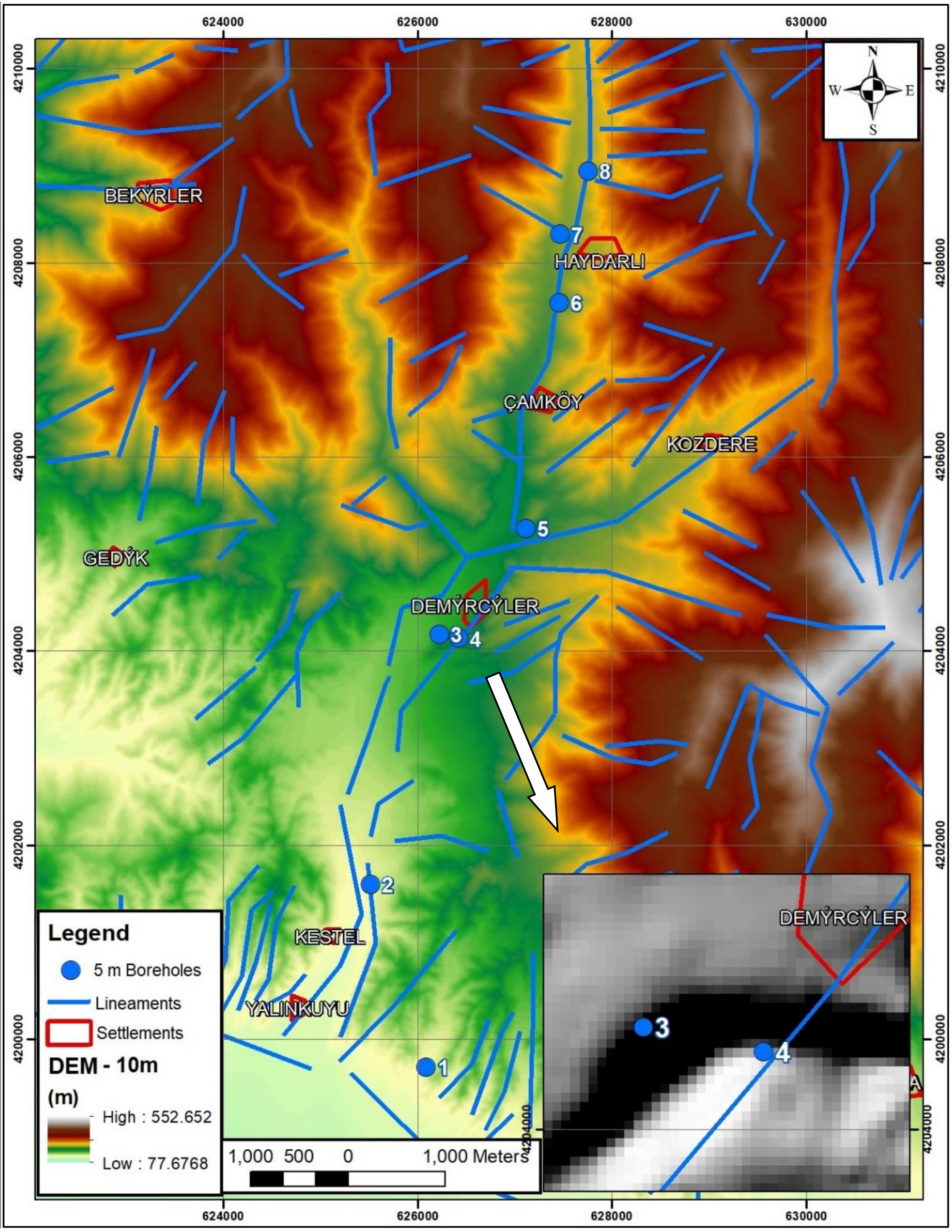

Figure 5.15. Drilling locations.

Figure 5.16. KS1 location drilling operation.

Figure 5.17. KS1 location logger preparation.

Figure 5.18. KS1 location deployed logger.

Figure 5.19. Backfilling PVC casing.

5.3.2 Second Fieldwork

As mentioned above, there are 8 locations where loggers with four sensors at 1, 2, 3 and 5 m depths were deployed on 22nd and 24th of September, 2021 following the drilling operation on 22ndof September.

In order to replace the batteries of the data loggers, a second fieldwork was conducted on 25th and 26th of February, 2022. Out of eight loggers, batteries of five loggers were successfully replaced and data from these loggers were collected such that battery of three loggers out of five remaining data loggers lasted until the replacement date.

Logger 11 at location 8 lasted until January 2nd, 2022, which is further discussed below, Logger 8 at Location 5 – Tabela, lasted until January 29, and the Logger 10 at Location 6 – Yatık, Logger 7 at Location 4: Kule and Logger 2 at Location 1: KS2 were still operational. Unfortunately, 2 loggers, namely Logger 6 at Location 3: Benzinlik and Logger 5 at Location 2: KS-1 had severe water damage and the last data was collected by these loggers on January 2nd, 2022 and January 4th, 2022, respectively. Finally, Logger 12 at Location 7: Köprü Altı could not be located. which is further discussed below.

5.3.2.1 Data Collection and Battery Replacement Steps

The process of data retrieval and battery replacement was as follows: First, logger and battery were completely dug up. The battery-logger sets have a six cable extension separate from the main package. These 6 cables can be used for data transfer without tampering with the main battery-logger package. However, since the batteries were to be replaced as well, entire setup was dug up during this fieldwork. Otherwise, four out of the mentioned six cables could be used for data transfer. The name and color code of the cables are given below (Table 5.12).

Table 5.12. Logger to UART cable connections.

Connection	Cable Color	Definition
BLK (GND)	Black	Reset PIN
GND	Blue	Ground
VCC	Red	5V Power
RXI	Green	Receive Input PIN
TXO	Yellow	Transmit Output PIN
GRN	White	Ground

If the battery of the logger has not depleted, then only wires 1 and 3 through 6 would be required since VCC and GND would be connected to the operational battery. Therefore, the process of data collection was arranged in steps.

- If the 4 wire connected allow data transfer, this means the battery is still providing power to the logger and all data up-to that point should be available.
- If this does not work, then all 6 wires are connected to the UART (Universal Asynchronous Reception and Transmission) module and data is transferred as such, which should result in transfer of all data up to loss of power.
- If this also does not work, this would suggest a problem with the logger, then all packaging was opened, micro SD card was retrieved manually and the problem was investigated.

Therefore, the data collection was conducted by following this three step process.

After data was transferred, the batteries were replaced. As the setting was not socketed in order to avoid as little connection as possible which would fail, but soldered, a USB soldering iron was brought to the field as well as a 12V to 220V car lighter inverter and a regular soldering iron. Since inverter operated properly, USB was not used for desoldering/soldering process. The two cables connecting the 12V to 5V buck converter (voltage regulator) to the battery was desoldered or cut and re-soldered to a new battery.

After the replacement, the battery was connected, the 4 wires were connected to the UART and a one loop (8 second) version of the code was uploaded to the Arduino Pro Mini microcontroller (logger). The reason behind this was to check that battery was connected properly and also check if any shorts have occurred during the replacement process, which may reset the time of RTC (real time clock) module. Therefore, after it was confirmed that the system was operational and date/time and probe temperatures were correct, the five-minute loop was uploaded to the micro controller and logger and battery setup was repacked and buried once again. These steps were followed at each location.

Out of eight locations, one logger at location 7, Köprü-altı could not be located due to the flooding event that occurred earlier that year. Two loggers, namely location 3 Benzinlik and location 2 KS-1 had water damage and loggers were freed from the sensors and retrieved. Batteries of the remaining five loggers were replaced successfully.

A summary of the data collection is given in Table 5.13.

Figure 5.20. Location 8, KS-2, data retrieval.

Figure 5.21. Location 8, KS-2, data retrieval.

Figure 5.22. Location 8, KS-2, location market.

Figure 5.23.Location 6, tabela, data collection preparation.

Figure 5.24. Location 6, tabela, data collection preparation.

Figure 5.25. Location 3, Benzinlik, water damage.

Figure 5.26. Location 3, Benzinlik, water damage.

Figure 5.27. Location 4, Kule, re-deployment.

Table 5.13. Summary table for each data logger from the second fieldwork for battery replacement.

Loc. ID	Defnition	Log. ID	Deployed	First Retrieved	Second Retrieved	Second Deployed	Data Available Until	Notes	Old Battery Voltage
1	KS-2	Log-2	24/09/2021 – 9:40	NA	25/02/2022 – 11:00	25/02/2022 – 11:50	25/02/2022 – 11:00-ALL	OK All data collected.	11.53
2	KS-1	Log-5	22/09/2021 – 19:45	24/09/2021 – 13:05	26/02/2022 -18:00	NA	04/12/2021 – 20:52	Severe water damage.	Oxidation apparent.
3	Benzinlik	Log-6	22/09/2021 – 18:40	24/09/2021 – 12:51	26/02/2022 – 15:00	NA	30/11/2021 – 00:26	Severe water damage.	12V Oxidation apparent.
4	Kule	Log-7	22/09/2021 – 17:30	24/09/2021 – 12:25	26/02/2022 – 15:50	26/02/2022 – 16:00	26/02/2022 – 15:50-ALL	OK All data collected.	11
5	Tabela	Log-8	22/09/2021 – 16:15	24/09/2021 – 11:55	25/02/2022 – 16:30	26/02/2022 – 17:00	29/01/2022 – 15:25	Data repeated itself during transfer.	11
6	Yatık	Log-10	22/09/2021 – 14:45	24/09/2021 – 11:20	26/02/2022 – 09:45	26/02/2022 – 11:00	26/02/2022 – 09:49-ALL	OK All data collected.	11.46
7	Köprü Altı	Log-12	22/09/2021 – 11:50	24/09/2021 – 10:55	NA	NA	NA	Could not be located.	NA
8	Dolmuşlar	Log-11	22/09/2021 – 13:10	24/09/2021 – 10:30	25/02/2022 – 15:30	26/02/2022 – 11:50	02/01/2022 – 01:38	Data missing, battery at 3V. Data retrieved from SD card. No water damage. Battery replaced two times.	3.36

5.3.2.2 Collected Data and Data Fits

According to previously identified relations based on sensor co-calibration, best fit for each logger was identified. The relation for each sensor with the best fit result is given below.

Therefore, the collected data from the seven locations were plotted following the calibration relations and each chart is given below.

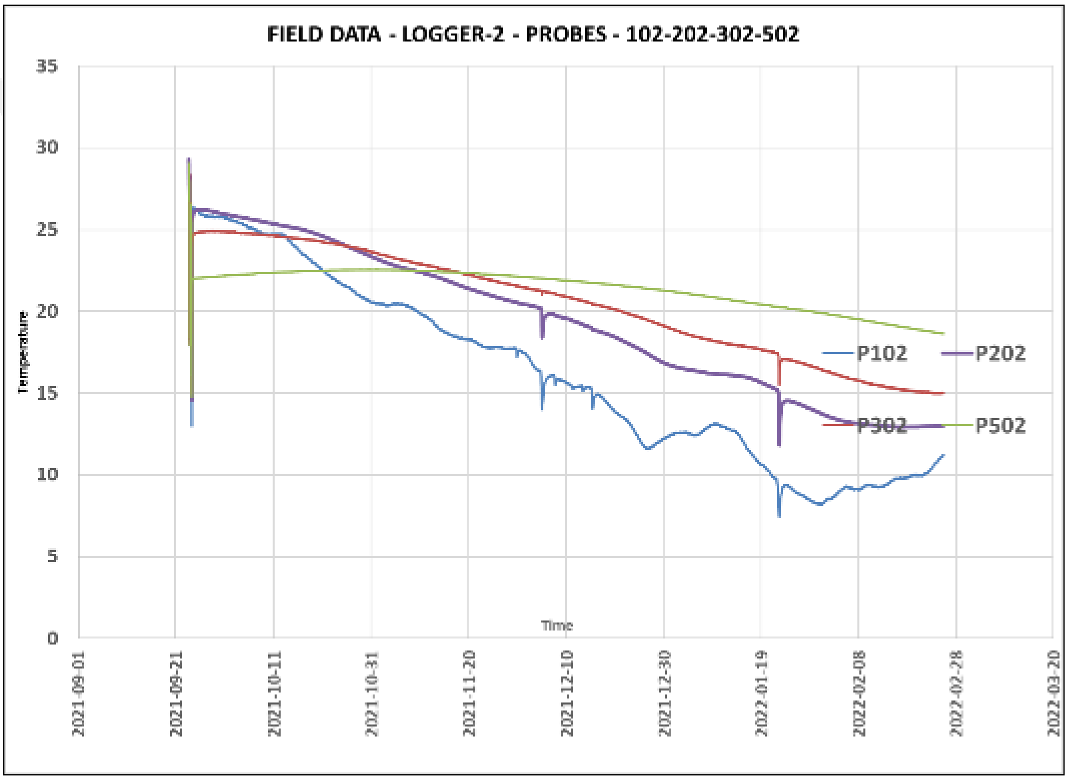

Figure 5.28. Location 1, KS-2, Logger 2, all data up-to 25 February data collection.

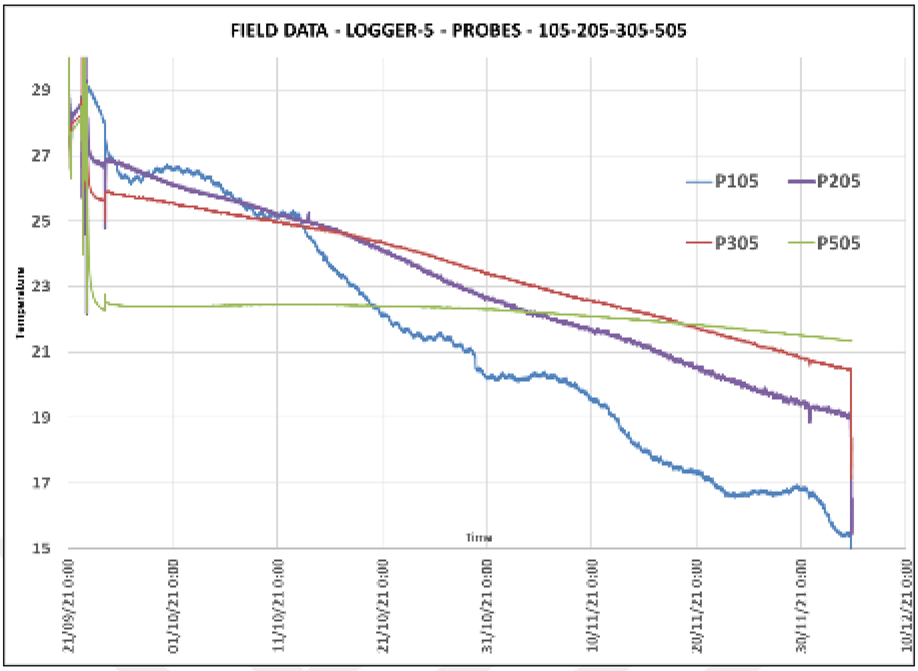

Figure 5.29. Location 2, KS-1, Logger-5, water damage, data until 4th of December, 2021.

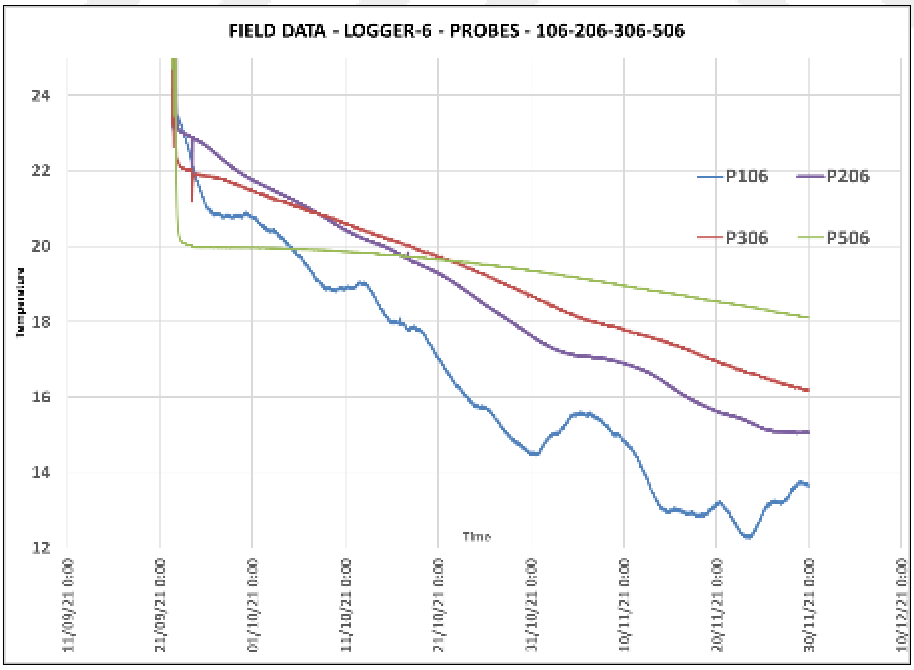

Figure 5.30. Location 3, Benzinlik, Logger-6, water damage, data until 30th of November, 2021.

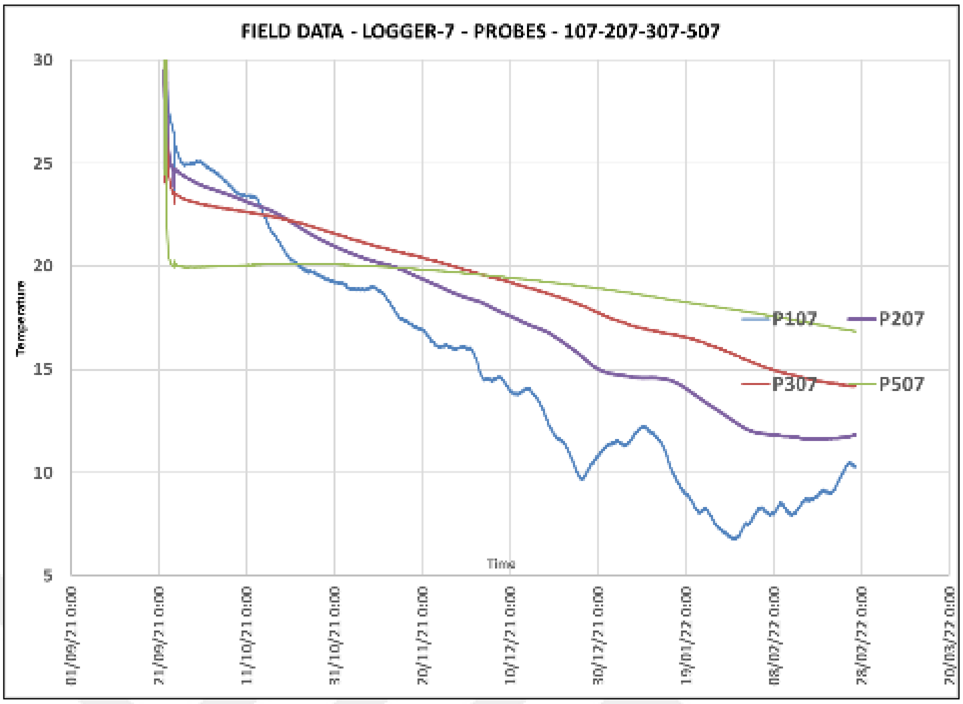

Figure 5.31. Location 4, Logger-7, Kule, all data compete until data collection on 26th of February.

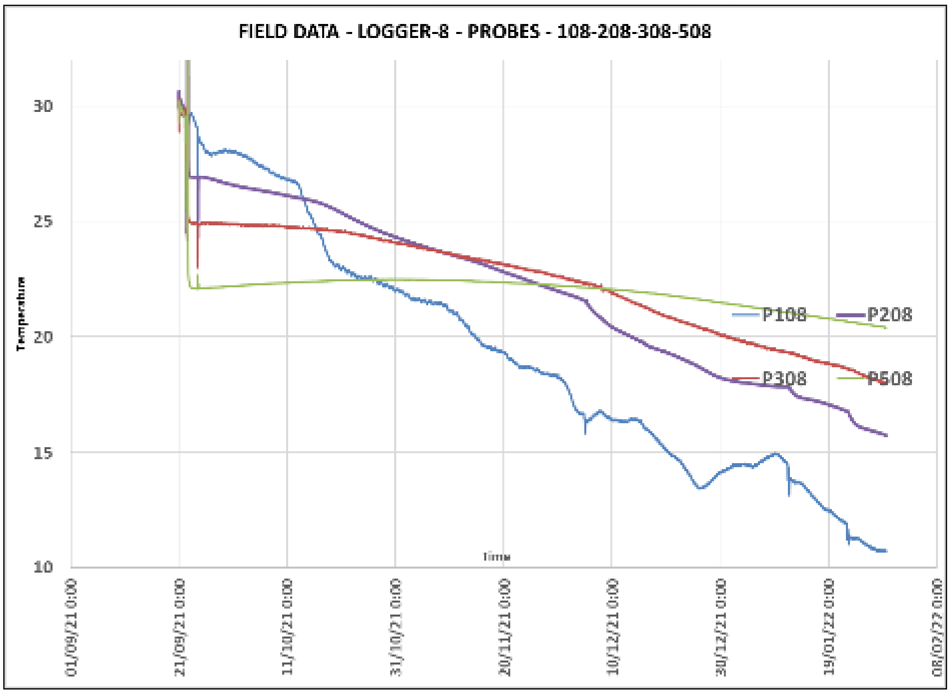

Figure 5.32. Location 5, Tabela, Logger-8, data collected, until 29.01.2022

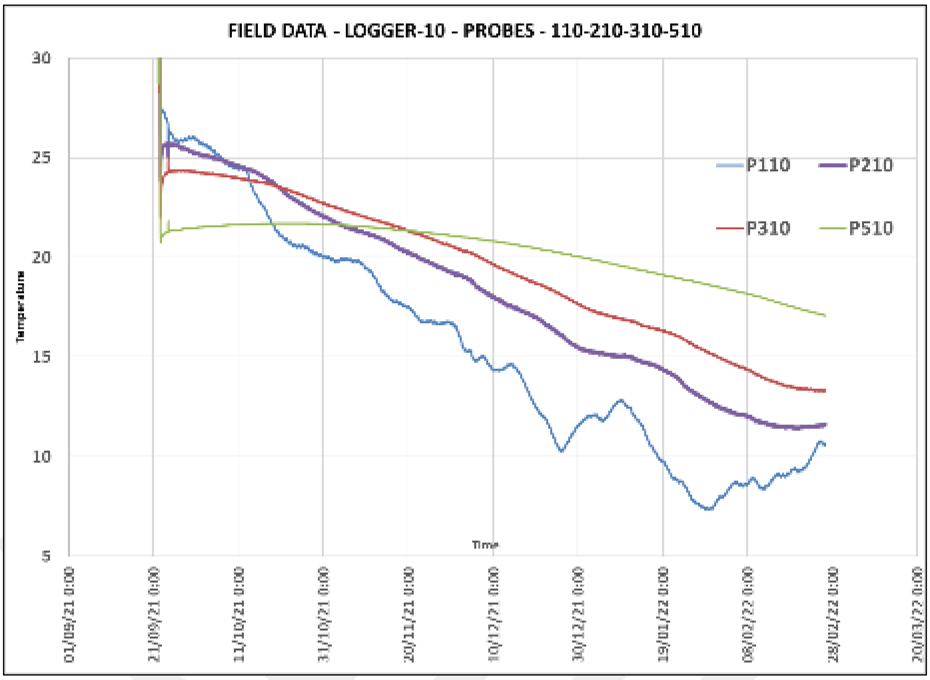

Figure 5.33. Location 6, Yatık, Logger-10, all data complete until data collection on 26 February

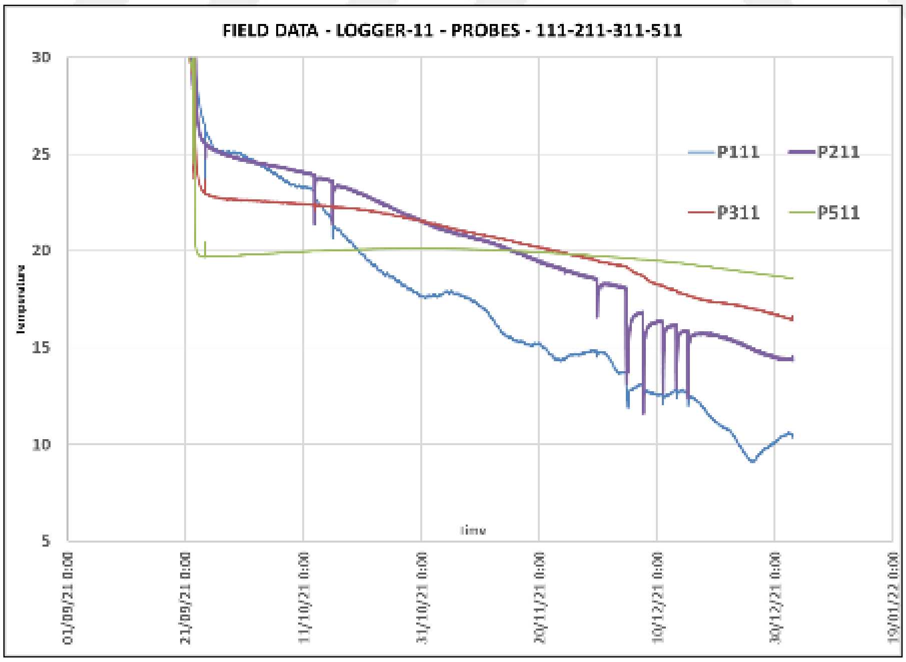

Figure 5.34. Location 8, Dolmuslar, Logger-11, data available until January 2nd, 2022, battery at 3.36V.

5.3.3 Third Fieldwork

This fieldwork was performed in order to collect data from the 8 loggers previously deployed in the Kuyucak field in N-S trend and change the batteries which is estimated to last around 160 days. Eight locations where loggers with four sensors at 1, 2, 3 and 5 m depths were deployed on 22nd and 24th of September, 2021 following the drilling operation on 22nd.

In two days of fieldwork on 25 and 26th of February 2022, batteries of five loggers were successfully replaced, 2 logger had severe water damage (Location 2 and 3) and data was salvaged from SD cards and 1 logger could not be located (Location 7).

During fieldwork on February 11th 2023, the remaining five data loggers were collected from the field where batteries were not replaced and entire logger setup was separated from the sensors and collected for each location, except the Kopru Alti location where the logger could not be located during this fieldwork as well.

Table 5.14. Logger ID and location list with summary notes.

Loc. ID	Definition	Log. ID	Deployed	February 2022 Fieldwork End Date	February 2023 Fieldwork Data Range	2022 Remarks	2023 Remarks
1	KS-2	Log-2	24/09/2021 – 9:40	25/02/2022 – 11:00 - ALL	02.03.2022, 19:55:08	OK All data collected.	Water damage.
2	KS-1	Log-5	22/09/2021 – 19:45	04/12/2021 – 20:52	Damaged	Severe water damage. Logger separated from sensors. PVC marker at the location missing, cause of water seepage.	Not replaced.
3	Benzinlik	Log-6	22/09/2021 – 18:40	30/11/2021 – 00:26	Damaged	Severe water damage. Logger separated from sensors. Possibly hard ground caused water collection.	Not replaced.
4	Kule	Log-7	22/09/2021 – 17:30	26/02/2022 – 15:50 - ALL	27.08.2022, 11:59:06	OK All data collected.	Battery Depleated
5	Tabela	Log-8	22/09/2021 – 16:15	29/01/2022 – 15:25	25.07.2022, 21:08:05	Data repeated itself during transfer. Reason unknown. Successfully re-deployed.	Battery Depleated
6	Yatık	Log-10	22/09/2021 – 14:45	26/02/2022 – 09:49 - ALL	24.06.2022, 20:18:45	OK All data collected.	Battery Depleated
7	Köprü Altı	Log-12	22/09/2021 – 11:50	NA	NA	Could not be located, missing covering tarp and human activity in the location.	Could not be located due to flood occurred in 2022.
8	Dolmuşlar	Log-11	22/09/2021 – 13:10	02/01/2022 – 01:38	27.04.2022, 06:33:23	Data missing, battery at 3V. Data retrieved from SD card. No apparent water damage. Battery replaced 2 times.	Water damage.

5.3.3.1 Collected Data and Data Fits

Therefore, the collected data from the seven locations were plotted following the calibration relations and each chart is given below.

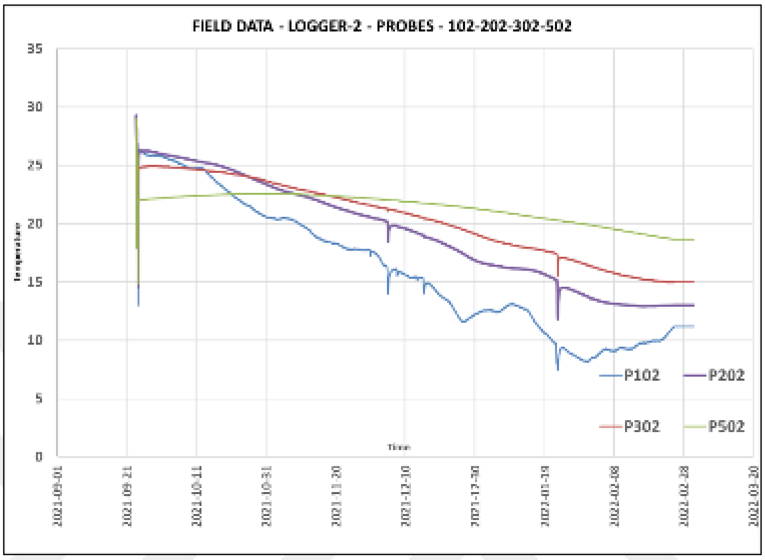

Figure 5.35. Location 1, KS-2, Logger 2, data up to March 2.

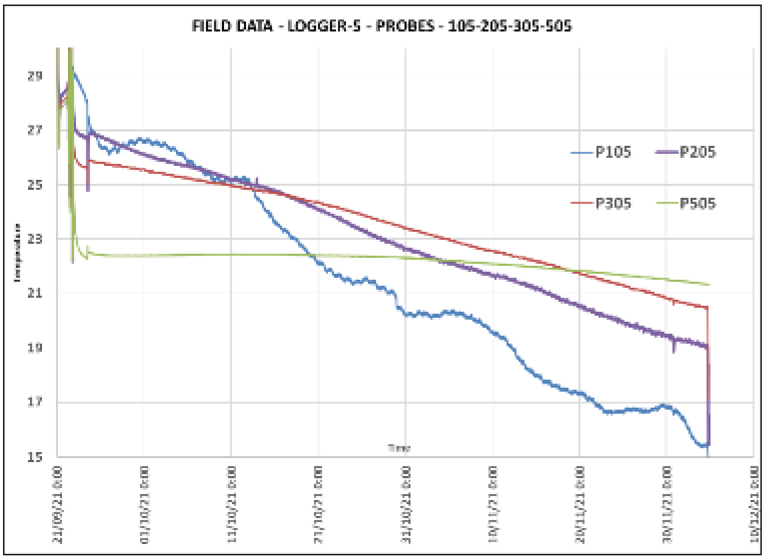

Figure 5.36. Location 2, KS-1, Logger-5, water damage, data until 4th of December, 2021.

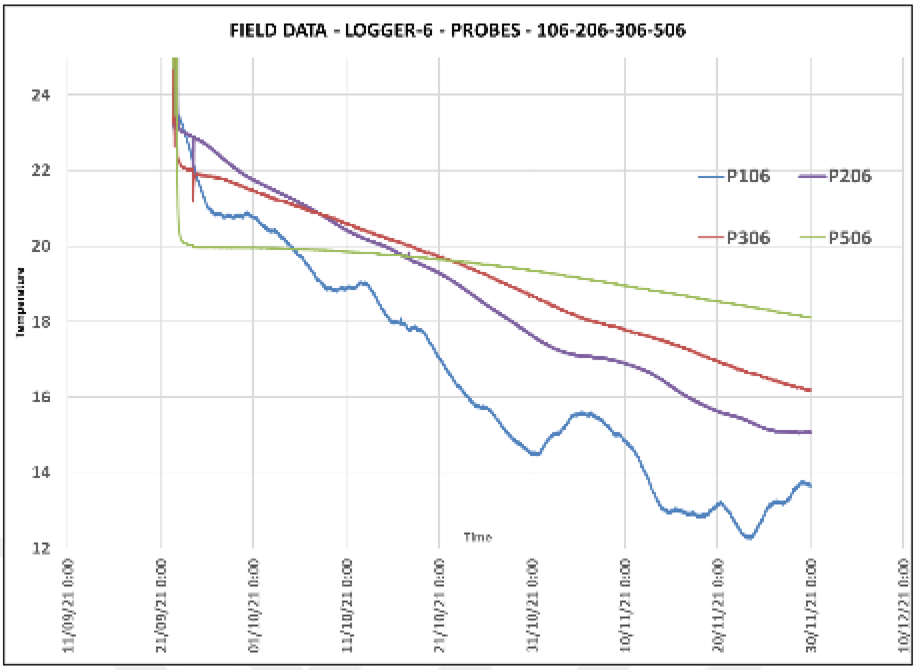

Figure 5.37. Location 3, Benzinlik, Logger-6, water damage, data until 30th of November, 2021.

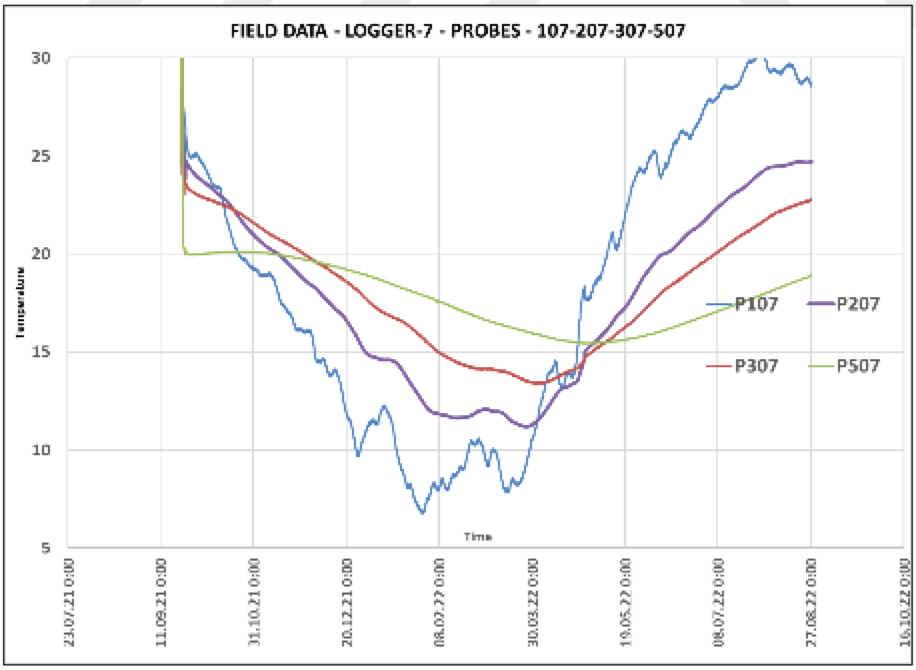

Figure 5.38. Location 4, Logger-7, Kule, data until data 27/08/2023.

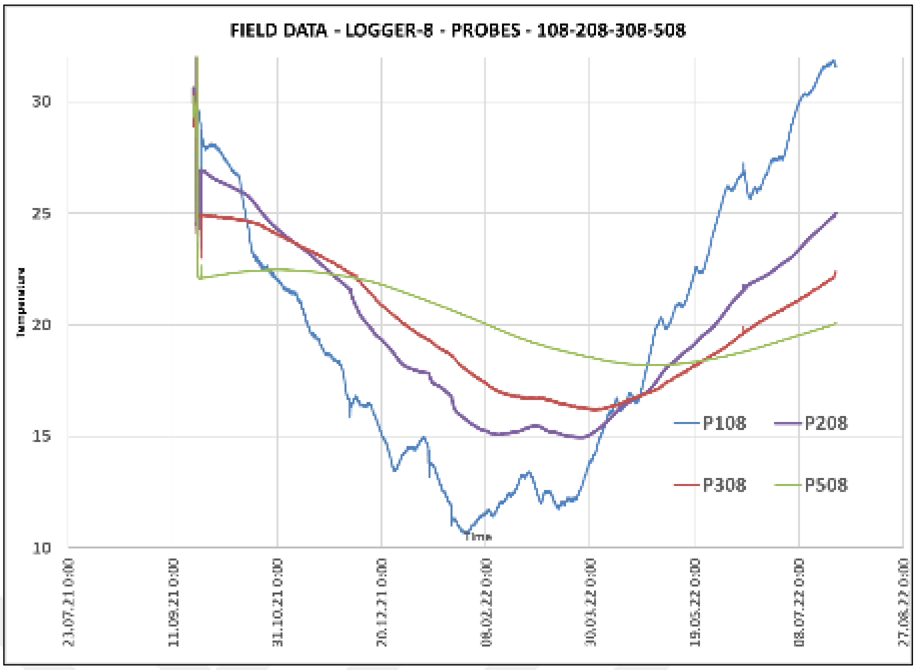

Figure 5.39. Location 5, Tabela, Logger-8, data collected, until 25.07.2022

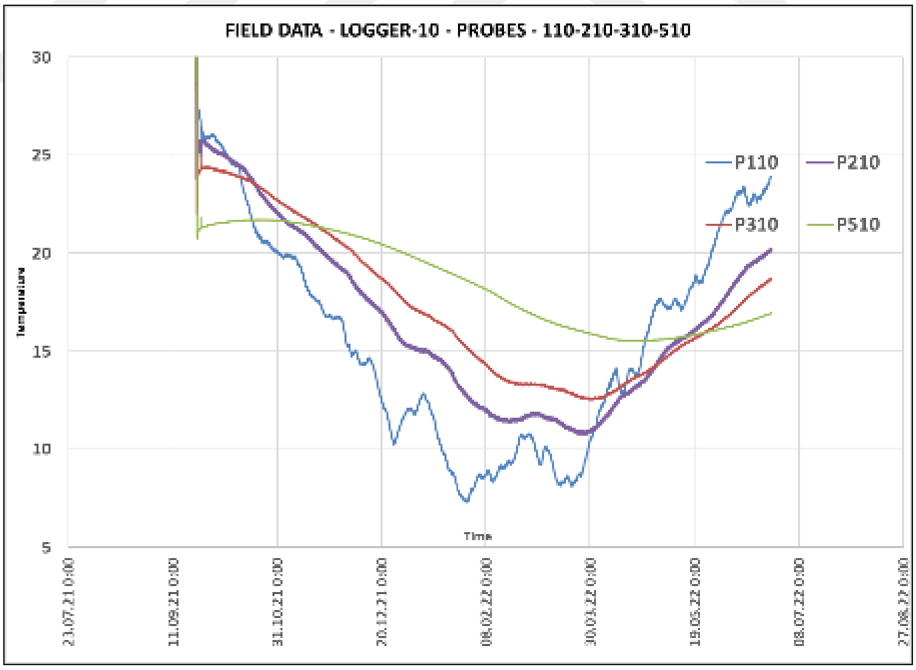

Figure 5.40. Location 6, Yatık, Logger-10, all data complete until data collection on 24/06/2023

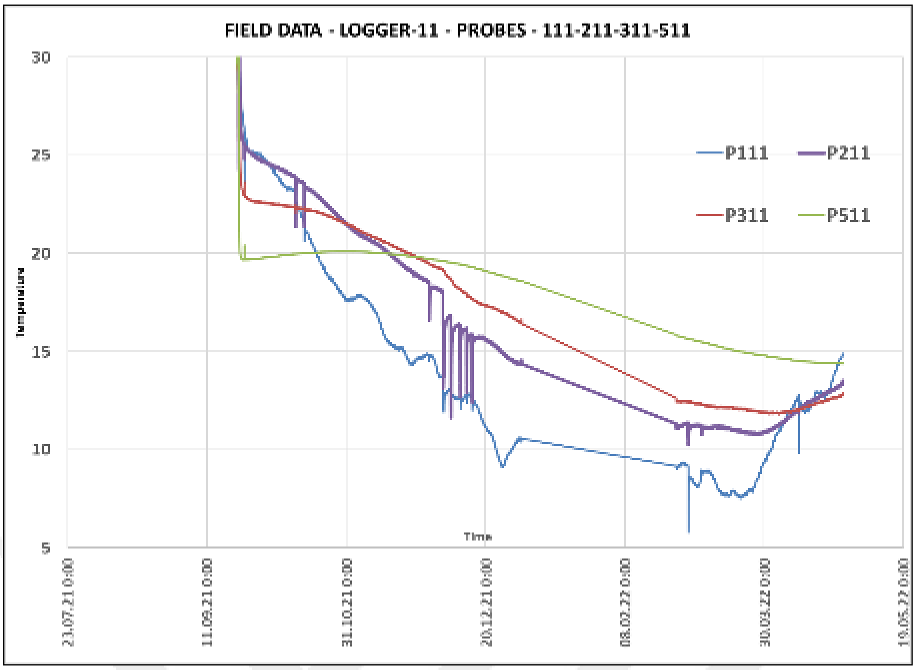

Figure 5.41. Location 8, Dolmuslar, Logger-11, data available until 02/01/2022, 27.04.2022 final date.

5.4 Results of the Data Collected from the Field

Due to different reasons as discussed above, the temperature loggers deployed in the field could not collect data covering the same interval. The data collection interval of each logger and temperature statistics are provided in Table 5.15. The results are provided for the calibrated sensor readings where calibration equation is defined in parentheses (e.g., quadratic or cubic). As can be seen in Table 5.15, the maximum recording duration was achieved at Logger-7, with total of 336 days of data recorded, whereas, due to water damage, the shortest duration for the data recorded was at Logger-5 and 6, with 71 and 68 days of data recording, respectively.

Table 5.15. Summary statistics of the data collected from the field.

Sensor ID	Min. Temp. (°C)	Max. Temp (°C)	Average Temp. (°C)	Recording Duration (Days)
P102	8.138	26.306	15.948	159
P202 (CUBIC)	12.913	26.244	19.099	
P302 (QUAD.)	14.956	24.947	20.274	
P502 (QUAD.)	18.631	22.551	21.283	
P105	15.344	27.369	21.200	71
P205 (QUAD.)	18.987	26.896	22.927	
P305 (QUAD.)	20.457	25.929	23.411	
P505 (CUBIC)	21.333	22.514	22.148	
P106	12.250	23.331	16.475	68
P206 (CUBIC)	15.041	23.069	18.530	
P306 (CUBIC)	16.155	22.163	19.103	
P506 (CUBIC)	18.104	20.211	19.322	
P107	6.763	30.331	18.144	336
P207 (QUAD.)	11.187	24.726	17.691	
P307 (QUAD.)	13.359	23.512	18.025	
P507 (CUBIC)	15.433	20.111	17.679	
P108	10.656	31.888	19.305	304
P208 (QUAD.)	14.931	26.921	19.771	
P308 (QUAD.)	16.147	24.976	19.849	
P508 (QUAD.)	18.191	22.496	20.193	
P110	7.313	26.263	15.442	273
P210 (QUAD.)	10.773	25.720	16.480	
P310 (QUAD.)	12.513	24.389	17.283	
P510 (QUAD.)	15.520	21.719	18.448	
P111	5.813	25.888	14.283	214
P211 (QUAD.)	9.769	24.740	16.198	
P311 (QUAD.)	12.101	22.911	17.355	
P511 (QUAD.)	14.715	20.270	18.123	

According to the study conducted by Lange et al. (1982), temperatures measured at shallow depths outside the influence of 24-hr diel temperature fluctuations can be approximated by a sinusoidal annual curve. Applicability of this approach was also shown by Sladek et al. (2012). Therefore, in order to be able to compare the data collected from different locations, the data of each logger was fit into sinusoidal wave function for a full one-year cycle by utilizing GRG (generalized reduced gradient) nonlinear option of Microsoft Excel's Solver tool. The GRG nonlinear method utilized in this tool is based on the study by Lasdon et al. (1974). Results of the sinusoidal wave fitting is presented in Table 5.16. Charts showing sinusoidal wave fit of each logger is presented in Figure 5.42 through Figure 5.48.

Table 5.16. Summary statistics of the temperature data fit to sinusoidal wave function.

Logger ID.	**Min. Temp. (°C)**	**Max. Temp (°C)**	**Average Temp. (°C)**
P102	9.760	28.246	19.020
P202 (CUBIC)	12.669	26.264	19.482
P302 (QUAD.)	14.430	24.766	19.611
P502 (QUAD.)	17.198	22.529	19.869
P105	13.566	35.302	24.442
P205 (QUAD.)	16.096	29.684	22.899
P305 (QUAD.)	16.355	26.626	21.501
P505 (CUBIC)	17.241	22.452	19.853
P106	12.642	37.145	24.887
P206 (CUBIC)	13.885	29.439	21.665
P306 (CUBIC)	14.097	24.531	19.321
P506 (CUBIC)	14.145	20.002	17.081
P107	8.127	29.003	18.583
P207 (QUAD.)	11.512	24.496	18.019
P307 (QUAD.)	13.710	22.781	18.257
P507 (CUBIC)	15.479	20.026	17.757
P108	11.368	30.956	21.179
P208 (QUAD.)	14.946	26.867	20.920
P308 (QUAD.)	16.284	24.848	20.577
P508 (QUAD.)	18.229	22.498	20.368
P110	8.653	27.572	18.131
P210 (QUAD.)	11.065	26.773	18.937
P310 (QUAD.)	12.871	24.038	18.468
P510 (QUAD.)	15.571	21.692	18.638
P111	7.001	26.999	17.018
P211 (QUAD.)	10.053	24.694	17.390
P311 (QUAD.)	12.210	22.642	17.438
P511 (QUAD.)	14.689	20.275	17.488

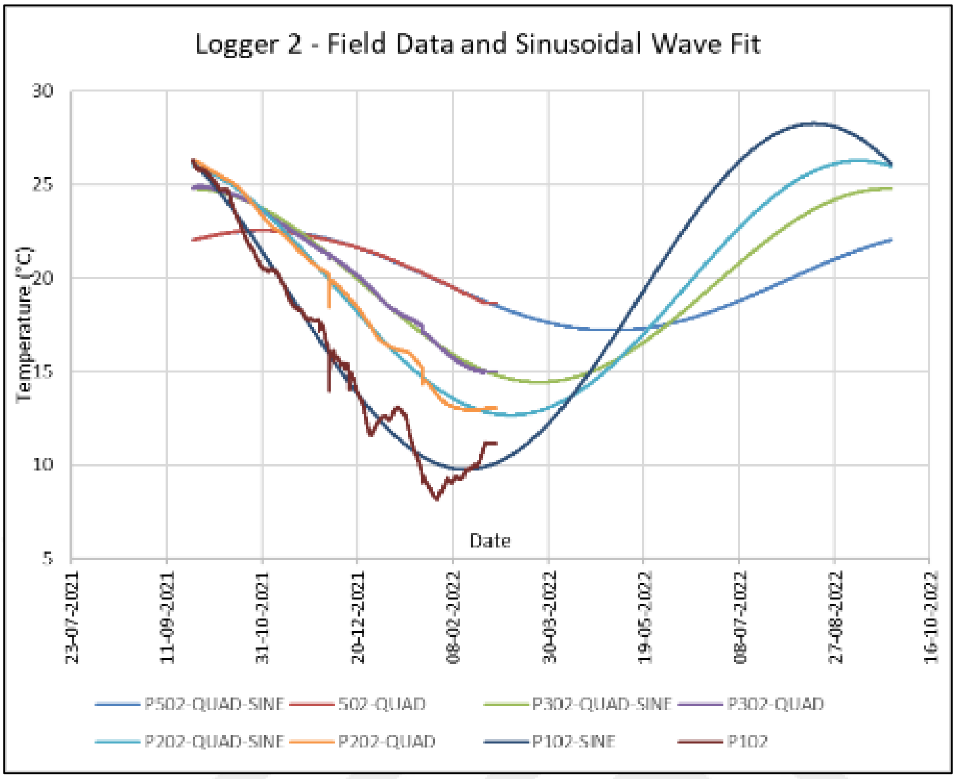

Figure 5.42. Location 1, KS-2, Logger 2, sinusoidal data fit.

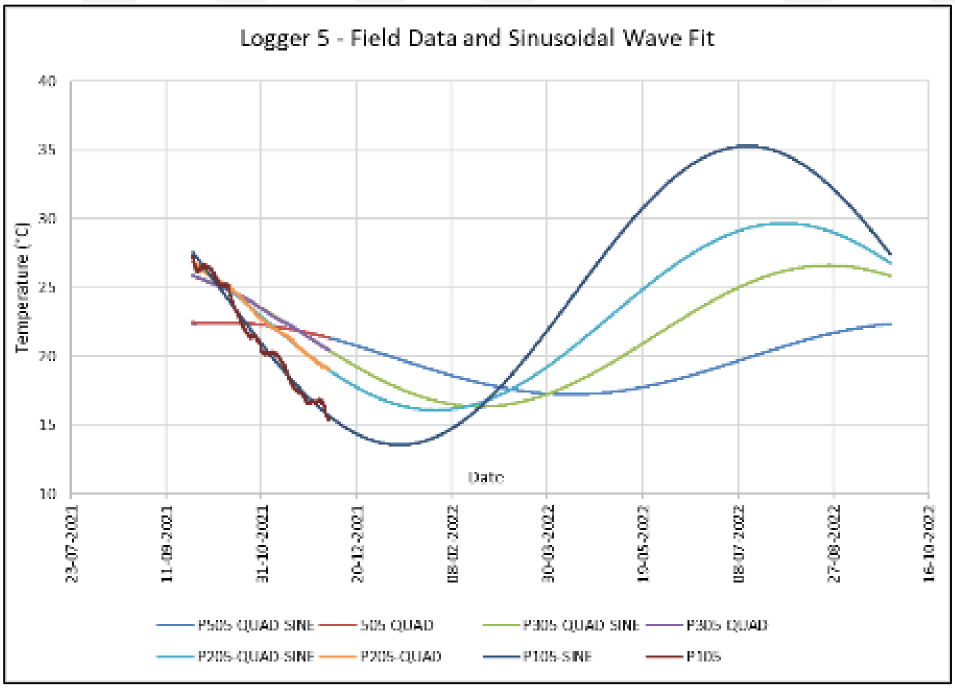

Figure 5.43. Location 2, KS-1, Logger-5, sinusoidal data fit.

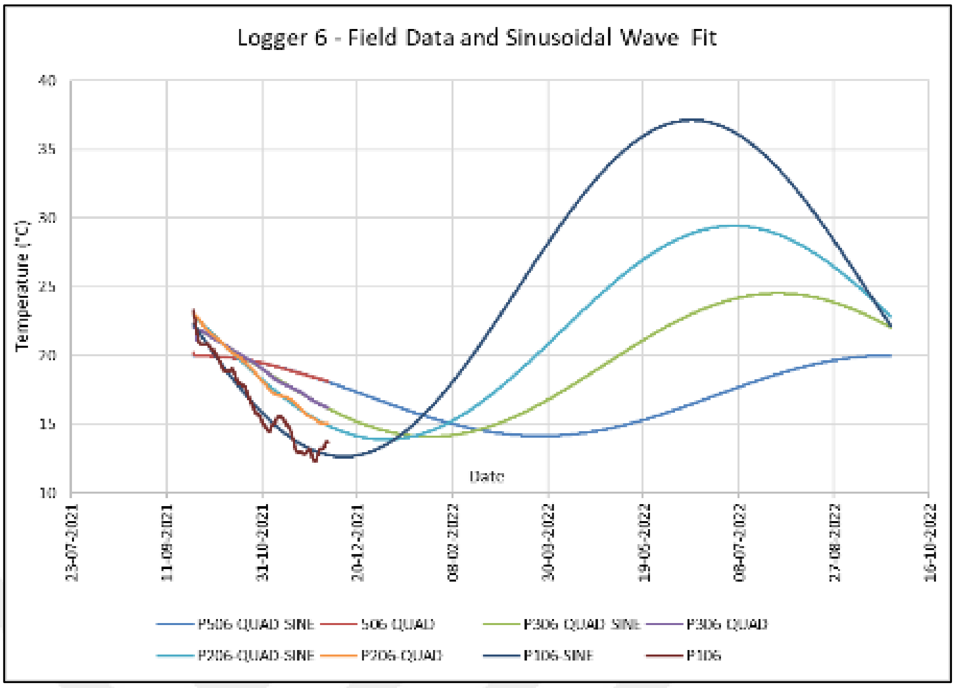

Figure 5.44. Location 3, Benzinlik, Logger-6, sinusoidal data fit.

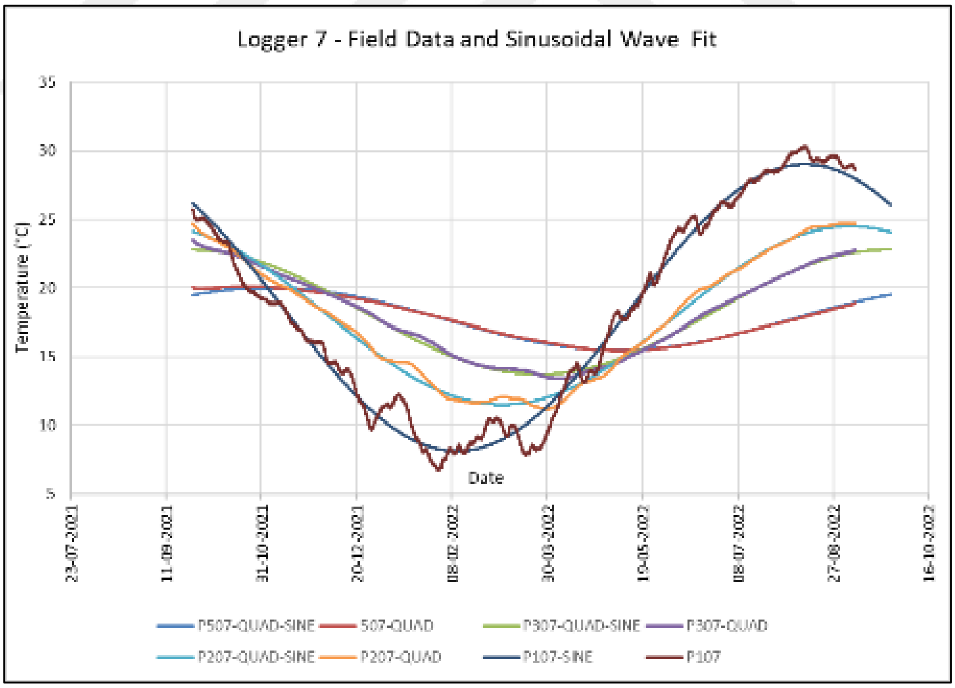

Figure 5.45. Location 4, Logger-7, Kule, sinusoidal data fit.

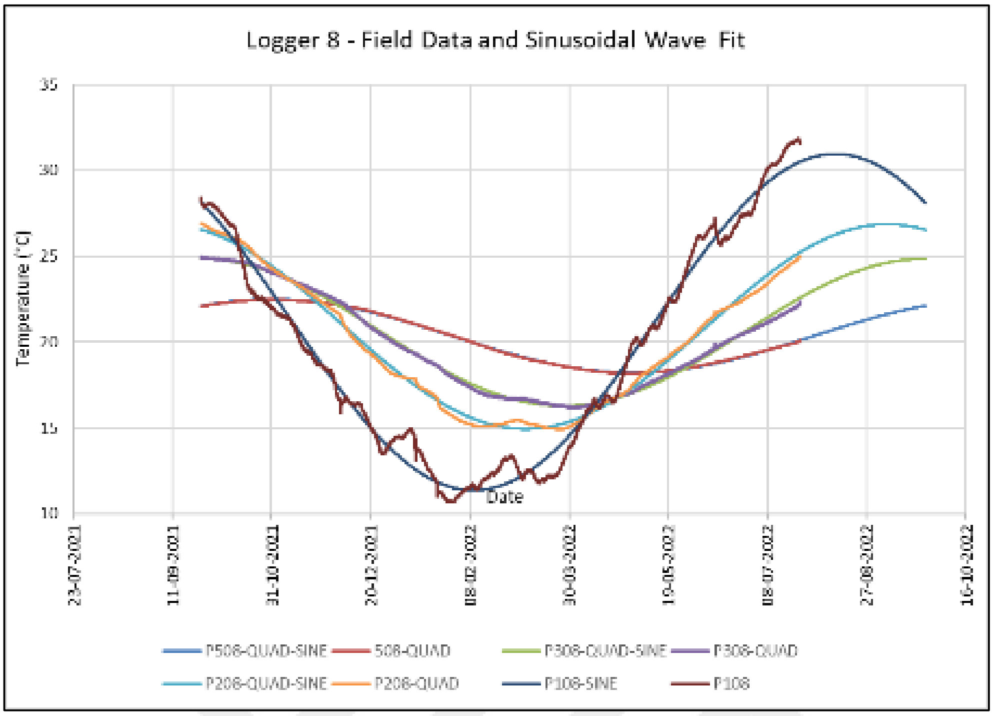

Figure 5.46. Location 5, Tabela, Logger-8, sinusoidal data fit.

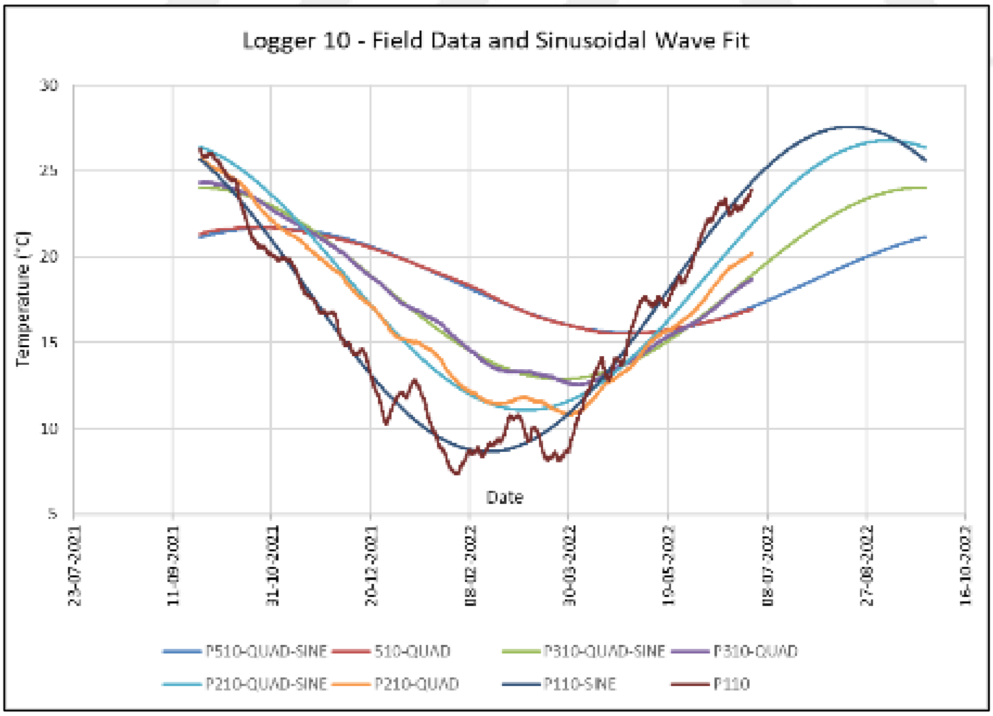

Figure 5.47. Location 6, Yatık, Logger-10, sinusoidal data fit.

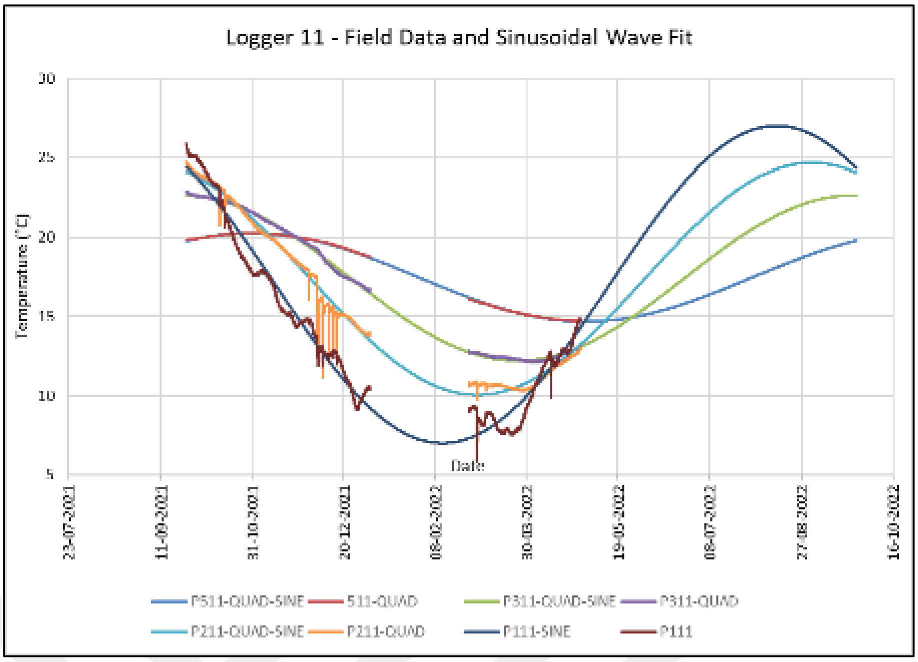

Figure 5.48. Location 8, Dolmuslar, Logger-11, sinusoidal data fit.

According to field data collection and sinusoidal wave fits to the data to complete a one-year cycle, when average temperature values are compared, it was observed that in an entire annual cycle, loggers 2, 10 and 11 at locations KS-2, Yatık and Dolmuşlar, respectively, have positive temperature gradient. On the other hand, loggers 5, 6, 7 and 8 at locations KS-1, Benzinlik, Kule and Tabela have negative annual average temperature gradient.

It has been suggested by Sladek et al. (2012) and Coolbaugh et al. (2010) that the ideal time for temperature measurements to be taken is shortly after equinoxes since temperature inversion occurs at these dates and also weather is relatively more stable during this period. Therefore, when measurements taken (or sine wave fit) following spring equinox is considered on April 21st, it was observed that, starting from logger 7 at Kule location, there is an increasing trend from south to north in temperature gradient values, especially for the 3 m to 5 m depth measurements' gradient. Furthermore, positive thermal gradient was also observed at logger 2 at KS-2 well location. As previously mentioned, KS-2 is a successful deep geothermal well with

>150°C temperature. Since it was observed from the field collected data that 2 m sensor was affected from surface temperature differences as observed in temperature fluctuations, the gradient value calculated from 3 m and 5 m sensor's difference was considered to be most reliable.

Table 5.17. Annual average temperature gradient values of each logger.

Loc. Id.	**Definition**	**Log. Id.**	**Annual Average Gradient, 1 and 5 m (°C/m)**	**Annual Average Gradient, 2 and 5 m (°C/m)**	**Annual Average Gradient, 3 and 5 m (°C/m)**
1	KS-2	Log-2	0.2122	0.1289	0.1291
2	KS-1	Log-5	-1.1472	-1.0156	-0.8241
3	Benzinlik	Log-6	-1.9516	-1.5281	-1.1199
4	Kule	Log-7	-0.2065	-0.0873	-0.2498
5	Tabela	Log-8	-0.2027	-0.1840	-0.1042
6	Yatık	Log-10	0.1268	-0.0998	0.0848
8	Dolmuşlar	Log-11	0.1174	0.0325	0.0246

On the other hand, loggers 5 and 6 have shown negative thermal gradient. Although logger 5 is located at the deep geothermal well location, it was observed during drilling operations that shallow groundwater at approximately 150 m is present at the location, which is considered to mask any thermal signature. Finally, logger 6 is located at the Benzinlik location which is situated at hard soil-weathered rock site. Due to limited data collected from this location with 68 days in total due to water damage to the sensor, sinusoidal wave fit does not provide conclusive results. When dates of coldest temperature according to sinusoidal wave fits, in other words, seasonal shift according to depth is considered, it was observed that for logger 5 and 6 at KS-1 and Benzinlik locations with most limited data collection time of 71 days and 68 days, respectively, shows the earlies date for the coldest temperature. On the other hand, all the remaining loggers present lowest temperatures during early to mid-February for the 1 m depth sensor and at the beginning of May for the deepest, 5 m sensor (Table 5.18). This indicates that the sinusoidal data fit with limited data have provided inconclusive results. Similarly, when arrival times of lowest temperature between different depths are compared, it was observed that for the 1 m to 3 m depth range, arrival times range between 37 to 45 days and arrival times between 1 m and 5 m depth range changes between 73 and 85 days, except the loggers with limited data, which are outliers.

When compared with the Y coordinate of the measurement points, the increase in thermal gradient between 3 m and 5 m depth sensors at April 21, 2022 can be clearly seen as shown in Figure 5.49 and R^2 coefficient of determination value was calculated as 0.9807.

Table 5.18. Dates of minimum temperatures for each sensor according to sinusoidal fit results.

Sensor Id.	Date and Time of Minimum Temperature	Sensor Id.	Date and Time of Minimum Temperature
P102	14-02-22 18:49	P105	11-01-22 9:39
P202	10-03-22 5:31	P205	30-01-22 12:06
P302	25-03-22 6:33	P305	23-02-22 0:03
P502	02-05-22 5:24	P505	11-04-22 13:10
P106	13-12-21 1:24	P107	10-02-22 15:34
P206	03-01-22 23:54	P207	06-03-22 7:37
P306	27-01-22 5:45	P307	25-03-22 11:44
P506	26-03-22 8:38	P507	06-05-22 3:58
P108	09-02-22 19:50	P110	17-02-22 4:20
P208	08-03-22 1:56	P210	08-03-22 10:37
P308(	26-03-22 19:40	P310	26-03-22 1:32
P508	01-05-22 4:44	P510	01-05-22 0:19
P111	12-02-22 1:11		
P211	03-03-22 5:02		
P311	25-03-22 1:27		
P511	01-05-22 4:55		

Table 5.19. April 21st, 2022 gradient values of each logger.

Loc. Id.	Defin.	Log. Id.	Thermal Gradient, 1 and 5 m (°C/m)	Thermal Gradient, 2 and 5 m (°C/m)	Thermal Gradient, 3 and 5 m (°C/m)	Data Source
1	KS-2	Log-2	0.5435	0.9511	0.7520	Sine Fit
2	KS-1	Log-5	-2.2009	-1.4726	-0.4641	Sine Fit
3	Benzinlik	Log-6	-4.4859	-3.1243	-1.4169	Sine Fit
4	Kule	Log-7	0.4118	0.5886	0.6944	Field Mea.
5	Tabela	Log-8	0.4135	0.7346	0.7223	Field Mea.
6	Yatık	Log-10	0.3597	0.5317	0.8783	Field Mea.
8	Dolmuş.	Log-11	0.4800	0.7794	0.9803	Field Mea.

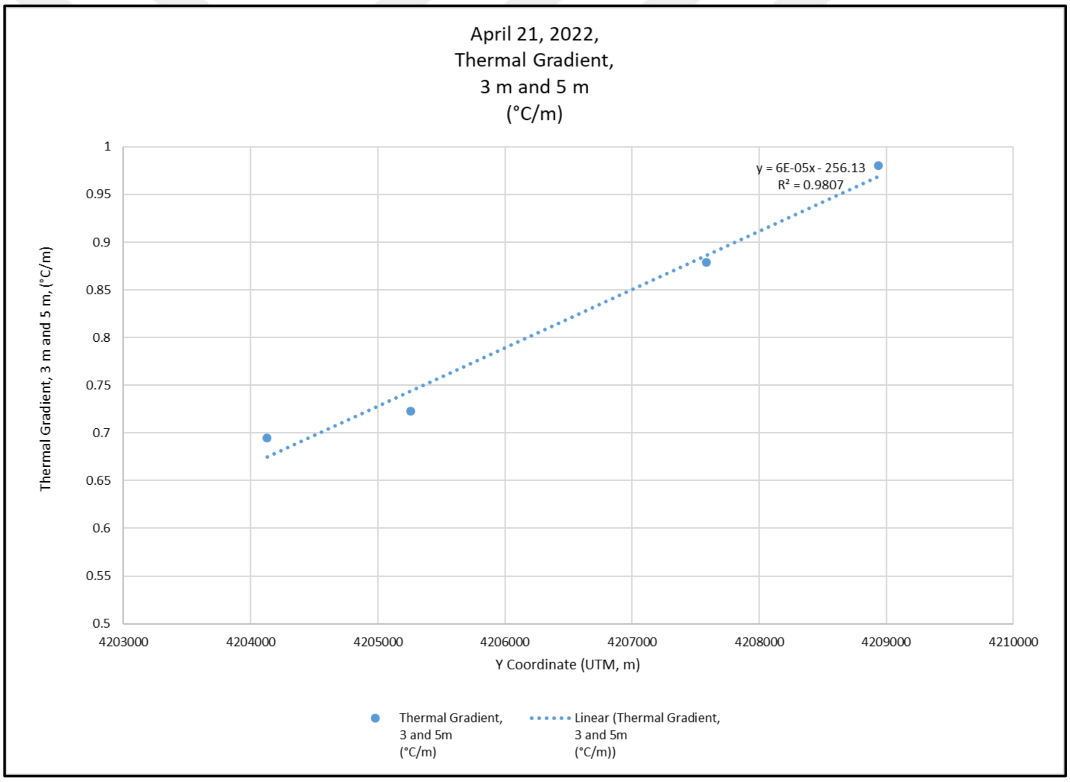

Figure 5.49. Linear regression fit between UTM Y Coordinate and Thermal Gradient at sensors on April 21st, 2022 for sensors between 3 m and 5 m.

5.5 Satellite Image Analysis

Satellite image analysis was performed in order to generate a temperature by utilizing day-night image pair for the study area. For this purpose, ASTER images were utilized where one image from day-time with the acquisition date of 16.04.2015 and two images from night-time with the acquisition date of 23.04.2015 were purchased. Details of ASTER images are presented in Table 5.20. ASTER data accessed courtesy of the NASA Land Processes Distributed Active Archive Center (LP DAAC), USGS/Earth Resources Observation and Science (EROS) Center, Sioux Falls, South Dakota.

Table 5.20. ASTER image information for images utilized in the analyses.

ASTER Id.	**Image Acquisition Date**	**Acquisition Time (Local Time - UTC+3)**
AST_L1T_00304162015085802_20150626082610_81821	16 April 2015	11:58:02
AST_L1T_00304232015200802_20150626150704_64389	23 April 2015	23:08:02
AST_L1T_00304232015200753_20150626150704_64366	23 April 2015	23:07:53

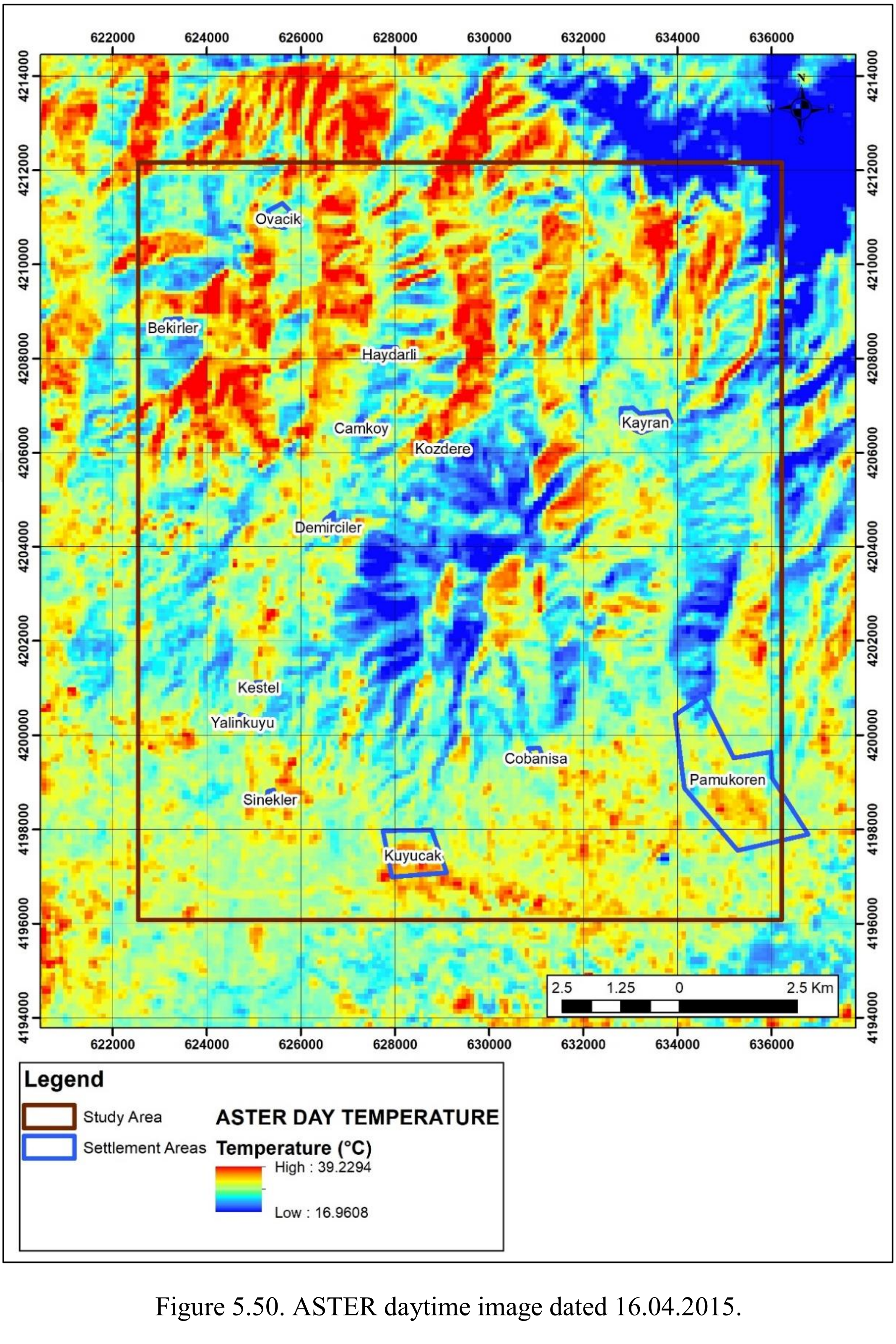

Figure 5.50. ASTER daytime image dated 16.04.2015.

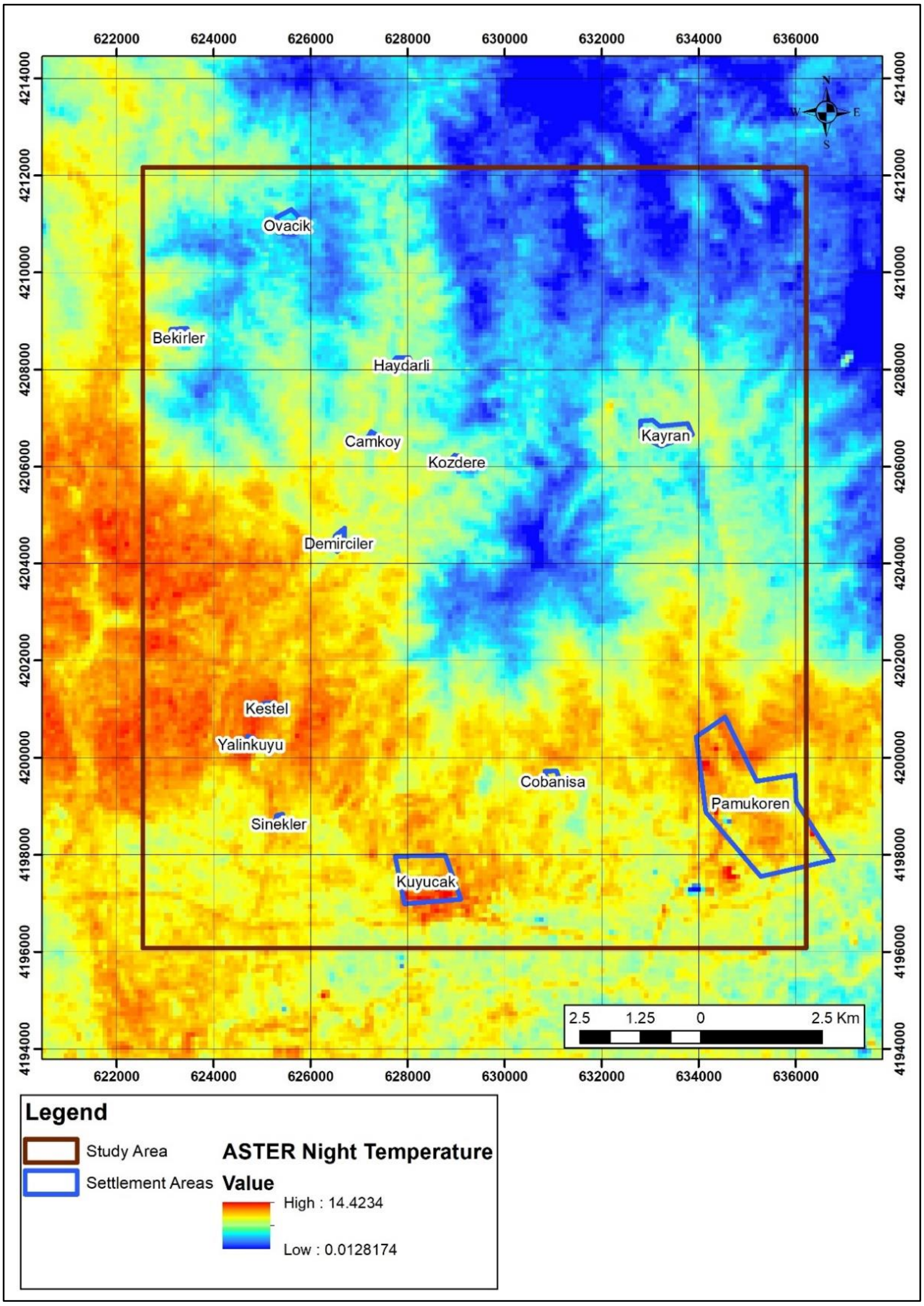

Figure 5.51. ASTER night-time image dated 23.04.2015.

Primarily, pre-processing steps were performed on the satellite images to prepare for further analysis. Following the pre-processing, methodology proposed by Coolbaugh et al. (2007a) was utilized in order to correct the images for non-geothermal effects such as topography, surface material (albedo) and diurnal effects, and final relative temperature map was generated. The following sections provide details of each processing step as listed below:

1. Conversion of ASTER L1T images from Digital Number (DN) to Radiance-at-sensor,
2. Conversion of day-time ASTER radiance image to reflectance,
3. Generation of Digital Elevation Model (DEM) from General Command of Mapping (GCM) 1:25,000 scale topographical maps,
4. Generation of Hill-Shade (Shaded Relief) images for day- and night-time ASTER images by utilizing sun elevation and sun azimuth angles according to image center coordinate information and relevant day and time information,
5. Generation of albedo image
6. Generation of pseudo heat energy image (Coolbaugh et al., 2007a) to compensate for solar irradiance
7. Thermal inertia correction by utilizing meteorological station data
8. Elevation correction (Gutierrez et al., 2012).

5.5.1 Pre-processing of ASTER Images

In order to generate surface temperature map of the study area, three ASTER satellite images, 1 day-time image and 2 consecutively acquired night-time image was utilized.

Primarily, digital number of L1T images were converted to Radiance-at-sensor data. The L1T images of ASTER sensor are Level 1 Precision Terrain Corrected Registered At-Sensor Radiance (AST_L1T) data that contains calibrated at-sensor radiance, which corresponds with the ASTER Level 1B (AST_L1B), that has been geometrically corrected, and rotated to a north-up UTM projection (NASA, 2015). The Digital Numbers (DNs) of each band of the images are converted to Radiance at-sensor (RaT) data by utilizing Eq. 1 and relevant gain coefficients as provided in Abrams, 2000. Metadata of each scene was checked to observe actual gain coefficients where all three scenes were observed to be High for B1 and B2, and Normal Gain for the remaining 7 VNIR and SWIR bands.

$$\text{Radiance} = (\text{DN value} - 1) \times \text{Unit conversion coefficient} \qquad \text{Eq. 1}$$

Table 5.21. Gain coefficients of ASTER bands (Abrams, 2000).

Band No.	Coefficient (W/(m2*sr*µm)/DN)			
	High Gain	Normal Gain	Low Gain 1	Low Gain 2
1	0.676	1.688	2.25	NA
2	0.708	1.415	1.89	
3N	0.423	0.862	1.15	
3B	0.423	0.862	1.15	
4	0.1087	0.2174	0.290	0.290
5	0.0348	0.0696	0.0925	0.409
6	0.0313	0.0625	0.0830	0.390
7	0.0299	0.0597	0.0795	0.332
8	0.0209	0.0417	0.0556	0.245
9	0.0159	0.0318	0.0424	0.265
10	NA	6.822×10^{-3}	NA	NA
11		6.780×10^{-3}		
12		6.590×10^{-3}		
13		5.693×10^{-3}		
14		5.225×10^{-3}		

Following conversion of data to radiance at-sensor, FLAASH module of ENVI Software was utilized to convert data into surface reflectance (Matthew et al., 2000). FLAASH module utilizes the MODTRAN4 radiation transfer code to accurately compensate for atmospheric effects and correct wavelengths in the visible through near-infrared and shortwave infrared regions, up to 2.5 µm to generate surface reflectance image.

5.5.2 Topographical Slope and Albedo Correction

Topographical slope correction was applied to the image in order to correct slope aspect and thus solar heating effects. In order to correct for topographic effects, methodology proposed by Coolbaugh et al. (2007a) was utilized based on Eq. 2:

$$R = K2\ (S * A) + b \qquad \text{Eq. 2}$$

where, R is reflection image acquired from ASTER b1, b2 and b3, S is shaded relief, A is albedo.

In ideal conditions, the coefficients K2 and b are 1 and 0, respectively. This is applicable if preprocessing had been successful in removing all atmospheric absorption and scattering effects, the constant "K" should be near 1 and the constant "b" should be near zero (Coolbaugh et al., 2007a). Since no field spectrometer measurements were taken as part of this study to compare pixel value of the reflectance image with the field data, this assumption was considered.

- Shaded relief generated from DEM from GCM 1/25.000 topographical map contours based on ASTER day-time acquisition date, time and image central coordinates to calculate sun azimuth and sun elevation angles (Figure 5.52).
- Reflection value is acquired from conversion by utilizing FLAASH module of ENVI software.
- Average albedo image generated by utilizing weighted average albedo was then computed for all 3 bands, using as weighting factors the wavelength-dependent solar irradiance (at the top of the atmosphere), atmospheric transmittance, and the band width (Figure 5.53.

Table 5.22. Weighing coefficients for albedo image for VNIR bands of ASTER day-time image.

ASTER Band	Exoatmospheric Solar Irradiance W*m2*/micrometer	% Atmospheric Transmission	Band Width	Relative Weight
b1	1,847	66.5	80	0.395886
b2	1,553	71.0	60	0.266489
b3	1,117	75.0	100	0.337626

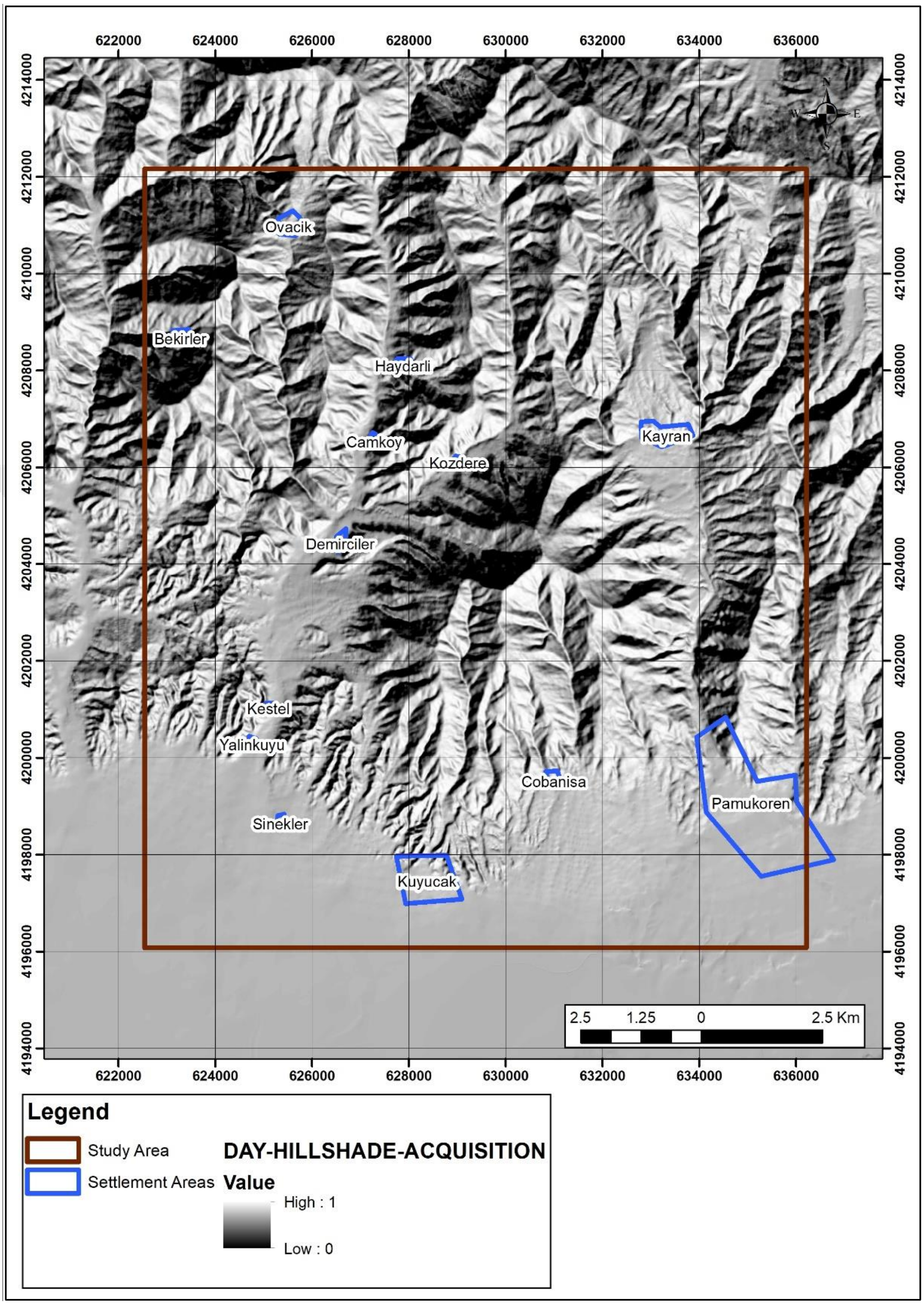

Figure 5.52. Shaded relief (hillshade) map of the study area at the date and time of ASTER day-time image acquisition on 16.04.2015.

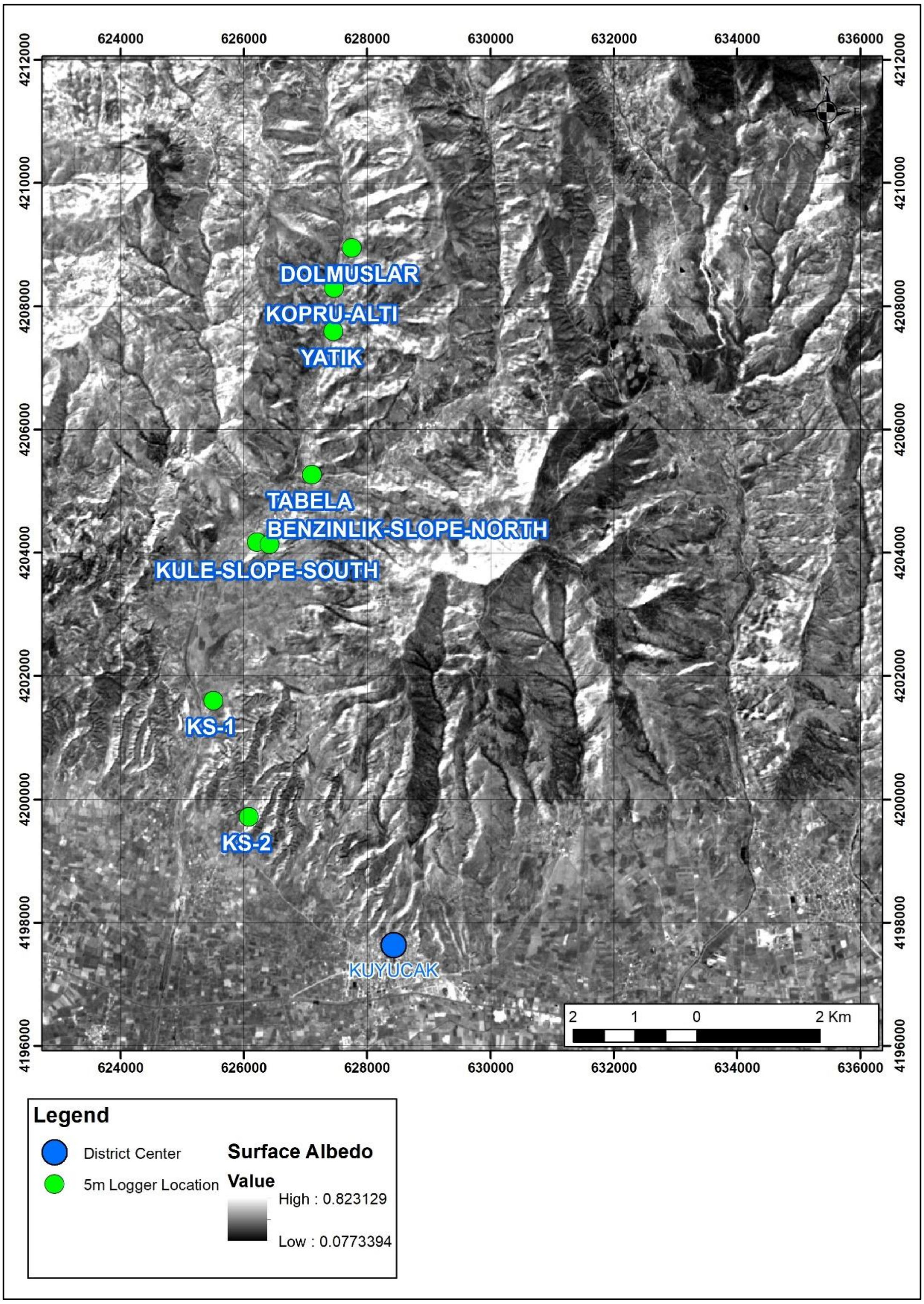

Figure 5.53. Surface albedo map generated from day-time ASTER image.

5.5.3 Heat Energy Correction

In order to identify heat energy absorbed by the surface and extract this from day-time and night-time images individually, Eq. 3 proposed by Coolbaugh et al. (2007a) was utilized.

$$Eq = S_0(1 - A)\sum_t [M(Z)t\ cosZ'tDt]\Delta t_t \qquad \text{Eq. 3}$$

where, Eq is the solar heat energy absorbed per unit area over the course of a day; So is Solar Constant; A is Albedo, Z is Zenith Angle, M(Z) is atmospheric transmission as a function of the zenith angle Z (from Allen, 1963 approximation) according to Eq. 4:

$$M(Z) = 1 - 0.2\sqrt{secZ} \qquad \text{Eq. 4}$$

Also, cosZ' is the cosine of the angle between the surface normal and the sun's rays (shaded relief map), Δt is the time interval, "Dt" is a time "decay factor" which is calculated for each one-hour time step by Eq. 5 as follows:

$$D(t) = 1/t-t_a + 0.9615) - 0.0401 \qquad \text{Eq. 5}$$

Heat energy image was generated for day-time and night-time images and extracted from surface temperature images individually. An iterative approach proposed by Coolbaugh et al. (2007a) was followed where the minimum variance value was identified by extracting heat energy image from day- and night-time images with varying coefficients. The change in image variance values and coefficients is presented in Figure 5.57. Coefficient values were identified as 5.5 for day-time image and 6.5 for night-time image.

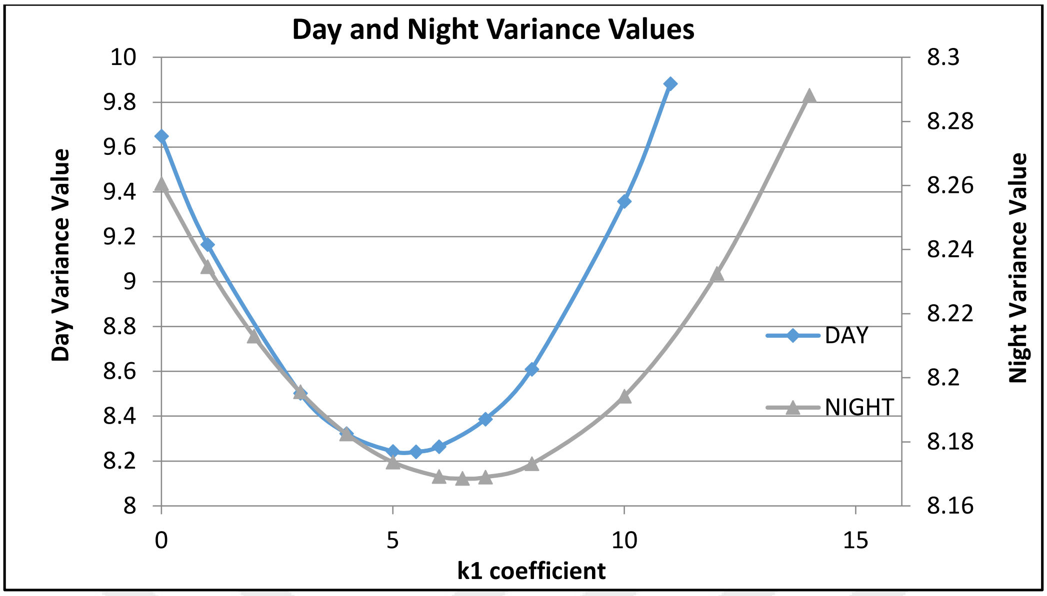

Figure 5.54. Variance values of day-time and night-time images.

5.5.4 Thermal Inertia Correction

In order to correct for diurnal effects of thermal inertia, day- and night-time images corrected for heat energy was combined according to temperature variation in comparison to the meteorological station data covering the image extent (Figure 5.55). For this purpose, the average of the 24 temperature measurements of the meteorological stations were correlated with the day and night-time ASTER image temperatures with different weighting factors to identify which weighing factor resulted in the minimum error of the combined image. In other words, temperatures at noon and 11 pm (the ASTER flyover times) were combined using different weighting factors, to see which combination predicted the actual 24-hour mean temperatures with the least error (Coolbaugh et al., 2007a). A weighting factor of 0.63 (night) and 0.37 (day) was acquired (Figure 5.55).

Following all these corrections, relative temperature map of the study area was generated as shown in Figure 5.56.

Table 5.23. Temperature comparison of ASTER image data and meteorological station data (units are in °C).

Station ID	17850	17860	18428	18429	18430	18441	18447	18596	18599
Station Name	**SULTAN-HISAR**	**NAZILLI**	**KOSK**	**KUYU-CAK**	**AYDIN/ YENI-PAZAR**	**BEYDAG**	**KIRAZ**	**KUYUCAK -2**	**ODE-MIS**
AVER DAY - April 16 – Meteorology Station Day Average	13.93	14.38	13.98	13.57	13.94	13.44	13.45	8.63	12.39
AVER NIGHT - April 23 – Meteorology Station Day Average	11.03	10.76	11.38	9.68	10.20	8.10	8.56	3.39	4.11
ASTER - Day Image Temperature Vaule	21.28	21.05	19.22	18.60	17.50	17.11	19.10	15.56	18.17
ASTER Night Image Temperature Vaule	10.11	7.33	7.52	7.43	8.52	5.98	5.35	1.59	2.79
ASTER-Combined According to Weight Coefficients	14.25	12.41	11.85	11.56	11.84	10.10	10.44	6.76	8.48
DIFFERENCE FROM 24 HR – Day	0.32	-1.97	-2.13	-2.01	-2.10	-3.34	-3.01	-1.87	-3.91
DIFFERENCE FROM 24 HR - Night	3.22	1.65	0.47	1.88	1.64	2.00	1.88	3.37	4.37

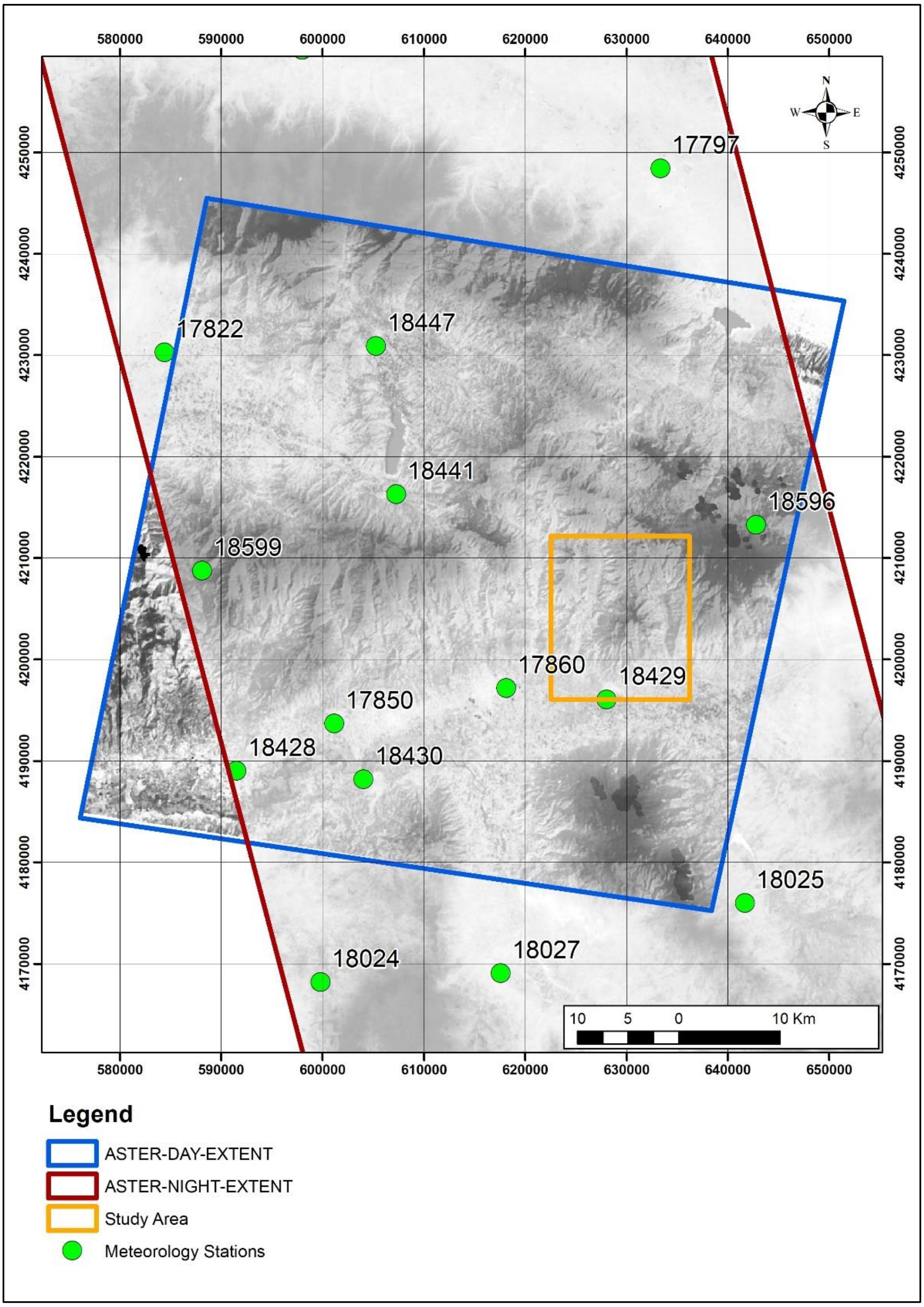

580000
590000
600000
610000
620000
630000
640000
650000
4250000
4240000
4230000
4220000
4210000
4200000
4190000
4180000
4170000
N
W
E
S
17797
17822
18447
18441
18596
18599
17860
18429
17850
18428
18430
18025
18024
18027
10 5 0 10 Km
Legend
ASTER-DAY-EXTENT
ASTER-NIGHT-EXTENT
Study Area
Meteorology Stations

Figure 5.55. Distribution of meteorology stations and ASTER day-, night-time image coverage.

Table 5.24. Day-night image combination coefficients.

Variable	Day-Time Image	Night-Time Image
Average Difference between Station Data and Combined Image	-2.23	2.27
Coefficients	0.37	0.63

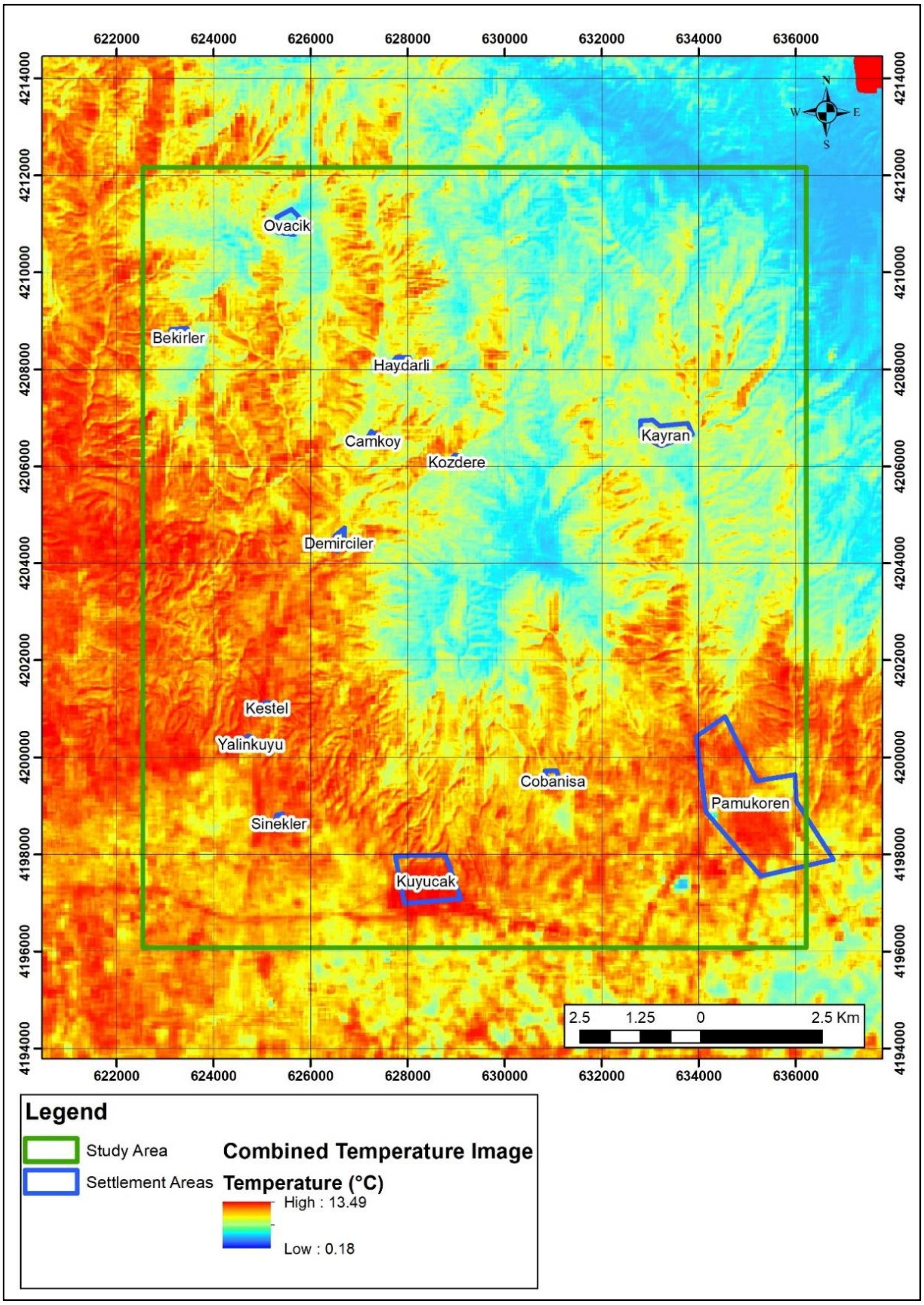

Figure 5.56. Corrected relative temperature map of the study area.

5.5.5 Elevation Correction

In order to correct for the environmental lapse rate difference, in other words, decrease of temperature with the elevation, night time temperature image was compared with the DEM (Figure 5.57) (Gutierrez et al., 2012). It can be seen that the temperature decrease is 5.69°C /km. Accordingly, the combined temperature image was corrected for elevation according to Eq. 6 given below:

$$(b1) + 0.00569415 \times (b2) \qquad \text{Eq. 6}$$

where b1 is the combined temperature image and b2 is the DEM.

Final image is presented in Figure 5.58. It can be seen from this figure that the surface temperature increases from south to north.

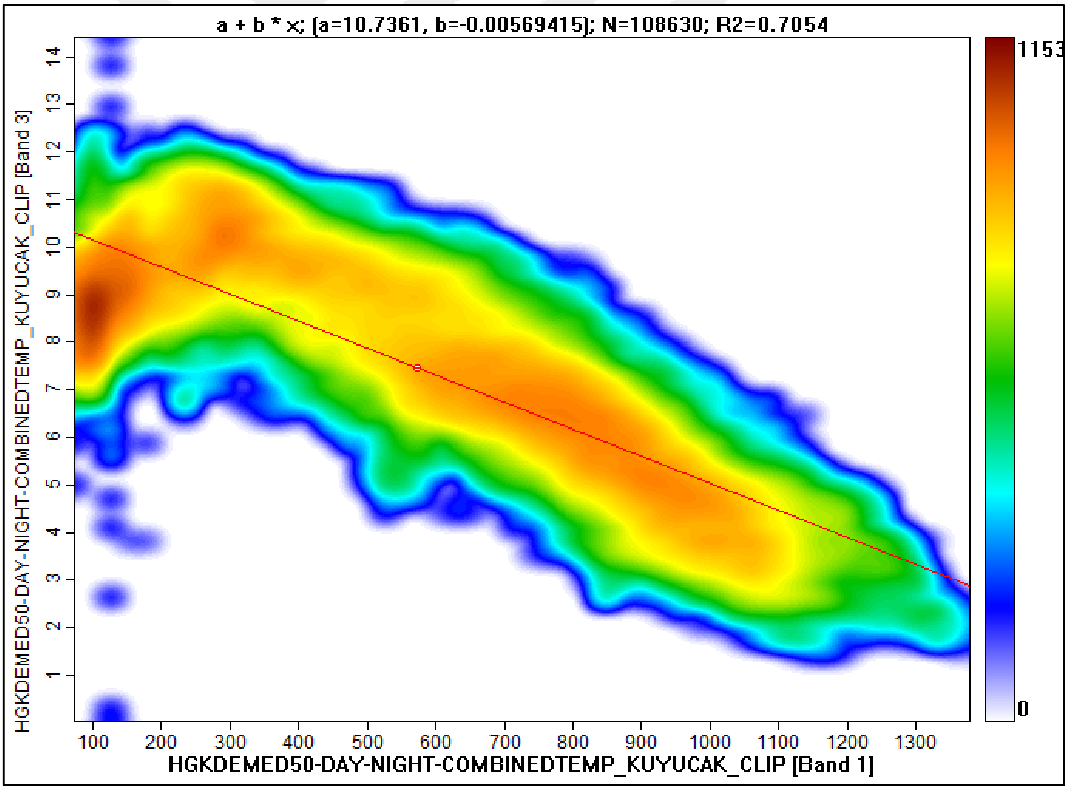

Figure 5.57. Scatter-plot of night-time ASTER surface temperature vs. elevation (DEM).

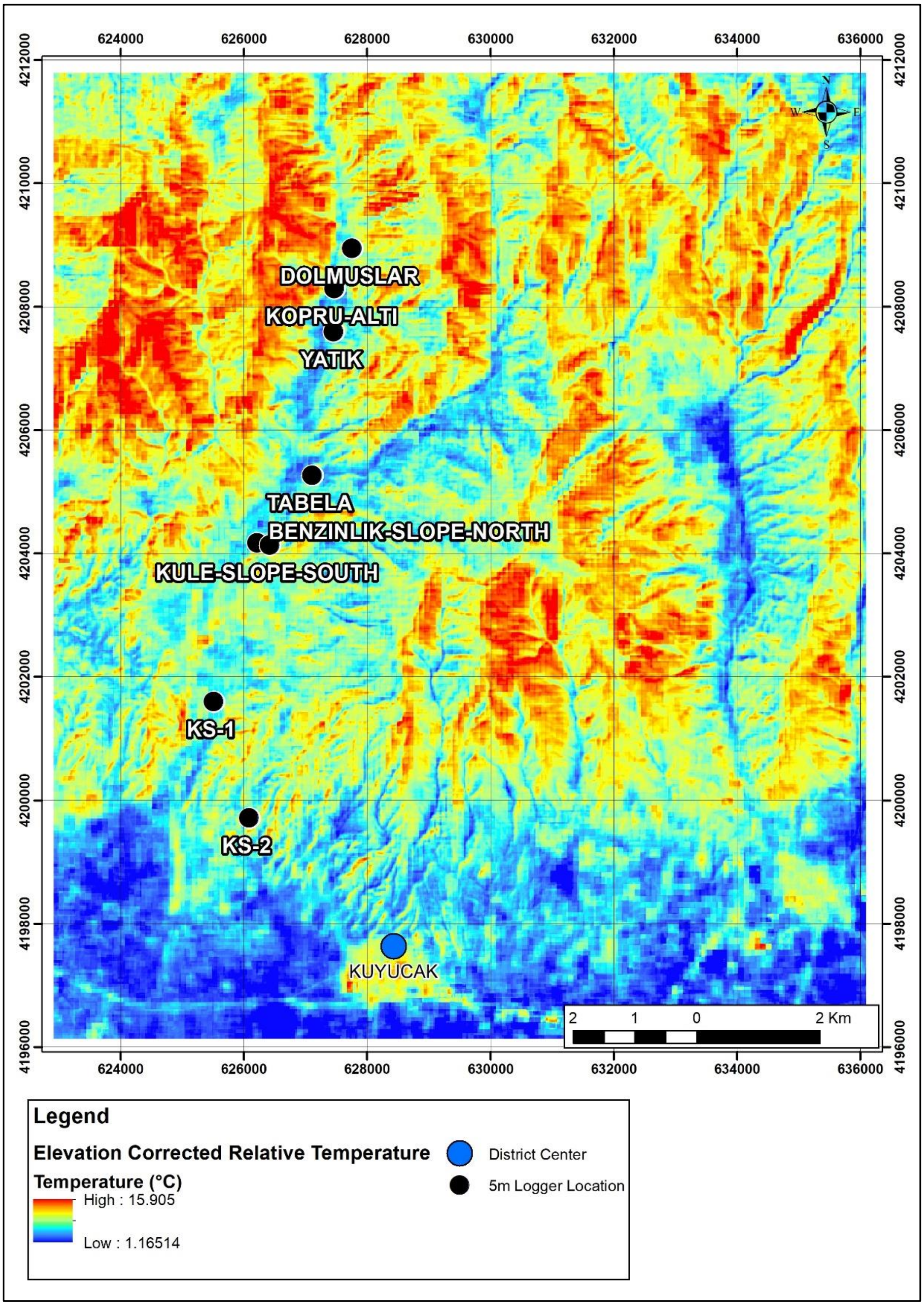

Figure 5.58. Elevation corrected surface temperature image.

5.6 Results of the Satellite Based Temperature Mapping

In order to check the result of the surface temperature image, the final image was compared with two different layers. Since it is known that the geothermal system in Büyük Menderes Graben is a fracture and fault controlled system where younger normal faults that cross-cut the main graben fault (detachment fault) transfer the geothermal fluid to the highly fractured metamorphic marble and limestone units of the Büyük Menderes Graben. Therefore, it is considered that the main controlling factor within the study area is lineament density. Secondarily, based on the results of the geophysical 3D magnetotellouric studies performed by Yal et al. (2017), the reservoir within the extent of the study area is shallowed from south to north.

Consequently, the final surface temperature map was compared with lineament density and south-to-north index map. The south to north index map was generated by considering value of each line of the image beginning from the southern edge of the study area and indicates a constant increase towards north.

Linear regression resultant density scatter plot for the comparison are generated for lineament density and south-to-north index map versus final surface temperature map as shown in Figure 5.61 and Figure 5.62, respectively.

It can be seen that the coefficient of determination R^2 for the lineament density map against surface temperature map is 0.4086 whereas the R^2 for the south-to-north index versus surface temperature map is 0.3108. According to the results of multivariable regression where final temperature map is the dependent variable, and lineament density and south-to-north index are independent variables, the coefficient of determination R^2 is found as 0.448.

Furthermore, robust multivariate linear regression via "robustfit" function of Matlab software was run and the coefficient of determination R^2 was found as 0.44815. The limited increase in R^2 shows that the outliers in the data is limited and thus results do not improve significantly.

Finally, in order to check the impact of vegetation on the temperature image, NDVI image was generated from NIR and R bands of the day-time ASTER image by utilizing Eq. 7 given below:

$$NDVI = (NIR–R)/(NIR+R) \qquad \text{Eq. 7}$$

The resultant image and histogram is given in Figure 5.60 and Figure 5.59, respectively, and statistics of the layer is given in Table 5.25 below.

In the NDVI image, the brighter colors indicate denser and healthier vegetation.

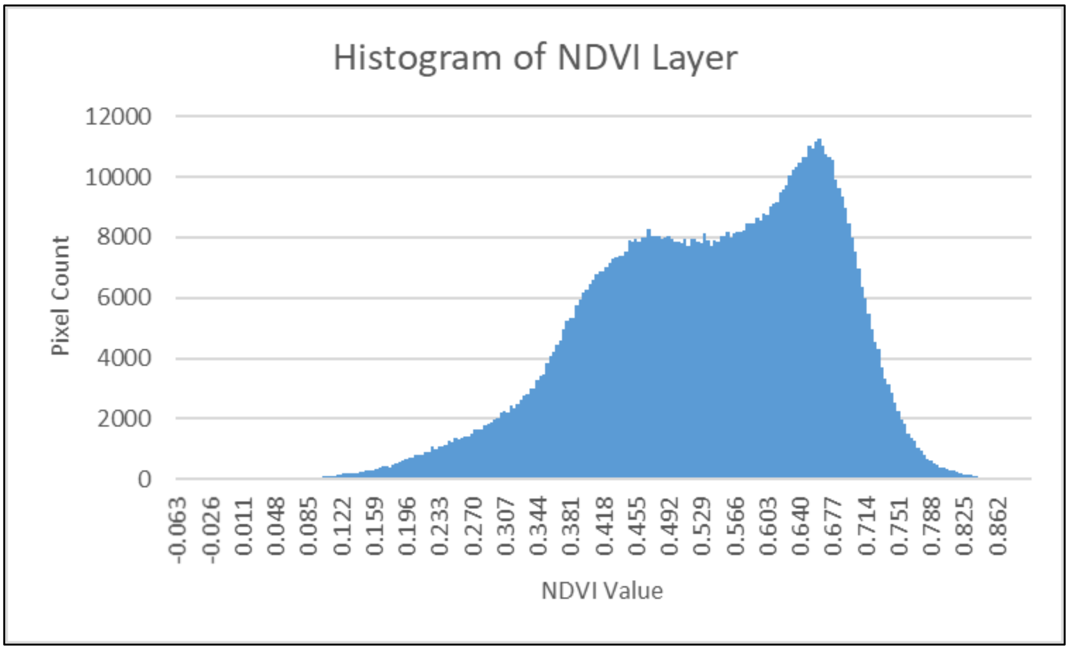

Figure 5.59. Histogram of the NDVI layer.

Table 5.25. Descriptive statistics of the NDVI layer.

Min	Max	Mean	St.dev.	Pixel Count
-0.06346	0.880419	0.53932	0.132518	912242

According to descriptive statistics of the NDVI layer, three separate mask layers were generated by utilizing threshold values of 0.406802, 0.53932 and 0.671838, by considering mean and ± one σ (standard deviation).

Following masking the final surface temperature, and lineament density and south-to-north index map, regression analyses were repeated. Results of these analyses are presented in Table 5.26 below.

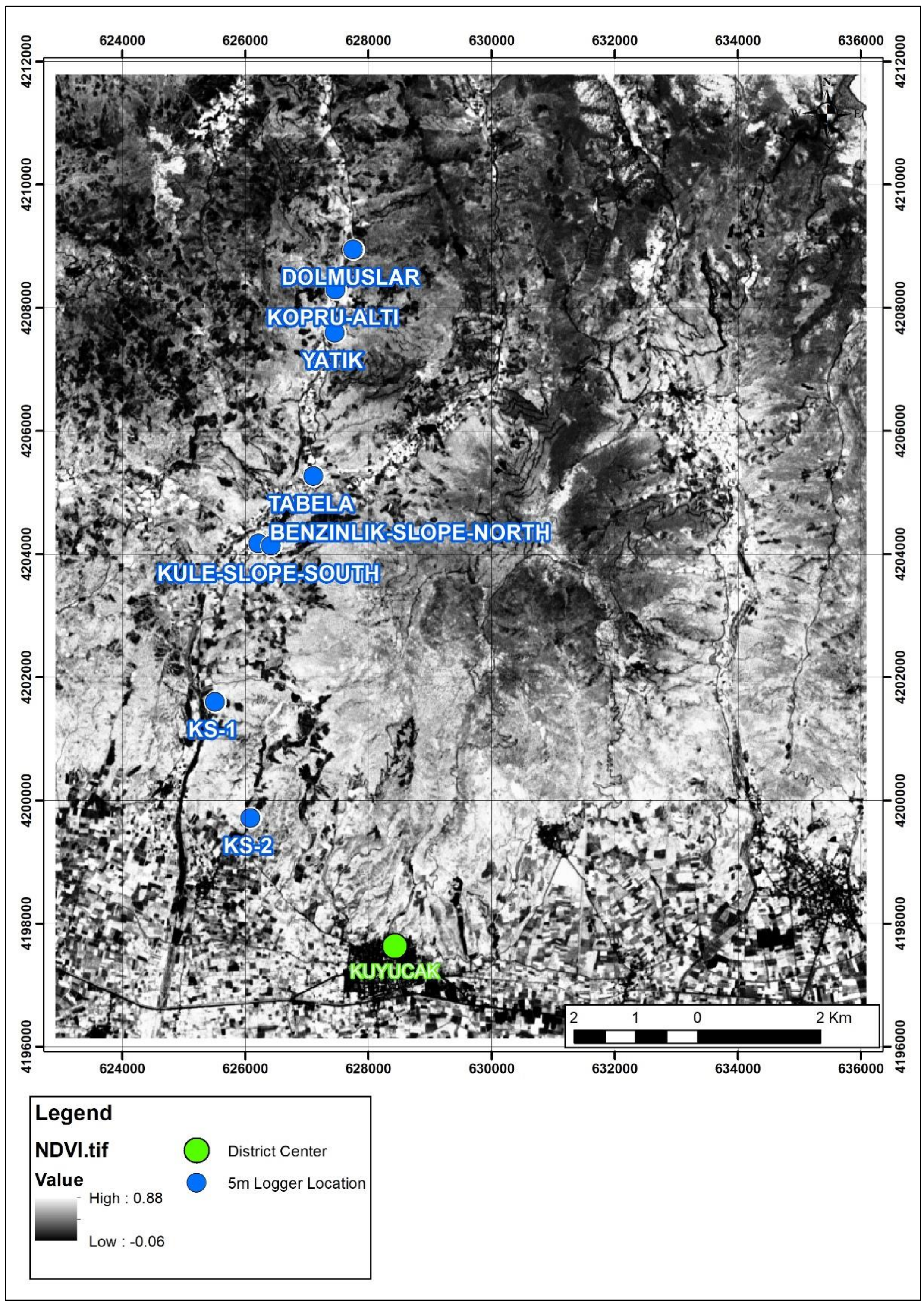

Figure 5.60. NDVI image of the study area.

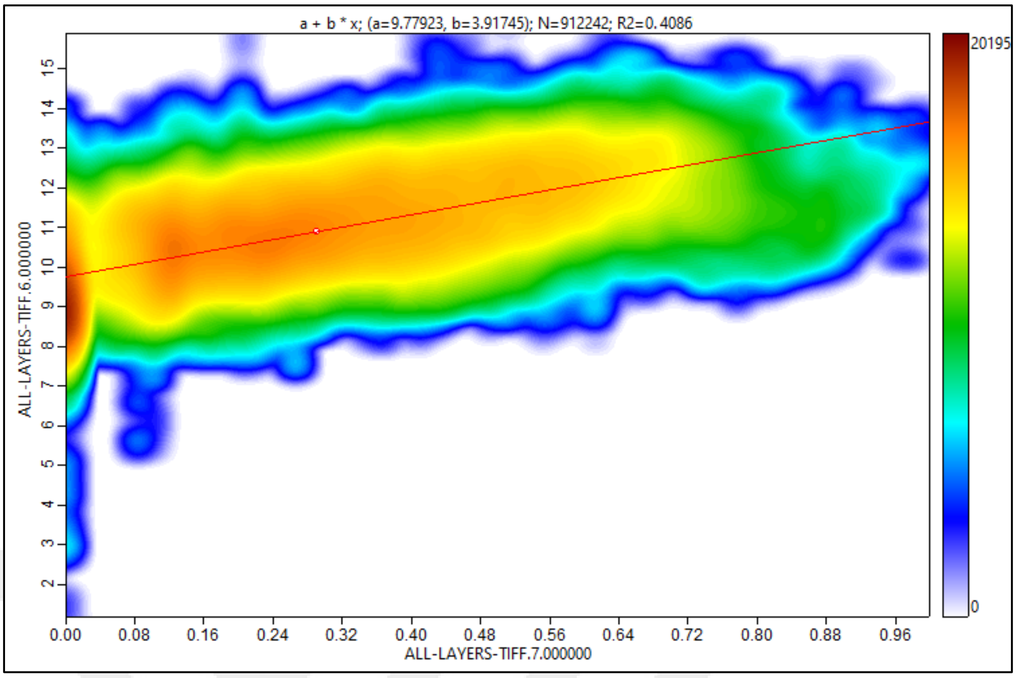

Figure 5.61. Scatterplot of final surface temperature image versus lineament density map.

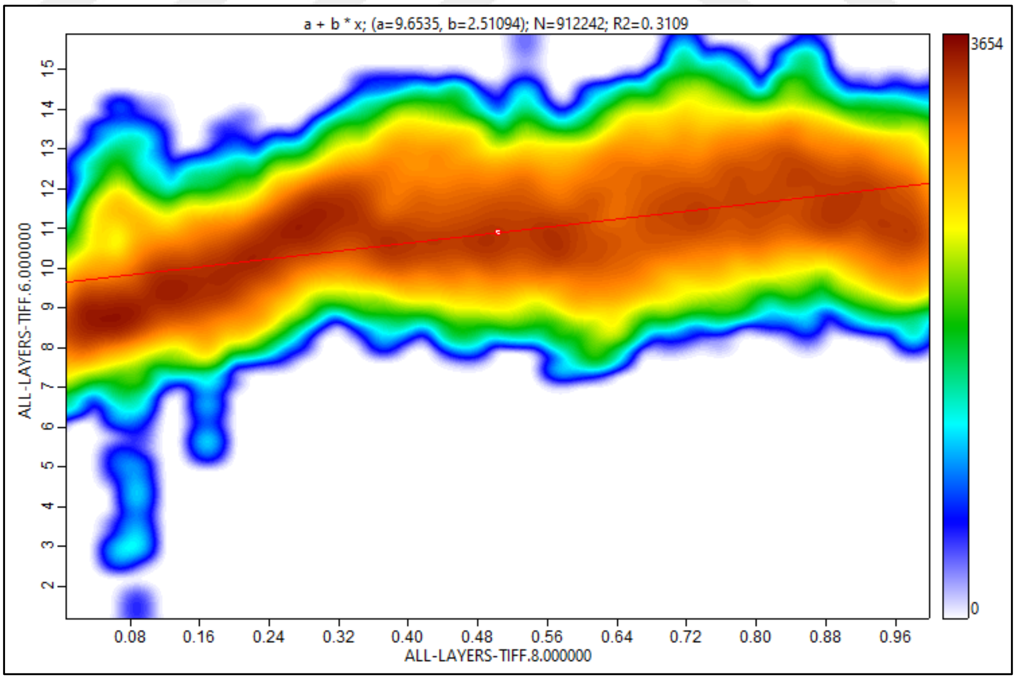

Figure 5.62. Scatterplot of final surface temperature image versus south-to-north index map.

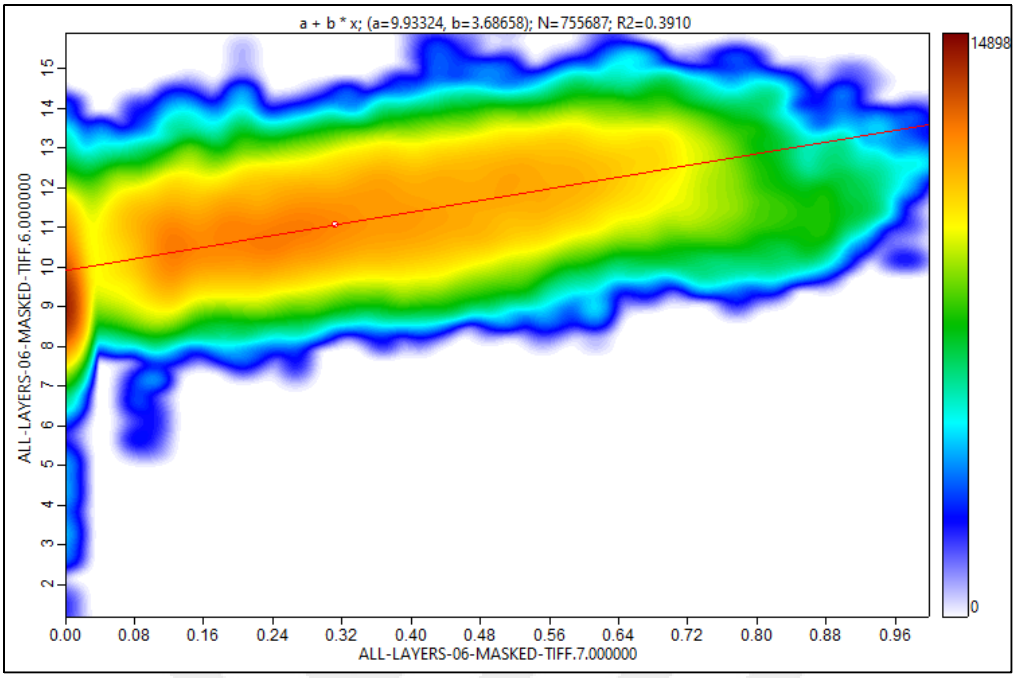

Figure 5.63. Scatterplot of final surface temperature image versus lineament density map with 0.671838 NDVI threshold value.

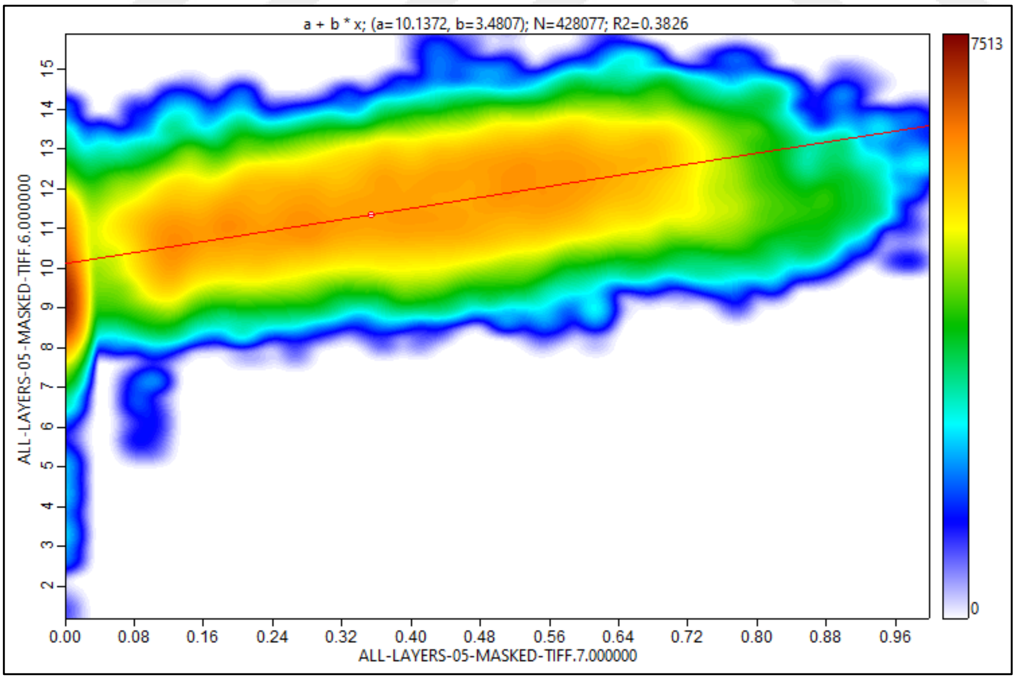

Figure 5.64. Scatterplot of final surface temperature image versus lineament density map with 0.53932 NDVI threshold value.

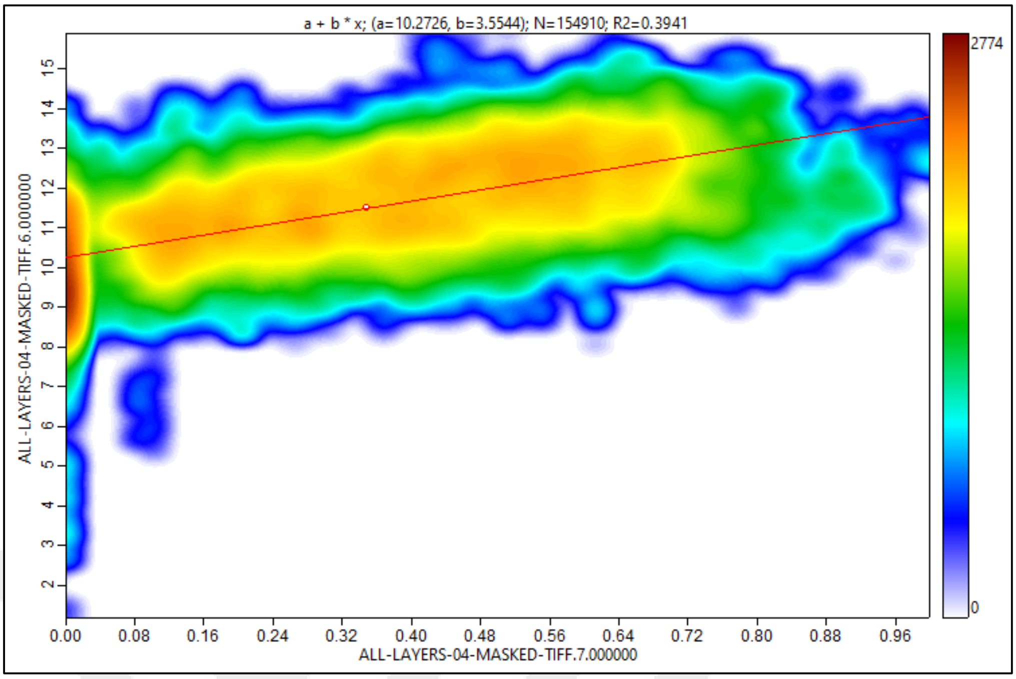

Figure 5.65. Scatterplot of final surface temperature image versus lineament density map with 0. 0.406802 NDVI threshold value.

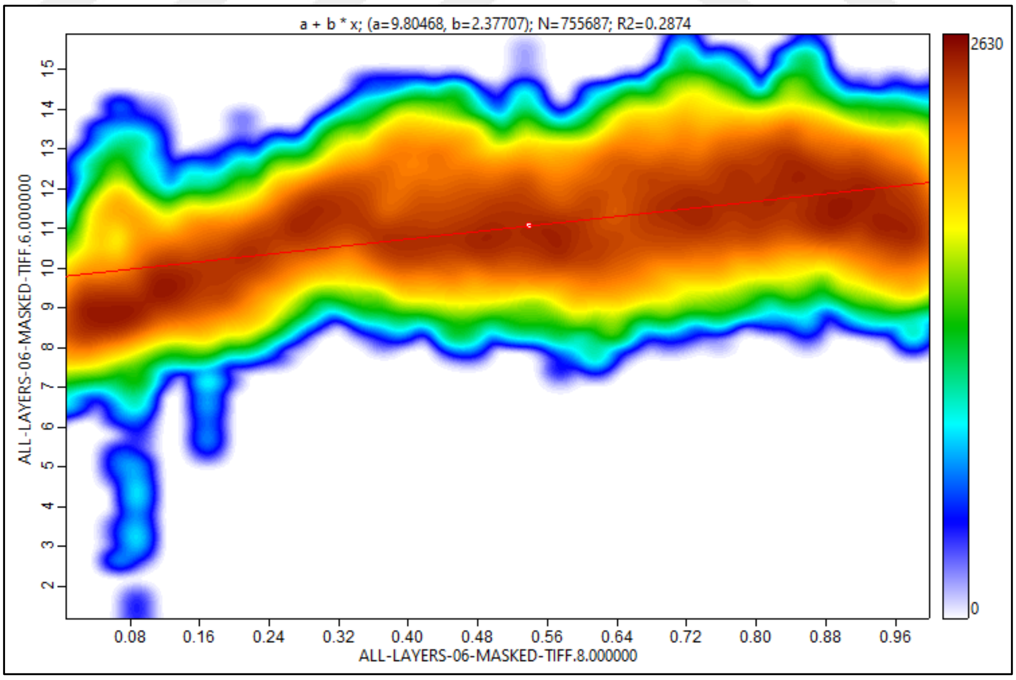

Figure 5.66. Scatterplot of final surface temperature image versus south-to-north index with 0.671838 NDVI threshold value.

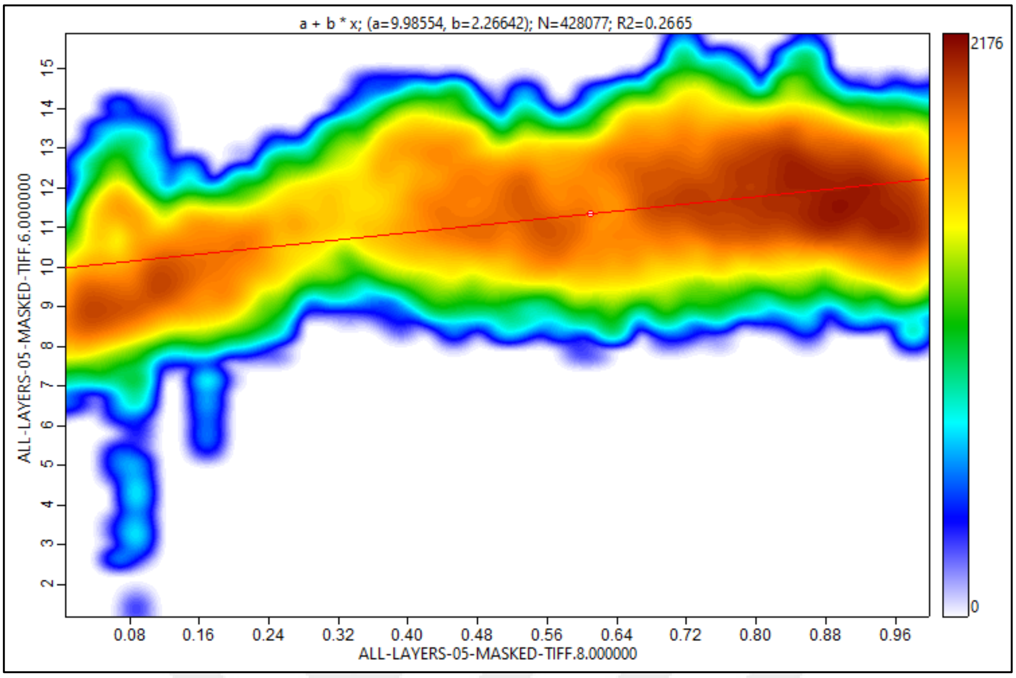

Figure 5.67. Scatterplot of final surface temperature image versus south-to-north index with 0.53932 NDVI threshold value.

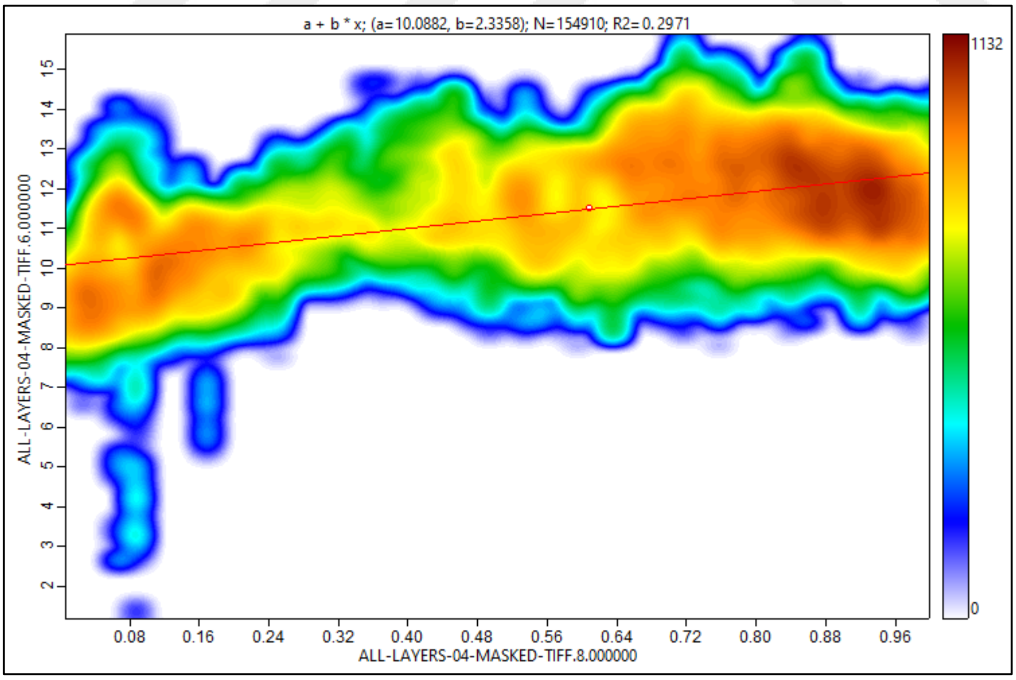

Figure 5.68. Scatterplot of final surface temperature image versus south-to-north index with 0.406802 NDVI threshold value.

Table 5.26. Coefficients of determination for the main and masked images.

NDVI Threshold Value	Final Temperature vs. Lineament Density Map	Final Temperature vs. South-to-North Index	Pixel Count
No Threshold	0.4086	0.3109	912242
0.671838	0.3910	0.2874	755687
0.539320	0.3826	0.2665	428077
0.406802	0.3941	0.2971	154910

As can be seen from the above table, after applying 0.406802 NDVI threshold on the image, the remaining pixels are 17% of the initial image. Therefore, no further threshold mask was applied on the image. Furthermore, it can also be seen that the R^2 does not improve better than the initial image with decreasing vegetated pixels.

Furthermore, a regression analyses was performed between NDVI (i.e., vegetation) and final surface temperature map. The resultant coefficient of determination R^2 of 0.0103 clearly shows that there is no relation with the vegetation and surface temperature.

5.7 Results and Conclusion on Shallow Temperature Mapping

As part of shallow temperature mapping, ASTER satellite images were assessed and corrected following the methodology proposed by Coolbaugh et al. (2007a) and Gutierrez et al. (2012). Furthermore, in order to provide a ground truth and alternative data to assess the geothermal anomalies of the study area, long term temperature data loggers with four different sensors having 1 m, 2 m, 3 m and 5 m was designed and deployed to the study area at eight different locations with a south to north distribution by considering accessibility, different surface materials, slope aspect and depth to reservoir conditions.

It is known that solar radiation is the primary natural source of energy of the earth and other sources such as the geothermal heat flux generated by the earth interior, natural terrestrial radioactivity, and cosmic radiation, are all negligible relative to solar radiation (Wald, 2018). This is also apparent when daily average direct normal irradiation values for the study area and its vicinity are to be considered according to Global Solar Atlas V2 (ESMAP, 2019), which ranges between 3.88 and 5.37 kWh/m2, corresponding to 596.92 and 826.15 W/m2 solar irradiance by considering 6.5 average daily direct sunshine (State Meteorology Works, 2024). [Data/information/map] obtained from the "Global Solar Atlas 2.0, a free, web-based application developed and operated by the company Solargis s.r.o. on behalf of the World Bank Group, utilizing Solargis data, with funding provided by the Energy Sector Management Assistance Program (ESMAP). Whereas, terrestrial surface heat flow in western Turkey varies from ~50 to 140 mW/m^2, with values exceeding ~100 mW/m^2 in most areas (Tezcan, 1995) and average value of approximately 109mW/m^2 (Serpen, 2009). The solar irradiation and geothermal heat flux values clearly shows the importance of corrections, especially heat energy correction performed on the satellite images. However, regardless of the corrections performed on the images, as previously mentioned, due to climatic and groundwater conditions in the study area, the results of the satellite image based geothermal anomaly detection was not compatible with the expected increasing temperatures from south to north of the study area in connection with the decrease in the depth to reservoir in this direction (Yal et al., 2017) or lineament density map, which is considered to be one of the primary indicators in the fault and fracture controlled geothermal system in Western Anatolia (Faulds et al., 2010; Moeck, 2014; Koçyiğit, 2015). The R^2 coefficient of determination value through multivariable regression was found as 0.448.

In order to assess the impact of surface vegetation on the anomaly detection, the final corrected image was masked by utilizing three threshold values to the NDVI image. However, no improvement was observed in the coefficient of determination value even when the highest vegetation masking was applied to the image with only 17% of the total pixels remaining after the masking operation. Therefore, it was concluded that vegetation does not have impact on the geothermal anomaly detection in the study area.

On the other hand, the data acquired from temperature data loggers deployed to the study area have provided valuable information. Apart from logger 5 deployed at KS-1 well location having known shallow groundwater at 150 m depth and data logger 6 with limited data collection duration (66 days) deployed at Benzinlik location having hard soil-weathered rock conditions, both of which presented inverse thermal gradient, the remaining loggers have recorded important thermal gradient between the 3 m and 5 m temperature sensors. Loggers 7, 8, 10 and 11 have shown increasing thermal gradient from south to north, which was the main expectation since geothermal reservoir depth is known to decrease towards north of the study area (Yal et al., 2017). The Y-coordinate versus geothermal gradient comparison have also presented R^2 coefficient of determination value of 0.9807. Finally, logger 2 located at KS-2 well location have shown positive thermal gradient, consistent with the known geothermal reservoir at depth at this location.

In conclusion, although satellite based geothermal anomaly mapping yielded inconclusive results possibly due to shallow groundwater presence in the area, the data collected from the field have presented compatible results with the decreasing depth to reservoir towards the north of the study area.

CHAPTER 6

GIS BASED MULTI CRITERIA DECISION ANALYSIS

In order to combine all the results from alteration mineral mapping, lineament mapping and temperature mapping generated as part of this study and to compare the resultant map with the a-priori knowledge of the study area, Geographical Information Systems (GIS) based Multi Criteria Decision Analysis (MCDA) was performed. For this purpose, four alteration mineral maps, lineament density and geothermal anomaly temperature map previously generated as part of this study as well as distance to cover units map generated based on 1/25.000 scale geological map of the study area (MTA, 2012) were selected as input layers in Technique for Order Preference by Similarity to Ideal Solution (TOPSIS) MCDA method. The methodology followed for the analysis is presented in Section 6.2 below and a summary flow chart of the processing steps is given in Figure 6.1.

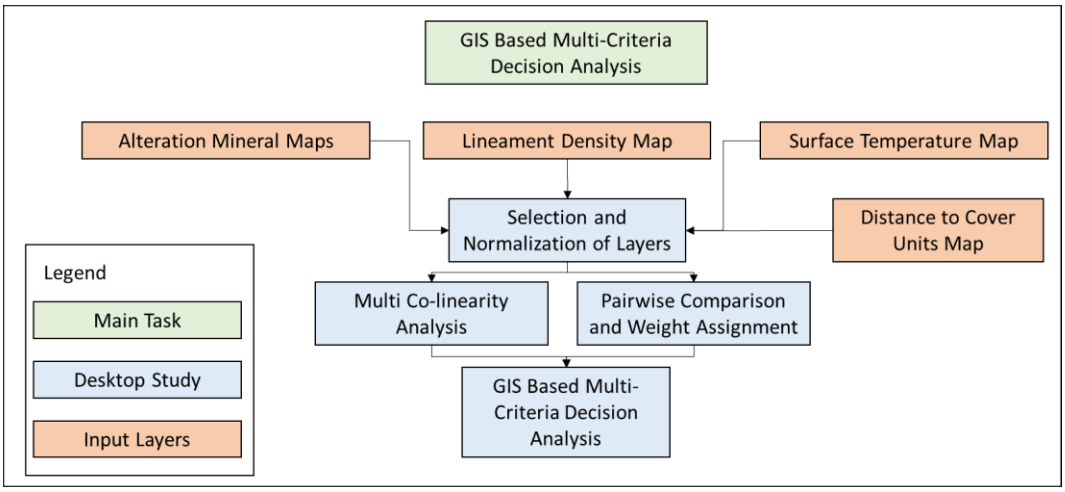

Figure 6.1. Flow chart for the GIS based MCDA studies.

6.1 Literature Review

After the initial reconnaissance phase of a geothermal project, a more detailed exploration stage is typically conducted and geothermal favorability maps are generated before selecting well sites due to high drilling costs.

As summarized by Cambazoğlu et al. (2019); Geographic Information Systems (GIS) have proven invaluable for analyzing spatial correlations among various data types (such as geological and geophysical data) collected during preliminary exploration, helping to pinpoint potential resource zones (Bonham-Carter et al., 1988; Chung et al., 1992). Additionally, Multi-Criteria Decision Analysis (MCDA) methods, used in conjunction with GIS, enhance decision-making by integrating geographical data with decision-maker preferences through specific decision rules (Malczewski, 1999). GIS-based MCDA has been widely adopted for geothermal prospectivity mapping, with methods categorized into deterministic (knowledge-driven) and data-driven approaches (Bonham-Carter, 1994).

Data-driven methods use known resource occurrences as training sites to relate to evidence layers and predict resources. Examples include the weight-of-evidence method (Bonham-Carter et al., 1988; Coolbaugh et al., 2003; Coolbaugh and Bedell, 2006; Coolbaugh et al., 2007b; Tufekci et al., 2010; Moghaddam et al., 2014), the Evidential Belief Function method (Carranza et al., 2008; Moghaddam et al., 2013), and Certainty Factor models (Li and Zhang, 2017).

Knowledge-driven methods rely on expert judgment to determine the relative importance of criteria. Examples include Index Overlay (Prol-Ledesma, 2000; Noorollahi et al., 2008), Weighted Linear Combination (Noorollahi et al., 2007; Yalcin and Kilic Gul, 2017; Kiavarz and Jelokhani-Niaraki, 2017), Fuzzy Scheme models (Prol-Ledesma, 2000), and Boolean logic (Yousefi et al., 2007; Noorollahi et al., 2008; Yousefi et al., 2010). For instance, Noorollahi et al. (2008) used Boolean and Index Overlay methods based on exploration and environmental suitability data to find optimal geothermal exploration areas. Yousefi et al. (2010) applied Boolean logic to geological, geochemical, and geophysical data layers to identify geothermal potential areas. Kiavarz and Jelokhani-Niaraki (2017) created geothermal prospectivity maps using Ordered Weight Averaging Method with various criteria. Prol-Ledesma (2000) compared Boolean, Fuzzy Scheme, and Index Overlay methods, finding that Boolean and Low-Risk models were more restrictive and suited for well site selection, while Index Overlay and High-Risk models were better for detailed exploration planning.

Recently, the play fairway analysis method, borrowed from the petroleum industry, has been adopted by the geothermal community (Shervais et al., 2015; Ito et al., 2017; Siler et al., 2017; Faulds et al., 2018; Olvera-Garcia et al., 2023; Shervais et al., 2024). This method systematically identifies prospective geothermal exploration areas through a quantitative risk-based decision process. Ito et al. (2017) proposed a new knowledge-driven approach using Bayesian statistics to predict relative probabilities rather than just resource favorability.

In this study, a knowledge driven ideal point methodology, namely, the Technique for Order Preference by Similarity to Ideal Solution (TOPSIS) (Jankowski and Ewart, 1996; Malczewski, 1996; Chen et al., 2001) has been employed in order to produce a geothermal favorability map of the study area. The study performed herein represents the first application of the TOPSIS to geothermal favorability mapping to the knowledge of the authors. The TOPSIS methodology has been implemented in many areas such as landfill site selection (Yal and Akgün, 2013, 2014), environmental assessment (Liu et al., 2006), and mineral mapping (Pazanda et al., 2012; Abedi and Norouzi, 2016). The TOPSIS method, first introduced by Hwang and Yoon (1981), is based on selecting the best alternative with the shortest Euclidean distance from the ideal solution and farthest from the negative ideal solution (Malczewski and Rinner, 2015). The alternative with the highest closeness measure is selected (Zanakis et al., 1998). Some advantages of the TOPSIS methodology are its good computational efficiency and its ability to account for both the best and worst alternatives in a simple mathematical form (Hung and Chen, 2009). Also, ideal point methods do not assume preference independence of attributes (Zeleny, 1982; Pereira and Duckstein, 1993; Prato, 2008), thus allowing them to be particularly preferable in spatial decision processes where complex interdependencies among attributes are involved (Malczewski, 1999).

GIS based TOPSIS method was previously used in assessment of geothermal favorability by Cambazoğlu et al. (2019) and Yal et al. (2021) where TOPSIS method was utilized to assess geothermal favorability of Gediz and Büyük Menderes Grabens in Türkiye, respectively. Zhang et al. (2024) utilized TOPSIS method to assess geothermal resources in Eryuan County, China. Li et al. (2022) utilized entropy weight and TOPSIS methods to assess suitability of shallow geothermal energy implementation in Nantong, China.

6.2 Methodology

The Technique for Order Preference by Similarity to the Ideal Solution (TOPSIS) methodology was performed to generate the favorability map by using a number of datasets. The datasets and the criteria constructed from these datasets are given in Table 6.2. Each dataset was used to generate a criteria map and was further weighted according to its relative importance. For criteria weighting, the pairwise comparison method was used and a weight value was assigned to each criterion. For the layers, only outputs generated as part of this study, except distance to cover rock units, were considered. The data sources utilized in TOPSIS analysis are presented in Table 6.1 below.

In addition, a multi co-linearity analysis was performed on each variable data set to avoid any major interdependency. In the multi colinearity analysis, the tolerance is the percent of the variance in a given variable that cannot be explained by other variables and tolerance values close to 0 indicate high multi co-linearity and inflated regression coefficients (Norusis, 2004). According to the results of the multi colinearity analysis on variables (Table 6.1), no co-linearity was observed since the

VIF (Variance İnflation Factor) values were below 5 and the tolerance values were above 0.2 (Menard, 1995; Rogerson, 2001).

Table 6.1. Layers and data sources utilized in TOPSIS analysis.

Layer	Data Source	Tolerance	VIF
Lineament Density	**Lineament Map Generated as part of this study**	.555	1.803
Surface Temperature	**Results of the ASTER satellite image analyses in this study**	.517	1.934
Cover Units	**1/25.000 scale map of General Directorate of Mineral Exploration**	.662	1.510
Advanced Argillic Alteration Map	**Generated as part of ASTER satellite alteration assessment in this study**	.287	3.483
Kaolinite Index	**Generated as part of ASTER satellite alteration assessment in this study**	.348	2.877
Phyllic Alteration Map	**Generated as part of ASTER satellite alteration assessment in this study**	.533	1.878
Alunite Index	**Generated as part of alteration assessment in this study**	.709	1.410

The Pairwise Comparison (paired comparison) Method, developed by Saaty (1980), allows to determine the relative importance of an entity by comparing all entities in pairs. The process consists of three main steps; 1) development of the pairwise comparison matrix where a scale of 1–8 is used to express judgments (9 being equal importance and 1 being extreme importance) (Saaty, 1980), 2) criterion weights computation through column-wise normalization of the pairwise comparison matrix and computation of the average of the elements in each row of the normalized matrix, and finally, 3) the consistency ratio estimation to check the consistency of comparisons. For this purpose, first, the consistency vector is determined through the ratio of weighted sum vector to the criterion the weights. Then, two terms; the average value of the consistency vector (λ) and consistency index ($CI = (\lambda - n)/(n - 1)$) are determined. The pairwise comparison matrix is consistent if $\lambda > n$, where n is the number of the criteria (Malczewski, 1999). The λ for this study is calculated as 7.26 which is greater than the number of criteria (7) showing consistency. Along with this, the consistency ratio (CR) can be determined in order to measure the level of consistency by dividing the consistency index (CI) by the random index that depends on the number of elements being compared (Saaty, 1980; Malczewski, 1999). $CR < 0.1$ indicates an acceptable level of consistency, and $CR \geq 0.1$ indicates inconsistency. The CR value for this study is calculated as 0.043 showing that there is no inconsistency for the criteria.

Following calculation of weights and checking the multi co-linearity, each layer was standardized and further multiplied by its corresponding weight value. Negative ideal and positive ideal points for each weighted standardized map were obtained by determining the minimum and maximum values, respectively. The Euclidean distance between the negative and positive ideal layers and the weighted standardized maps were determined. Further, the relative closeness to the ideal point was determined by adding the Euclidean separations and by dividing the resultant map to the Euclidean distance to positive ideal (Malczewski, 1999).

Table 6.2. Pairwise comparison matrix and weights of layers

Layers	Lineament Density	Cover Units	Temperature	Argillic	Alunite	Kaolinite	Phyllic	Weight
Lineament Density	1	3	4	5	6	7	8	0.3796
Relative Temperature	1/3	1	3	4	5	6	7	0.2373
Cover Units	1/4	1/3	1	3	4	5	6	0.1540
Argillic Alteration	1/5	1/4	1/3	1	3	4	5	0.1002
Kaolinite Index	1/6	1/5	1/4	1/3	1	3	4	0.0642
Phyllic Alteration	1/7	1/6	1/5	1/4	1/3	1	3	0.0401
Alunite Index	1/8	1/7	1/6	1/5	1/4	1/3	1	0.0246

6.3 Data Layers

For the analyses, seven layers were utilized where six of these layers were generated as part of this study, namely: 1) Surface Temperature, 2) Distance to Lineaments, 3) Advanced Argillic Alteration Map, 4) Phyllic Alteration Map, 5) Alunite Index Map, 6) Kaolinite Index Map, and one layer, namely Distance to Cover Units, based on geology was generated by utilizing 1/25.000 scale geological map of General Directorate of Mineral Research and Exploration.

The elevation corrected surface relative temperature map was generated as discussed in Section 5.5 in this study.

The lineament density layer was generated by utilizing the manually extracted lineaments as discussed in Section 4.1 of this study with a search radius of 579 m based on the average nearest neighborhood relation of the line features.

The distance to cover units layer was generated by utilizing 1/25.000 scale geological map of General Directorate of Mineral Exploration (MTA, 2002) by utilizing a 250 m buffer on the Cenozoic units. The older units are considered to host the reservoir units of the BMG and therefore any younger unit overlying the Menderes Metamorphics are primarily considered to constitute cover unit characteristics.

Satellite based alteration maps were generated by utilizing ASTER satellite imagery as discussed in Section 3.5 of this study and four different layers were generated from the satellite images and compared with the XRD analyses conducted on samples collected from the field. The layers generated from satellite image alteration assessment are, Advanced Argillic Alteration, Phyllic Alteration, Alunite Index and Kaolinite Index maps.

Following generation of all these maps, each layer was normalized in order to provide a consistent set of inputs. Each of these layers are presented in Figure 6.2 through Figure 6.8.

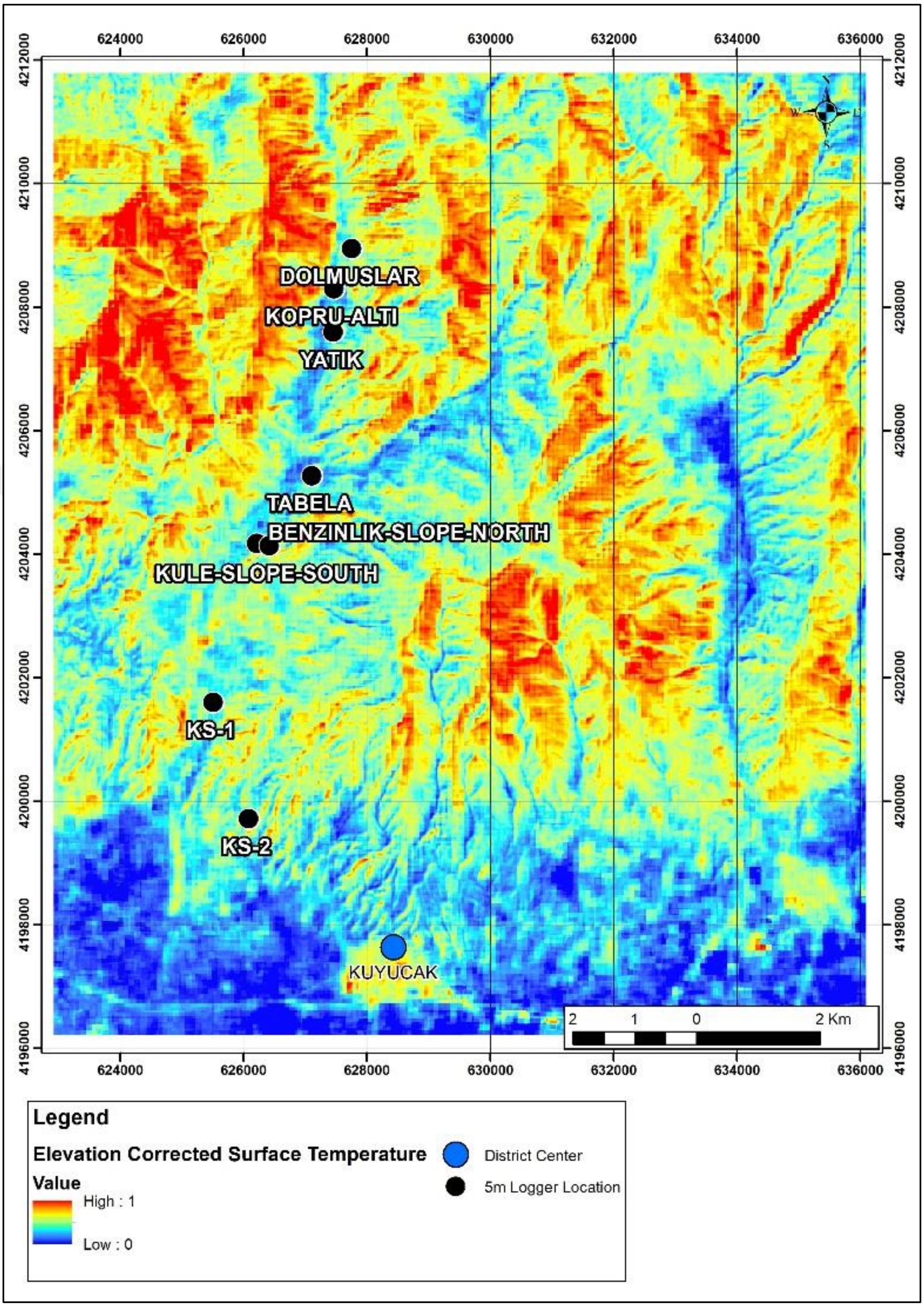

Figure 6.2. Elevation corrected surface temperature image.

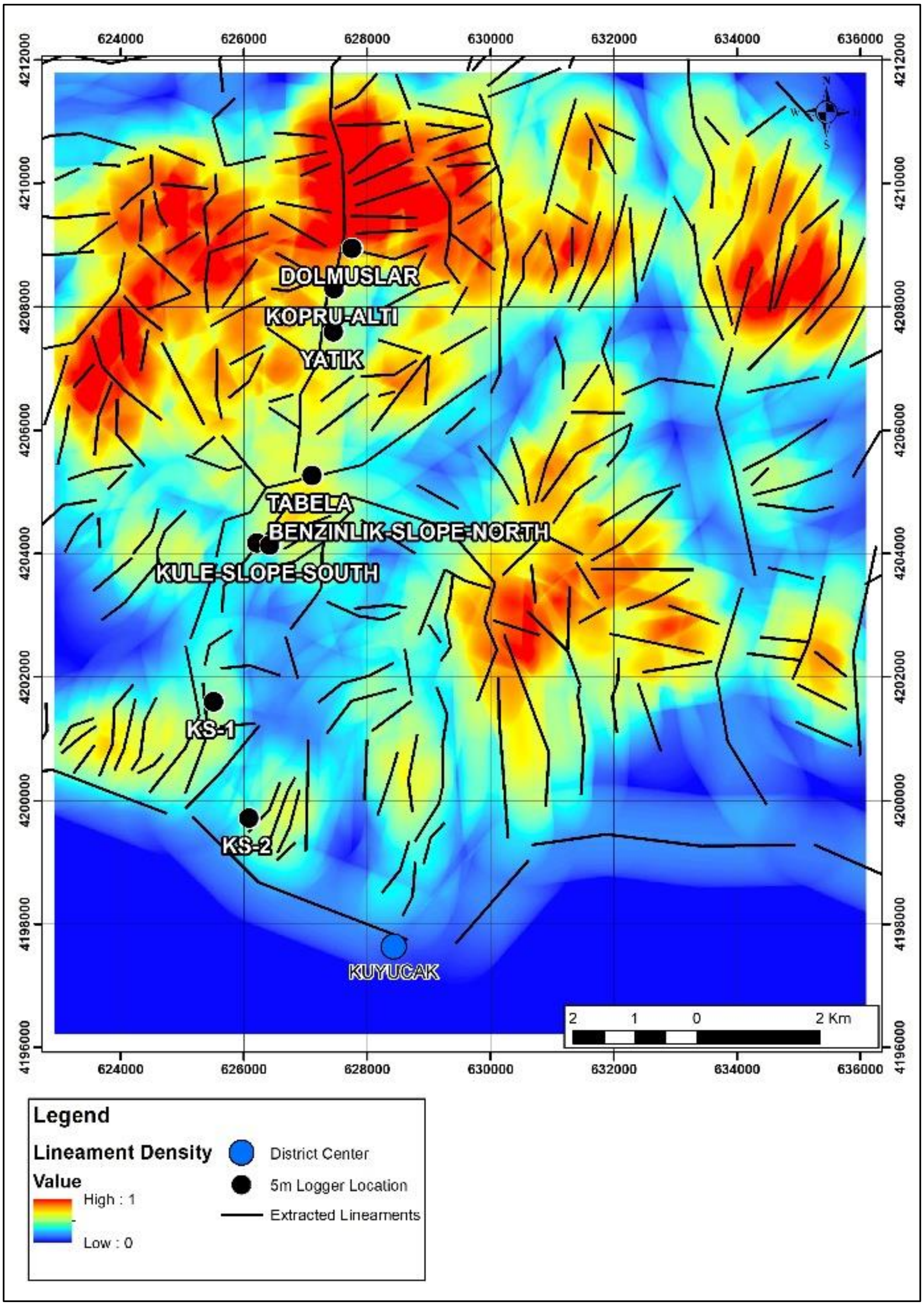

Figure 6.3. Lineament Density layer.

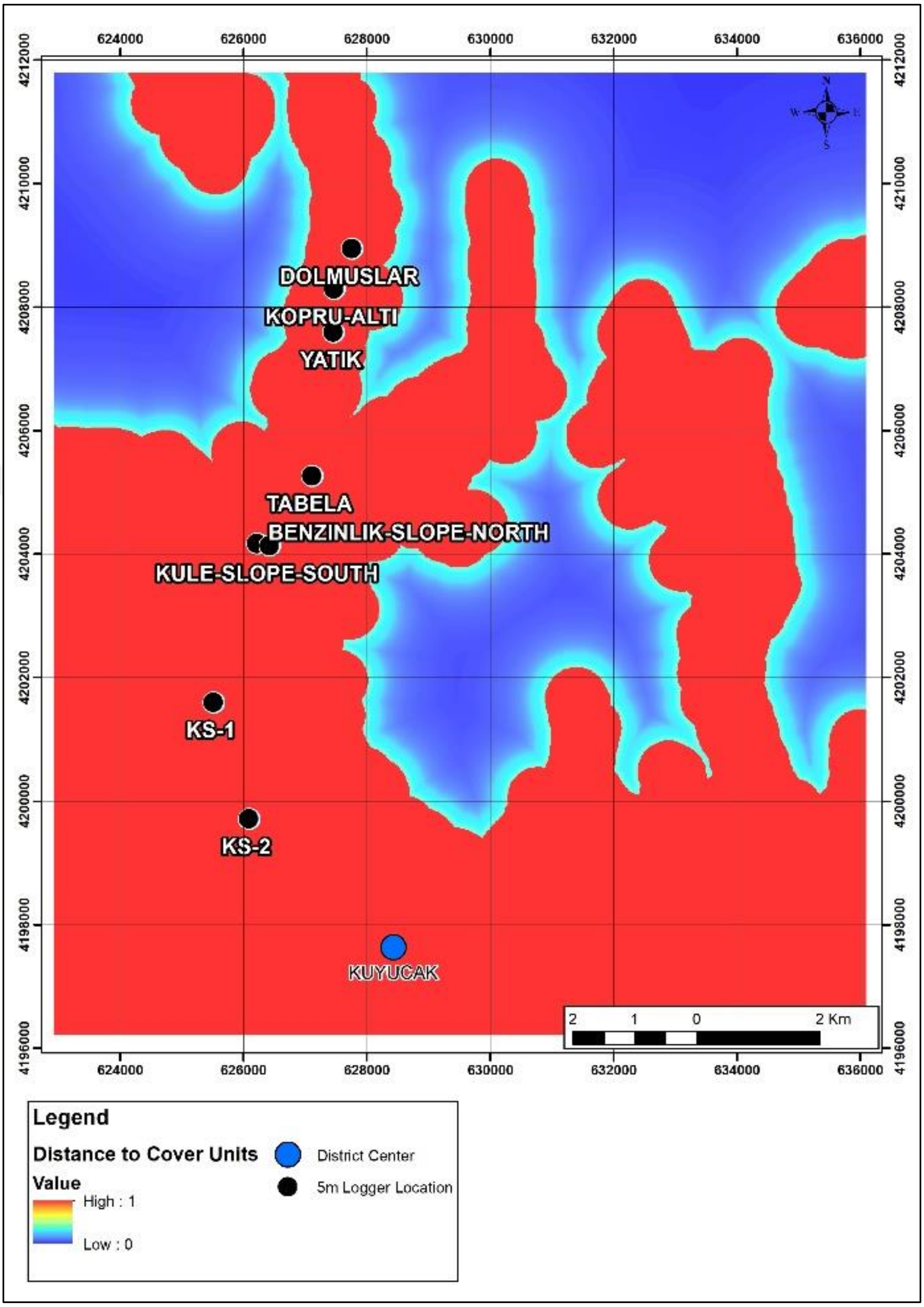

Figure 6.4. Distance to Cover Units layer.

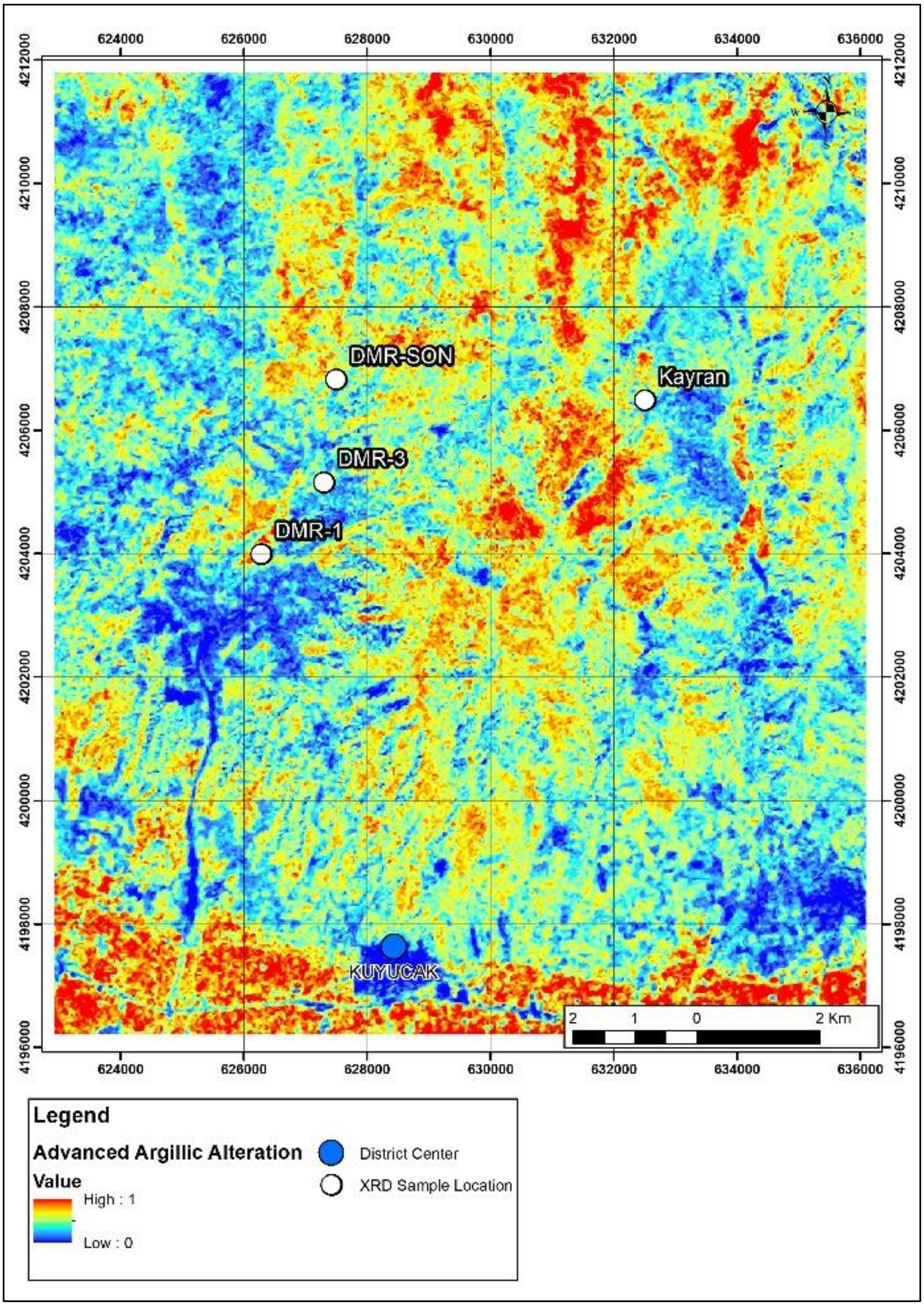

Figure 6.5. Advanced Argillic Alteration layer.

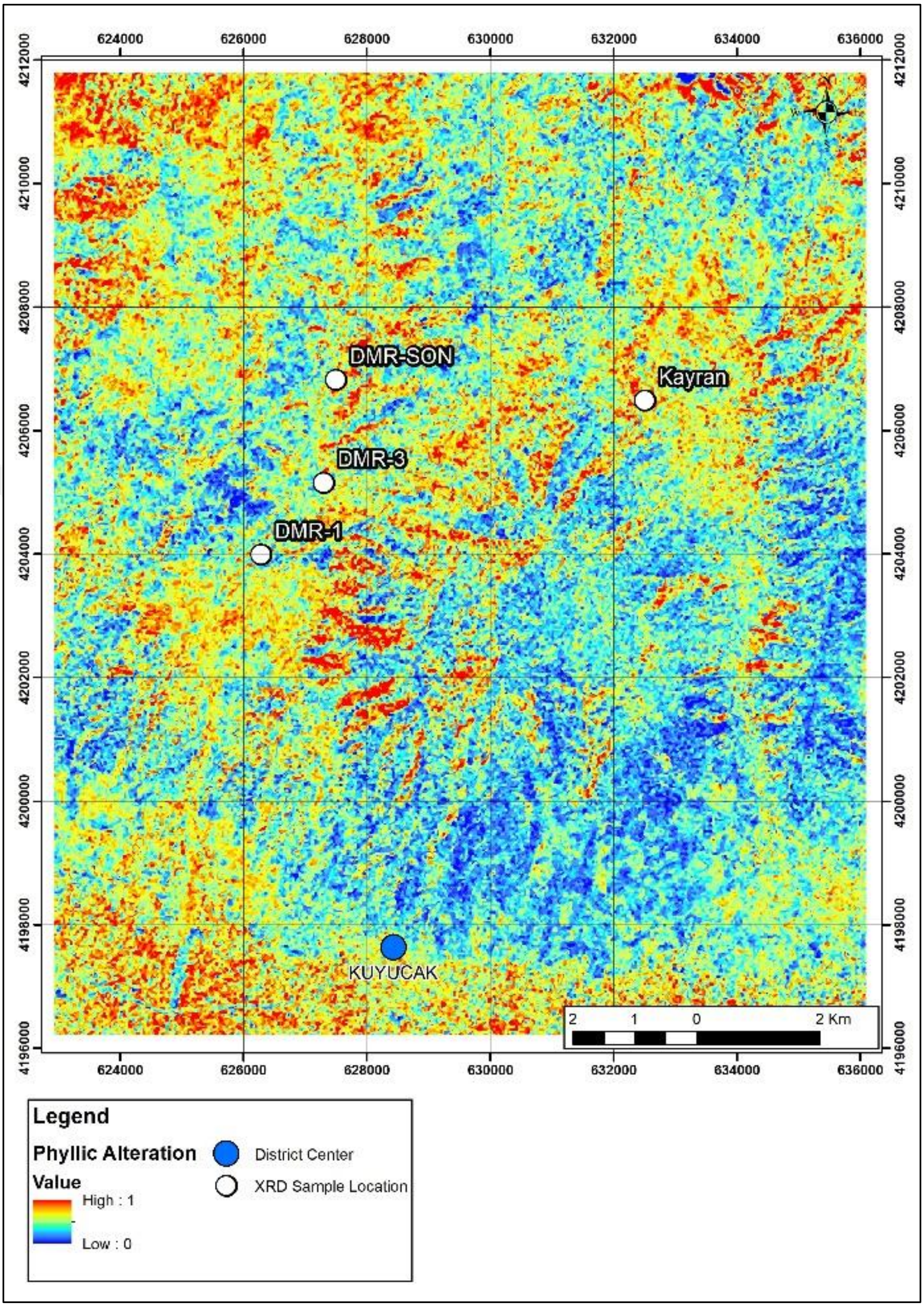

Figure 6.6. Phyllic Alteration Layer.

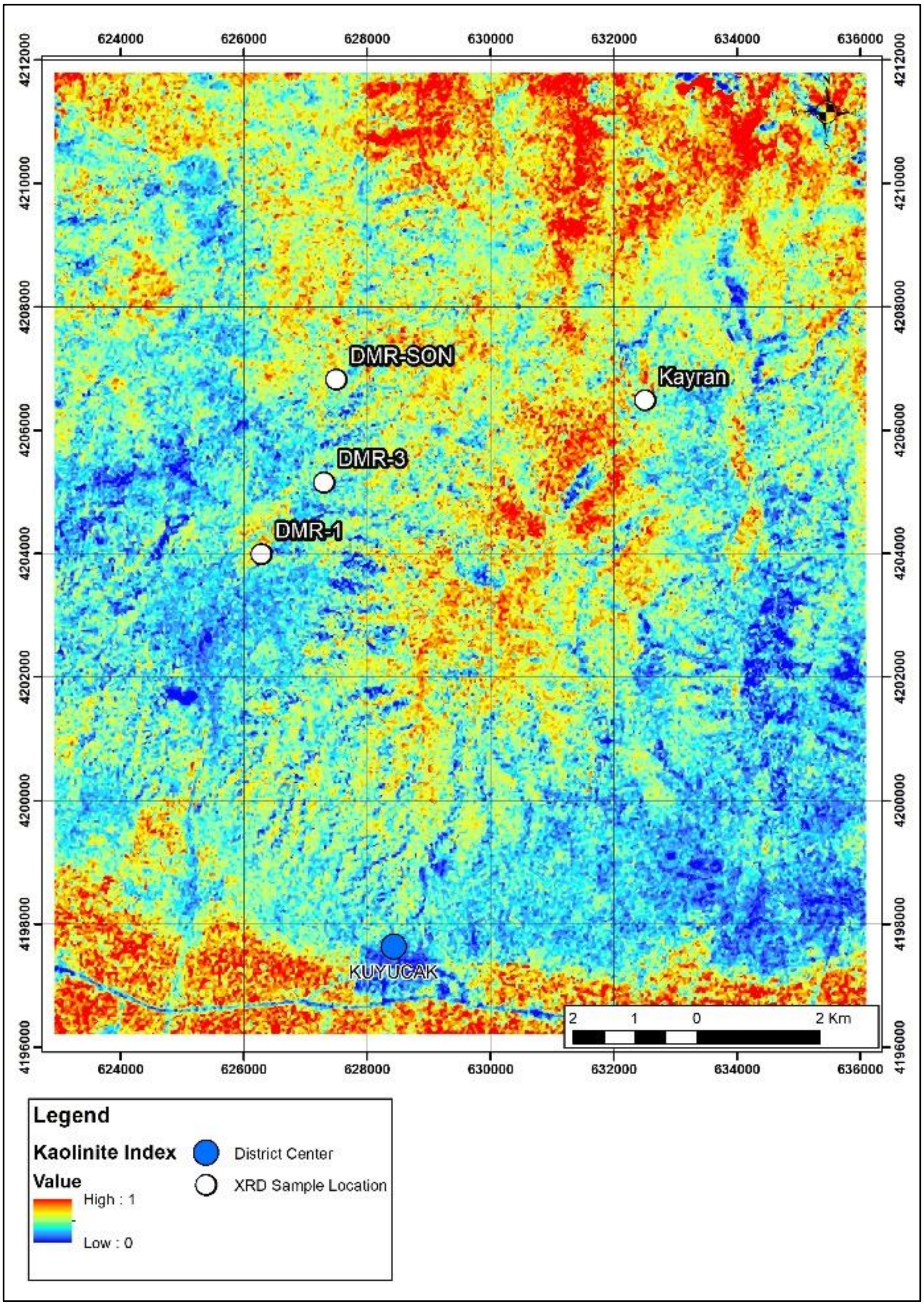

Figure 6.7. Kaolinite Index Layer.

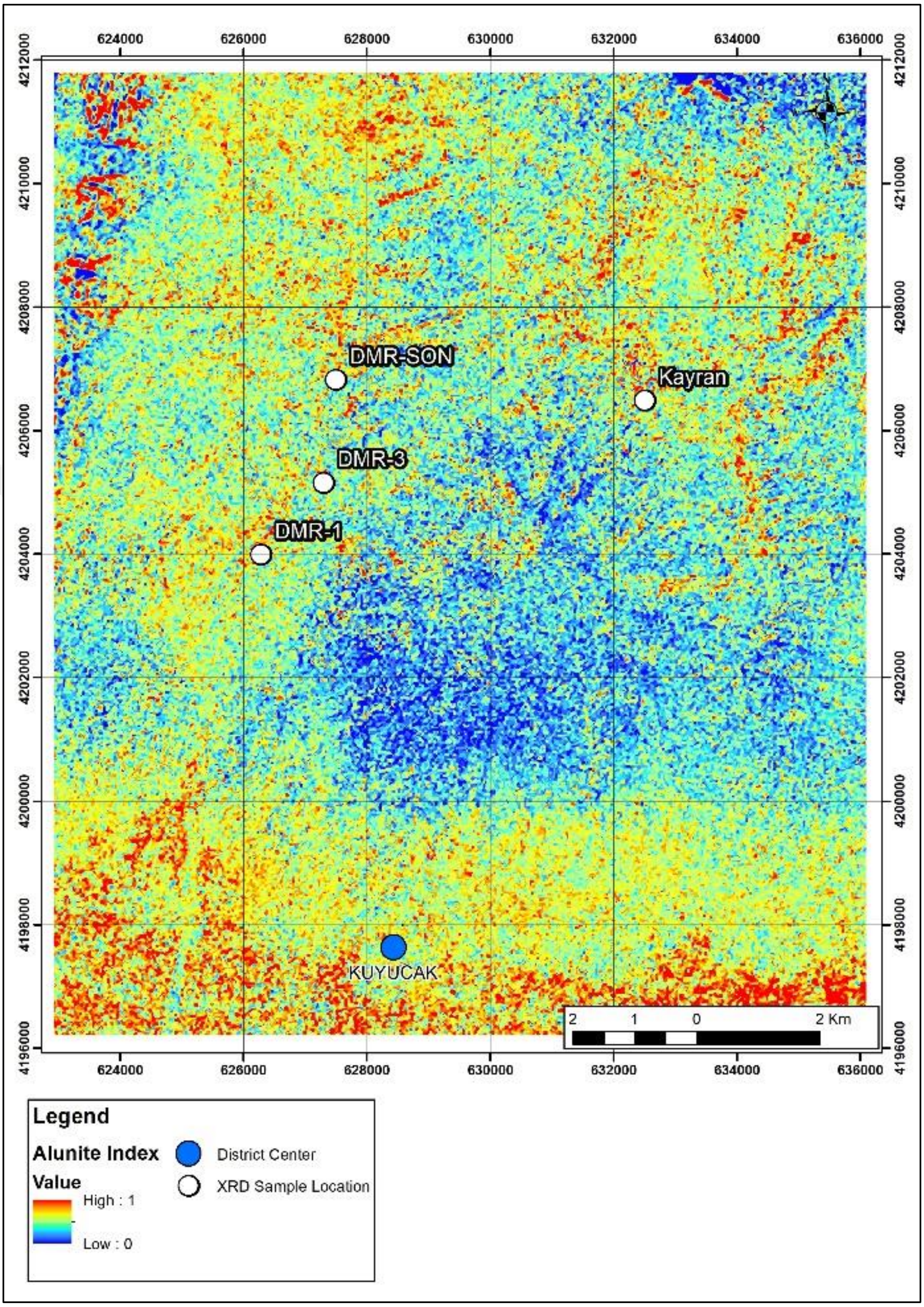

Figure 6.8. Alunite Index Layer.

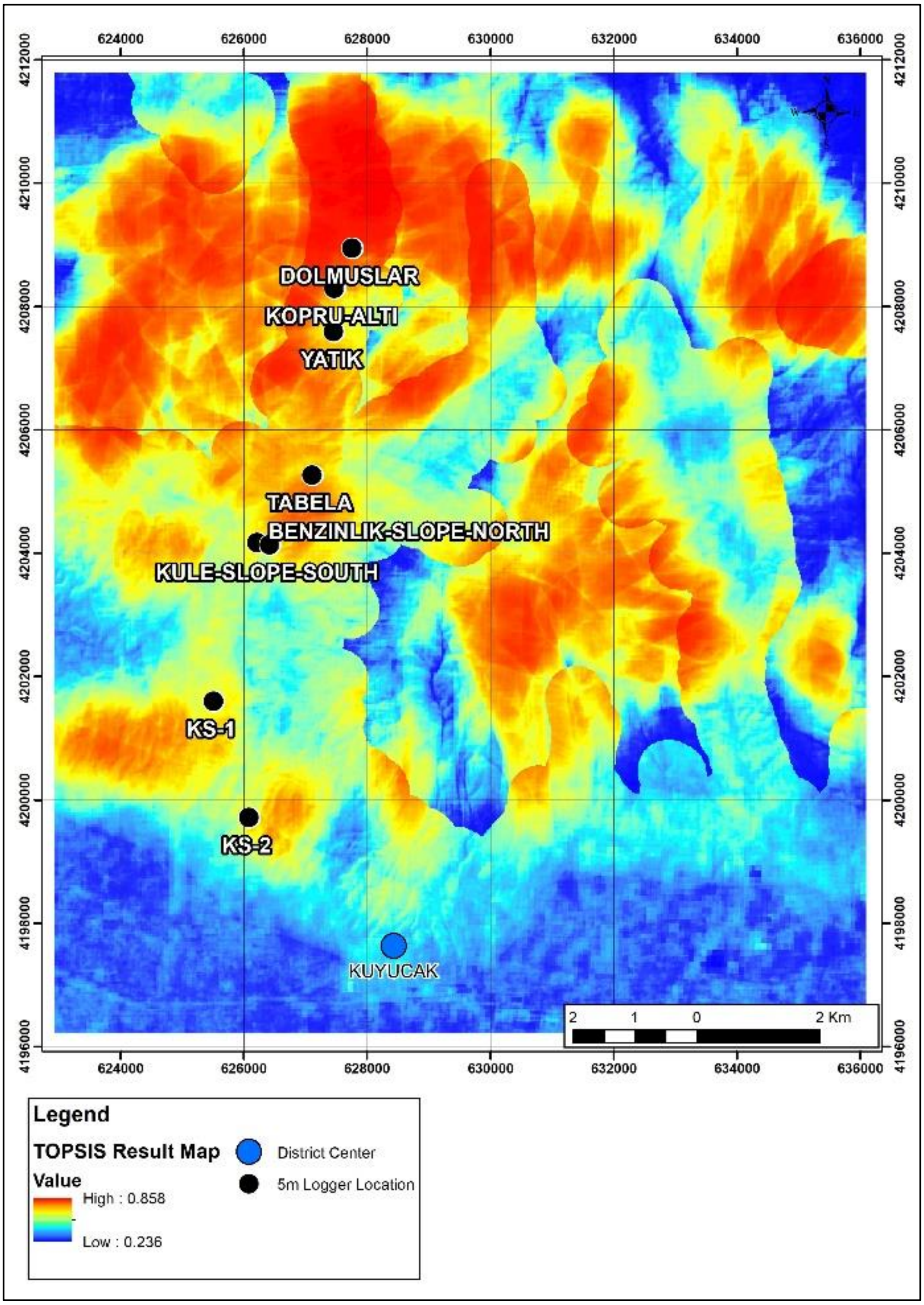

Figure 6.9. TOPSIS result map.

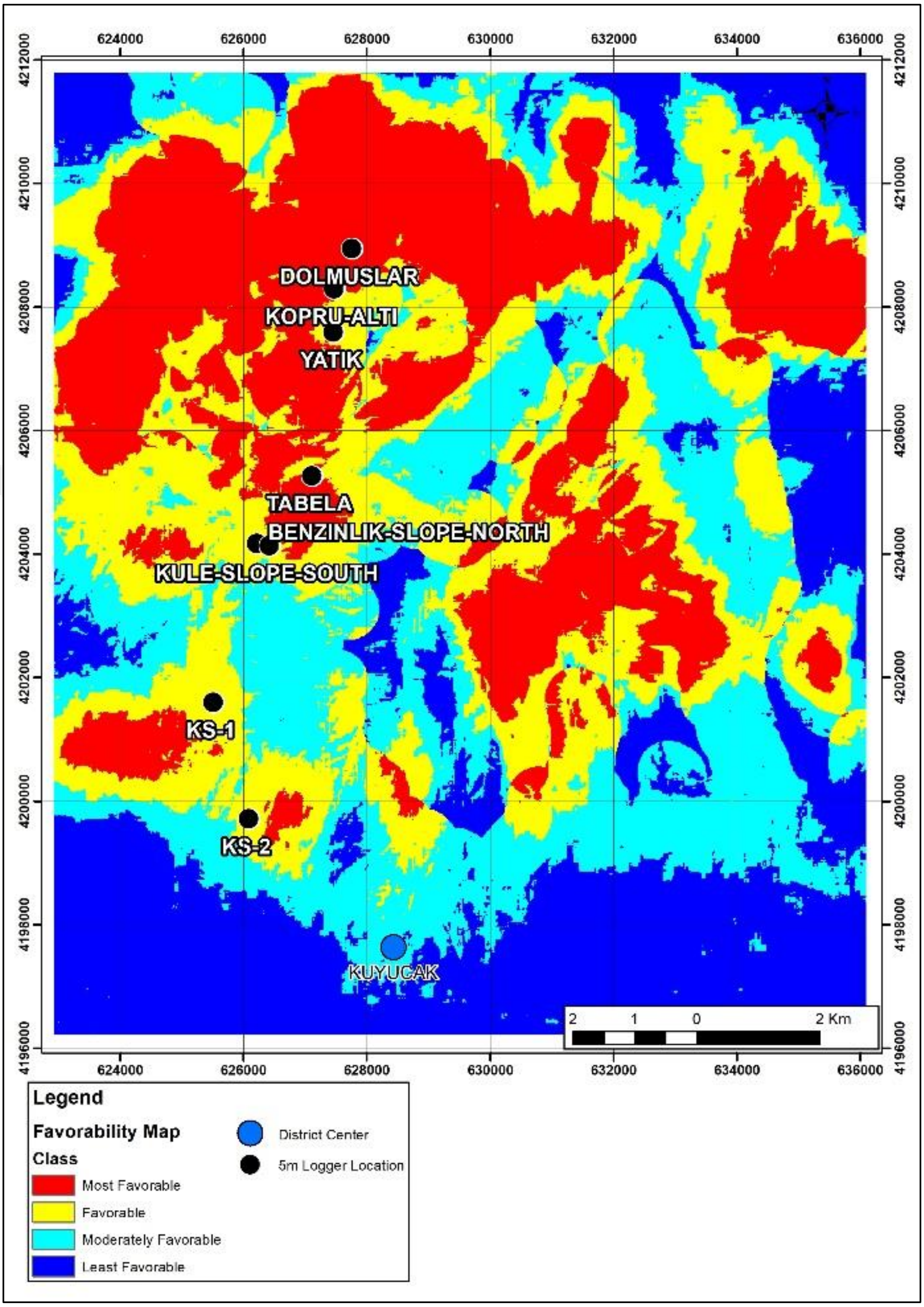

Figure 6.10. Favorability classes.

6.4 Results and Conclusion on GIS Based MCDA

In order to assess the compatibility of the results of the datasets developed as part of this study and to provide a geothermal favorability map for the study area, four different alteration mineral maps, lineament density map, surface temperature map generated as part of this study and distance to cover units map generated from 1/25.000 scale geological map of the study area (MTA, 2002) was utilized. It is known that the main factor controlling the geothermal system in Western Anatolia is the fault and fracture system developed as a result of extensional regime in the region (Faulds et al., 2010; Moeck, 2014; Koçyiğit, 2015), therefore in terms of relative importance, the highest rank was assigned to the fault density layer.

According to results of the TOPSIS analysis, both KS-1 and KS-2 wells are located within favorable areas. Furthermore, the logger locations Dolmuşlar at the northernmost location which have the highest thermal gradient value on the April 21 measurements as well as third location from the north, namely Tabela is located within the most favorable class. Also, the second location from the north, Yatık, which also has the second highest thermal gradient value is located within the favorable class.

CHAPTER 7

RESULTS AND DISCUSSION

The study was comprised of temperature measurements and analyses, alteration mineral analyses, lineament analyses, each method with desktop and field applications for comparison, and finally GIS based MCDA application to assess geothermal favorability and compare the final map with the field measurements.

For the temperature analyses, results acquired from the temperature loggers deployed at 1 m, 2 m, 3 m and 5 m depth at eight locations were assessed. As provided in detail in Section 5.4, when measurements taken (or sine wave fit) following spring equinox is considered on April 21st, 2022, it was observed that, starting from logger 7 at Kule location, there is an increasing trend from south to north in temperature gradient values, especially for the 3 m to 5 m depth measurements' gradient. It is known from previous studies conducted by Yal et al. (2017) that the reservoir is shallower towards the north of the study area and the measurements taken from the field are in agreement with this study yielding a coefficient of determination value of 0.9807. Furthermore, positive thermal gradient was also observed at logger 2 at KS-2 well location where a successful deep geothermal well with >150°C temperature is located.

On the other hand, loggers 5 and 6 have shown negative thermal gradient. Although logger 5 is located at the deep geothermal well location, it is known that shallow groundwater at a depth of approximately 150 m is present at the location, which is considered to mask any thermal signature. Finally, for logger 6, located at the Benzinlik location consisting of hard soil-weathered rock site does not provide conclusive results for sinusoidal wave fit data due to limited data collected from this location with 68 days in total due to water damage to the sensor.

As for the satellite derived surface temperature map, the final map was compared with the lineament density, since it is known that Büyük Menderes Graben fault and fracture controlled geothermal system (Moeck, 2014), and also compared with south-to-north increasing index map, since results of the study conducted by Yal et al. (2017) have presented that the reservoir is shallower towards the north of the study area. It was observed that the coefficient of determination (R^2) for the lineament density map against surface temperature map is 40.86% whereas the R^2 for the south-to-north index versus surface temperature map is 31.08%. According to the results of multivariable regression where final temperature map is the dependent variable, and lineament density and south-to-north index are independent variables, the coefficient of determination (R^2) is found as 44.8%.

Therefore, although a thermal gradient increase was observed from the field measurements, the same could not be confidently derived from the satellite based surface temperature map. The main reason for this is considered to be humid climate of the study area and presence of shallow groundwater table masking the thermal signature of the reservoir without presenting any surface thermal anomalies.

Along with the temperature surveys, alteration samples were collected from the field for XRD analyses and ASTER satellite images were analyzed to derive alteration maps. According to quantitative assessment of the XRD analyses and comparison with the satellite based alteration maps, the highest pixel values for the argillic alteration map have been observed for the XRD samples 14 and 13 where for XRD results of sample 14 all three alteration minerals, namely alunite, kaolinite and pyrophyllite were observed, and for sample 13 both kaolinite and pyrophyllite were observed. For the phyllic alteration map results, the highest pixel value was observed in sample no. 15 and both illite and smectite were observed in this sample. For the alunite index map, the only sample where alunite was interpreted from XRD results had the highest pixel value. For kaolinite index, since all samples have kaolinite, no distinct interpretation has been made. Furthermore, the samples collected from the north of the study area, namely, DMR-Son, DMR-3, AY-2 and Kayran showed presence of Albite which is an indicator of a high temperature system. Therefore, this also supports that geothermal activity and presence of higher temperatures is shallower and have surface alteration minerals present towards the north of the study area.

Additionally, in order to characterize the fractured and faulted characteristics of the study area, satellite based lineament analyses was performed from DEM and ASTER images. Along with this, a drone survey was conducted at the north, outside the main study area. The results of satellite images have shown azimuth distribution along the N0°E, N30°E and N60°E dominant directions. Also, drone based analyses led to dominant lineament direction between N300°E and N330°E with the secondary azimuth direction between N0°E and N30°E. The drone based analyses was supported by the scanline field surveys where bedding plane with N330°E trend and joint set-1 with N25°E trend were observed.

Finally, the entire data were utilized to execute a GIS based Multi-Criteria Decision Analysis (MCDA), namely TOPSIS analysis. The input layers for the TOPSIS analysis, except the cover unit layer, was generated as part of this study. A total of 7 layers were utilized for the analysis, Lineament Density, Surface Temperature, Cover Units, Advanced Argillic Alteration Map, Kaolinite Index, Phyllic Alteration Map and Alunite Index. Following pairwise comparison of the layers based on rankings and multi-colinearity analysis, each layer was utilized for the TOPSIS analysis.

According to results of the TOPSIS analysis, both KS-1 and KS-2 wells were determined to be located within favorable areas. Furthermore, the logger locations Dolmuşlar at the northernmost location which had the highest thermal gradient value at the April 21st, 2022 measurements as well as third location from the north, namely Tabela has been determined to be located within the most favorable class. Also, the second location from the north, Yatık, which had the second highest thermal gradient value was determined to be located within the favorable class.

Therefore, it was observed that the field measurements and GIS based MCDA results were consistent with each other.

In summary, it was observed that satellite based alteration mineral mapping and lineament mapping were compatible with field and laboratory measurements, however, satellite based geothermal anomaly map could not be conclusively correlated with neither lineament density nor with south-to-north index map representing the decreasing reservoir depth in this direction. In order to check the impact of vegetation on the final surface temperature map, the map was masked by layers generated from thresholding NDVI map according to mean and ± one σ (standard deviation) values. It was observed from correlation of masked temperature map, and descriptive layers of lineament density and south-to-north index layer that the vegetation does not have an impact on the assessment. The main reason for these inconclusive results is considered to be the presence of shallow groundwater within the study area which masks any thermal signature from the deep seated reservoir to reach the surface. On the other hand, field measurements have presented strong correlation with the south-to-north direction having 0.9807 R^2 value, indicating importance of field measurements in assessment and exploration of blind geothermal systems.

CHAPTER 8

CONCLUSION AND RECOMMENDATION FOR FUTURE STUDIES

This study was comprised of field surveys and measurements, satellite image analyses and laboratory works. The purpose of this study was to provide a cost effective method to identify geothermal anomalies at a blind geothermal area where no surface manifestations are present.

The study was divided into three main parts, namely, temperature surveys and analyses, alteration mineral analyses and laboratory tests, and lineament extraction. All the field, laboratory and satellite based image results were combined to acquire a geothermal feasibility map of the study area by utilizing GIS based TOPSIS methodology.

To the knowledge of the author, this study is first of its kind in terms of long term shallow temperature measurements in Türkiye and in Mediterranean climate region. Furthermore, to the knowledge of the author, this is the first study combining desktop studies, field measurements and laboratory tests in terms of alteration mineral mapping, temperature mapping and lineament mapping to provide a comprehensive geothermal feasibility assessment through utilization of GIS based MCDA methodology at a blind geothermal area in Türkiye.

The geothermal temperature anomaly detection and alteration mineral mapping was conducted based on satellite images and the field temperature measurements as well as XRD laboratory analyses that were conducted to support and verify the satellite based assessments.

Due to the climate of the region and presence of shallow groundwater, satellite based temperature anomaly assessment could not provide concrete evidence of geothermal anomalies for the study area. On the other hand, field temperature surveys have shown that thermal gradient is increasing from south-to-north. Therefore, importance of field measurements, rather than only satellite based assessment, in non-arid climates was observed.

Comparison of satellite based alteration maps and XRD laboratory assessment have shown that the results of two methodologies are consistent.

Furthermore, assessment of geothermal favorability through GIS based MCDA method TOPSIS have provided consistent results with the field temperature measurements, indicating that, compilation of all datasets is important.

It can be concluded that, combination of field surveys and satellite image analysis can be utilized to assess geothermal favorability of a blind geothermal system. However, in order to provide more location precise results, it is deemed necessary to increase the number of measurement points for the temperature surveys and to increase the number of samples and XRD analyses in conjunction with the utilization of satellite imagery.

In order to improve upon this study and provide guidance for similar studies, it is recommended to increase the number of sampling points for XRD analyses by considering results of an initial alteration mineral mapping and selecting sampling points both at high alteration areas and also from areas where alteration was not observed through satellite image analysis. This would provide a further detailed comparison between image analysis results and field data, and would allow quantitative comparison of results. Furthermore, sampling from zones with low alteration values in the satellite image analysis results would provide a baseline. Along with this, utilization of other alteration mineral mapping methods such as Crosta analysis (Crosta et al., 2003) and additional band combinations as well as band ratios analyses would allow further comparison of mineral mapping results and provide a basis for a sensitivity assessment.

In terms of temperature measurements, this study focused on identification of thermal anomalies and thermal gradient anomalies through selection of measurement points at possible upflow locations at intersections of previously identified lineaments. In the future studies, in addition to the long term measurements, it would be beneficial to increase the number of individual measurement locations which may cover a larger area including both thermal anomaly detection targets and background locations as well. These measurements can be collected at different times and seasonal correction can be applied by utilizing long term measurement datasets. This would allow generation of an area based temperature anomaly map rather than the point based assessment performed as part of this study and further facilitate comparison of field data with the satellite based image interpretation.

Finally, through increasing the field measurement points, it would be possible to further improve upon this study by utilizing different GIS based MCDA methodologies and statistical assessments such as analytical hierarchy process (AHP), fuzzy logic, logistic regression and random forest analysis which would allow comparison of multiple methodologies with the ground truth data.

REFERENCES

Abrams, M. (2000). The Advanced Spaceborne Thermal Emission and Reflection Radiometer (ASTER): Data products for the high spatial resolution imager on NASA's Terra platform. *International Journal of Remote Sensing, 21*(5), 847–859.

Abrams, M., Tsu, H., Hulley, G., Iwao, K., Pieri, D., Cudahy, T., & Kargel, J. (2015). The Advanced Spaceborne Thermal Emission and Reflection Radiometer (ASTER) after fifteen years: Review of global products. *International Journal of Applied Earth Observation and Geoinformation, 38*, 292–301.

Abubakar, A. J. A., Hashim, M., & Pour, A. B. (2019). Remote sensing satellite imagery for prospecting geothermal systems in an aseismic geologic setting: Yankari Park, Nigeria. *International Journal of Applied Earth Observation and Geoinformation, 80,* 157–172.

Abubakar, A. J. A., Hashim, M., Pour, A. B., & Shehu, K. (2017). A review of geothermal mapping techniques using remotely sensed data. *Science World Journal, 12*(4), 72–82.

Aden, I. I. (2020). Application of Landsat 8 satellite images, hydrothermal alteration mapping, thermal anomalies and correlation with XRD analysis: Case study of Ne Ghoubbet area (Djibouti) [Unpublished master's thesis].

Akgün, H., Koç, A., Yal, G. P., Cambazoğlu, S., Koçkar, M. K., & Eker, A. M. (2024). Geomechanical and thermal field characterization final report, GAP-309-2020-10185 scientific research project (p. 97). Middle East Technical University.

Atif, Y., Soulaimani, A., Ait lamqadem, A., Pour, A. B., Pradhan, B., Nouamane, E. A., ... & Hossain, M. S. (2022). Identifying hydrothermally altered rocks using ASTER satellite imageries in Eastern Anti-Atlas of Morocco: A case study from Imiter silver mine. *International Journal of Image and Data Fusion, 13*(4), 337–361.

Atmel. (2015). *ATmega328P datasheet* (7810D–AVR–01/15). Accessed on 12 June 2024, https://ww1.microchip.com/downloads/en/DeviceDoc/Atmel-7810-Automotive-Microcontrollers-ATmega328P_Datasheet.pdf

Aydın, A., & Akçay, S. (2023). Evaluation of water use management performances for irrigation cooperatives in Aydın province. *Ege Üniversitesi Ziraat Fakültesi Dergisi, 60*(3), 385–398.

Beck, H. E., Zimmermann, N. E., McVicar, T. R., Vergopolan, N., Berg, A., & Wood, E. F. (2018). Present and future Köppen-Geiger climate classification maps at 1-km resolution. *Scientific Data, 5*(1), 1–12.

Bonham-Carter, G. (1994). Geographic information systems for geoscientists: modelling with GIS (No. 13). Elsevier.

Bonham-Carter, G. F., Agterberg, F. P., & Wright, D. F. (1988). Integration of geological datasets for gold exploration in Nova Scotia. *Photogrammetric Engineering & Remote Sensing, 54*(11), 1585–1592.

Bozkurt, E., & Park, R. G. (1997). Evolution of a mid-Tertiary extensional shear zone in the Southern Menderes Massif, Western Turkey. *Bulletin de la Société Géologique de France, 168*(1), 3–14.

Bozkurt, E., & Sözbilir, H. (2006). Evolution of the large-scale active Manisa Fault, Southwest Turkey: Implications on fault development and regional tectonics. *Geodinamica Acta, 19*(6), 427–453.

Bozkurt, E. (2001). Neotectonics of Turkey: A synthesis. *Geodinamica Acta, 14*(1–3), 3–30.

Brogi, A. (2004). Faults linkage, damage rocks and hydrothermal fluid circulation: Tectonic interpretation of the Rapolano Terme travertines (southern Tuscany, Italy) in the context of the Northern Apennines Neogene-Quaternary extension. *Eclogae Geologicae Helvetiae, 97*, 307–320. https://doi.org/10.1007/s00015-004-1134-5

Brogi, A., Alçiçek, M. C., Liotta, D., Capezzuoli, E., Zucchi, M., & Matera, P. F. (2021). Step-over fault zones controlling geothermal fluid-flow and travertine formation (Denizli Basin, Turkey). *Geothermics, 89*, 101941.

Brogi, A., Liotta, D., Ruggieri, G., Capezzuoli, E., Meccheri, M., & Dini, A. (2016). An overview on the characteristics of geothermal carbonate reservoirs in southern Tuscany. *Italian Journal of Geosciences, 135*, 17–29. https://doi.org/10.3301/IJG.2014.41

Browne, P. R. L. (1978). Hydrothermal alteration in active geothermal fields. *Annual Review of Earth and Planetary Sciences, 6*, 229–250.

Burns, E. (2015). Snake River Plain play fairway analysis—Phase 1 report. *GRC Transactions, 39*, 123–126.

Calvin, W. M., Littlefield, E. F., & Kratt, C. (2015). Remote sensing of geothermal-related minerals for resource exploration in Nevada. *Geothermics, 53*, 517–526.

Camanni, G., Roche, V., Childs, C., Manzocchi, T., Walsh, J. J., Coneally, J., Saqab, M. M., & Delogkos, S. (2019). The three-dimensional geometry of relay zones within segmented normal faults. *Journal of Structural Geology, 129*, 103895. https://doi.org/10.1016/j.jsg.2019.103895

Cambazoğlu, S. (2012). *Preparation of a source model for the Eastern Marmara Region along the North Anatolian fault segments and probabilistic seismic hazard assessment of Düzce Province* [Master's thesis, Middle East Technical University].

Cambazoğlu, S., Koçkar, M. K., & Akgün, H. (2016). A generalized seismic source model for the Eastern Marmara Region along the segments of the North

Anatolian Fault System. *Soil Dynamics and Earthquake Engineering, 88*, 412–426.

Cambazoğlu, S., Yal, G. P., Eker, A. M., Şen, O., & Akgün, H. (2019). Geothermal resource assessment of the Gediz Graben utilizing TOPSIS methodology. *Geothermics, 80*, 92-102.

Canbaz, O., Gürsoy, Ö., & Gökce, A. (2018). Detecting clay minerals in hydrothermal alteration areas with integration of ASTER image and spectral data in Kösedag-Zara (Sivas), Turkey. *Journal of the Geological Society of India, 91*, 483–488.

Carranza, E. J. M., Wibowo, H., Barritt, S. D., & Sumintadireja, P. (2008). Spatial data analysis and integration for regional-scale geothermal potential mapping, West Java, Indonesia. *Geothermics, 37*(3), 267–299.

Casas, A. M., Cortes, A. L., Maestro, A., Soriano, M. A., Riaguas, A., & Bernal, J. (2000). A program for lineament length and density analysis. *Computers & Geosciences, 26*(9–10), 1011–1022.

Chan, H. P., Chang, C. P., & Dao, P. D. (2018). Geothermal anomaly mapping using Landsat ETM+ data in ilan plain, northeastern Taiwan. *Pure and Applied Geophysics, 175*, 303-323.

Chao, J., Zhao, Z., Lai, Z., Xu, S., Liu, J., Li, Z., ... & Zhao, X. (2023). Detecting geothermal anomalies using Landsat 8 thermal infrared remote sensing data in the Ruili Basin, Southwest China. *Environmental Science and Pollution Research, 30*(11), 32065–32082.

Chen, K., Blong, R., & Jacobson, C. (2001). MCE-RISK: Integrating multicriteria evaluation and GIS for risk decision-making in natural hazards. *Environmental Modelling & Software, 16*(4), 387–397.

Chen, P. Y. (1977). *Table of key lines in X-ray powder diffraction patterns of minerals in clays and associated rocks*. Indiana Geological & Water Survey.

Chung, C. F., Jeoerson, C. W., & Singer, D. A. (1992). A quantitative link among mineral deposit modeling, geoscience mapping, and exploration-resource assessment. *Economic Geology, 87*(2), 194–197.

Clark, R. N., Swayze, G. A., Gallagher, A. J., King, T. V. V., & Calvin, W. M. (1993). The US Geological Survey Digital Spectral Library: Version 1: 0.2 to 3.0 microns (US Geological Survey Open File Report 93–592). In R. N. Clark, G. A. Swayze, A. J. Gallagher, T. V. V. King, & W. M. Calvin (Eds.), *US Geological Survey Open File Report* (p. 1340).

Coolbaugh, M. F., Kratt, C., Fallacaro, A., Calvin, W. M., & Taranik, J. V. (2007a). Detection of geothermal anomalies using advanced spaceborne thermal emission and reflection radiometer (ASTER) thermal infrared images at Bradys Hot Springs, Nevada, USA. *Remote Sensing of Environment, 106*(3), 350–359.

Coolbaugh, M. F., Sladek, C., & Kratt, C. (2010). Compensation for seasonal and surface effects of shallow (two-meter) temperature measurements. *Geothermal Resources Council Transactions, 34*, 851–856.

Coolbaugh, M., Taranik, J., & Kruse, F. (2000). Mapping of surface geothermal anomalies at Steamboat Springs, NV using NASA Thermal Infrared Multispectral Scanner (TIMS) and Advanced Visible and Infrared Imaging Spectrometer (AVIRIS) data. In *Proceedings of the 14th Thematic Conference on Applied Geologic Remote Sensing* (pp. 623–630).

Coolbaugh, M. F., & Bedell, R. (2006). A simplification of weights of evidence using a density function and fuzzy distributions for geothermal systems. In J. R. Harris (Ed.), *GIS for the Earth Sciences* (pp. 115–130). Geological Association of Canada Special Publication 44.

Coolbaugh, M. F., Sladek, C., Faulds, J. E., Zehner, R. E., & Oppliger, G. L. (2007b). Use of rapid temperature measurements at a 2-meter depth to augment deeper temperature gradient drilling. In *Proceedings of the 32nd Workshop on Geothermal Reservoir Engineering* (pp. 109–116). Stanford University.

Craig, J. W., Faulds, J. E., Hinz, N. H., Earney, T. E., Schermerhorn, W. D., Siler, D. L., Glen, J. M., Peacock, J., Coolbaugh, M. F., & Deoreo, S. B. (2021). Discovery and analysis of a blind geothermal system in southeastern Gabbs Valley, western Nevada, USA. *Geothermics, 97*, 102177.

Crosta, A. P., De Souza, C. R., Azevedo, F., & Brodie, C. (2003). Targeting key alteration minerals in epithermal deposits in Patagonia, Argentina, using ASTER imagery and principal component analysis. *International Journal of Remote Sensing, 24*(21), 4233–4240.

Crowley, J. K., Brickey, D. W., & Rowan, L. C. (1989). Airborne imaging spectrometer data of the Ruby Mountains, Montana: Mineral discrimination using relative absorption band-depth images. *Remote Sensing of Environment, 29*(2), 121–134.

Curewitz, D., & Karson, J. A. (1997). Structural settings of hydrothermal outflow: Fracture permeability maintained by fault propagation and interaction. *Journal of Volcanology and Geothermal Research, 79*, 149–168. https://doi.org/10.1016/S0377-0273(97)00027-0

Demirbağ, E., Ersoy, Ş., Algan, O., Güneysu, C., & Akyol, A. (1995). Rift formation in the Gökova region, Southwest Anatolia: Implications for the opening of the Aegean Sea. *Geological Magazine, 132*(5), 637–650.

Deon, F., Förster, H. J., van Ruitenbeek, F., & Appelt, O. (2022). Performance of analytical techniques (SWIR imaging, XRD, EPMA) for the identification of minerals frequently formed during natural and technological geothermal processes. *International Journal of Terrestrial Heat Flow and Applied Geothermics, 5*(1), 34–44.

Di Tommaso, I., & Rubinstein, N. (2007). Hydrothermal alteration mapping using ASTER data in the Infiernillo porphyry deposit, Argentina. *Ore Geology Reviews, 32*(1–2), 275–290.

DSİ. (2012). *Aydın Water Well Reports* (Unpublished).

Duda, K., Daucsavage, J., Siemonsma, D., Brooks, B., Oleson, R., Meyer, D., & Doescher, C. (2015). Advanced spaceborne thermal emission and reflection radiometer (ASTER) level 1 precision terrain corrected registered at-sensor radiance product (AST_L1T). US Geological Survey, USA.

Elders, W. A., Hoagland, J. R., & Williams, A. E. (1981). Distribution of hydrothermal mineral zones in the Cerro Prieto geothermal field of Baja California, Mexico. *Geothermics, 10*(3–4), 245–253.

El-Desoky, H. M., Soliman, N., Heikal, M. A., & Abdel-Rahman, A. M. (2021). Mapping hydrothermal alteration zones using ASTER images in the Arabian–Nubian Shield: A case study of the northwestern Allaqi District, South Eastern Desert, Egypt. *Journal of Asian Earth Sciences: X, 5*, 100060.

Energy Sector Management Assistance Programme (ESMAP). (2019). *Validation report: Global Solar Atlas 2.0 validation report*. Washington, DC: World Bank.

Eneva, M., Coolbaugh, M., & Combs, J. (2006). Application of satellite thermal infrared imagery to geothermal exploration in East Central California. *Geothermal Resources Council Transactions, 30*, 407–411.

Eneva, M., & Coolbaugh, M. (2009). Importance of elevation and temperature inversions for the interpretation of thermal infrared satellite images used in geothermal exploration. *Geothermal Resources Council Transactions, 33*, 467–470.

Erinç, Ş. (1996). *Klimatoloji ve metodları* (Genişletilmiş 4. cü baskı). [In Turkish].

Eyidoğan, H., & Jackson, J. A. (1985). A seismological study of normal faulting in the Demirci, Alasehir, and Gediz earthquakes of 1969–1970 in western Turkey: Implications for the nature and geometry of deformation in the continental crust. *Geophysical Journal of the Royal Astronomical Society, 81*, 569–607.

Faulds, J. E., Hinz, N., Kreemer, C., & Coolbaugh, M. (2012). Regional patterns of geothermal activity in the Great Basin region, western USA: Correlation with strain rates. *Geothermal Resources Council Transactions, 36*, 897–902.

Faulds, J., Coolbaugh, M., Bouchot, V., Moeck, I., & Oğuz, K. (2010). Characterizing structural controls of geothermal reservoirs in the Great Basin, USA, and Western Turkey: Developing successful exploration strategies in extended terranes. In *Proceedings of World Geothermal Congress* (pp. 11).

Faulds, J., Craig, J., Hinz, N., Coolbaugh, M., Glen, J., Earney, T., & Siler, D. (2018). Discovery of a blind geothermal system in southern Gabbs Valley, western Nevada, through application of the play fairway analysis at multiple scales. *Geothermal Resources Council Transactions, 42*(DOE-UNR-06731-08).

Faulds, J. E., Bouchot, V., Moeck, I., & Oğuz, K. (2009). Structural controls of geothermal systems in western Turkey: A preliminary report. *Geothermal Resources Council Transactions, 33*, 375–383.

Faulds, J. E., Coolbaugh, M. F., Hinz, N. H., Cashman, P. H., Kratt, C., Dering, G., Edwards, J., Mayhew, B., & McLachlan, H. (2011). Assessment of favorable structural settings of geothermal systems in the Great Basin, western USA. *Geothermal Resources Council Transactions, 35*, 777–784.

Faulds, J. E., Coolbaugh, M. F., Hinz, N. H., Cashman, P. H., Kratt, C., Dering, G., Edwards, J., Mayhew, B., & McLachlan, H. (2011). Assessment of favorable structural settings of geothermal systems in the Great Basin, western USA.

Geothermal Resources Council Transactions, 35, 777–784. [Duplicate of the previous citation]

Faulds, J. E., & Hinz, N. H. (2015). Favorable tectonic and structural settings of geothermal systems in the Great Basin region, Western USA: Proxies for discovering blind geothermal systems. In *Proceedings of the World Geothermal Congress 2015* (pp. 1-9). Melbourne, Australia.

Faulds, J. E., Hinz, N. H., Dering, G. M., & Drew, D. L. (2013). The hybrid model – the most accommodating structural setting for geothermal power generation in the Great Basin, western USA. *Geothermal Resources Council Transactions, 37*, 3–10.

Ferrill, D. A., Stamatakos, J. A., Jones, S. M., Rahe, B., McKague, H. L., Martin, R. H., & Morris, A. P. (1996). Quaternary slip history of the Bare Mountain fault (Nevada) from the morphology and distribution of alluvial fan deposits. *Geology, 24*(6), 559−562.

Fitts, C. R. (2013). Subsurface heat flow and geothermal energy. In *Groundwater Science* (pp. 587-620). Academic Press.

Fossen, H., & Rotevatn, A. (2016). Fault linkage and relay structures in extensional settings: A review. *Earth-Science Reviews, 156*, 14–28. https://doi.org/10.1016/j.earscirev.2015.11.014

Geiger, R. (1961). Überarbeitete Neuausgabe von Geiger, R. *Köppen-Geiger/Klima der Erde* (Wandkarte 1: 16 Mill.). Klett-Perthes.

General Command of Mapping. (2000). *1:25,000 scale topographic maps of Turkey*. Ankara.

Gessner, K., Piazolo, S., Gungor, T., Ring, U., Kroner, A., & Passchier, C. W. (2001). Tectonic significance of the deformation patterns in granitoid rocks of the Menderes nappes, Anatolide belt, southwest Turkey. *International Journal of Earth Sciences, 89*(4), 766–780.

Ghulam, A. (2009). How to calculate reflectance and temperature using ASTER data. *Center for Environmental Sciences at Saint Louis University.*

Görür, N., Şengör, A. M. C., Sakınç, M., Tüysüz, O., Akkök, R., Yiğitbaşı, E., Oktay, F. Y., Barka, A. A., Sarıca, N., & Ecevitoğlu, B. (2006). Image processing of ASTER multispectral data. Geological Survey of Western Australia.

Guha, A., & Kumar, V. (2016). New ASTER derived thermal indices to delineate mineralogy of different granitoids of an Archaean Craton and analysis of their potentials with reference to Ninomiya's indices for delineating quartz and mafic minerals of granitoids: An analysis in Dharwar Craton, India. *Ore Geology Reviews, 74*, 76-87.

Gupta, R. P. (2003). *Remote sensing geology*. Springer-Verlag.

Gutiérrez, F. J., Lemus, M., Parada, M. A., Benavente, O. M., & Aguilera, F. A. (2012). Contribution of ground surface altitude difference to thermal anomaly detection using satellite images: Application to volcanic/geothermal complexes in the Andes of Central Chile. *Journal of Volcanology and Geothermal Research, 237*, 69-80.

Hancock, P. L., Chalmers, R. M. L., & Altunel, E. (1999). Travitonics: Using travertines in active fault studies. *Journal of Structural Geology, 21*(7), 903–916. https://doi.org/10.1016/S0191-8141(99)00061-9

Hanson, M. C., Oze, C., & Horton, T. W. (2014). Identifying blind geothermal systems with soil CO2 surveys. *Applied Geochemistry, 50*, 106-114.

Haselwimmer, C., & Prakash, A. (2013). Thermal infrared remote sensing of geothermal systems. In C. Kuenzer & S. Dech (Eds.), *Thermal infrared remote sensing* (Vol. 17, pp. 453–473). Springer.

Hayashi, M. (1973). Hydrothermal alteration in the Otake geothermal area, Kyushu. *Journal of Japan Geothermal Energy Association, 10*, 9-46.

Heasler, H. P., Jaworowski, C., & Foley, D. (2009). Geothermal systems and monitoring hydrothermal features. In *Geothermal Energy* (pp. 105-140).

Hellman, M. J., & Ramsey, M. S. (2004). Analysis of hot springs and associated deposits in Yellowstone National Park using ASTER and AVIRIS remote sensing. *Journal of Volcanology and Geothermal Research, 135*(1–2), 195–219.

Henley, R. W., & Ellis, A. J. (1983). Geothermal systems, ancient and modern. *Earth Science Reviews, 19*, 1-50.

Hewson, R., Mshiu, E., Hecker, C., van der Werff, H., van Ruitenbeek, F., Alkema, D., & van der Meer, F. (2020). The application of day and night time ASTER satellite imagery for geothermal and mineral mapping in East Africa. *International Journal of Applied Earth Observation and Geoinformation, 85*, 101991.

Hewson, R. D., Cudahy, T. J., & Mizuhiko, S. (2004). Seamless geological map generation using ASTER in the Broken Hill-Curnamona Province of Australia. *Remote Sensing of Environment, 99*(2), 159–172.

Hewson, R. D., Cudahy, T. J., & Huntington, J. F. (2001). Geologic and alteration mapping at Mt Fitton, South Australia, using ASTER satellite-borne data. *International Geosciences and Remote Sensing Symposium*, 2, 724–726.

Hodder, D. T. (1970). Application of remote sensing to geothermal prospecting. *Geothermics, 2*(6), 368-380.

Hubbard, B. E., Crowley, J. K., & Zimbelman, D. R. (2003). Comparative alteration mineral mapping using visible to shortwave infrared (0.4–2.4 µm) Hyperion, ALI, and ASTER imagery. *IEEE Transactions on Geoscience and Remote Sensing, 41*(6), 1401–1410.

Hung, C. C., & Chen, L. H. (2009). A fuzzy TOPSIS decision making model with entropy weight under intuitionistic fuzzy environment. *Proceedings of the*

International Multi-Conference of Engineers and Computer Scientists IMECS, 1, 152-157.

Hunt, G. R. (1979). Near-infrared (1.3–2.4 μm) spectra of alteration minerals: Potential for use in remote sensing. *Geophysics, 44*(12), 1974-1986.

Hunt, G. R., & Ashley, R. P. (1979). Spectra of altered rocks in the visible and near infrared. *Economic Geology, 74*(7), 1613-1629.

Hwang, C. L., & Yoon, K. (1981). *Multiple attribute decision making: Methods and applications: A state-of-the-art survey*. Springer-Verlag. https://doi.org/10.1007/978-3-642-48318-9

Ito, G., Frazer, N., Lautze, N., Thomas, D., Hinz, N., Waller, D., Whittier, R., & Wallin, E. (2017). Play fairway analysis of geothermal resources across the state of Hawaii: 2. Resource probability mapping. *Geothermics, 70*, 393–405.

Jankowski, P., & Ewart, G. (1996). Spatial decision support system for health practitioners: Selecting a location for rural health practice. *Geographical Systems, 3*(2), 279–299.

Kahle, H.-G., Cocard, M., Peter, Y., Geiger, A., Reilinger, R., Barka, A. A., & Veis, G. (2000). GPS-derived strain rate field within the boundary zones of the Eurasian, African, and Arabian plates. *Journal of Geophysical Research, 105*, 23353−23370.

Kaiser, M. F., & Ahmed, S. (2013). Optimal thermal water locations along the Gulf of Suez coastal zones, Egypt. *Renewable Energy, 55*, 374–379.

Karamanderesi, İ. H. (2013). *Characteristics of geothermal reservoirs in Turkey*. IGA Academy Report, 102.

Kiavarz, M., & Jelokhani-Niaraki, M. (2017). Geothermal prospectivity mapping using GIS-based ordered weighted averaging approach: A case study in Japan's Akita and Iwate Provinces. *Geothermics, 70*, 295-304.

Koçyiğit, A., Yusufoğlu, H., & Bozkurt, E. (1999). Evidence from the Gediz Graben for episodic two-stage extension in western Turkey. *Journal of the Geological Society, London, 156*(4), 605–616.

Koçyiğit, A. (2015). An overview on the main stratigraphic and structural features of a geothermal area: The case of Nazilli-Buharkent section of the Büyük Menderes Graben, SW Turkey. *Geodinamica Acta, 27*(2-3), 85-109.

Koppen, W. (1936). *Das geographische System der Klimate*. In *Handbuch der klimatologie*. Berlin, Germany.

Kraal, K. O., Lindsey, C., Zimmerman, J., Sladek, C., & Burgess, Q. (2024). Development of shallow (2-m) temperature survey standard operating procedures and interpretation workbook. In *Proceedings of the 49th Workshop on Geothermal Reservoir Engineering* (SGP-TR-227). Stanford University, Stanford, California, February 12-14, 2024.

Kratt, C., Sladek, C., & Coolbaugh, M. (2010). Boom and bust with the latest two-meter temperature surveys: Dead Horse Wells, Hawthorne Army Depot, Terraced Hills, and other areas in Nevada. *Geothermal Resources Council Transactions, 34*, 567-574.

Kratt, C., Coolbaugh, M., & Calvin, W. (2006). Remote detection of Quaternary borate deposits with ASTER satellite imagery as a geothermal exploration tool. *Geothermal Resources Council Transactions, 30*, 435-439.

Kratt, C., Coolbaugh, M., Peppin, B., & Sladek, C. (2009). Identification of a new, blind geothermal system with hyperspectral remote sensing and shallow temperature measurements at Columbus Salt Marsh, Esmeralda County, Nevada. *Geothermal Resources Council Transactions, 33*, 481-485.

Kratt, C., Coolbaugh, M., Sladek, C., Zehner, R., Penfield, R., & Delwiche, B. (2008). A new gold pan for the west: Discovering blind geothermal systems with shallow temperature surveys. *Geothermal Resources Council Transactions, 32*, 153-158.

Lange, A. L., Pilkington, H. D., & Deymonaz, J. (1982). Comparative studies of geothermal surveys in 3-meter and temperature-gradient holes. *Geothermal Resources Council Transactions, 6*, 133-136.

Lasdon, L. S., Fox, R. L., & Ratner, M. W. (1974). Nonlinear optimization using the generalized reduced gradient method. *Revue française d'automatique, informatique, recherche opérationnelle. Recherche opérationnelle, 8*(V3), 73-103.

Lashin, A., & Al Arifi, N. (2014). Geothermal energy potential of southwestern Saudi Arabia: Exploration and possible power generation: A case study at Al Khouba area–Jizan. *Renewable and Sustainable Energy Reviews, 30*, 771-789.

LeSchack, L. A., & Lewis, J. E. (1983). Geothermal prospecting with shallow-temperature surveys. *Geophysics, 48*(7), 975-996.

Li, J., & Zhang, Z. (2017). GIS-supported certainty factor (CF) models for assessment of geothermal potential: A case study of Tengchong County, Southwest China. *Energy, 140*, 552–565.

Li, Y., Zhang, Y., Zhang, X., Zhao, J., Huang, Y., Wang, Z., & Yi, Y. (2024). Distribution of geothermal resources in Eryuan County based on entropy weight TOPSIS and AHP–TOPSIS methods. *Natural Gas Industry B, 11*(2), 213-226.

Li, Z., Luo, Z., Wang, Y., Fan, G., & Zhang, J. (2022). Suitability evaluation system for the shallow geothermal energy implementation in a region by Entropy Weight Method and TOPSIS method. *Renewable Energy, 184*, 564-576.

Liotta, D., & Brogi, A. (2020). Pliocene-Quaternary fault kinematics in the Larderello geothermal area (Italy): Insights for the interpretation of the present stress field. *Geothermics, 83*, 101714.

Liu, C., Frazier, P., Kumar, L., Macgregor, C., & Blake, N. (2006). Catchment-wide wetland assessment and prioritization using the multi-criteria decision-making method TOPSIS. *Environmental Management, 32*(2), 316–326.

Malczewski, J. (1996). A GIS-based approach to multiple criteria group decision-making. *International Journal of Geographical Information Science, 10*, 955–971.

Malczewski, J., & Rinner, C. (2015). *Multicriteria decision analysis in geographic information science*. Springer.

Malczewski, J. (1999). *GIS and multicriteria decision analysis*. John Wiley & Sons.

Mars, J. C., & Rowan, L. C. (2006). Regional mapping of phyllic- and argillic-altered rocks in the Zagros magmatic arc, Iran, using Advanced Spaceborne Thermal Emission and Reflection Radiometer (ASTER) data and logical operator algorithms. *Geosphere, 2*(3), 161-186.

Mars, J. C., & Rowan, L. C. (2010). Spectral assessment of new ASTER SWIR surface reflectance data products for spectroscopic mapping of rocks and minerals. *Remote Sensing of Environment, 114*(9), 2011–2025. https://doi.org/10.1016/j.rse.2010.04.006

Maswi, M. S., & Mshiu, E. E. (2024). Remote sensing mapping of geothermal systems around Lake Natron in the East Africa Rift System, northeastern Tanzania. *Geothermics, 119*, 102930. https://doi.org/10.1016/j.geothermics.2024.102930

Matthew, M. W., Adler-Golden, M. S. M., Berk, A., Richtsmeier, S. C., Levine, R. Y., Bernstein, L. S., Acharya, P. K., Anderson, G. P., Felde, G. W., Hoke, M. L., Ratkowski, A. J., Burke, H.-H., & Miller, D. (2000). Status of atmospheric correction using a MODTRAN4-based algorithm. In S. S. Chen & M. R. Descour (Eds.), *Algorithms for multispectral, hyperspectral, and ultraspectral imagery VI* (Vol. 4049, p. 207). SPIE. https://doi.org/10.1117/12.388326

Maxim Integrated. (2019). *DS18B20 Programmable resolution 1-wire digital thermometer datasheet*.

McKenzie, D. (1978). Some remarks on the development of sedimentary basins. *Earth and Planetary Science Letters, 40*(1), 25–32. https://doi.org/10.1016/0012-821X(78)90071-5

Menard, S. (1978). *Applied logistic regression analysis*. Sage University Series on Quantitative Applications in the Social Sciences. Sage.

Mia, M. B., Bromley, C. J., & Fujimitsu, Y. (2012). Monitoring heat flux using Landsat TM/ETM+ thermal infrared data—A case study at Karapiti ('Craters of the Moon') thermal area, New Zealand. *Journal of Volcanology and Geothermal Research, 235*, 1-10. https://doi.org/10.1016/j.jvolgeores.2012.05.015

Moeck, I. S. (2014). Catalog of geothermal play types based on geologic controls. *Renewable and Sustainable Energy Reviews, 37*, 867-882. https://doi.org/10.1016/j.rser.2014.05.039

Moghaddam, M. K., Noorollahi, Y., Samadzadegan, M. K., Sharifi, M. A., & Itoi, R. (2013). Spatial data analysis for exploration of regional scale geothermal resources. *Geothermics, 41*, 69–83. https://doi.org/10.1016/j.geothermics.2012.11.001

Moghaddam, M. K., Samadzadegan, F., Noorollahi, Y., Sharifi, M. A., & Itoi, R. (2014). Spatial analysis and multi-criteria decision making for regional-scale geothermal favorability map. *Geothermics, 50*, 189–201. https://doi.org/10.1016/j.geothermics.2014.02.002

Monolithic Power Systems. (2014). *MP158 small, energy-efficient, off-line regulator 30mW no-load power consumption* (Rev. 1.0).

MTA. (2002). *1/500,000 scale geological maps*. General Directorate of Mineral Research and Exploration (MTA), Turkey.

Nama, E. E. (2004). Lineament detection on Mount Cameroon during the 1999 volcanic eruptions using Landsat ETM. *International Journal of Remote Sensing*, *25*(3), 501-510. https://doi.org/10.1080/0143116031000160251б

NASA LP DAAC. (2015). ASTER Level 1 Precision Terrain Corrected Registered At-Sensor Radiance V003 [Data set]. NASA EOSDIS Land Processes Distributed Active Archive Center. Accessed January 22, 2024, from https://doi.org/10.5067/ASTER/AST_L1T.003

Nevada State Climate Office. (2024). *Nevada is the driest state in the U.S.* Retrieved June 15, 2024, from https://www.unr.edu/nevada-climate-office/about-our-climate#:~:text=Nevada%20is%20the%20driest%20state,northeastern%20 Nevada%2C%20averaging%2012.85%E2%80%B3.

Ninomiya, Y. (2004, February). Lithologic mapping with multispectral ASTER TIR and SWIR data. In *Sensors, Systems, and Next-Generation Satellites VII* (Vol. 5234, pp. 180-190). SPIE. https://doi.org/10.1117/12.505076

Ninomiya, Y., & Fu, B. (2019). Thermal infrared multispectral remote sensing of lithology and mineralogy based on spectral properties of materials. *Ore Geology Reviews*, *108*, 54-72. https://doi.org/10.1016/j.oregeorev.2019.03.002

Ninomiya, Y. (2002). Mapping quartz, carbonate minerals, and mafic–ultramafic rocks using remotely sensed multispectral thermal infrared ASTER data. In *Proceedings of SPIE* (Vol. 4710, pp. 191–202). SPIE. https://doi.org/10.1117/12.471646

Ninomiya, Y. (2003). Rock type mapping with indices defined for multispectral thermal infrared ASTER data: Case studies. In *Proceedings of SPIE* (Vol. 4886, pp. 123–132). SPIE. https://doi.org/10.1117/12.459735

Ninomiya, Y., & Fu, B. (2001). Spectral indices for lithologic mapping with ASTER thermal infrared data applying to a part of Beishan Mountains, Gansu, China.

In *IGARSS 2001* (Vol. 7, pp. 2988–2990). IEEE. https://doi.org/10.1109/IGARSS.2001.976464

Ninomiya, Y., & Fu, B. (2002). Quartz index, carbonate index, and SiO2 content index defined for ASTER TIR data. *Journal of the Remote Sensing Society of Japan, 22*(1), 50–61. https://doi.org/10.11440/rssj.22.50

Ninomiya, Y., & Fu, B. (2003). Extracting lithologic information from ASTER multispectral thermal infrared data in the northeastern Pamirs. *Xinjiang Geology, 21*, 22–30.

Ninomiya, Y., & Fu, B. (2016). Regional lithological mapping using ASTER-TIR data: Case study for the Tibetan Plateau and the surrounding area. *Geosciences, 6*(2), 39. https://doi.org/10.3390/geosciences6020039

Ninomiya, Y., Fu, B., & Cudahy, T. J. (2005). Detecting lithology with Advanced Spaceborne Thermal Emission and Reflection Radiometer (ASTER) multispectral thermal infrared "radiance-at-sensor" data. *Remote Sensing of Environment, 99*(1), 127–139. https://doi.org/10.1016/j.rse.2005.01.016

Nishar, A., Richards, S., Breen, D., Robertson, J., & Breen, B. (2016). Thermal infrared imaging of geothermal environments by an unmanned aerial vehicle (UAV): A case study of the Wairakei–Tauhara geothermal field, Taupo, New Zealand. *Renewable Energy, 86*, 1256-1264. https://doi.org/10.1016/j.renene.2015.09.041

Noorollahi, Y., Itoi, R., Fujii, H., & Tanaka, T. (2008). GIS integration model for geothermal exploration and well siting. *Geothermics, 37*(2), 107–131. https://doi.org/10.1016/j.geothermics.2008.01.002

Norusis, M. (2004). *SPSS 13.0 guide to data analysis*. Prentice Hall.

Okay, A. I. (2001). Stratigraphic and metamorphic inversions in the central Menderes Massif: A new structural model. *International Journal of Earth Sciences, 89*(4), 709–727. https://doi.org/10.1007/s005310000152

Olmsted, F. H., & Ingebritsen, S. E. (1986). Shallow subsurface temperature surveys in the Basin and Range Province—II. Ground temperatures in the Upsal Hogback geothermal area, West-Central Nevada, USA. *Geothermics, 15*(3), 267–275. https://doi.org/10.1016/0375-6505(86)90012-1

Olmsted, F. H. (1977). Use of temperature surveys at a depth of 1 meter in geothermal exploration in Nevada. *United States Geological Survey Professional Paper 1044-B*, 25 p.

Olvera-García, E., Ayling, B. F., Rueda-Gutiérrez, J. B., Rivera, A. M. M., Rodríguez-Rodríguez, G. F., Malo, J., ... & Alfaro-Valero, C. M. (2023). Expert-driven play fairway analysis applied to the Azufral Volcano Geothermal Area in southwestern Colombia. *Geothermics, 115*, 102827. https://doi.org/10.1016/j.geothermics.2023.102827

Olvera-García, E., Garduño-Monroy, V. H., Liotta, D., Brogi, A., Bermejo-Santoyo, G., & Guevara-Alday, J. A. (2020). Neogene-Quaternary normal and transfer faults controlling deep-seated T geothermal systems: The case of San Agustín del Maíz (central Trans-Mexican Volcanic Belt, México). *Geothermics, 86*, 101791. https://doi.org/10.1016/j.geothermics.2019.101791

Pandarinath, K., Torres-Alvarado, I. S., Pushparani, D. E., & Verma, S. P. (2006). X-ray diffraction analysis of hydrothermal minerals from the Los Azufres geothermal system, Mexico. *International Geology Review, 48*(2), 174–190. https://doi.org/10.2747/0020-6814.48.2.174

Pazanda, K., Hezarkhani, A., & Mohammad, A. (2012). Using TOPSIS approaches for predictive porphyry Cu potential mapping: A case study in Ahar-Arasbaran area (NW, Iran). *Computers & Geosciences, 49*, 62–71. https://doi.org/10.1016/j.cageo.2012.06.007

PCI Geomatics Enterprises Inc. (2010). *PCI Geomatica-10, version 10.3.1*. Richmond Hill, Ontario, Canada.

Pereira, J. M. C., & Duckstein, L. (1993). A multiple criteria decision-making approach to GIS-based land suitability evaluation. *International Journal of Geographical Information Science, 7*(5), 407–424. https://doi.org/10.1080/02693799308901916

Pour, A. B., & Hashim, M. (2012). The application of ASTER remote sensing data to porphyry copper and epithermal gold deposits. *Ore Geology Reviews, 44*, 1–9. https://doi.org/10.1016/j.oregeorev.2011.12.001

Pour, A. B., Hashim, M., & van Genderen, J. (2013). Detection of hydrothermal alteration zones in a tropical region using satellite remote sensing data: Bau goldfield, Sarawak, Malaysia. *Ore Geology Reviews, 54*, 181–196. https://doi.org/10.1016/j.oregeorev.2013.05.003

Pournamdari, M., & Hashim, M. (2014). Detection of chromite-bearing mineralized zones in Abdasht ophiolite complex using ASTER and ETM+ remote sensing data. *Arabian Journal of Geosciences, 7*(5), 1973–1983. https://doi.org/10.1007/s12517-013-1074-6

Prato, T. (2008). Stochastic multiple attribute evaluation of land use policies. *Ecological Modelling, 219*(1–2), 115–124. https://doi.org/10.1016/j.ecolmodel.2008.07.016

Prol-Ledesma, R. (2000). Evaluation of the reconnaissance results in geothermal exploration using GIS. *Geothermics, 29*(1), 83–103. https://doi.org/10.1016/S0375-6505(99)00053-2

Qin, Q., Zhang, N., Nan, P., & Chai, L. (2011). Geothermal area detection using Landsat ETM+ thermal infrared data and its mechanistic analysis—A case study in Tengchong, China. *International Journal of Applied Earth Observation and Geoinformation, 13*(4), 552–559. https://doi.org/10.1016/j.jag.2011.01.006

Reath, K. A., & Ramsey, M. S. (2013). Exploration of geothermal systems using hyperspectral thermal infrared remote sensing. *Journal of Volcanology and*

Geothermal Research, 265, 27–38. https://doi.org/10.1016/j.jvolgeores.2013.07.007

Ring, U., Willner, A., & Lackmann, W. (2001). Nappe stacking and clockwise versus anticlockwise pressure-temperature paths: An example from the Menderes nappes of western Turkey. *American Journal of Science, 301*(10), 912–944. https://doi.org/10.2475/ajs.301.10.912

Ring, U., Laws, S., & Bernet, M. (1999). Structural analysis of a complex nappe sequence and late-orogenic basins from the Aegean Island of Samos, Greece. *Journal of Structural Geology, 21*(11), 1575–1601. https://doi.org/10.1016/S0191-8141(99)00040-4

Roche, V., Bouchot, V., Beccaletto, L., Jolivet, L., Guillou-Frottier, L., Tuduri, J., ... & Tokay, B. (2019). Structural, lithological, and geodynamic controls on geothermal activity in the Menderes geothermal Province (Western Anatolia, Turkey). *International Journal of Earth Sciences, 108*(1), 301–328. https://doi.org/10.1007/s00531-019-01760-8

Rockwell, B. W., & Hofstra, A. H. (2008). Identification of quartz and carbonate minerals across northern Nevada using ASTER thermal infrared emissivity data—Implications for geologic mapping and mineral resource investigations in well-studied and frontier areas. *Geosphere, 4*(1), 218–246. https://doi.org/10.1130/GES00107.1

Rogerson, P. A. (2001). *Statistical methods for geography*. Sage.

Romaguera, M., Vaughan, R. G., Ettema, J., Izquierdo-Verdiguier, E., Hecker, C. A., & Van der Meer, F. D. (2018). Detecting geothermal anomalies and evaluating LST geothermal component by combining thermal remote sensing time series and land surface model data. *Remote Sensing of Environment, 204*, 534–552. https://doi.org/10.1016/j.rse.2017.10.027

Rowan, L. C., & Mars, J. C. (2003). Lithologic mapping in the Mountain Pass, California area using advanced spaceborne thermal emission and reflection radiometer (ASTER) data. *Remote Sensing of Environment, 84*(3), 350–366. https://doi.org/10.1016/S0034-4257(02)00145-7

Rowan, L. C., Hook, S. J., Abrams, M. J., & Mars, J. C. (2003). Mapping hydrothermally altered rocks at Cuprite, Nevada, using the Advanced Spaceborne Thermal Emission and Reflection Radiometer (ASTER), a new satellite-imaging system. *Economic Geology, 98*(5), 1019–102

Rowan, L. C., & Mars, J. C. (2003). Lithologic mapping in the Mountain Pass, California, using Advanced Spaceborne Thermal Emission and Reflection Radiometer (ASTER) data. *Remote Sensing of Environment, 84*(3), 350–366. https://doi.org/10.1016/S0034-4257(02)00145-7

Saaty, T. L. (1980). *The analytic hierarchy process*. McGraw-Hill.

Schiffman, P., & Fridleifsson, G. O. (1991). The smectite–chlorite transition in drillhole NJ-15, Nesjavellir geothermal field, Iceland: XRD, BSE, and electron microprobe investigations. *Journal of Metamorphic Geology, 9*(6), 679–696. https://doi.org/10.1111/j.1525-1314.1991.tb00495.x

Schlumberger. (2015). *3D modelling of magnetotelluric data Kuyucak, Aydın-Turkey* (unpublished).

SDS Energy. (2012). *Kuyucak geothermal field report* (unpublished). Ankara.

Sekandari, M., Masoumi, I., Pour, A. B., Muslim, A. M., Hossain, M. S., & Misra, A. (2022). ASTER and WorldView-3 satellite data for mapping lithology and alteration minerals associated with Pb-Zn mineralization. *Geocarto International, 37*(6), 1782–1812. https://doi.org/10.1080/10106049.2021.1908775

Şengör, A. M. C., Görür, N., & Şaroğlu, F. (1985). Strike-slip faulting and related basin formation in zones of tectonic escape: Turkey as a case study. In K. T. Biddle & N. Christie-Blick (Eds.), *Strike-slip faulting and basin formation*

(Vol. 37, pp. 227–264). Society of Economic Paleontologists and Mineralogists.

Seyitoğlu, G., & Scott, B. (1991). Late Cenozoic crustal extension and basin formation in west Turkey. *Geological Magazine, 12*(2), 155–166. https://doi.org/10.1017/S0016756800012122

Shervais, J. W., DeAngelo, J., Glen, J. M., Nielson, D. L., Garg, S., Dobson, P., ... & Evans, J. P. (2024). Geothermal play fairway analysis, part 1: Example from the Snake River Plain, Idaho. *Geothermics, 117*, 102865. https://doi.org/10.1016/j.geothermics.2023.102865

Shervais, J. W., Glen, J. M., Liberty, L. M., Dobson, P., Gasperikova, E., Sonnenthal, E., Shevenell, L., Coolbaugh, M., Zehner, R., Johnson, G., Ehni, W., & Noel, D. (2014). Geothermal exploration at Emerson Pass, Pyramid Paiute Tribal Lands, Nevada. *GRC Transactions, 38*, 29–37.

Siler, D. L., Zhang, Y., Spycer, N. F., Dobson, P. F., McClain, J. S., Gasperikova, E., Sladek, C., Coolbaugh, M. F., & Kratt, C. (2009). Improvements in shallow (two-meter) temperature measurements and data interpretation. *Geothermal Resources Council Transactions, 33*, 535–541.

Sladek, C., Coolbaugh, M. F., & Zehner, R. E. (2007). Development of 2-meter soil temperature probes and results of temperature survey conducted at Desert Peak, Nevada, USA. *Geothermal Resources Council Transactions, 31*, 363–368.

Sladek, C., Coolbaugh, M. F., Penfield, R., Skord, J., & Williamson, L. (2012). The influences of thermal diffusivity and weather on shallow (2-meter) temperature measurements. *Geothermal Resources Council Transactions, 36*, 793–797.

Spatz, D. M., Wilson, R. T., Pierce, F. W., & Bolm, J. G. (1995). Remote sensing characteristics of porphyry copper systems, western American Cordillera. *Arizona Geological Society Digest, 20*, 94–108.

Tanjung, F. H., Rahmadhani, A. U., Sihombing, F. M. H., & Sahdarani, D. N. (2020, July). Lineament mapping using remote sensing and correlation on surface manifestation distribution in Gunung Endut, Banten Province, Indonesia. In *IOP Conference Series: Earth and Environmental Science* (Vol. 538, No. 1, p. 012051). IOP Publishing. https://doi.org/10.1088/1755-1315/538/1/012051

Tezcan, A. K. (1995). Geothermal explorations and heat flow in Turkey. In M. L. Gupta & M. Yamano (Eds.), *Terrestrial heat flow and geothermal energy in Asia* (pp. 23–42). Oxford and IBH Publishing Co., Pvt. Ltd.

Tian, B., Wang, L., Kashiwaya, K., & Koike, K. (2015). Combination of well-logging temperature and thermal remote sensing for characterization of geothermal resources in Hokkaido, northern Japan. *Remote Sensing, 7*(3), 2647–2667. https://doi.org/10.3390/rs70302647

Trexler, D. T., Koenig, B. A., Ghusn, G. Jr., Flynn, T., & Bell, E. J. (1981). Low-to-moderate-temperature geothermal resource assessment for Nevada: Area specific studies, Hawthorne, Paradise Valley, and southern Carson Sink. *United States Department of Energy Geothermal Energy Report DOE/NV/10039-3* (DE81030487), 203 p.

Trexler, D. T., Koenig, B. A., Ghusn, G. Jr., Flynn, T., & Bell, E. J. (1982). Low-to-moderate-temperature geothermal resource assessment for Nevada: Area specific studies, Pumpernickel Valley, Carlin, and Moana. *United States Department of Energy Geothermal Energy Report DOE/NV/1022-1* (DE82018598), 177 p.

Tüfekçi, N., Süzen, M. L., & Güleç, N. (2010). GIS based geothermal potential assessment: A case study from Western Anatolia, Turkey. *Energy, 35*(1), 246–261. https://doi.org/10.1016/j.energy.2009.08.013

Turkish State Meteorology Service. (2024). *Veri değerlendirme: İl ve ilçeler istatistik*. Retrieved June 15, 2024, from https://www.mgm.gov.tr/veridegerlendirme/il-ve-ilceler-istatistik.aspx?m=AYDIN

Van der Meer, F., Hecker, C., van Ruitenbeek, F., van der Werff, H., de Wijkerslooth, C., & Wechsler, C. (2014). Geologic remote sensing for geothermal exploration: A review. *International Journal of Applied Earth Observation and Geoinformation*, *33*, 255–269. https://doi.org/10.1016/j.jag.2014.05.002

Vaughan, R. G., Keszthelyi, L. P., Davies, A. G., Schneider, D. J., Jaworowski, C., & Heasler, H. (2010). Exploring the limits of identifying sub-pixel thermal features using ASTER TIR data. *Journal of Volcanology and Geothermal Research*, *189*(3-4), 225–237. https://doi.org/10.1016/j.jvolgeores.2009.10.010

Vaughan, R. G., Keszthelyi, L. P., Lowenstern, J. B., Jaworowski, C., & Heasler, H. (2012). Use of ASTER and MODIS thermal infrared data to quantify heat flow and hydrothermal change at Yellowstone National Park. *Journal of Volcanology and Geothermal Research*, *233*, 72–89. https://doi.org/10.1016/j.jvolgeores.2012.03.002

Vázquez, M., Nieto, F., Morata, D., Droguett, B., Carrillo-Rosua, F. J., & Morales, S. (2014). Evolution of clay mineral assemblages in the Tinguiririca geothermal field, Andean Cordillera of central Chile: An XRD and HRTEM-AEM study. *Journal of Volcanology and Geothermal Research*, *282*, 43–59. https://doi.org/10.1016/j.jvolgeores.2014.07.002

Verge, N. J. (1995). Oligo-Miocene extensional exhumation of the Menderes Massif, Western Anatolia. *Terra Abstracts*, *7*, 117.

Visse, C., Nielson, D., Sabodh, G. G., Evans, J. P., Siler, D., DeAngelo, J., Athens, N., & Wald, L. (2018). Basics in solar radiation at Earth surface.

Warr, L. N. (2020). Recommended abbreviations for the names of clay minerals and associated phases. *Clay Minerals, 55*(3), 261–264. https://doi.org/10.1180/claymin.2020.055.3.01

Warr, L. N. (2021). IMA–CNMNC approved mineral symbols. *Mineralogical Magazine, 85*(3), 291–320. https://doi.org/10.1180/mgm.2021.41

Yal, G. P., & Akgün, H. (2013). Landfill site selection and landfill liner design for Ankara, Turkey. *Environmental Earth Sciences, 70*(7), 2729–2752. https://doi.org/10.1007/s12665-013-2322-6

Yal, G. P., & Akgün, H. (2014). Landfill site selection utilizing TOPSIS methodology and clay liner geotechnical characterization: A case study for Ankara, Turkey. *Bulletin of Engineering Geology and the Environment, 73*(2), 369–388. https://doi.org/10.1007/s10064-013-0540-x

Yal, G. P., Cambazoğlu, S., Eker, A. M., Sen, O., & Akgün, H. (2021, April-October). Assessment of the ability of GIS based MCDA methods to reveal the geothermal potential of the Büyük Menderes Graben. In *World Geothermal Congress 2020+1*, Reykjavik, Iceland. [Conference presentation].

Yal, G. P., Eker, A. M., Cambazoğlu, S., Akgün, H., & Şen, O. (2017, February 13-15). Assessment of the early development work for Kuyucak Geothermal Field, Turkey. In *42nd Workshop on Geothermal Reservoir Engineering*, Stanford, California, USA. [Conference presentation].

Yalcin, M., Kilic Gul, F., Yildiz, A., Polat, N., & Basaran, C. (2020). The mapping of hydrothermal alteration related to geothermal activities with remote sensing at Akarcay Basin (Afyonkarahisar), using ASTER data. *Arabian Journal of Geosciences, 13*(21), 1166. https://doi.org/10.1007/s12517-020-05328-4

Yalcin, M., & Kilic Gul, F. (2017). A GIS-based multi-criteria decision analysis approach for exploring geothermal resources: Akarcay Basin

(Afyonkarahisar). *Geothermics, 67*, 18–28. https://doi.org/10.1016/j.geothermics.2017.01.002

Yıldız, A., Başaran, C., Bağcı, M., Dülger, A., & Ulutürk, Y. (2020). Borehole geology and alteration mineralogy of well Bayatcık-1, Bayatcık Geothermal Area, Afyonkarahisar. *Afyon Kocatepe Üniversitesi Fen ve Mühendislik Bilimleri Dergisi, 20*(4), 683–692. https://doi.org/10.5505/akufemubid.2020.547559

Yousefi, H., Ehara, S., & Noorollahi, Y. (2007). Geothermal potential site selection using GIS in Iran. In *Proceedings of the 32nd Workshop on Geothermal Reservoir Engineering*, Stanford University, Stanford, CA (pp. 174–182).

Yousefi, H., Noorollahi, Y., Ehara, S., Itoi, R., Yousefi, A., Fujimitsu, Y., Nishijima, J., & Sasaki, K. (2010). Developing the geothermal resources map of Iran. *Geothermics, 39*(3), 140–151. https://doi.org/10.1016/j.geothermics.2010.02.001

Zhang, Y., Xie, Y., Zhang, T., Liu, T., & Zhang, C. (2016). 2 m survey method and its improved device application in Dongshan geothermal field in Xiamen, China. *Environmental Earth Sciences, 75*(1), 1–16. https://doi.org/10.1007/s12665-015-4997-5

Zierenberg, R. A., Schiffman, P., Ferguson, C., Fowler, A., & Cantwell, C. (2017). Play fairway analysis for geothermal resources and exploration risk in the Modoc Plateau region. *Geothermics, 69*, 15–33. https://doi.org/10.1016/j.geothermics.2017.01.003

Zlatopolsky, A. A. (1992). Program LESSA (Lineament Extraction and Stripe Statistical Analysis) automated linear image features analysis—Experimental results. *Computers & Geosciences, 18*(9), 1121–1126. https://doi.org/10.1016/0098-3004(92)90066-9

Zlatopolsky, A. A. (1997). Description of texture orientation in remote sensing data using computer program LESSA. *Computers & Geosciences, 23*(1), 45–62. https://doi.org/10.1016/S0098-3004(96)00128-1

APPENDICES

A. Example Arduino Code for Data Loggers

```
#include <DallasTemperature.h>
#include <OneWire.h>
#include <SD.h>
#include <SPI.h>
#include <DS3231.h>
#include <OneWire.h>
#include <LowPower.h>
#include "LowPower.h"
float arrayProbe102[10], sum102 = 0.0, avg102;
float arrayProbe202[10], sum202 = 0.0, avg202;
float arrayProbe302[10], sum302 = 0.0, avg302;
float arrayProbe502[10], sum502 = 0.0, avg502;
int size = 10;
File data_file; //FOR SD
DS3231 rtc(SDA, SCL); //FOR RTC
#define ONE_WIRE_BUS_PIN 2 // The pin that we are using for sensors
OneWire oneWire(ONE_WIRE_BUS_PIN); // Setup oneWire
DallasTemperature sensors(&oneWire); // oneWire to Dallas Temperature.
int chip_select_pin = 10; //pin 53 for arduino mega 2560 FOR TEMP
// Assign the addresses of your temp sensors.
//Every sensor has it own address.You must use 1 wire adress finder.
DeviceAddress Probe102 = { 0x28, 0xF5, 0x5A, 0x76, 0xE0, 0x01, 0x3C,
0x10}; //inox1
DeviceAddress Probe202 = { 0x28, 0xFF, 0xAD, 0xB3, 0x30, 0x18, 0x01,
0x94}; //Inox2
```

```
DeviceAddress Probe302 = { 0x28, 0x81, 0x3F, 0x75, 0xD0, 0x01, 0x3C, 0xC1}; //Inox3
DeviceAddress Probe502 = { 0x28, 0x1F, 0x90, 0xEE, 0x17, 0x20, 0x06, 0xA6}; //Inox4
void setup()
{
(SD.begin());
Serial.begin(9600);
sensors.begin();
rtc.begin();
pinMode(chip_select_pin, OUTPUT);

sensors.setResolution(Probe102, 12);
sensors.setResolution(Probe202, 12);
sensors.setResolution(Probe302, 12);
sensors.setResolution(Probe502, 12);
}
void loop() {
 // Enter power down state for 8 s with ADC and BOD module disabled
for (int i=0; i<35; i++) {
LowPower.powerDown(SLEEP_8S, ADC_OFF, BOD_OFF);
}
float sum102 = 0, sum202 = 0, sum302 = 0, sum502 = 0;
for (int j=0; j<10; j++) {

sensors.requestTemperatures(); // Command all devices on bus to read temperature
   float tempC1 = sensors.getTempC(Probe102);
   float tempC2 = sensors.getTempC(Probe202);
   float tempC3 = sensors.getTempC(Probe302);
```

```
float tempC4 = sensors.getTempC(Probe502);

arrayProbe102[j] = tempC1;
sum102 += arrayProbe102[j];
avg102 = sum102/ size;

arrayProbe202[j] = tempC2;
sum202 += arrayProbe202[j];
avg202 = sum202 / size;

arrayProbe302[j] = tempC3;
sum302 += arrayProbe302[j];
avg302 = sum302/ size;

arrayProbe502[j] = tempC4;
sum502+= arrayProbe502[j];
avg502 = sum502 / size;

if (j == 9) {
data_file = SD.open("logger2.txt", FILE_WRITE);
{ (data_file) ;
data_file.print(rtc.getDateStr());
Serial.print(rtc.getDateStr());
data_file.print(", ");
Serial.print(", ");
data_file.print(rtc.getTimeStr());
Serial.print(rtc.getTimeStr());
data_file.print(", ");
Serial.print(", ");
Serial.print (avg102, 5);
```

```
    data_file.print (avg102, 5);
    Serial.print(", ");
    data_file.print(", ");
    Serial.print (avg202, 5);
    data_file.print (avg202, 5);
    Serial.print(", ");
    data_file.print(", ");
    Serial.print (avg302, 5);
    data_file.print (avg302, 5);
    Serial.print(", ");
    data_file.print(", ");
    Serial.print (avg502, 5);
    data_file.print (avg502, 5);
    Serial.println(); //New Line
    data_file.println(); //New Line

    data_file.close(); //Print saved
}
    delay(100);
}
}
```

CURRICULUM VITAE

Surname, Name: Cambazoğlu, Selim

EDUCATION

Degree	Institution	Year of Graduation
M.Sc.	METU, Geological Engineering	2012
B.S.	METU Geological Engineering	2008
High School	İzmir Atatürk High School, İzmir	2001

FOREIGN LANGUAGES

Fluent English

PUBLICATIONS

Cambazoglu, S., Yal, G. P., Arslan Kelam, A., Akgün, H., & Koçkar, M. K. (2023). *Use of ASTER satellite images along with field applications for alteration mineral mapping for the Aydın-Kuyucak geothermal field*. Paper presented at the 19th National Clay Symposium, Eskişehir Teknik Üniversitesi, Eskişehir, Türkiye.

Cambazoglu, S., Yal, G. P., Eker, A. M., Sen, O., & Akgün, H. (2021). *Geothermal favorability assessment of the Gediz Graben through correlation and GIS-based MCDA methodologies*. Paper presented at the World Geothermal Congress 2020+1, Reykjavik, Iceland.

Yal, G. P., Cambazoglu, S., Eker, A. M., Sen, O., & Akgün, H. (2021). *Assessment of the ability of GIS-based MCDA methods to reveal the geothermal potential of the Büyük Menderes Graben*. Paper presented at the World Geothermal Congress 2020+1, Reykjavik, Iceland.

Cambazoglu, S., Yal, G. P., Eker, A. M., Sen, O., & Akgün, H. (2019). Geothermal resource assessment of the Gediz Graben utilizing TOPSIS methodology. *Geothermics, 80*, 92–102. https://doi.org/10.1016/j.geothermics.2019.04.003

Cambazoğlu, S., Koçkar, M. K., & Akgün, H. (2017). *Generation of a seismic source model for the Eastern Marmara region by using lineament extraction from ASTER satellite imagery and literature sources*. Paper presented at the 4th Conference on Earthquake Engineering and Seismology of Turkey, Anadolu University, Eskişehir, Türkiye.

Yal, G. P., Eker, A. M., Cambazoğlu, S., Akgün, H., & Şen, O. (2017). *Assessment of the early development work for Kuyucak geothermal field, Turkey*. Paper presented at the 42nd Workshop on Geothermal Reservoir Engineering, Stanford, California, USA.

Cambazoğlu, S., Eker, A. M., Yal, G. P., Akgün, H., Dünya, H., & Şen, O. (2017). *Assessment of the geothermal potential of the Gediz Graben, Manisa, Turkey*. Paper presented at the 42nd Workshop on Geothermal Reservoir Engineering, Stanford, California, USA.

Eker, A. M., Yal, G. P., Cambazoğlu, S., Şen, O., & Dünya, H. (2017). *Enhancement of geothermal reservoir through varying acidizing operation procedures in Aydın Kuyucak geothermal field*. Paper presented at the 42nd Workshop on Geothermal Reservoir Engineering, Stanford, California, USA.

Cambazoğlu, S., Koçkar, M. K., & Akgün, H. (2016). A generalized seismic source model for the Eastern Marmara region along the segments of the North Anatolian Fault System. *Soil Dynamics and Earthquake Engineering, 88*, 412–426. https://doi.org/10.1016/j.soildyn.2016.07.004

Hou, Z., Şen, O., Gou, Y., Eker, A. M., Li, M., Yal, G. P., Cambazoğlu, S., & Were, P. (2015). Preliminary geological, geochemical, and numerical study on the first EGS project in Turkey. *Environmental Earth Sciences, 73*(11), 6747–6767. https://doi.org/10.1007/s12665-015-4231-7

Yousefi-Bavil, K., Akgün, H., Eker, A. M., Cambazoğlu, S., & Koçkar, M. K. (2015). *Integration of surface wave seismic survey testing results and segmented seismic source model of NAFS for PSHA of the Gölyaka-Düzce Tectonic Basin, Turkey*. Paper presented at the 6th International Conference on Earthquake Geotechnical Engineering, Christchurch, New Zealand.

Yousefi-Bavil, Eker, A. M., Cambazoğlu, S., Koçkar, M. K., & Akgün, H. (2015). *PSHA of Gölyaka-Düzce Tectonic Basin through integration of surface wave survey results*. Paper presented at the 3rd Earthquake Engineering and Seismology Conference of Turkey, DEU, Izmir, Turkey.

Şen, O., Dünya, H., Yal, G. P., Cambazoğlu, S., & Eker, A. M. (2015). *Spatial assessment of geothermal potential with current geothermal data and geological factors: Büyük Menderes Graben example*. Paper presented at the 3rd Geothermal Resources Symposium and Exhibition, Ankara, Turkey.

Şen, O., Eker, A. M., Cambazoğlu, S., Yal, G. P., & Hou, M. Z. (2015). *First Enhanced Geothermal Systems project in Turkey, Dikili-İzmir*. Paper presented at the Geothermal Resources Symposium, İzmir, Turkey.

Cambazoğlu, S., Yal, G. P., Eker, A. M., Koçkar, M. K., Şen, O., & Akgün, H. (2015). *Surface temperature mapping and investigation of geothermal anomalies by using ASTER images for geothermal exploration*. Paper presented at the 68th Geological Congress of Turkey, Ankara, Turkey.

Eker, A. M., Dikmen, M., Cambazoğlu, S., Düzgün, Ş. H., & Akgün, H. (2014). Evaluation and comparison of landslide susceptibility mapping methods: A case study for the Ulus district, Bartın, northern Turkey. *International Journal of Geographical Information Science, 29*(1), 132–158. https://doi.org/10.1080/13658816.2014.976143

Yal, G. P., Cambazoğlu, S., Eker, A. M., Şen, O., Koçkar, M. K., & Akgün, H. (2014). *Thermal anomaly and alteration mineral mapping at İzmir-Dikili region by using ASTER and investigation of geothermal potential of the region*. Paper presented at the 3rd Turkey National Geological Remote Sensing Symposium (JEOUZAL-3), 81–84.

Dikmen, M., Eker, A. M., Cambazoğlu, S., & Akgün, H. (2014). *Effect of spatial resolution on landslide susceptibility mapping*. Paper presented at the 3rd Turkey National Geological Remote Sensing Symposium (JEOUZAL-3), 49–52.

Cambazoğlu, S., Akgün, H., Eker, A. M., & Koçkar, M. K. (2013). *Probabilistic seismic hazard assessment with the integration of local site characterization studies for Düzce Province, Turkey*. Paper presented at the SE-50EEE International Conference on Earthquake Engineering, Skopje, North Macedonia.

Cambazoğlu, S., Eker, A. M., Koçkar, M. K., & Akgün, H. (2013). *Preparation of a seismic source model for Kilis and its vicinity, and an example seismic hazard assessment study for the Şahinbey District*. Paper presented at the 2nd Conference on Earthquake Engineering and Seismology of Turkey, Mustafa Kemal University, Hatay, Turkey.

Cambazoğlu, S., Koçkar, M. K., & Akgün, H. (2013). *A seismic source model for seismic hazard assessment of the Eastern Marmara region: An application for the segments of the North Anatolian Fault System*. Paper presented at the 2nd Conference on Earthquake Engineering and Seismology of Turkey, Mustafa Kemal University, Hatay, Turkey.

Eker, A. M., Dikmen, M., Cambazoğlu, S., Düzgün, Ş. H., & Akgün, H. (2012). Application of artificial neural network and logistic regression methods to landslide susceptibility mapping and comparison of the results for the Ulus District, Bartın. *Journal of the Faculty of Engineering and Architecture of Gazi University, 27*(1), 163–173.

Cambazoğlu, S., Akgün, H., & Koçkar, M. K. (2012). *Preparation of a line source model for probabilistic seismic hazard analyses of Düzce Province, Turkey*. Paper presented at the 15th World Conference on Earthquake Engineering, Lisbon, Portugal.

Koçkar, M. K., Akgün, H., Eker, A. M., & Cambazoğlu, S. (2011). *Engineering geological and geotechnical characteristics of Ankara clay*. Abstract presented at the European Clay Conference, Antalya, Turkey.

Eker, A. M., Dikmen, M., Cambazoğlu, S., Düzgün, Ş. H., & Akgün, H. (2011). *Preparation and analysis of data sets in landslide susceptibility mapping*. Abstract presented at the 64th Geology Congress of Turkey, Ankara, Turkey.

HOBBIES

Rock climbing.